2020

Experimental and Computational Investigation of Plume Surface Interactions in Vacuum Microgravity

Wesley Chambers
University of Central Florida

STARS Citation

Chambers, Wesley, "Experimental and Computational Investigation of Plume Surface Interactions in Vacuum Microgravity" (2020). *Electronic Theses and Dissertations, 2020-*. 192.
https://stars.library.ucf.edu/etd2020/192

EXPERIMENTAL AND COMPUTATIONAL INVESTIGATIONS OF PLUME SURFACE INTERACTIONS IN VACUUM MICROGRAVITY

by

WESLEY ALLEN CHAMBERS
B.S. University of Central Florida, 2012

A dissertation submitted in partial fulfillment of the requirements
for the degree of Doctor of Philosophy
in the Department of Physics
in the College of Sciences
at the University of Central Florida
Orlando, Florida

Summer Term
2020

Major Professors: Daniel T. Britt and Adrienne R. Dove

ABSTRACT

Plume surface interactions (PSI) are caused by rocket exhaust impinging on planetary surfaces. PSI-induced environmental changes pose hazards to spacecraft and astronauts; thus, it is crucial to understand the gas-particle dynamics of these systems. We have conducted novel experimental and computational work to study PSI effects in relevant vacuum microgravity environments. To study flow effects and regolith instability we developed a computational model that describes the gas flow through a porous medium based on Darcy's Law. This flow depends on regolith properties, and the resulting subsurface pressure distribution is used to estimate ejecta mass. We find flow behaviors and the resulting ejecta are significantly affected by the surface pressure distribution, pulse duration, and material properties. We have also developed an experimental apparatus, the Gas Regolith Interaction Testbed (GRIT), for studying PSI in vacuum microgravity in the UCF Center for Microgravity Research Drop Tower. It consists of a small, cylindrical vacuum chamber in which a cold gas jet interacts with a bed of regolith simulant. Video data is analyzed to determine PSI trends based on gravity level, nozzle distance, simulant type, and plume duration. We observe PSI effects ranging from perturbation of the granular media to ejection of the entire simulant mass. Phenomena are significantly more pronounced for experiments conducted at microgravity than at Earth gravity (1*g*). We measure peak ejecta velocities up to tens of m/s, and note how particle properties, jet distance, and pulse duration affect ejecta angle and cratering depth. Our numerical and experimental results have implications for the validity of existing studies of PSI that are conducted in 1*g* and under ambient conditions, and can be used to inform modeling, lander design, and risk assessment for future missions that will aim to land on or interact with planetary surfaces.

Deus pro nobis.

ACKNOWLEDGMENTS

This dissertation is the culmination of seven years of work, but it is fitting to begin by recognizing those who put me on this path. A hearty thanks to my high school teachers: Scott Smith, Lucy-Kate Walton, Missy Duncan, Gregg Thompson, Michael Phillips, and my track coach Michael Lambert. Lawrence Bigelow and Cheryl Cantwell taught the college classes which led me to switch my undergraduate major to physics. Professor Cantwell was exacting and taught with extraordinary care. Professor Bigelow won me over to physics with his clarity and wit. I hope this work demonstrates at least some of the mastery he expects from his students.

I am particularly grateful for the instruction of Joseph Harrington, Robert Peale, Niels da Vitoria Lobo, Michael Artiaga, and Samuel Gaustad, as well as the kindness and encouragement of Humberto Campins, Elena Flitsiyan, and Masahiro Ishigami.

I would like to thank my dissertation committee for their help and encouragement over the years: Daniel Britt, for his support, advice, expertise, and motivation; Philip Metzger, for giving me the opportunity to get involved in his area of research; Adrienne Dove, who has gone above and beyond the call of duty to support and advise me; Joshua Colwell, who taught me to value both precision and concision; and Zhisheng Shuai, who has kindly provided advice and feedback on computational mathematics.

To Patricia Szczerba at Florida Space Institute, and Esperanza Soto, Elizabeth Rivera, and the other administrative staff at the UCF Physics Department, I owe a huge debt of gratitude. The wheels of science would grind to a halt instantly without their support. And Esperanza, thank you for graciously putting up with all my late registration forms.

I could not have completed my research without the assistance of Seamus Anderson, Jacob Anthony, Tyler Cox, Michael Fraser, Gillian Gomer, Raquel Guzman, Anthony Meola, Cody Schultz, and the other students who have worked at the Center for Microgravity Research.

I am grateful for my fellow graduate students in this journey, including Jon Lee, Tommy Boykin, Ryan Challener, Katie McIntyre, Jenny Larson, Mary Hinkle, and Stephanie Eckert. Special thanks to Stephanie Jarmak, my academic cousin, for her encouragement, friendship, and keeping me on track for those pesky academic deadlines.

Thank you to Glenn Perez, whose invitation to tour Kennedy Space Center first put NASA on my radar as a potential career goal. He encouraged me to apply to several opportunities at NASA and has continued to encourage me in my career.

My thesis work began through an internship at Langley Research Center. Thank you to David Reeves and Daniel Mazanek for their mentorship, support, and encouragement during and after my internship. To LaRC’s Space Mission Analysis Branch, my summer intern cohort, and our intern band Wooden House, thank you for an unforgettable summer.

Robert Suggs and Manish Mehta were invaluable mentors during my two semesters on site at Marshall Space Flight Center. Michael Goodman always showed interest in my work and provided thoughtful feedback. Nathan Curtis was a huge encouragement to me, a weather advisor, and a friend.

To the baristas and coffee shops which have kept me caffeinated and provided an office away from the office, I am eternally grateful: Axum, House Blend, the short-lived Kaioen, Palate, Duo58, and, especially during my last year of writing, Foxtail.

My friends and community have brought a special joy to this academic journey. At the risk of omitting someone I ought not, there are few people I should mention by name: Burk

Parsons, for his loving and faithful leadership; Don Bailey, a shepherd and friend; Kevin Struyk; Rey Villavicencio; David Zima; Kevin and Lisa Kennedy; Eric and Debbie Johnson; Uncle Johnny and Kim Armstrong; Timmy and Courtney Johnson; Sam and Lillian Johnson; Matt and Chelsea Armstrong, who let me crash at their place during my final writing stint; Tekkie; Joseph Jackson; Timothy Fretwell; Ethan and Sarah Kern; Drew and Amanda Pace; Mike and Mindy Tedeschi; Robert Krahn; Andrew and Melodie Desmond; Chase Chazal; Bruno and Sloan Silva; Rachel Clunn; David and Jessie Ayuso; Chris and Juli Erickson; Josh and Ashley Foltz; Callie Parsons; Vivi and Jake del Campo; Bob Johnson; John Miles; Bradley Knudsen; Steve Simkins; Michael Rogers; Kelly Chambers. To quote the Irish, “It is in the shelter of each other that the people live.”

Thank you to my Virginia family who hosted, supported, and encouraged me during my summer stint at Langley: Uncle Jon and Aunt Chris, Megan, and Lindsey; Uncle Kent and Aunt Darlene; and my grandmother, Toney Chambers.

To those who have put up with more than I know and supported me unfailingly through this whole endeavor, to my father, Mark, who first taught me to love space, to my mother, Alana, an ever-ready ear and support, and to my siblings and siblings-in-law, Gisele, Aaron, Robyn, and Ethan: I love you all and thank God for the blessing you are to me.

TABLE OF CONTENTS

LIST OF FIGURES

LIST OF TABLES

LIST OF ABBREVIATIONS AND ACRONYMS

ARM	Asteroid Redirect Mission
BCF	Bearing Capacity Failure
CLASS	Center for Lunar and Asteroid Surface Science
CMR	Center for Microgravity Research
DDF	Diffusion Driven Flow
DGE	Diffused Gas Erosion
DGEE	Diffuse Gas Explosive Eruption
FDM	Finite Difference Method
GRIT	Gas Regolith Interaction Testbed
LaRC	Langley Research Center
MSFC	Marshall Space Flight Center
NASA	National Aeronautics and Space Administration
NEA	Near Earth Asteroid
OSIRIS-REx	Origins, Spectral Interpretation, Resource Identification, Security, Regolith Explorer
PSI	Plume Surface Interaction
PyRIC	Python Regolith Instability Calculator
UCF	University of Central Florida
VSE	Viscous Shear Erosion

INTRODUCTION

Earth, air, and gravity. Interaction between these components form the basis of this investigation into plume surface interactions (PSI). Earth, or more specifically granular material, resists general description and scaling laws because its properties vary widely. Fluid dynamics is notoriously difficult as solutions must be tailored to individual problems. Fluid dynamic equations do not typically admit analytic solutions and demand significant computing resources. Gravity is ostensibly simpler, mathematically speaking, but only a handful of people have intuition for what life is like in its absence. And gravity stubbornly refuses to cooperate when we might wish to shut it off for experiment’s sake.

Granular media, gas, and gravity—or lack thereof. Understanding each individually is a challenge, and this investigation seeks to understand something of their interactions. We care because these are the types of interactions which do and will occur as spacecraft land on other planetary surfaces. Spacecraft landing on airless bodies must either use retro-propulsion to land or else mechanically dampen the landing impact force. When the former method is employed, rocket exhaust interacts with the planetary surface and may create hazardous conditions—either to the descending spacecraft itself, or to surrounding assets, or both. These interactions between a rocket exhaust plume and a nearby surface are aptly termed Plume Surface Interactions, or PSI.

Planetary surface operations are on the rise. China has landed the second lunar rover in its Chang’e Project, and NASA’s Artemis Program aims to return humans to the lunar surface by 2024. Indian and Israeli spacecraft recently attempted lunar landings. Japan’s space agency has recently collected samples from an asteroid with its Hayabusa2 mission, and it has another mission in the works to sample the Martian moon Phobos. NASA’s own OSIRIS-REx spacecraft will make an asteroid sampling attempt in late 2020 of the asteroid Bennu. As missions to planetary surfaces become more frequent, understanding PSI becomes increasingly important.

Physics Background

A plume is the jet of exhaust gas expelled from a rocket engine, out the nozzle, into the engine's environment. The behavior of rocket plumes is itself a subject of research, and their thermal and chemical effects must be considered in rocket design. For our purposes, however, the source of the plume is relevant only insofar as it determines plume properties: the composition, velocity, density, and temperature of flow, whatever its origin might be. Exhaust gasses from a rocket nozzle exit at supersonic speeds and are considered over- or under-expanded based on the relative density of the exhaust gas to the ambient atmosphere. Over-expanded plumes are less dense than ambient pressure and pressed inward after exiting the nozzle; under-expanded plumes grow in width after exiting. In either case, supersonic jets may produce a shock structure in the resulting plume which produces variations in pressure along the jet. Ideally, exhaust gas pressure matches ambient pressure when exiting a rocket nozzle, since over- or under-expansion reduces thrust efficiency. In the vacuum of space this means using the largest nozzle bell practicable, since the ambient pressure is effectively zero.

Figure 1: The exhaust plume trails out beneath this Atlas V rocket as it launches from the Florida coast. The edges of the plume are rough, indicating turbulent flow due to Earth's relatively thick atmosphere.

Source: NASA
https://www.nasa.gov/image-feature/atlas-v-lift-off-for-osiris-rex-mission

Besides affecting expansion of the exhaust plume, ambient pressure also affects collimation and dissipation of the flow. All other things equal, higher exhaust gas density is more likely to be turbulent. Figure 1 shows the turbulent exhaust flow due to a rocket launch from Earth. Thicker atmospheres will dissipate exhaust flows more efficiently. Thinner atmospheres less so, while still collimating flow. As the ambient pressure tends toward zero, flow is no longer collimated by the surrounding atmosphere and expands freely. This expansion may rarefy the flow, meaning gas molecules are more accurately treated as particles rather than a fluid. In the free-molecular flow regime, the Navier-Stokes equations, which describe fluid motion, are no longer applicable. In between, the flow is considered in a transition regime. The exhaust plume then, like PSI itself, is determined by the characteristics of the rocket engine and its environment.

On reaching a surface, the flow impinges and imparts momentum to the surface. In our study, we consider gas jets directed orthogonally against a flat surface. In this case, flow away from this impingement centerline is axisymmetric. A stagnation region results directly underneath the engine, and flow is directed outward along the surface. This effectively produces an axisymmetric pressure distribution across the surface, into which gas will diffuse if the substrate is porous. This diffusion is described Darcy's Law, which is derived from the Navier-Stokes equation and calculates continuum flow of a fluid through a porous medium. We will discuss this equation and detail its use in the next chapter.

Rocky planetary bodies do not typically have a uniform, solid surface. They are covered in *regolith*, lit. “blanket of stone”: unconsolidated material varying in grain size depending on the planet's size, mechanics, evolution, and the presence of an atmosphere. This material is also often referred to as soil, dust, or even dirt, though not without some pushback. Soil on Earth implies the presence of life and organic material. As of yet, while organic matter has been found on other bodies, life is only known to exist on our planet. Dust has no clear definition, though it typically refers to fine material, and dirt is borrowed as a colloquial term. We will use some of these terms interchangeably where their descriptions are appropriately analogous to regolith.

Our investigation is interested first in plume interactions with asteroid surfaces, but we also consider PSI experiments related to the lunar surface, and our results have applicability to PSI in general. Asteroid regolith properties vary considerably. Unlike depictions in popular media, most small asteroids are not monolithic structures, but rather aggregate structures of loosely consolidated material. The few exceptions to this are so-called metallic asteroids, which may be the surviving cores of differentiated bodies. More commonly, asteroids formed by aggregation over the history of the solar system and the majority did not differentiate. Their surfaces, however, vary from the surface of Itokawa—with its regions of mm and cm size regolith (Susorney et al., 2019)—to the blocky regolith of Bennu with its high prevalence of boulders (Walsh et al., 2019) shown in Figure 2. Lunar regolith is fine grained and abrasive, pulverized by tiny meteoroids impacting the surface and churning it over the past few billion years (McKay et al., 1991). This process, termed impact gardening, variously fuses and breaks regolith grains, creating a glassy texture to individual particles. The surface is fluffy, low in density, and relatively impermeable due to small particle size.

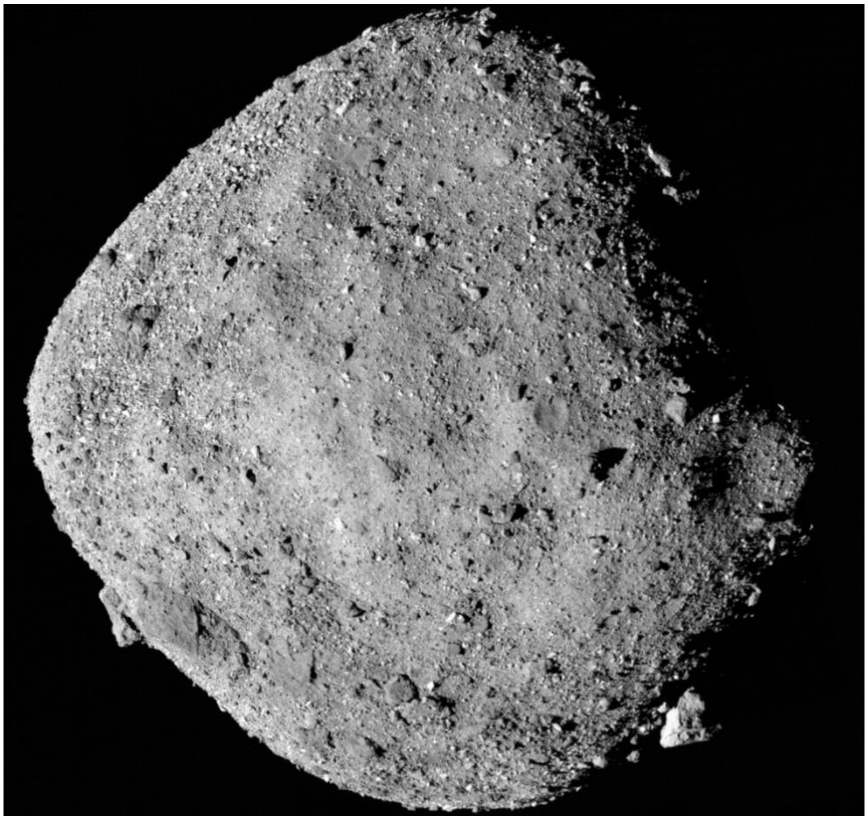

Figure 2: The asteroid Bennu, seen from the OSIRIS-REx spacecraft. Approximately half a kilometer in diameter, Bennu's surface is covered with unconsolidated regolith and boulders. Over 200 of these boulders exceed 10 meters in size (Walsh et al., 2019).

Source: NASA/Goddard/University of Arizona
https://www.nasa.gov/press-release/nasa-s-newly-arrived-osiris-rex-spacecraft-already-discovers-water-on-asteroid

PSI as a whole, the focus of our endeavor, combines two complex phenomena—rocket plumes and planetary surfaces—and as such resists general description or analysis. This is why, as we will see shortly, efforts to study PSI so far have primarily focused on studying specific missions. The work that has been done, however, reveals a few distinct behaviors. The erosive and cratering interactions between rocket exhaust and a particulate medium have been classified into five phenomena (Mehta, 2010). Bearing capacity failure (BCF) results when downward plume pressure exceeds the strength of the medium. Viscous shear erosion (VSE) is caused by gas drag across the surface of the medium, such as during an Apollo lunar landing shown in Figure 3. Exhaust gasses moving through the regolith cause diffusion driven flow (DDF). In the event of engine shutdown, diffuse gas erosion (DGE) may result. Most recently, a subset of DGE was identified in the case of engine pulsing; this was termed diffuse gas explosive eruption (DGEE) (Mehta, 2010).

Gas flow may occur in two different states—continuous or discrete—and granular materials behave in solid-like or fluid-like fashion, depending on grain size, packing density, and other physical properties. As PSI combines these two complex phenomena, which themselves resist prediction, we should not be surprised to see similar complexity in its behavior. We gain insight, however, by conducting a systematic test of PSI as a general investigation into its phenomena.

Figure 3: Apollo 11 landing on the Moon. The Lunar Module obscures the bottom of the frame, while the lunar surface is seen in the upper two-thirds of the image. Radial streams of dust entrained in the exhaust flow move up and left across the frame.

Source: NASA/GoneToPlaid
https://www.hq.nasa.gov/alsj/a11/video11.html

Prior Research

Historically, many studies into PSI effects have been tailored to fit a specific mission. Research into PSI began in support of the Apollo and Surveyor programs. A preliminary PSI theory was developed by Roberts (1964), which attempted to predict soil erosion due to shear stresses on regolith caused by gas flow. He developed semi-empirical equations to calculate plume impingement pressure in a vacuum and then applied these to erosion predictions for the lunar surface (Roberts, 1964).

Cold gas PSI experiments were conducted in vacuum at NASA's Langley Research Center (LaRC) (Land & Clark, 1965; Land & Scholl, 1969), taking advantage of LaRC's large, spherical vacuum chambers. The former of these conducted tests aluminum oxide particles with a supersonic jet and surface pressures ranging from 80 to 112 kPa. They determined cratering rate increased with particle size, and cratering profiles show a depth maximum off-center; that is, a minor peak sits in the center of the ejecta region. Experiments reported in the latter study used a helium gas thruster mounted on a track to simulate the lunar landing. These experiments were also conducted in ambient vacuum, with glass beads and gravel as simulant. The researchers note that erosion increases significantly with thrusting duration and recommended as fast a descent as possible to minimize erosive effects. In both cases, the mission-focused mindset is clear by the researcher's priorities: visibility beneath the plume is a primary focus, and the latter study gives its results in units scaled up to full-size from the model test conducted. We will return to latter this study in the next chapter as we compare our computational results to their experiment.

Other cold gas and hot fire tests were conducted at ambient pressure (Alexander et al., 1966). These used glass beads and various soils as material substrates and describe erosive phenomena similar to that of Land and Clark (1965). Above a certain thrusting threshold, however, they describe a different set of phenomena: after a brief pocket is formed in the surface, jet impingement produces explosive soil blowout, followed by erosive action which deepens but does not as significantly widen the erosion crater.

Contemporary to this work, researchers developed a physics model for understanding gas flow through regolith (Scott & Ko, 1968). It employs Darcy's Law, the equation governing fluid flow through granular media, to give insight into the phenomena of PSI and quantitatively estimate regolith ejecta. It is Scott and Ko (1968) who first define and label three of the five PSI mechanisms we described above: viscous erosion, diffused gas erosion, and bearing capacity failure. Scott and Ko posit pressure differentials caused by gas diffusion as causing instability which then ejects regolith. Their key insight is into the nature of gas flow, and the nature of soil instability, which may occur on or off center depending on pulse duration Their model forms the basis for our investigation, and we will return to it in more detail in the next chapter.

The next series of investigations concerned the Viking missions, and were concerned with how PSI might affect those spacecraft's landings. A brief investigation by Clark found canted thrusters reduce the volume eroded by PSI, compared to engines pointed directly downward (Clark, 1970). Three years later, a more comprehensive investigation would follow—a two-part report on site alteration effects predicted by the Viking spacecraft landing (Romine et al., 1973). Part I was concerned with site alteration effects, or PSI, and tested an array of rocket nozzle designs to mitigate these potential effects. They note a shift in PSI behavior from viscous erosion to either bearing capacity failure or diffused gas erosion as nozzle distance to the surface decreases in time.

A gap in the literature extends from the early 1970's until the early 2000's. As PSI research was primarily mission-driven, there was a gap in interest during these years. The next study to take up PSI was a conference paper in by Donahue et al. (2005), where aside from a loosely related hydraulics paper, the authors pick up by citing the body of work conducted for the Lunar and Martian exploration campaigns. The hydraulics paper studied crater formation from impinging water jets and found crater depth increases with the logarithm of time (Rajaratnam & Beltaos, 1977). Donahue et al. (2005) test the time-dependence of crater formation during PSI in 1*g* and find it also increases with the logarithm of time .

The most recent work on PSI is divided between interest in various destinations. The work of Philip Metzger and others has focused on the moon as a destination as the Constellation program was ramping up. Work out of Kennedy Space Center was performed to analyze Apollo landing video and determine dust ejection angles and particle densities (Immer et al., 2011). Later experimental and forensic analysis of the lunar landings determined problems with Robert's (1964) understanding of soil erosion by shear stresses, as he assumed ideal transfer of momentum from gas to grains (Metzger et al., 2008). Later experimental and computational work on crater formation (Metzger et al., 2010) confirmed the cratering depth/time relationship seen by Donahue et al. (2005). This work also noted how transport within a deepening crater occurs tangential to the crater's surface, carried along by gas flow as it circulates back up and out of the forming crater.

As Mars was again the target of interest for the Phoenix and Mars Science Laboratory missions, work to study PSI effects in this environment was conducted by Manish Mehta, published in his dissertation (Mehta, 2010) and in a paper on the Phoenix landing itself (Mehta et al., 2011). His experimental work discovered the fifth PSI effect described above, Diffuse Gas Explosive Eruption, which occurs during pulsed thrusting and caused significantly higher erosive effects.

Research Outline

Our work expands on previous PSI investigations by conducting novel research into a previously unexamined regime of PSI: interactions in vacuum microgravity. The microgravity environment provides insight into so-called “masked phenomena;” behaviors that go unnoticed or simply do not appear in 1*g*. We also benefit from systematizing our experimental approach to understand PSI phenomena generally, rather than targeting a desired mission outcome. We seek to understand, what are the underlying physics to PSI?

In Chapter 2, we conduct computational investigations into PSI. We pick up where the work Scott and Ko (1968) left off, exploring the role of gas diffusion in regolith instability and ejecta. Motivated by the Asteroid Redirect Mission concept, we developed a gas diffusion and regolith instability solver to estimate ejecta mass and crater size. This was compared applied to a notional landing on an asteroid to determine whether or not a powered landing would produce hazardous ejecta. Results from this code were then applied to the experimental results of Land and Scholl (1969)in their 1*g*, vacuum chamber investigations of PSI to compare predictions of ejecta mass and crater shape.

Chapter 3 describes our novel experimental apparatus, Gas Regolith Interaction Testbed (GRIT), for studying PSI in vacuum microgravity in the UCF Drop Tower. It allows us to address the question, what are the effects of gas-jet interactions in vacuum microgravity, and how do they differ from interactions in 1*g*? We conducted an experiment campaign with four simulants, at two nozzle distances, and five pulse durations, in both microgravity and at 1*g*. The phenomena observed in this campaign are described and characterized in this chapter.

Chapter 4 describes the quantitative analysis performed on our dataset. Particle velocities, and crater size and mass are characterized. We then compare our results to prior work, and to the trends found in our own computational modeling.

MODELING PLUME SURFACE INTERACTIONS

Portions of this chapter and several figures are taken from "Regolith Instability Caused by Gas Diffusion: A Case Study of the Asteroid Redirect Mission" (Chambers & Metzger, 2016). This material is included with the permission of ASCE and may be downloaded for personal use only. Any other use requires prior permission of the American Society of Civil Engineers. This material may be found at https://doi.org/10.1061/9780784479971.008.

The Python Regolith Instability Calculator, or PyRIC, has been developed to predict regolith ejecta due to exhaust-plume interactions by modeling gas diffusion through a regolith substrate and determine potential instability from the resulting pressure gradients. When rocket exhaust impinges on a porous surface, it diffuses into the medium at a rate determined by the impingement pressure, exhaust gas properties, and the physical properties of the regolith. The flow of gas through a porous medium is described by Darcy's Law. Diffusing gas creates a pressure differential between the regolith and ambient atmosphere, destabilizing the region where gas flows, and lofting material if cohesion and gravity are insufficient to prevent ejecta. Model development was initially motivated by the possibility of an off-nominal powered ascent for NASA's Asteroid Redirect Mission (ARM), and this is the first case study we examine. Our broader goal, however, is to develop a physics-based model that allows rapid calculation of ejecta caused by plume surface interaction. We model this regolith destabilization by expanding on the method of Scott and Ko which uses Darcy's Law to calculate exhaust gas diffusion through regolith (1968).

Method and Model Description

Consider a rocket engine pointed toward the center of a cylindrical container of regolith. The engine may move vertically along this center axis. Its exhaust gasses impinge on the surface of the regolith and flow through the medium. This flow results in a subsurface pressure distribution which we use as a proxy for regolith instability. PyRIC consists of three components: a surface pressure calculator or data input, a flow solver, and an instability calculator. We will treat the flow solver first, then discuss surface pressure as an upper boundary condition, and finally discuss treatment of regolith instability.

Solving Darcy's Law

Gas flow through a porous medium is described by Darcy's Law. We apply it to rocket exhaust flowing through unconsolidated regolith. Because the engine points straight down at the surface, we may assume an axisymmetric surface pressure distribution, and use the axisymmetric version of Darcy's Law given by Equation 1.

$$\frac{\partial^2 p^2}{\partial z^2} + \frac{1}{r}\frac{\partial}{\partial r}\left(r\frac{\partial p^2}{\partial r}\right) = \frac{2n\mu}{k}\frac{\partial p}{\partial t} \qquad (1)$$

Here p is the gas pore pressure, r is the radial distance from the engine centerline, z is the depth beneath the surface, n and k and the porosity and permeability of the medium, respectively, and μ is the dynamic viscosity of the exhaust gas (Scott & Ko, 1968).

Finite Difference Method

Darcy's Law is solved in Python by implementing a finite difference method (FDM). The solution area is represented on a square grid with dimensions of radius and depth. The FDM algorithm given by Scott and Ko (1968) to solve Darcy's Law on a square grid is given by Equations 2 to 5. The pressure, radius, and depth in Equation 2 have been divided by characteristic pressure and length scales as shown in Equation 4. The time variable is nondimensionalized by these factors as shown in Equation 5. The resulting constant derived from these parameters (n, μ, k) collectively form a characteristic time which governs the rate at which gas diffuses through the medium.

$$\boldsymbol{P_{0,T+\Delta T} = P_0 + M\left[P_2^2 + P_4^2 + \left(1 + \frac{\Delta R}{2R_0}\right)P_1^2 + \left(1 - \frac{\Delta R}{2R_0}\right)P_3^2 - 4P_0^2\right]} \quad (2)$$

$$\boldsymbol{M = \frac{\Delta T}{(\Delta Z)^2}} \quad (3)$$

$$\Delta T = \frac{t}{t_0};\ P = \frac{p}{p_0}; R = \frac{r}{r_0}; Z = \frac{z}{r_0} \quad (4)$$

$$t_0 = \frac{2\mu n r_0^2}{k p_0} \quad (5)$$

This characteristic time, or time constant, gives us a sense of how the physical properties of the material will affect gas flow. The time constant increases with porosity and gas viscosity. Most important to note is permeability, which varies over orders of magnitude depending on regolith or simulant properties. When regolith is impermeable, the value for permeability is small, and the time constant large. Permeable regolith results in a small time constant and rapid flow; thus the characteristic time gives us a sense of the temporal scale on which flow will occur.

The size of our computational grid is chosen either to match the experiment itself or, when simulating a real-world ascent or landing, large enough to mitigate or avoid edge effects due to the grid boundary. The upper boundary condition is a surface pressure distribution cause by impinging gas; we discuss this separately below. The lower and outer boundaries of the simulation grid are treated as hard surfaces. Equation 6, also given by Scott and Ko (1968), is used for the innermost grid squares as there is no flow across the centerline, and the equations above are not valid for a radius of zero.

$$P_{0,T+\Delta T} = P_0 + M[P_2^2 + P_4^2 + 4P_1^2 - 6P_0^2] \qquad (6)$$

Algorithm Stability and Model Improvements

The factor M described above depends on both the choice of time step and grid size. The stability of our numerical solution depends on the size of this factor. Choosing too small a grid size or too large a step size leads to computational errors. We do not have an analytic solution to algorithmic stability for this form of the equation, so stability is achieved by a trial and error approach, and find stable solutions generally obtain for $M = \frac{1}{10}$, though we also use smaller values to increase computational accuracy.

As noted by Scott and Ko (1968), sources of error in the FDM algorithm are rounding errors inherent in computational solutions, and truncation error due to the neglect of higher order terms in the approximation. Each of these necessitates a smaller simulation timestep, which increases computation time. In order to speed calculation time and improve stability, later version of our code implement adaptive time-stepping by pressure grid scaling.

Our algorithm becomes unstable when events happen too rapidly to calculate accurately. This happens when pressure gradients are at their highest. The timing of this maximum depends on whether the engine is ascending, descending, or stationary, and must be determined by trial and error. In this part of the simulation, we want a small time-step to accurately calculate the gas flow. Later on, however, as the simulation nears steady state, we may take larger time steps without significant loss of accuracy.

The maximum pressure in the simulation grid is used as a proxy for the maximum pressure gradient, as these two typically coincide. At each computational step, the simulation pressure grid is normalized by the maximum pressure, and the next time step is calculated using this scaled pressure. In this way, we maintain algorithm stability but also allow larger time steps as the simulation progresses, lower pressures are reached, and the resulting gradients shrink. We realize a significant reduction in computational time from this modification.

Surface Pressure Distribution

The upper boundary condition for the simulation grid is determined by the surface pressure distribution due to the rocket exhaust. This surface pressure distribution may be specified by the user if experimental data are available. When the data are incomplete, we may interpolate to fill out the boundary layer.

In some cases engine parameters are known but experimental data are unavailable. In this case we generate a surface pressure distribution according to Robert's (1964) semi-empirical model, given by Equations 7 and 8.

$$p = p_r \frac{k+2}{2}\left(\frac{h}{r_n}\right)^{-2}(\cos\theta)^{k+4} \qquad (7)$$

$$p_r = p_c(1+\gamma M_n^2)\left(1+\frac{\gamma-1}{2}M_n^2\right)^{-\frac{\gamma}{\gamma-1}} \qquad (8)$$

In these equations, θ is the angle as measured from the engine centerline, h is the height of the engine above the surface, p_c is the engine chamber pressure, r_n is the engine nozzle radius, M_n is the exhaust Mach number, γ is the exhaust heat capacity ratio, and $k \equiv \gamma(\gamma-1)M_n^2$. This distribution may be treated as static or vary with time to simulate engine ascent, descent, or pulsing behaviors. Below the critical engine height where the surface pressure equals the stagnation pressure, we treat the surface pressure distribution as equal to the stagnation pressure directly under the nozzle, and zero elsewhere.

Properties of Porous Materials

There several models in the literature for calculating regolith permeability. These all depend on the square of the mean particle diameter, meaning they differ by a constant factor, and estimates are typically within an order of magnitude. We use the Equation 9 and Equation 10 given by Krumbein and Monk (1943) to calculate regolith permeability.

$$k = 760 d_g^2 e^{-1.31\sigma_D} \tag{9}$$

$$\sigma_D = -\log_2 d \tag{10}$$

In this equation, d_g is the mean particle diameter in millimeters, and d is the standard deviation of the particle grains. The variable k is the soil permeability in darcys, a conventional unit of permeability with dimensions of length squared. For particle cohesion, we consult the values given by a survey of simulant materials which includes glass beads close in size to those used in some of our reference experiments (Klinkmüller et al., 2016).

Flow Behaviors and Instability Estimate

As exhaust gasses diffuse through regolith, they create a pore pressure difference between the regolith and the surface. This pressure difference may destabilize and loft regolith. We assume the regolith remains static and use the pressure difference to estimate the destabilization area. This approximation is more accurate for short-duration jetting. As we will see in comparison to experiment, however, the flow patterns provide insight even for longer-duration PSI events. Flow patterns are displayed by calculating pressure gradients within the simulation area. These may be displayed alongside or separately from contour plots of the subsurface pressure itself.

We consider two primary methods of calculating soil instability. Our goal is to determine whether or not the material in a given grid cell may be lofted during PSI. Our earlier work uses a method similar to that described by Scott and Ko (1968). The forces on a grid square are those due to the cell's own weight, the weight of cells above it, the differential pressure, and the cohesive forces binding it to surrounding material. This method simplifies the situation by considering the differential pressure across the cell in the vertical direction, the weight of the column above the grid square, and the cohesive force between the grid cell and its lower neighbor. This neglects frictional and cohesive forces along the sides of the grid cell. This method was applied to ARM where gravitational forces were nearly negligible, and so the weight of the column above had a relatively minor effect on results.

The second method considers the overall pressure differential between a grid square and the ambient pressure. If this difference exceeds the weight of the grid cell plus a cohesive strength calculated for the bottom surface of the cell, the grid cell is considered unstable. This is the method suggested by Mehta (2011) and employed in our treatment of the Land and Scholl (1969) experiment described below. In either case, these unstable grid cells are interpreted as ejected material and used to calculated ejecta radius and volume. This region is roughly crater shaped, and the widest point is taken to the radius. This point typically occurs at or just below the surface. Ejecta volume is calculated by integrating the ejecta profile around the central axis.

Python Method Description

The algorithm described above is implemented in Python, relying on the Numpy module to facilitate and speed array calculations. This program, the Python Regolith Instability Calculator (PyRIC) reads in a configuration file set up for the current simulation case. This configuration file may specify one or more runs varying parameters of interest. After setting the current parameter set, it checks to see whether or not this combination of parameters has been calculated already. If not, it begins a fresh calculation. If so, and the run is incomplete, it picks up where the incomplete calculation left off. If complete, the run is skipped.

For a new calculation set, PyRIC initializes the simulation grid and sets the upper boundary condition as a calculated or interpolated surface pressure distribution according to the method described above. This is illustrated in Figure 4 below. PyRIC implements the FDM described in Equations 2 through 6 by array addition. Rather than looping through each individual array, a significant reduction in computational time is achieved by copying and shifting arrays rather than looping through them. This method takes advantage of Numpy’s optimized array operations rather than relatively slow Python loops.

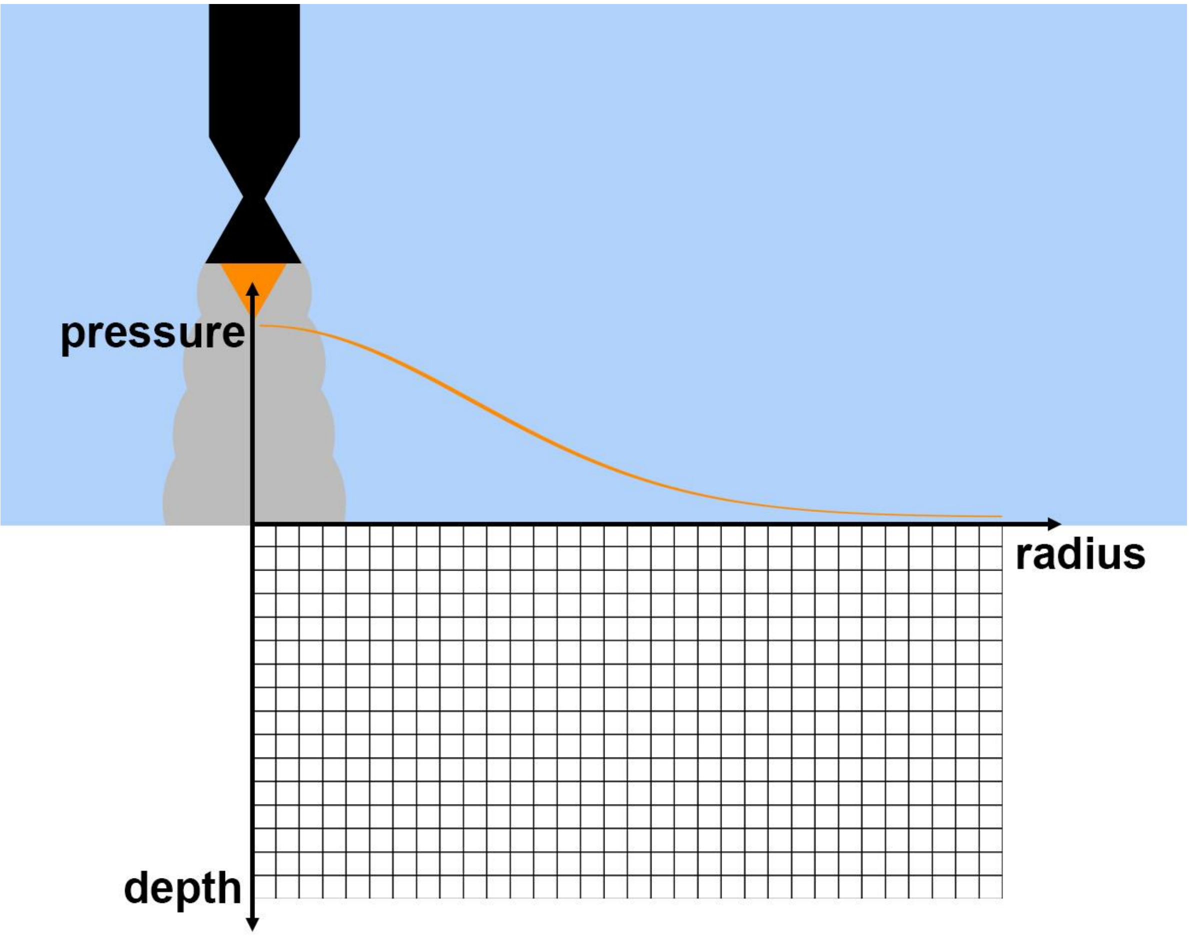

Figure 4: This cartoon illustrates the concept behind our model. An engine pointed downward produces exhaust gasses which impinge on a surface. The pressure distribution is axisymmetric. We solve an axisymmetric version of Darcy's Law on a square grid using this pressure distribution as the upper boundary condition.

After each timestep, the pressure grid is binned. Full bins are saved out to a compressed data file. The program then loops to the next time step and the algorithm repeats until the simulation time is complete. This first Python routine generates the flow profile for a given set of regolith properties, engine parameters, and ascent/descent profile. Once the flow has been solved for, a second routine takes this data as an input and applies one of the instability methods described above. This routine also generates the graphs and visualizations used below.

Model Verification

As a sanity check to this Python routine, we choose a standard model run with engine chamber pressure at $1000\ kPa$, soil density at $1500\,\frac{kg}{m^3}$, permeability at $1\ \times 10^{-10}\ m^2$, nozzle height at $1\ m$, and impingement duration at $1\ s$. These are chosen to be round numbers in the neighborhood of our actual experimental parameters. We vary these model parameters to observe how instability behavior changes with each variable. This verification series uses Mehta's (2011) ambient pressure difference method to calculate soil instability area. This method was found to be more accurate when compared to the experimental data in Land and Scholl (1969).

Figure 5 and Figure 6 below show results for microgravity (here set to $10^{-4}g$; the term "microgravity" is used broadly for very low gravity environments) and Earth gravity. Many of the trends are intuitive. Instability, interpreted as regolith ejecta, decreases with increased soil density (and therefore weight) or cohesion. It increases with gas impingement duration and engine chamber pressure.

The nature of these trends, however, may not be as intuitive in microgravity. While ejecta does decrease with density in microgravity, the magnitude of the effect is much less pronounced. This is because gravity is no longer the dominant force. The stair-step behavior we see is likely due to grid layers and may not be physical. Ejecta volume grows rapidly with impingement time in microgravity. It also increases in 1 g, but the increase tapers toward a maximum, due to the pressure gradient reaching a steady state. Small irregularities are again likely an artifact of grid size; the point worth noting is gravity's effect in both reducing ejecta magnitude and in governing the effect of impingement duration.

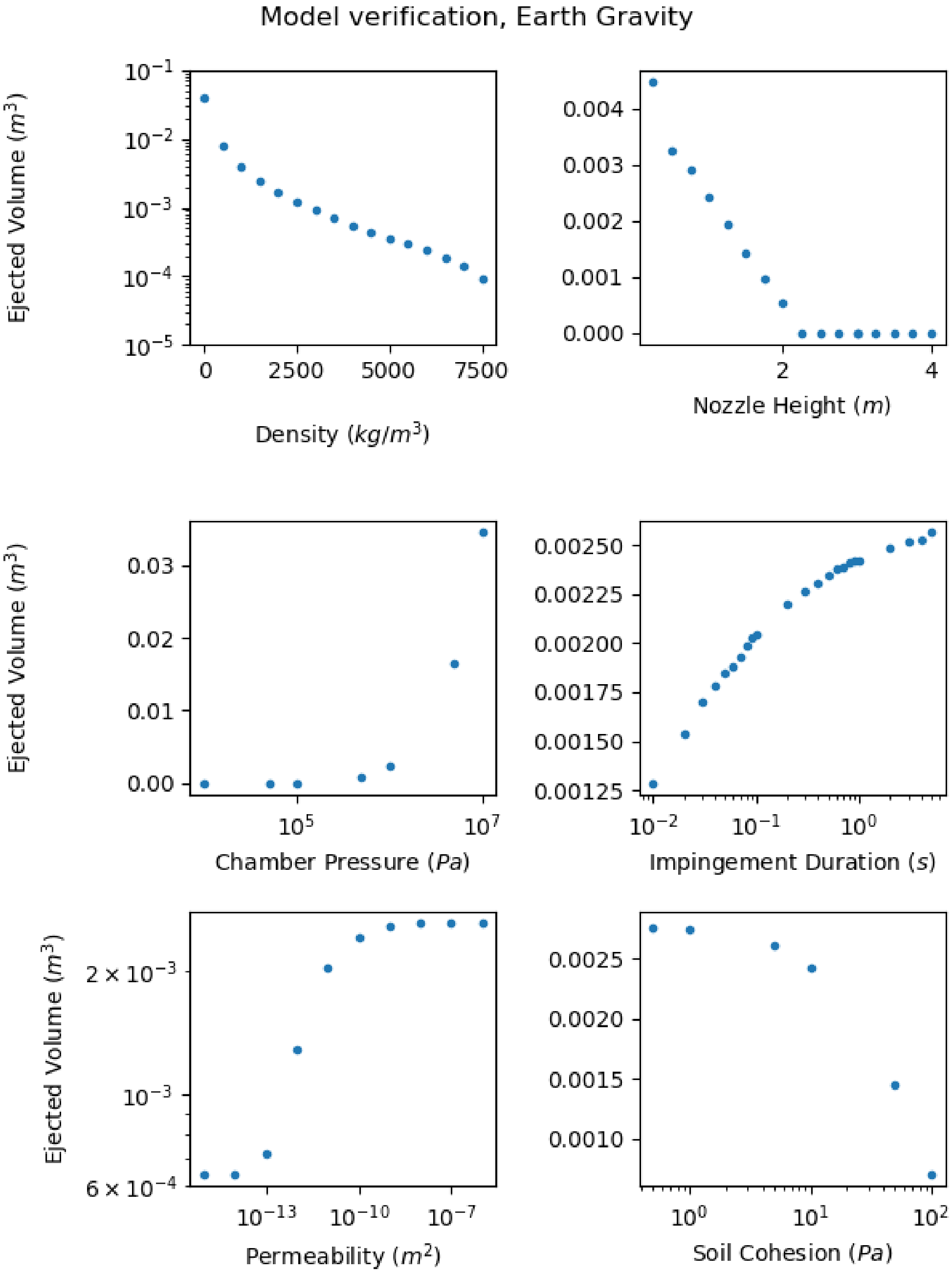

Figure 5: Ejecta verification trends for model runs at 1*g*. Note the presence of both logarithmic and linear axes, chosen to highlight each trend. Ejecta volume decreases with increasing regolith density, nozzle height, and soil cohesion. Just above two meters nozzle height, regolith ejected drops to zero. Ejecta volume increases with engine chamber pressure (a proxy for surface pressure), impingement duration, and permeability. The increase with permeability approaches an asymptotic maximum, beyond which the region of instability no longer increases.

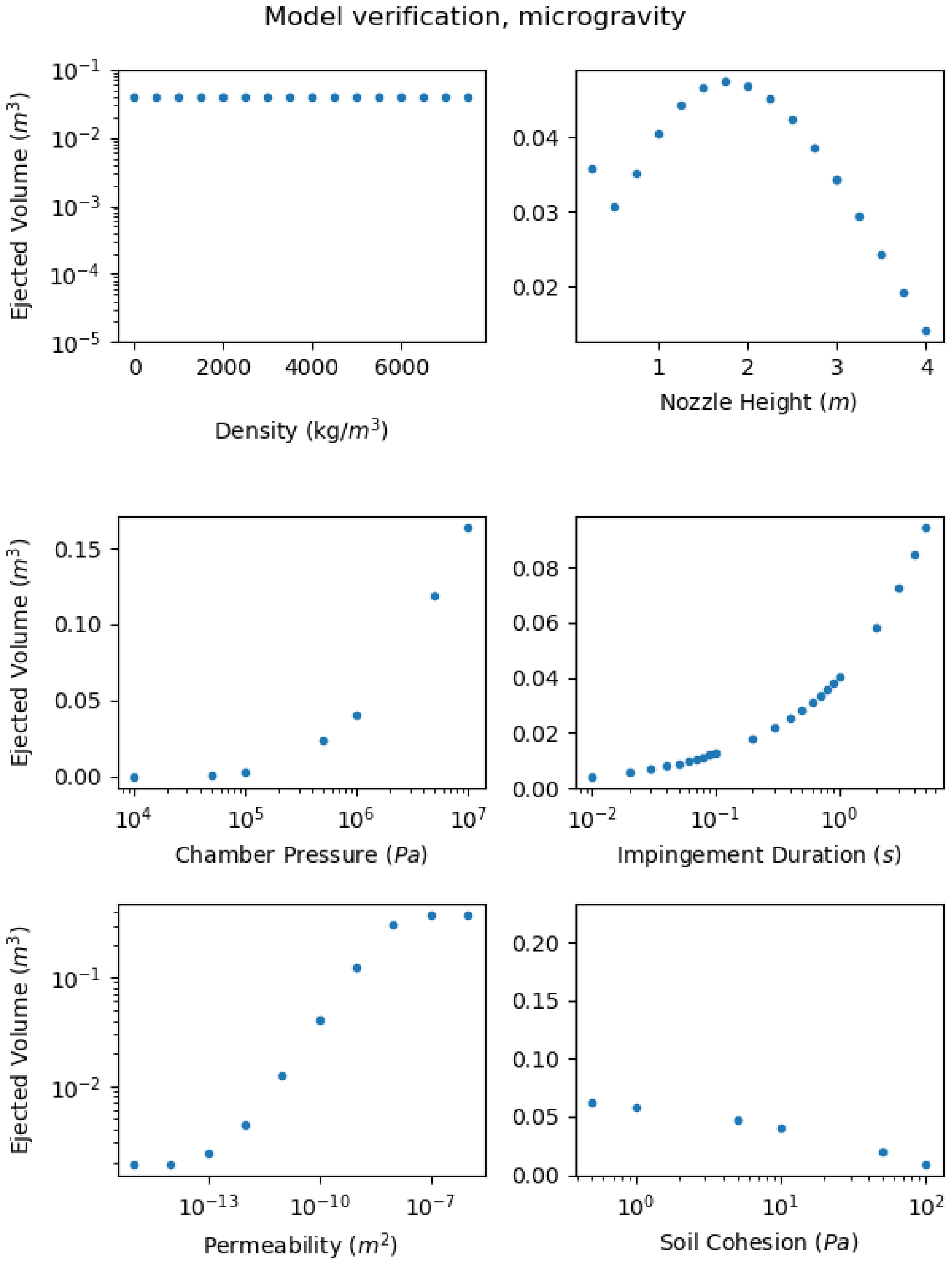

Figure 6: Ejecta verification trends for model runs in microgravity. Note the presence of both logarithmic and linear axes, chosen to highlight each trend. Trends with chamber pressure, permeability, and cohesion are similar to the 1*g* trial. Density does not affect the instability area significantly. Behavior of the impingement duration curve differs from the 1*g* trial. Most notably, ejecta due to gas diffusion might decrease below a certain height due to narrowing of the exhaust plume.

Most unintuitive may be the effect of nozzle height on ejecta volume in microgravity. Since a smaller pressure differential will loft regolith, the shape of the surface pressure distribution has an interesting effect. The narrower distribution caused by a nozzle close to the surface causes a smaller region of instability which broadens as the nozzle is tested further away. Our model predicts ejecta volume will increase first as the nozzle moves away, then decrease as the magnitude of the pressure distribution falls.

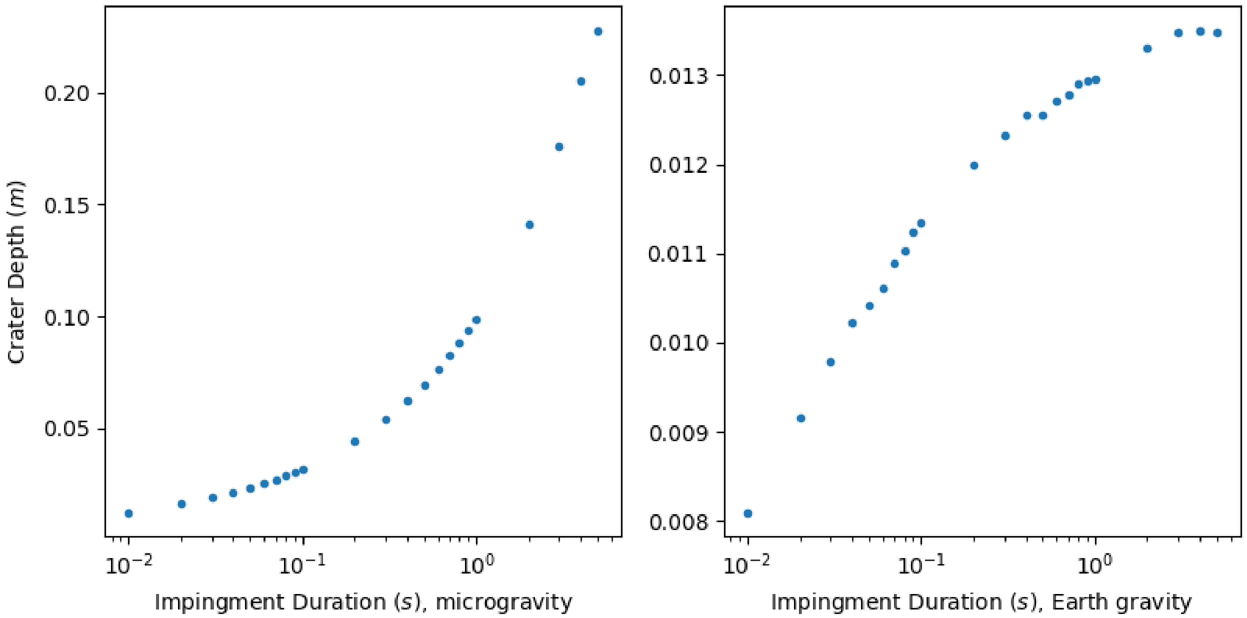

Figure 7: Crater depth as a function of impingement duration. At longer jetting durations, our model does not follow the log-linear trend observed by Donahue et al. (2005).

We may also compare our simulation results to the work of Donahue et al. (2005), which suggested depth increases with the logarithm of time. As seen in Figure 7, our model suggests this relationship holds for the beginning stages of crater growth when we consider PSI in 1*g*, then proceeds more slowly. The behavior seen in microgravity also deviates from this log-time relation.

Case Studies

Modeling the Asteroid Redirect Mission

The now-canceled Asteroid Redirect Mission (ARM) motivated the development of PyRIC and our work here represents the earliest efforts at PSI modeling. ARM had planned to visit, survey, and collect a boulder from a NEA (Mazanek et al., 2014). ARM's planned final approach to sample collection would have forgone use of nadir thrusters, coasting the final portion of its decent assisted only by gravity (Reeves et al., 2014). Due to uncertainty in our knowledge of asteroid properties, however, it was conceivable that thruster assisted ascent might become necessary. In this case, exhaust effects would be of primary importance.

We modeled PSI to understand the nature of exhaust-regolith interactions at a small body and quantify risk to the ARM spacecraft. In accordance with that goal, we chose values as conservatively as possible. Where parameters are well known but given as a range, the value most likely to cause an effect has been chosen. Where values were uncertain, parameters have been varied significantly in an attempt to capture the range of possible outcomes.

Surface pressure generated by the ARM spacecraft's engines was calculated using Equations 7 and 8 described above for an engine in the class of thrusters planned for use on the ARM spacecraft (Shen et al., 2014). In keeping with our goal of a conservative analysis, values for the engine parameters were independently chosen within the engine's operating range to maximize surface pressure, whether or not such a combination is physically possible.

The target asteroid properties at the time we conducted this study were poorly known. We chose parameters for Darcy's Law in accordance with best estimates for the target. Porosity is a numeric fraction and allowed to vary between 20-80%. Permeability depends on the regolith size distribution, which may vary over many orders of magnitude. Scott and Ko (1968) give values corresponding to a grain size of up to 1 mm; we extend this estimate to include values up to cm size particles by using the equation in Krumbein and Monk (1943). Finally, gas viscosity must be estimated for vacuum conditions and operating temperatures (Lemmon et al., n.d.). These choices are summarized in Table 1 and are used to vary the time constant given by Equation 5 over a range of possible values.

Table 1: ARM Simulation Parameter Ranges

Parameter	***Minimum***	***Maximum***	***Units***
Regolith Porosity	0.2	0.8	$fraction$
Gas Viscosity	1.00×10^{-6}	4.50×10^{-5}	$Pa \cdot s$
Regolith Permeability	1.00×10^{-14}	1.00×10^{-7}	m^2

We should note that Darcy's Law assumes a non-zero initial pressure within the porous medium. As an approximation, the initial inter-particulate pressure is set at $10^{-6} Pa$, well below the surface pressure values, and functionally zero for this simulation. The grid size is derived from examination of the surface pressure distribution, and the boundary terminated where it has tapered to a negligible amount; the depth of the grid is equal to half its width.

Regolith instability occurs when gas pressure gradients overcome weight and cohesive forces. These interactions are complex, and we make a few simplifying assumptions. First, we consider only the vertical component of the pressure gradient, assuming the horizontal component is comparatively small. Second, cohesion has been conservatively simplified by neglecting the effects of horizontally adjacent grid squares. An individual grid square is considered unstable if the block's weight and that above of the soil above it, together with the cohesive force directly beneath it, are unable to compensate for an upward gradient.

$$\Sigma F = F_{gas} - F_{cohesion} - F_{gravity} \tag{11}$$

This relationship is described by Equation 11, which is the sum of forces we consider. The gravitational contribution is small, but not entirely negligible, especially below the surface. At each grid square, the value we seek is the minimum cohesion necessary to hold the regolith together. We term this value the *critical cohesion*.

So far, we have turned a mission-oriented question into a physics question: Is the actual regolith cohesion on a near-earth asteroid larger than the critical cohesion? The answer depends on a few factors. Regolith properties, which wrap into the aforementioned time constant, have been discussed. The engine starting height determines peak pressure at the surface. The most recent configuration discussed in the literature places the spacecraft's engines seven meters above the ground (Belbin & Merrill, 2014; Shen et al., 2014). In the interest of examining where a problem might arise, we take this as our maximum height and step down at two meter intervals. Finally, the mass of the spacecraft determines the rate of ascent, and therefore the rate at which engine height increases over time. Our simulation is run for two cases: the spacecraft ascending with a boulder captured, and an ascent without payload. We assume these masses to be 78000 kg and 8000 kg, respectively. Runs are completed at an engine height of 50 meters.

Our program outputs a data visualization, which gives qualitative insight into the physical mechanisms leading to regolith instability. Figure 8 and Figure 9 show sample frames for runs with relatively high and relatively low time constants, respectively. Each run is classified by engine starting height, mass of the spacecraft, and time constant. The origin is in the upper left corner of each panel, with axes as indicated. The left panel of each frame shows relative pressure difference, where brighter regions correspond to higher values. The right panel indicates regions of potential instability; in this case, the lighter area. A grid square is *potentially unstable* where a non-zero, positive value of cohesion is required to keep the soil intact.

Recall that the time constant is primarily determined by regolith permeability, which in turn depends on grain size. A high time constant corresponds to fine regolith with low permeability. In this case, gas is unable to flow far into the soil, and remains near the radial centerline. As the spacecraft recedes, surface pressure decreases, and gas begins to reverse its flow. This creates an upward pressure gradient. Fine regolith tends to produce on-center instability due to this trapped "bubble" of gas just beneath the surface.

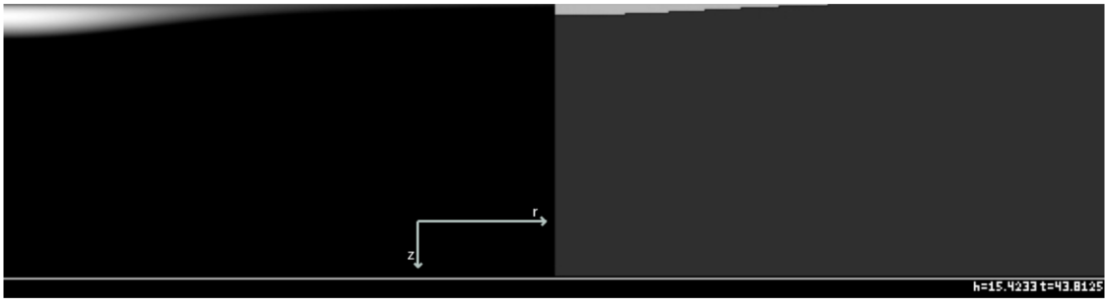

Figure 8: On the left, a visualization of the pressure gradient for a 5 m, 8000 kg, 10 s characteristic time model run. This demonstrates relatively impermeable regolith, as gas remains near the surface over the course of this simulation. At just over 43 seconds of simulated time, the engine has moved away, reducing the surface pressure and allowing trapped gas to diffuse upward. This creates an on-center region of instability, shown as the light region on the right half of this figure.

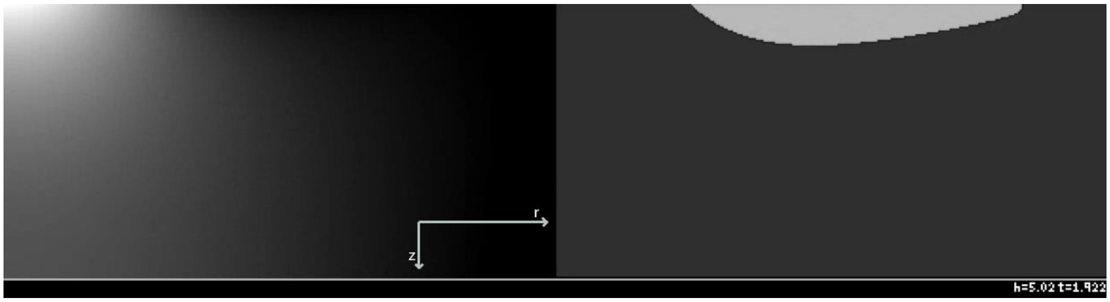

Figure 9: On the left, a visualization of the pressure gradient for a 5 m, 8000 kg, 1 ms characteristic time model run. At only 2 seconds of simulated time, gas has already diffused through the medium. Flow circulates outward and upward, creating an off-center region of instability shown on the right. As the engine ascends, gasses on-center diffuse upward and the unstable region shifts toward the center.

On the other hand, relatively permeable soil like that shown in Figure 9 first develops instability off center. Gas diffuses freely through the medium and, finding a much lower surface pressure off of centerline, circulates back up. As the engine ascends, and on-axis pressure decreases, instability develops on-center as well.

At each time step, critical cohesion values are generated for every grid square. Ultimately, however, we are only interested in the maximum value of critical cohesion for each entire run; that is, what must actual regolith cohesion be to prevent instability during the entire spacecraft ascent? These values are shown in Figure 10 for an 8000 kg spacecraft; the curves for a 78,000 kg spacecraft with captured boulder are qualitatively similar, though behaviors differ when the spacecraft ascends more slowly. A slower ascent increases jetting time near the surface, but peak pressure decreases over a longer period of time. As the time constant decreases, completing a run becomes much more computationally expensive. Because of this, the 1 and 3 m runs were not completed for all time constants. The general behavior of the 1 m curve, however has been captured.

Curiously, soil ejection is more likely for fine, relatively impermeable regolith. We reason this is due to the steeper pressure gradient resulting from the gas bubble trapped just under the surface. This only holds to a point, however, before the soil becomes fine enough (and the time constant high enough) to cut off gas diffusion. Though not displayed on the graph, the 3, 5, and 7 meter curves all drop off to zero as one moves toward the highest time constant. For very permeable regolith (relatively low time constant), critical cohesion moves back up. This appears to be due to gas diffusing rapidly through the medium. In between, we see intermediate behavior, where the regolith is prevents rapid diffusion, but is also permeable enough to prevent large pressure buildups. This corresponds to the lowest computed values of critical cohesion.

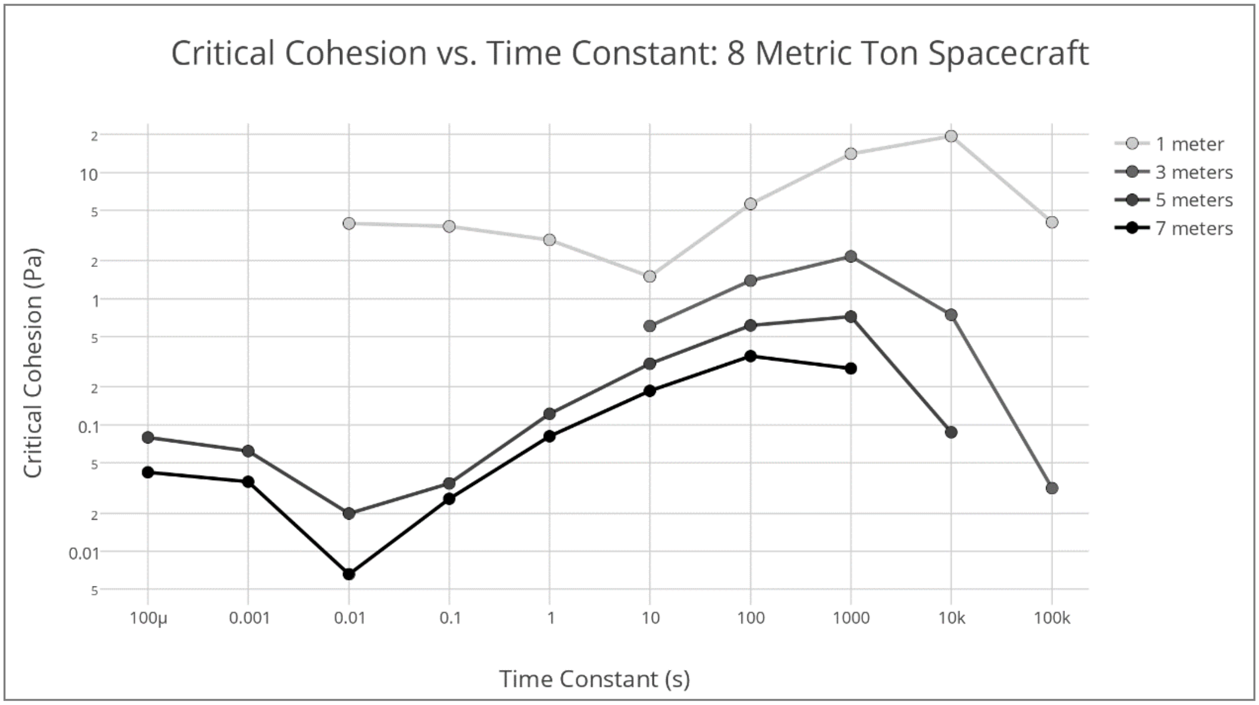

Figure 10: A log-log plot of critical cohesion vs. time constant, or characteristic time. A larger time constant corresponds to lower permeability regolith. The critical cohesion is the value of regolith cohesion needed to prevent ejecta during the simulation run. This value decreases as engine height increases.

Our program outputs visualization of both pressure magnitude and critical cohesion for time steps throughout the run. It appears that two distinct flow profiles are responsible for instability. For high permeability cases, gas can circulate quickly out and away from the engine centerline to regions of lower surface pressure. At this point gas migrates back to the surface, creating a negative pressure gradient. When permeability is low, gas penetration remains shallow, but subsiding surface pressure allows this bubble to escape back to the surface.

Critical cohesion values are condensed for each engine height in Table 2. This includes both the results plotted in Figure 10 and those computed for a 78 metric ton spacecraft. Though we believe rougher, more permeable soil to be likely on a target asteroid, we err on the side of caution by choosing the maximum value for each run.

Table 2: Maximum critical cohesion for all model runs as a function of engine height.

Initial height	Critical cohesion
1 m	19.46 Pa
3 m	2.16 Pa
5 m	0.76 Pa
7 m	0.40 Pa

We have developed a program to simulate potential instability in asteroid regolith caused by the exhaust plume of a thruster-assisted ascent of ARM’s spacecraft. This program produces a series of visualizations which aid in understanding the nature of regolith ejection beneath a rocket motor, as well as a quantitative analysis of required cohesion values. Due to uncertainty in asteroid properties, our goal has been to set as wide a buffer possible around actual mission parameters, hemming in the range of possible outcomes.

At present, the best estimate for actual regolith cohesion places a lower bound at 25 Pa (Small Bodies Assessment Group, 2014). For a nominal engine starting height of 7 m, over all time constants considered, actual regolith cohesion must be greater than 0.4 Pa to prevent soil ejection. Given this margin, and the conservative approach with which this analysis was conducted, we judge hazardous plume effects to be unlikely.

Even so, our qualitative results shed light on how soil ejection can occur. Gas trapped beneath the surface causes a pressure gradient, and in our case the spacecraft was allowed to recede gently under constant thrust. A sudden cutoff, however, would likely exacerbate the problem: a large drop in surface pressure would cause a steep gradient, increasing the chances of hazardous debris. Any mission planning to thrust near the surface of a small body must take effects such as these into consideration. Lowering the engine starting height to an impossible configuration of 1 meter, critical cohesion never exceeds 20 Pascals. Results at this height, however, should be considered inconclusive due to physical approximations.

Comparison to Land and Scholl Experiment

Introduction to Land/Scholl 1969

Leading up to the Apollo lunar landings, a research campaign into PSI was conducted by NASA scientists to assess mission hazards. One of these studies involved a series of experiments at Langley Research Center which took place in their large 50-foot vacuum chambers (Land & Scholl, 1969). They conducted 32 tests with a helium cold gas thruster rigged to translate vertically above a cylindrical tray of simulant. An experiment run consisted of the thruster being turned on and then lowered toward a simulant bed. Jetting typically continued after the nozzle reached its terminal height above the bed. The terminal nozzle height, particle size, descent rate, and other parameters were varied to study their effects on PSI. The parameters for these experiments are summarized in Table 3 below. We retrieve additional parameters for this set of experiments from a companion study by Hutton (1968).

The goal of this report was to aid Apollo engineers and mission planners; in the original report these quantities are given scaled up by constant factors to estimate actual erosion during a lunar landing. We convert the quantities from this paper before they are placed in Table 3. The goal of this report was to aid Apollo engineers and mission planners; our goal is to simulate the original experiments.

Table 3: Experiment parameters for each of the experiments conducted by Land and Scholl (1969). The original parameter table given in Land and Scholl's report is scaled up to represent values for an actual lunar landing. We recover the actual experiment values by dividing out these scaling factors.

Test	Thrust (N)	Descent Velocity (m/s)	Nozzle Terminal Height (cm)	Particle Diameter (mm)
1	24.5	2.36	4.2	0.21
2	27.1	2.22	9.0	0.21
6	9.4	0.31	4.0	0.58
7	6.5	0.24	3.6	0.32
5	8.7	0.34	4.0	1.3
9	8.7	0.22	3.4	4.8
10	8.8	0.34	3.6	7.91
4	9.4	1.05	3.4	1.3
3	23.6	1.88	7.3	1
24	56.0	0.73	2.3	0.49
25	81.0	0.73	1.9	0.49
26	30.1	0.82	2.2	0.49
35	22.0	0.59	3.7	0.49
37	21.9	0.68	4.8	0.49
38	22.3	0.73	6.8	0.49
39	21.7	0.64	9.5	0.49
28	33.3	0.67	2.5	0.49
29	21.3	1.28	3.1	0.49
31	21.3	2.28	1.2	0.49

Test	Thrust (N)	Descent Velocity (m/s)	Nozzle Terminal Height (cm)	Particle Diameter (mm)
32	24.1	0.61	1.1	0.49
8	9.4	0.24	3.9	0.11
15	30.0	0.81	1.4	0.07
16	23.1	0.72	2.2	0.07
19	24.5	1.19	1.5	9.54
46	36.3	0.79	1.9	0.49
47	17.1	0.77	1.9	0.49
48	11.1	0.75	1.9	0.49
49	72.2	0.76	2.0	0.49
51	25.4	0.71	1.7	1.3
52	47.7	0.73	1.7	1.3
54	24.5	0.77	1.4	1.3
55	68.1	0.77	1.5	1.3

For each experiment, Land and Scholl (1969) reported a time series of cratering cross-sections, derived by analyzing X-ray images taken during each experiment. We use these cross-sections to derive an ejected volume and use an estimate for simulant density to calculate ejected mass. Unfortunately, there are limitations to the data reported. For either commercial or security reasons, the X-ray method is only outlined briefly. No description of its method or accuracy are given. The data for each experiment are also often sparse. No upper boundary layer is clearly delineated, and the crater shapes retrieved often appear slanted or otherwise affected by systemic error.

It is also worth noting that the parameter space explored does not seem to conform to any pattern or method. Thrust, nozzle height and descent speed, and regolith particle size all seem chosen at random. Nonetheless, in spite of its shortcomings, this study contains one of the most comprehensively described and measured PSI experiment sets to date. It takes place in a vacuum, albeit at 1*g*, and these crater profiles allow us to validate our model against experimental data.

Figure 11 and Figure 12 below show experimental and simulated crater profiles, respectively, where each box in the figure above corresponds to a figure below. The former are taken from the Land and Scholl report, and show a time evolution of crater depth and diameter. Our simulated crater profiles are determined by a region of instability underneath the surface, using the absolute pressure method; that is, we determine where the subsurface pressure exceeds the cohesion of the soil and gravitational forces. The simulated crater profiles show moderate agreement with experiment profiles but tend to be narrower and deeper than the experiment profiles. For clarity, axes have been omitted from Figure 12 below; each chart may be seen in detail in Appendix C.

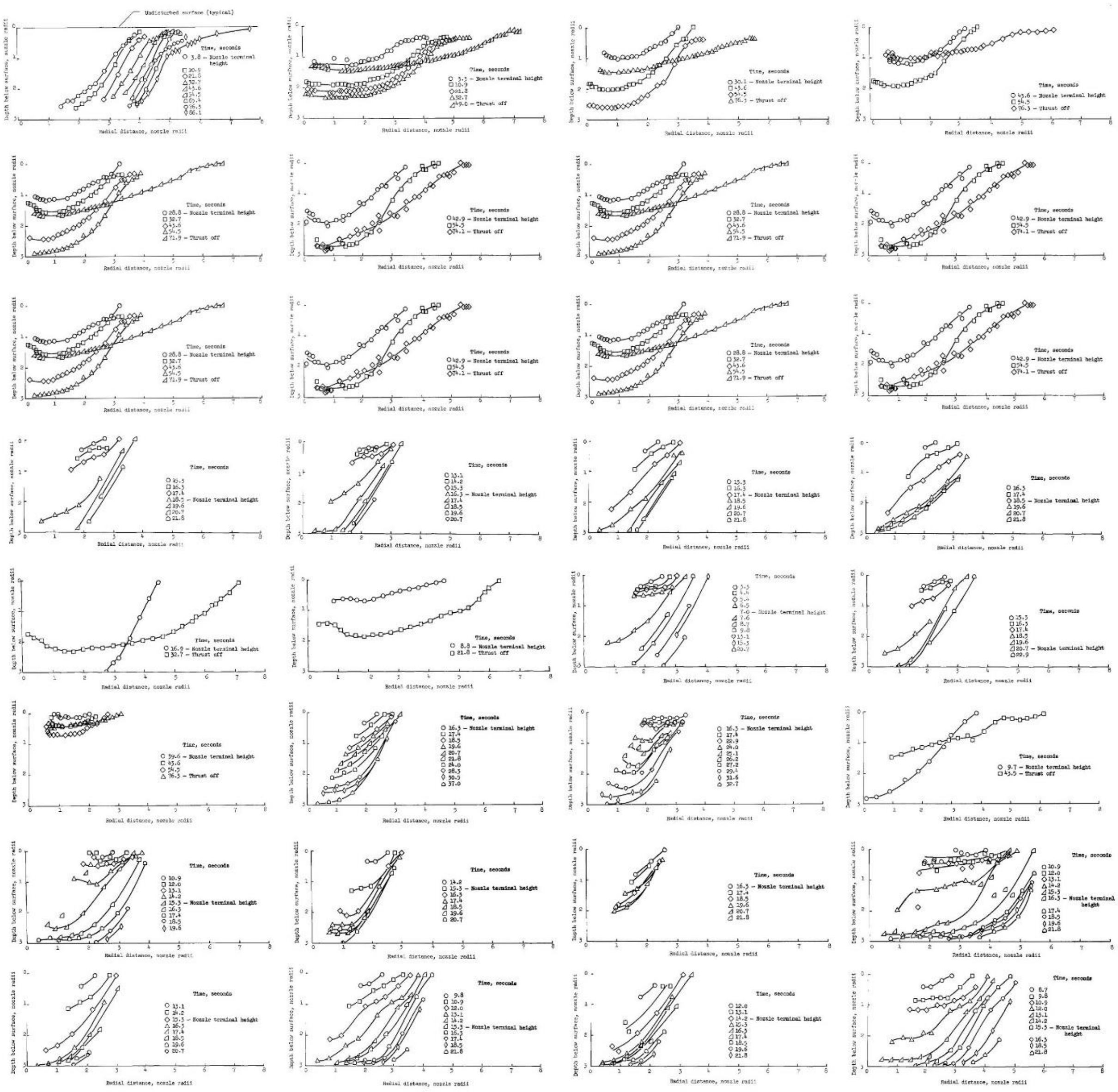

Figure 11: Transient crater profiles plotted for the 32 experiments conducted by Land and Scholl (1969). The data are often sparse, making rigorous comparison difficult. Original, high resolution figures may be found in the source report. Times are reported multiplied by a scaling factor which must be divided out to retrieve the experiment time elapsed. Images compiled from technical report by Land and Scholl (1969).

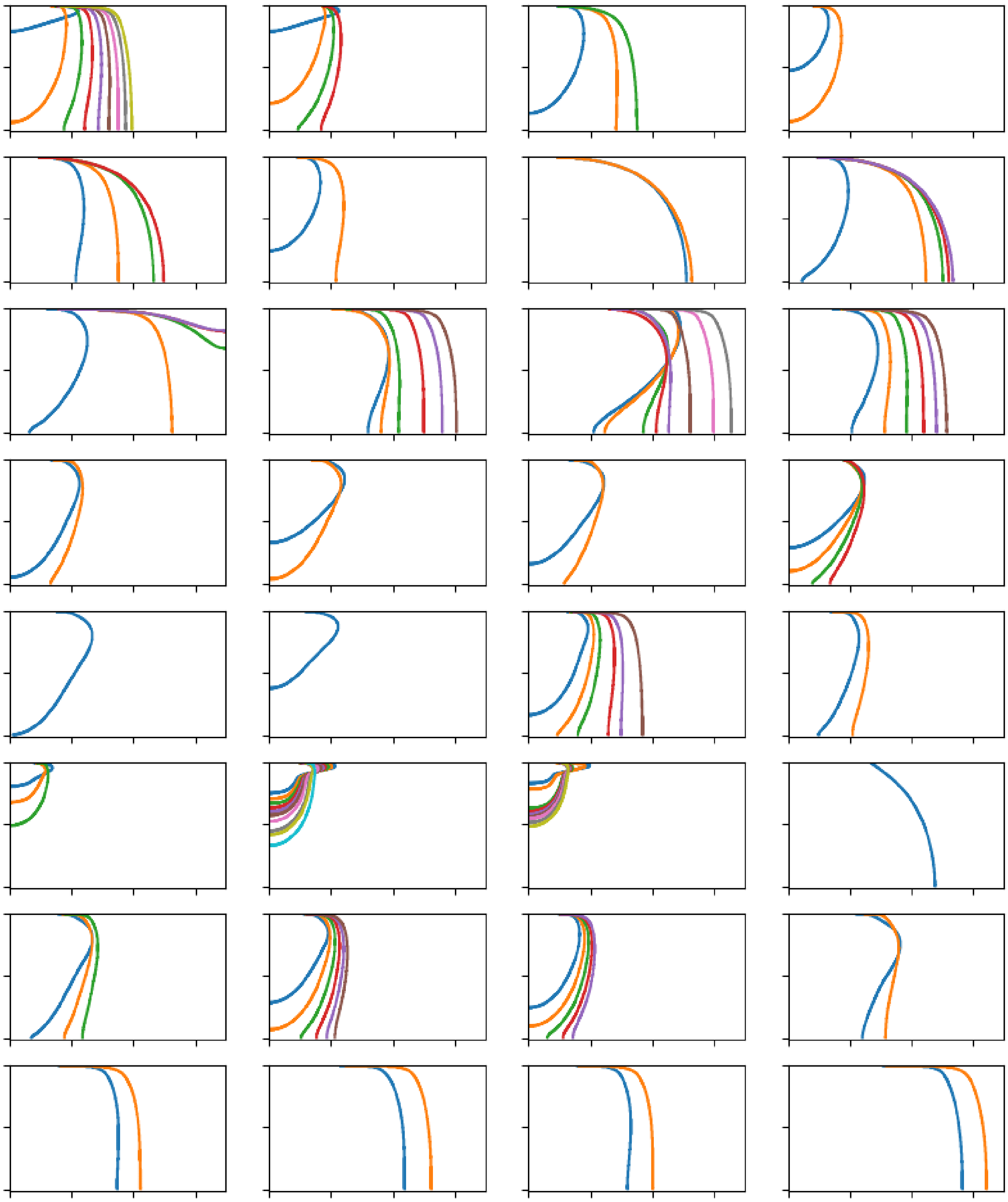

Figure 12: Regions of instability generated for each of 32 simulations. Each simulation was run to the experiment's thruster cutoff time so there may be fewer simulated profiles than measured by experiment. In comparison to the measured crater profiles shown in Figure 2, these regions of instability are often steeper.

Table 4: Experimental and simulated radii for each experiment, given for the last transient crater in each experiment before jetting cutoff. The simulated radius is calculated for a range of possible cohesion values. Both the values and ratio of simulated radius to experimental radius are given. Ratios are shaded red when the simulation radius is larger than experiment and blue when smaller. Test numbers and ordering corresponds to that given in Land and Scholl (1969).

		Simulation Radius (meters)								Simulation Radius (ratio)							
Test	**Measured Radius (m)**	**c = 0**	**5**	**10**	**25**	**50**	**100**	**250**	**500**	**c = 0**	**5**	**10**	**25**	**50**	**100**	**250**	**500**
1	**0.19**	0.18	0.18	0.18	0.17	0.16	0.15	0.13	0.10	0.96	0.95	0.94	0.91	0.86	0.80	0.67	0.55
2	**0.13**	0.13	0.12	0.12	0.11	0.11	0.10	0.09	0.07	0.95	0.91	0.89	0.85	0.80	0.75	0.65	0.55
6	**0.12**	0.16	0.15	0.15	0.13	0.11	0.09	0.07	0.05	1.32	1.26	1.20	1.06	0.91	0.76	0.57	0.44
7	**0.13**	0.09	0.09	0.09	0.08	0.07	0.07	0.05	0.04	0.69	0.67	0.65	0.60	0.56	0.50	0.41	0.33
5	**0.15**	0.22	0.19	0.17	0.14	0.12	0.09	0.07	0.05	1.40	1.26	1.13	0.92	0.75	0.60	0.44	0.34
9	**0.15**	0.12	0.12	0.11	0.10	0.09	0.08	0.06	0.05	0.78	0.75	0.72	0.66	0.60	0.52	0.41	0.32
10	**0.14**	0.21	0.19	0.17	0.14	0.11	0.09	0.07	0.05	1.58	1.40	1.25	1.01	0.83	0.66	0.49	0.38
4	**0.19**	0.23	0.20	0.18	0.15	0.12	0.10	0.07	0.05	1.21	1.07	0.97	0.79	0.64	0.51	0.38	0.29
3	**0.21**	0.35	0.35	0.30	0.25	0.21	0.18	0.13	0.10	1.67	1.67	1.44	1.20	1.03	0.86	0.64	0.49
24	**0.16**	0.29	0.28	0.28	0.27	0.26	0.24	0.21	0.18	1.75	1.73	1.71	1.65	1.59	1.49	1.30	1.11
25	**0.19**	0.31	0.31	0.30	0.30	0.29	0.28	0.25	0.22	1.65	1.63	1.62	1.58	1.53	1.46	1.31	1.16
26	**0.12**	0.24	0.24	0.23	0.22	0.21	0.19	0.15	0.12	1.94	1.90	1.86	1.77	1.66	1.50	1.22	0.98
35	**0.12**	0.13	0.12	0.12	0.11	0.11	0.10	0.09	0.08	1.13	1.03	0.98	0.93	0.89	0.85	0.77	0.68
37	**0.09**	0.15	0.13	0.12	0.11	0.10	0.09	0.08	0.08	1.62	1.45	1.33	1.16	1.08	1.01	0.92	0.83
38	**0.11**	0.15	0.13	0.12	0.11	0.11	0.10	0.09	0.08	1.28	1.15	1.06	0.98	0.93	0.89	0.81	0.72
39	**0.11**	0.14	0.13	0.12	0.11	0.11	0.10	0.08	0.07	1.33	1.21	1.16	1.08	1.00	0.92	0.79	0.67
28	**0.15**	0.17	0.15	0.14	0.12	0.11	0.10	0.09	0.08	1.11	0.99	0.91	0.79	0.71	0.65	0.59	0.54
29	**0.15**	0.16	0.14	0.13	0.11	0.10	0.08	0.07	0.06	1.05	0.93	0.85	0.72	0.62	0.54	0.45	0.41
31	**0.15**	0.17	0.17	0.17	0.16	0.15	0.14	0.12	0.09	1.13	1.11	1.10	1.05	0.99	0.91	0.76	0.62
32	**0.12**	0.13	0.13	0.13	0.12	0.12	0.11	0.10	0.08	1.10	1.06	1.04	1.00	0.96	0.91	0.80	0.70
8	**0.11**	0.08	0.07	0.07	0.06	0.06	0.06	0.05	0.05	0.79	0.68	0.62	0.59	0.57	0.54	0.49	0.44
15	**0.11**	0.14	0.12	0.10	0.08	0.07	0.07	0.07	0.06	1.27	1.06	0.91	0.69	0.65	0.63	0.60	0.57
16	**0.12**	0.14	0.11	0.10	0.07	0.06	0.06	0.06	0.06	1.10	0.92	0.80	0.60	0.51	0.49	0.47	0.45
19	**0.13**	0.23	0.21	0.20	0.17	0.15	0.13	0.10	0.07	1.76	1.60	1.50	1.33	1.19	1.03	0.78	0.57
46	**0.14**	0.15	0.14	0.14	0.13	0.13	0.12	0.11	0.10	1.09	1.02	0.99	0.95	0.92	0.89	0.81	0.73
47	**0.10**	0.13	0.12	0.12	0.12	0.11	0.10	0.09	0.07	1.22	1.19	1.17	1.12	1.06	0.98	0.84	0.69
48	**0.10**	0.11	0.11	0.10	0.10	0.09	0.08	0.07	0.06	1.08	1.05	1.02	0.97	0.91	0.83	0.69	0.57
49	**0.20**	0.21	0.19	0.17	0.16	0.16	0.15	0.15	0.14	1.07	0.96	0.89	0.83	0.81	0.79	0.75	0.70
51	**0.11**	0.20	0.20	0.19	0.18	0.17	0.16	0.13	0.10	1.83	1.79	1.75	1.67	1.57	1.43	1.18	0.95
52	**0.15**	0.25	0.24	0.24	0.23	0.22	0.21	0.19	0.16	1.61	1.59	1.57	1.53	1.47	1.38	1.22	1.04
54	**0.12**	0.19	0.19	0.18	0.17	0.16	0.15	0.13	0.10	1.63	1.60	1.57	1.50	1.42	1.30	1.09	0.88
55	**0.17**	0.30	0.30	0.30	0.29	0.28	0.26	0.23	0.20	1.78	1.76	1.74	1.70	1.64	1.54	1.36	1.18

Table 5: Experimental and simulated volumes for each experiment, given for the last transient crater in each experiment before jetting cutoff. The simulated volume is calculated for a range of possible cohesion values. Both the values and ratio of simulated volume to experimental radius are given. Ratios are shaded red when the simulation radius is larger than experiment and blue when smaller. Test numbers and ordering corresponds to that given in Land and Scholl (1969).

		Simulation Volume (cm^3)								Simulation Volume (ratio)							
Test	**Measured Volume (cm^3)**	**c = 0**	**5**	**10**	**25**	**50**	**100**	**250**	**500**	**c = 0**	**5**	**10**	**25**	**50**	**100**	**250**	**500**
1	**8450**	5720	5670	5610	5450	5190	4710	3580	2370	0.68	0.67	0.66	0.64	0.61	0.56	0.42	0.28
2	**4830**	1700	1680	1660	1600	1520	1370	1050	697	0.35	0.35	0.34	0.33	0.31	0.28	0.22	0.14
6	**2630**	1750	1680	1630	1470	1270	1000	593	314	0.67	0.64	0.62	0.56	0.48	0.38	0.23	0.12
7	**1630**	605	591	577	540	488	408	261	145	0.37	0.36	0.35	0.33	0.3	0.25	0.16	0.09
5	**2900**	2010	1860	1750	1510	1250	952	543	282	0.69	0.64	0.6	0.52	0.43	0.33	0.19	0.1
9	**2970**	1060	1030	1010	933	837	691	439	246	0.36	0.35	0.34	0.31	0.28	0.23	0.15	0.08
10	**2790**	1810	1670	1570	1360	1130	865	501	266	0.65	0.6	0.56	0.49	0.41	0.31	0.18	0.1
4	**5570**	2230	2080	1950	1690	1410	1070	613	320	0.4	0.37	0.35	0.3	0.25	0.19	0.11	0.06
3	**8980**	9010	8630	8270	7580	6780	5690	3820	2290	1	0.96	0.92	0.84	0.76	0.63	0.42	0.26
24	**5680**	16300	16200	16100	15800	15200	14200	11700	8830	2.88	2.86	2.84	2.78	2.68	2.51	2.07	1.56
25	**7140**	21500	21400	21300	20900	20400	19300	16600	13200	3.01	2.99	2.98	2.93	2.85	2.71	2.33	1.85
26	**3150**	9060	8960	8850	8550	8060	7230	5400	3590	2.87	2.84	2.81	2.71	2.56	2.29	1.71	1.14
35	**2550**	2000	1970	1950	1900	1820	1700	1400	1040	0.79	0.77	0.77	0.74	0.72	0.67	0.55	0.41
37	**1690**	1660	1610	1570	1510	1440	1340	1140	892	0.98	0.95	0.93	0.89	0.85	0.8	0.67	0.53
38	**1810**	2100	2050	2020	1970	1890	1770	1500	1160	1.16	1.13	1.12	1.08	1.04	0.98	0.83	0.64
39	**2450**	1660	1620	1590	1530	1430	1280	964	639	0.68	0.66	0.65	0.62	0.59	0.52	0.39	0.26
28	**5090**	2060	1990	1940	1850	1750	1630	1400	1150	0.41	0.39	0.38	0.36	0.34	0.32	0.28	0.23
29	**931**	1080	1020	972	884	797	698	565	456	1.16	1.09	1.04	0.95	0.86	0.75	0.61	0.49
31	**4840**	4760	4710	4660	4500	4260	3830	2830	1790	0.98	0.97	0.96	0.93	0.88	0.79	0.59	0.37
32	**2570**	2680	2650	2620	2560	2450	2260	1800	1280	1.04	1.03	1.02	0.99	0.95	0.88	0.7	0.5
8	**404**	362	349	342	331	315	290	232	165	0.89	0.86	0.85	0.82	0.78	0.72	0.57	0.41
15	**2090**	820	772	742	703	688	667	615	541	0.39	0.37	0.36	0.34	0.33	0.32	0.29	0.26
16	**2520**	543	498	471	432	413	398	363	315	0.22	0.2	0.19	0.17	0.16	0.16	0.14	0.12
19	**2150**	1980	1880	1810	1630	1420	1120	612	229	0.92	0.88	0.84	0.76	0.66	0.52	0.28	0.11
46	**3860**	3890	3860	3830	3760	3660	3480	3020	2410	1.01	1	0.99	0.98	0.95	0.9	0.78	0.63
47	**1820**	2070	2050	2020	1950	1840	1650	1220	796	1.14	1.13	1.11	1.07	1.01	0.91	0.67	0.44
48	**1180**	1190	1170	1150	1100	1020	889	620	377	1.01	0.99	0.97	0.93	0.86	0.75	0.52	0.32
49	**8410**	7170	7090	7040	6950	6840	6640	6150	5450	0.85	0.84	0.84	0.83	0.81	0.79	0.73	0.65
51	**1900**	6210	6140	6070	5860	5530	4960	3680	2380	3.27	3.23	3.19	3.08	2.91	2.61	1.94	1.25
52	**4550**	12400	12300	12200	11900	11500	10800	8940	6720	2.72	2.7	2.68	2.63	2.54	2.37	1.97	1.48
54	**2080**	5760	5700	5640	5450	5170	4670	3510	2300	2.77	2.74	2.7	2.62	2.48	2.24	1.69	1.1
55	**6050**	19200	19100	19000	18600	18100	17000	14300	11100	3.18	3.16	3.14	3.08	2.99	2.81	2.36	1.83

We ran our model for each of the 32 experiments conducted by Land and Scholl (1969) and compared ejecta predictions to their measured values. Once a flow field is calculated, the analysis may be varied over a range of soil cohesion values. Table 4 and Table 5 above show results for our analysis across a range of possible soil cohesion values. We find that our model fits best in a range of cohesion values between 50 Pa and 100 Pa.

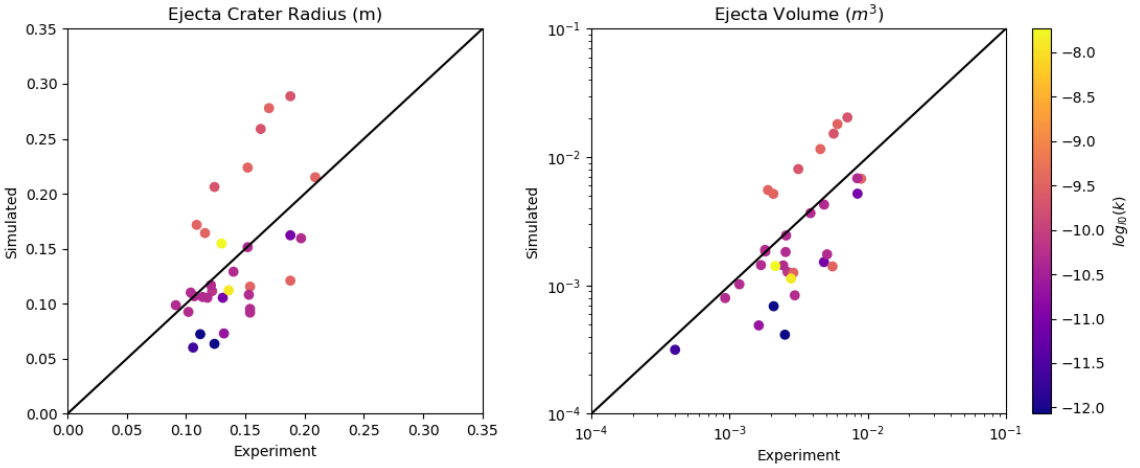

Figure 13: Simulated and experimental ejecta crater radii and volumes compared when regolith cohesion equals 50 Pa. Each dot represents one experiment, and the diagonal line lies along a 1-to-1 ratio. Values are color coded according to the regolith permeability value for that experiment. Yellow dots are relatively permeable, violet relatively impermeable.

Our model predicts the impingement crater radius to within a factor of two. While ejecta volume is predicted to within a factor of five for 80% of our simulations, a few outliers sit near a factor of ten error in predicted ejecta volume. Results for a regolith cohesion of 50 Pa are shown in Figure 13. Higher cohesion values reduce error and spread in our model results, but considerably greater than the near-zero cohesion values measured for glass beads (Klinkmüller et al., 2016). This indicates a limitation in our model; it does not capture the full range of PSI behaviors.

Summary

We have developed a physics-based model to rapidly calculate the ejecta caused by PSI. Gas flow into regolith is calculated using Darcy's Law. The resulting pressure gradients from gas diffusion cause regions of instability, which may be used to predict ejecta behavior and volumes. An assessment of the Asteroid Redirect Mission determined regolith ejecta to be unlikely. Comparison to an experiment set conducted in 1*g* shows our model can predict crater radius to within a factor of two, and ejecta volume to within an order of magnitude. Our model fits the experimental data best with a value of cohesion higher than expected for glass bead simulant. We also note the limitations of our model, as we assume a flow independent of particle motion. This indicates our model should be more accurate at shorter jetting durations.

EXPERIMENTS AND OBSERVATIONS

We present the first systematic investigation into the physics of PSI in vacuum microgravity. Tests at 1*g* were also conducted for comparison. Our work was initially motivated by ARM, but our goals broadened to study PSI systematically by conducting experiments with several simulants, in 1*g* and microgravity, and by varying nozzle distance and jetting duration. To achieve these goals, we needed to develop an experiment that could test PSI in conditions as close as possible to the surface of an asteroid. Asteroids lack an atmosphere, lack significant gravity, and are covered by rocky, unconsolidated material. We designed an experiment to simulate these conditions at the University of Central Florida's Center for Microgravity Research (CMR).

Research and drop tower experiments at CMR have historically focused on low-velocity collisions and other evolutionary mechanisms in the Solar System. To this end, the center houses a drop tower for small vacuum chamber experiments. This expertise enabled the step to small scale, cold gas PSI research in vacuum microgravity. To solve the second challenge of replicating an asteroid's surface, UCF's Exolith Lab provided high fidelity regolith simulant for use in this research. The result of this effort was the Gas Regolith Interaction Testbed, or GRIT, a vacuum chamber experiment which may be dropped to briefly simulate microgravity. We have conducted over 150 successful drop tower experiments with the GRIT chamber. We describe the experiment setup, testing, and phenomenological observations in this chapter, and attempt to quantify the observed behavior and compare to numerical simulations in the next chapter.

Preliminary Experiments

Along the way to developing GRIT, we conducted early experiments at 1*g* and ambient pressure as a proof of concept for small scale PSI experimentation. We recorded PSI behaviors and also tested a method for taking low intensity pressure measurements. This work informed our GRIT design and demonstrated the feasibility of a more sophisticated experiment.

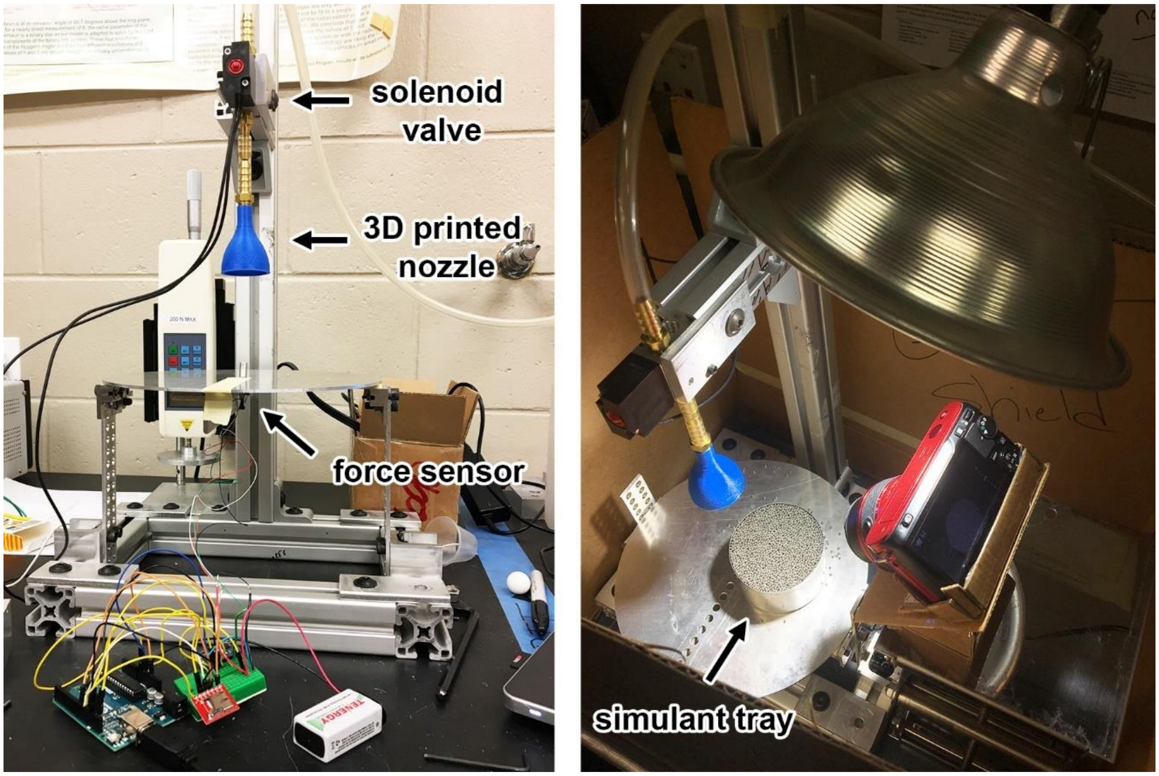

Figure 14: The preliminary, ambient pressure jetting experiment. On the left, an air line was attached to a solenoid valve which opened to pass air through a 3D printed nozzle. A force sensor was placed beneath a circular plate to measure impingement pressure. These measurements were recorded by an Arduino. On the right, a jetting experiment where a cup of steel beads has been placed beneath the nozzle. Video was taken by a camera angled at 45 degrees to the surface to observe PSI phenomena.

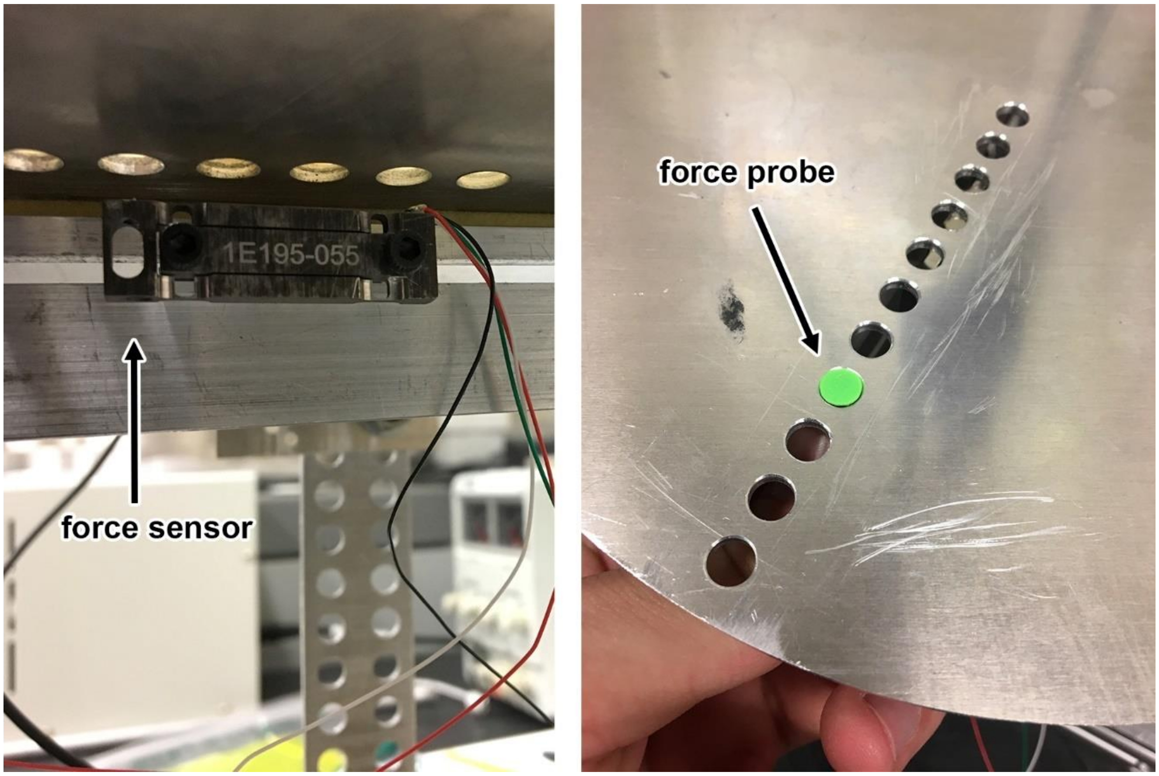

Figure 15: A cantilever force sensor mounted beneath the circular plate, which could be moved radially to take measurements along a cross section of the impinging flow. The probe screwed in through the top of the plate, and into the sensor, its surface sitting just above the plate.

Our initial setup, shown in Figure 14, consisted of a circular plate mounted below a 3D printed rocket nozzle. This plate could be raised and lowered, and the nozzle could also be moved up or down along an aluminum rail. This nozzle was connected to the laboratory’s compressed air supply with a solenoid valve in-line to switch flow on and off. This solenoid valve was controlled manually via a switch. As shown in Figure 15, the circular plate was drilled with holes at even intervals from the center outward along a radial line, under which we placed a sensor to measure impinging flow. A ¼” diameter circular disk placed just above one of these holes was attached to the top of 4-40 screw, which could be mounted into the cantilever force sensor, so that we could measure the flow at specific radial locations. Data from the pressure sensor was recorded with an Arduino to a text file.

We also conducted a few trial PSI experiments parallel to these pressure measurements. We placed a tray of steel beads below the nozzle and recorded high speed video from a camera mounted above the experiment and angled downward at approximately 45 degrees. Experiments were conducted to observe the reaction of steel beads to a gas jet at a scale similar to that planned for our drop tower experiment. These demonstrated our concept was feasible but did not produce results suitable for significant analysis.

Results

Ambient Prototype Pressure Measurements

We calibrated our force sensor before each jetting test by placing known weights on the sensor and recording its readout. Frequent calibration was needed due to baseline drift. For each pressure measurement, compressed air was pulsed several times for approximately three seconds, separated by a three second gap. We took measurements between 5 cm and 14 cm nozzle height, and from 0 cm to 4 cm radially out from the nozzle centerline. A sample of pulse data recorded is shown in Figure 16 below. Jetting data were noisy, possibly due to the cantilever force probe, but also because jetting flow was turbulent. The geometry of the setup and slight protrusion of the force probe may also have contributed.

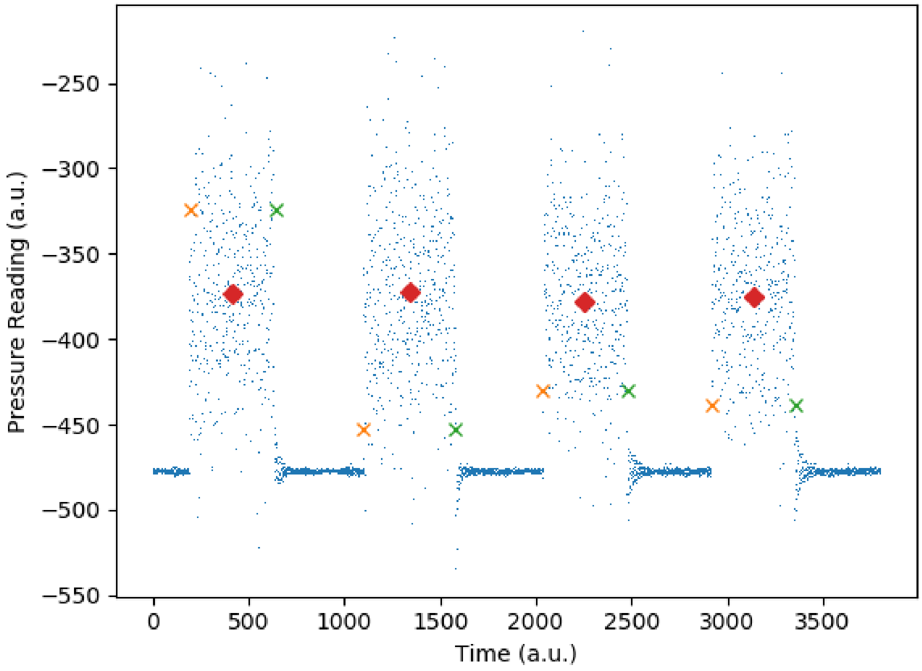

Figure 16: Sample uncalibrated pressure measurement shown with arbitrary units. The left and right boundaries of each pulse are marked with an X and the pulse average is marked with a diamond. X values are plotted at the height of the data point which marks the beginning and end of each pulse.

Results from these experiments are shown in Figure 17, where we plot the pressure measured radially away from the center of the plate, directly below the nozzle, each line representing a different nozzle height. These surface pressure measurements show some qualitative similarity to other surface pressure measurements (Romine et al., 1973). Because the flow of gas was narrow and columnated, there may be systematic error in the maximum value we measured if the probe was not placed directly within the stagnation region. These measurements are also consistent with flow spreading as nozzle height increases.

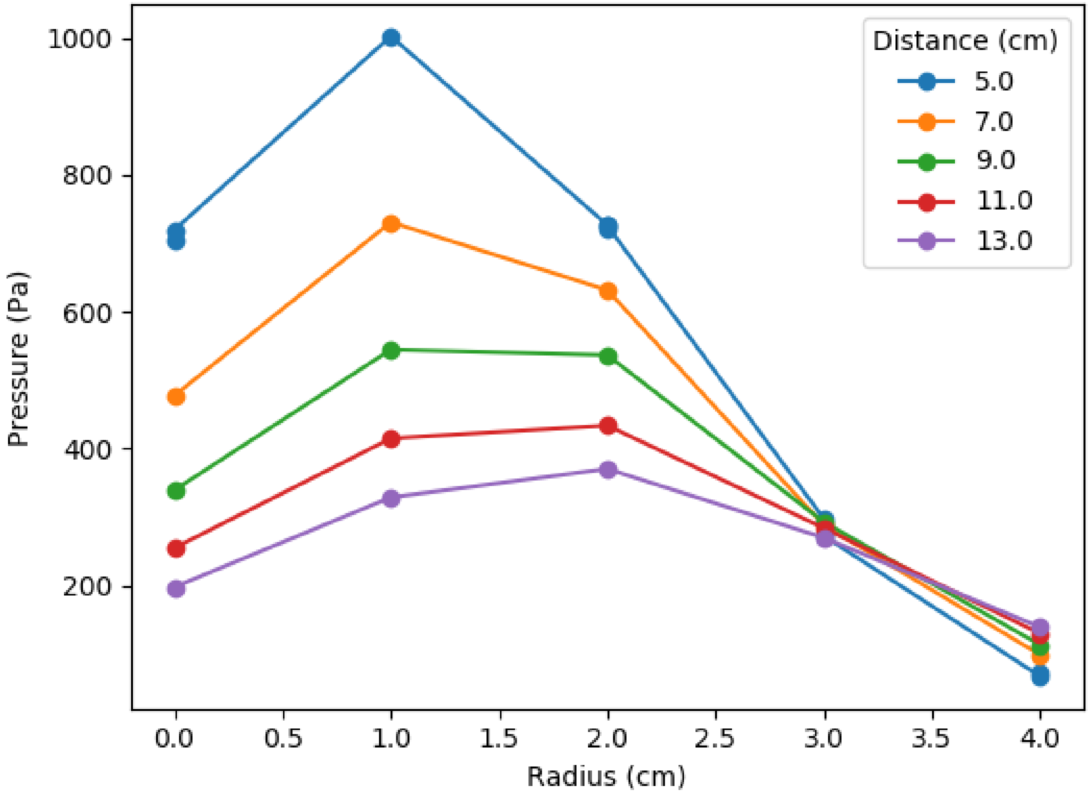

Figure 17: Pressure measurements as a function of radius and nozzle distance plotted from the benchtop jetting experiment. We are uncertain whether the off-center maximum is physical, due to plume structure, or a result of slight nozzle misalignment.

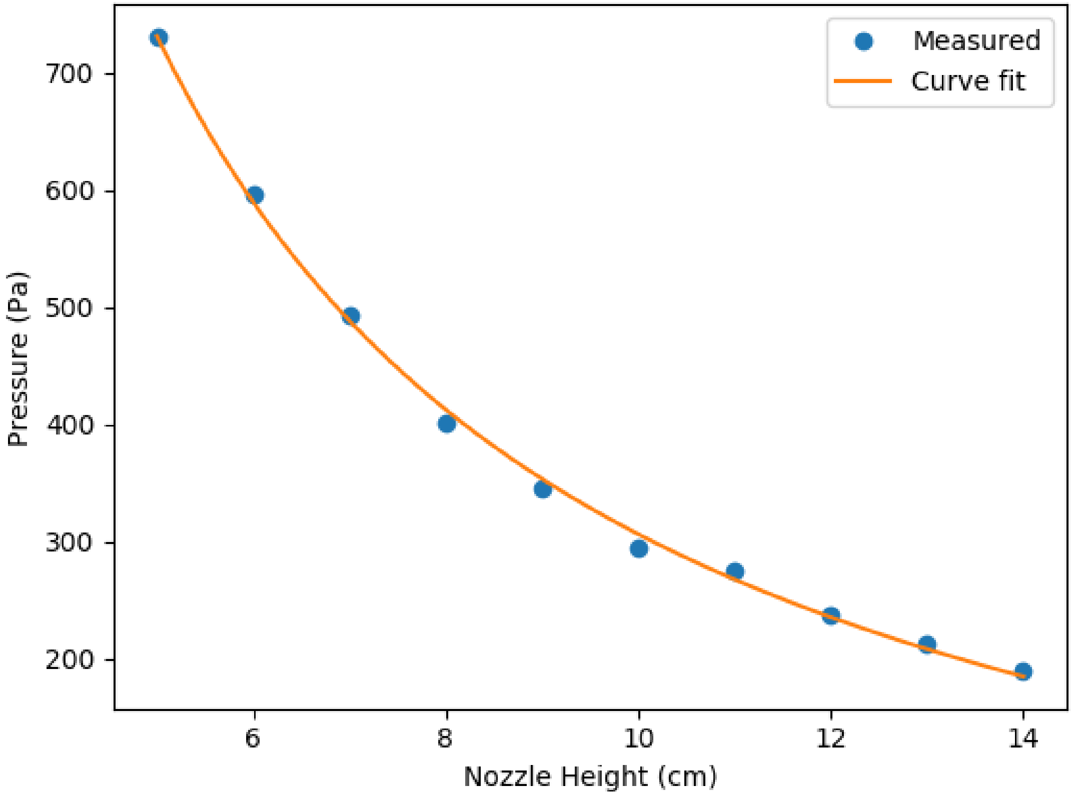

Figure 18: On-center pressure plotted as a function of distance from the nozzle. Pressure drops off proportionally to the inverse of the nozzle height, as shown by the fitted curve.

Robert’s (1964) equation predicts that maximum surface pressure will fall off with the radius squared. This equation is valid for plume impingement in ambient vacuum and places the maximum on-center. We test this relation for our dataset taken at ambient pressure by fitting a curve to the maximum pressure at each nozzle distance and find instead that the pressure maximum falls on inversely with radius, as shown in Figure 18. Our admittedly limited dataset is consistent with this relationship, as given by Equation 12.

$$\boldsymbol{P_{maximum}(h) \propto \frac{1}{h}} \tag{12}$$

Ambient Prototype PSI Observations

Prototype experiments to test jetting into a regolith bed were conducted with stainless steel beads in ambient atmosphere. 2-mm beads were placed in a metal measuring cup, and in a shallow glass tray. PSI behaviors were relatively consistent throughout the set. As gas impinged, beads are disturbed at the surface and begin to travel radially outward away from the flow. For longer pulses or lower nozzle heights, small craters were formed as shown in Figure 19.

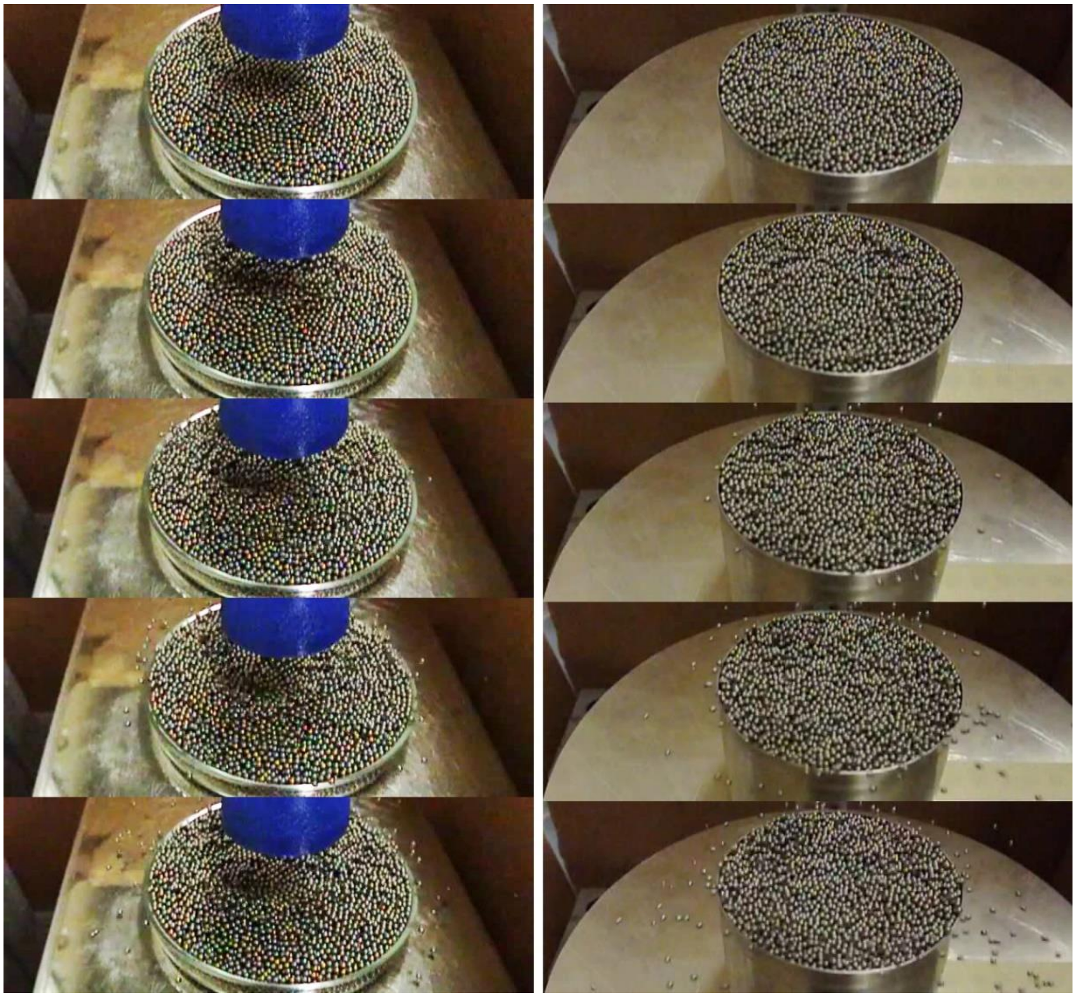

Figure 19: Frames from two preliminary experiments taken at 167 ms intervals. Steel beads are visible ejecting from the surface, forming a small crater by this interaction.

Lessons learned from our preliminary experiments were applied to the main experiment. We were able to determine that PSI could occur at a scale comparable to other CMR drop tower experiments. While we had hoped to take pressure measurements inside our vacuum chamber experiment, the force sensor required calibration regularly due to baseline drift. Because of this, we did not make pressure measurements for the primary drop tower experiment.

Primary Experiment

Setup and Procedure

The Gas Regolith Interaction Testbed, or GRIT, is an experimental apparatus capable of simulating PSI in vacuum microgravity. The GRIT apparatus consists of a cylindrical vacuum chamber constructed from a polycarbonate tube and aluminum end caps. Aluminum rings compress a viton O-ring onto the outer surface of the polycarbonate tube to create a vacuum seal. The interior space is roughly 30 cm high, measured from endcap to endcap, and 12.4 cm in radius. Usable space is slightly reduced by cameras mounted to the interior of the top cap. A full list of apparatus specifications appears in Table 6, and chamber features are illustrated in Figure 20. Two interior heights are listed due to replacement of the tube early on in our experiment campaign.

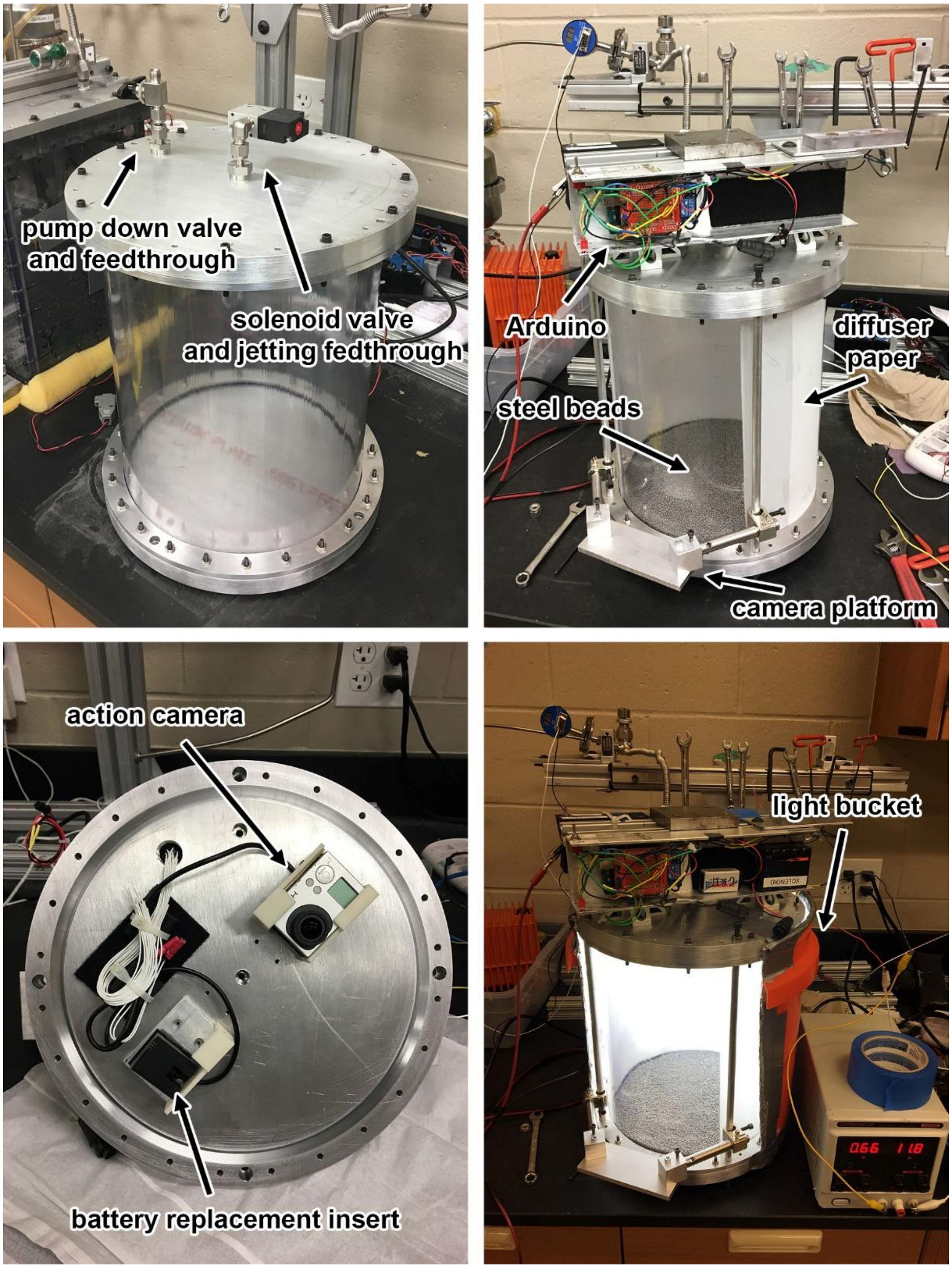

Figure 20: GRIT vacuum chamber. Top left: vacuum feedthrough lines are visible for pump-down and jetting. Top right: Superstructure has been added to house batteries, electronics, and allow mounting to the drop tower. Bottom left: Underside of the lid; electrical and vacuum feed through holes are visible, as well as the action camera mounts. Bottom right: Light bucket in place, which houses LED strips to backlight experiment.

Table 6: GRIT Apparatus Specifications

Measurement	**Value**
Interior radius	12.4 cm
Interior height (tube 1, tube 2)	29.9 cm, 29.4 cm
Interior base area	483 cm^2
Interior volume (tube 1, tube 2)	14,400 cm^3, 14,200 cm^3
Initial pressure (min, max, avg)	235 mTorr, 1.34 Torr, 514 mTorr
Orifice diameter	4.25 mm
Drop time	0.65 s

The GRIT vacuum chamber typically reaches pressure levels well under 1 Torr (133 Pa). For comparison, Earth atmospheric pressure is 760 Torr, while the Martian atmosphere measured by the InSight lander varies between about 5 and 6 Torr (Banfield et al., 2020). The average starting, closed-valve pressure for the GRIT experiment was 514 mTorr, but experiments were conducted with an initial pressure of 235 mTorr to 1.3 Torr. This varied based on simulant used, available pump down time, and quality of the vacuum seal. It took about a week for our vacuum to reach pressures around 600 mTorr with CI Orgueil simulant due to water diffusing out of the material, so a few of these experiments were conducted above 1 Torr.

To produce a gas plume, air is vented back into the chamber through a hole centered in the top cap. A Swagelok vacuum feedthrough with a 4.25 mm interior diameter is fitted to the hole. A vacuum rated solenoid valve is fitted to the exterior of the feedthrough and is controlled by an Arduino microprocessor. When the experiment is dropped, two electrical contacts disconnect from the drop tower harness, opening a circuit connected to the Arduino. The Arduino detects this change, delays 75 ms, then uses a relay to open the solenoid valve for a programmed duration. Figure 21 below illustrates an example pulse. Peaks appear when the solenoid opens and closes. The muffled sound of impact appears 0.65 s after the first peak.

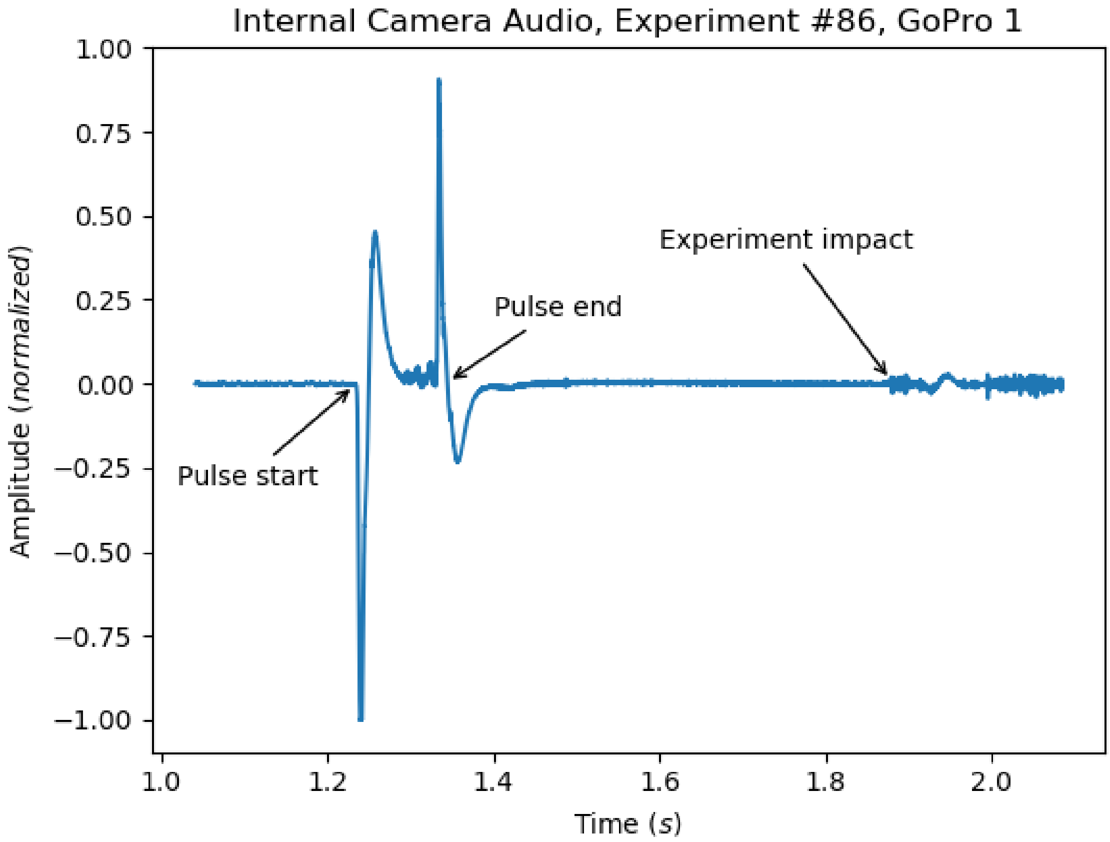

Figure 21: The audio waveform recorded by an internally mounted GoPro during an experiment drop. The pulse beginning and end are indicated by sharp peaks which are caused by flow starting and stopping. The effect of impact is muffled, its amplitude relatively low.

Three action cameras are used to record GRIT experiment runs; cameras used are listed in Table 7, and the camera mounting locations are shown in Figure 20. Two are mounted on the interior to give a top down view of the impingement behavior. One is mounted on the exterior to provide a side view of the experiment. The interior cameras are controlled remotely via WiFi connection and placed into standby mode when not in use. Power is supplied to the cameras via an electrical vacuum feedthrough. The cameras must be turned on manually, meaning loss of power requires the chamber be opened to switch them back on. We use an on-board battery when conducting an experiment, and a benchtop power supply when the experiment is on the bench between experiments. Diodes placed in-line with the battery and power supply connections allow power to be switched between the two sources without interruption. This solution improved upon a manual switch which could interrupt power when flipping between sources.

Table 7: Action Camera Specifications

Brand/Model	GoPro HERO3	EKEN
Video Resolution	1280 pixels x 720 pixels	1280 pixels x 720 pixels
Video Frame Rate	119.88 frames per second	120.00 frames per second
Audio Sampling Rate	48.000 kHz	44.100 kHz

The CMR tower is approximately 3.4 m high which allows experiments up to approximately .75 s of freefall. Due to the size of the GRIT experiment, triggering delay after experiment release, and cushioning height, we achieved drop durations of .65 s. The audio data shown in Figure 21 are recorded at a high sampling rate (48 kHz) which allows us to verify pulse duration.

Experiment Procedure

To ready GRIT for an experiment run, we place regolith simulant in the base of the vacuum chamber. The base may be elevated by an acrylic platform to reduce nozzle the distance between the top of the simulant and the venting hole, which we refer to as the nozzle “height”.

We turn on the internal cameras, place them into sleep mode with Wi-Fi activated, and finish assembling the chamber. It is then hooked up to a vacuum line to pump down.

Initial pump down times vary with simulant type, the presence of other objects in the chamber like a platform, and the time the chamber has spent at ambient pressure. Introducing new objects into the chamber increases initial pump-down time while the object dries out. Dry, impermeable simulants like glass or steel beads pump more quickly compared to asteroid regolith simulant, particularly if the asteroid simulant is freshly made. It takes a week or two for the asteroid simulant to dry out and achieve a minimum vacuum pressure. We measured higher minimum pressures for asteroid simulant compared to glass bead, sand, and steel bead simulants.

For repeat runs with the same simulant and platform height, we only need pump down the chamber back to its minimum pressure level after an experiment run. This typically takes an hour or two depending on the jetting duration, as longer pulse times let more air into the chamber. Because of this quick turnaround time, we were able to complete as many as 5 or 6 experiment runs in a day.

Experiment Run

Once the experiment chamber reaches its minimum pressure, we program the Arduino with the next jetting pulse duration. The chamber pressure (Pressure 1) is measured from a gauge in line with the experiment while the chamber is actively pumping down. Then the valve between the gauge and the vacuum chamber is closed and a second pressure reading is taken (Pressure 2). The valve onboard the GRIT chamber is closed, the vacuum line disconnected, and a cap screwed on to protect the valve threads.

Batteries to the Arduino and solenoid valve are connected, then internal camera power is switched from the auxiliary power supply to an onboard battery. The chamber is then placed into the drop tower harness, attached by an electromagnet on the harness to a steel plate on the top of the GRIT chamber. Two contacts on the GRIT experiment are aligned to a short-circuit on the harness; this circuit will break when the experiment falls, which triggers the jetting pulse. Exterior backlighting is attached to the chamber and connected to a dedicated battery. After a contact check, the experiment is hoisted to drop height. The Arduino is powered on, armed, and the exterior camera turned on and set to record. The interior cameras, controlled by mobile phone or a computer application via Wi-Fi, are set to record. All lights in the laboratory room are shut off to prevent tube reflections appearing in experiment videos, then the experiment is ready to drop.

After a brief count, the switch to the electromagnet is shut off, and the experiment falls for approximately 0.725 s. The solenoid fires for the specified pulse duration after a 75 ms delay, meaning the experiment duration is 0.65 s. After impact the electronics are shut off, the experiment returned to the bench, and internal cameras returned to auxiliary power. The vacuum line is reattached, pumped down to vacuum, then the valve to the pump is closed off. The experiment valve is opened to the line, and the post-drop chamber pressure (Pressure 3) is measured. If the next experiment run uses the same simulant and platform height, the experiment need only be shaken to reset the material and pumped down before a new drop.

Experiment Setup and Variables

For this experiment set, we varied jetting duration, nozzle height, and material type. A list of material and experiment parameters is shown below in Table 8 and Table 9. While not representative of a planetary surface, initial experiments were performed with steel beads due to the simulant being readily available in our laboratory. Since we were initially unsure how simulant would respond to jetting in microgravity, steel beads were an appropriate choice to test first because of their higher density.

Experiments were conducted with sand, glass beads, and CI Orgueil simulants, whose bulk properties are described in Table 8. Our CI Orgueil simulant, provided by Exolith Lab, is a high-fidelity replication of asteroid regolith based on the mineralogical properties of a CI1 chondritic meteorite (Britt et al., 2019). We received the simulant as a powder, then mixed with water and let the mixture dry in cakes to create our asteroid simulant. These cakes were broken up and sieved such that our particle sizes were between 0.475 cm and 3 cm.

We performed these experiments with a standard simulant depth of 5 cm and at two nozzle heights; of these, experiments with sand were not performed at a reduced nozzle height. Changing the nozzle height required putting a platform in the GRIT experiment, and a thin gap in the platform would have allowed sand to spill through to the bottom layer. No fix robust enough for the repeated stress of a drop tower experiment was readily available. Three drops and one bench run were nominally performed for each simulant/pulse/height combination. A summary of experiments conducted is given toward the conclusion of this chapter in Table 10.

Table 8: Simulant Properties

Type	Size Distribution	Depth (cm)	Mass (kg)
Steel	2 mm (uniform)	1.27	2.85 kg
Glass	600 µm – 850 µm	5	3.8 kg
Sand	150 µm – 200 µm	5	3.8 kg
CI Orgueil	.475 cm – 3 cm	5	1.8 kg - 2.1 kg

Table 9: Other GRIT Parameters

Platform height	0 cm, 10 cm
Pulse duration	0 ms (control), 10 ms, 25 ms, 50 ms, 100 ms, 250 ms
Gravity	1*g* (bench), ~0*g* (drop tower)

Off-nominal Chamber Events

While the majority of experiment runs were nominal, a few problems were encountered with the GRIT chamber. Chamber backlighting occasionally failed. Power cables for the interior cameras detached from the top lid and show up in several experiment videos. The solenoid valve occasionally pulsed twice during a drop. For a of couple drops, user error meant the experiment did not fire or a video was not recorded.

Once the second internal camera was installed, running two cameras for a drop was preferred, but occasional connectivity problems prevented duplicate video in all cases. A drop was still considered nominal if only one interior video was obtained.

Off-nominal runs were marked and repeated. While some chamber problems resulted in an unusable run, double pulses and no-pulse runs provide unique and control results, respectively. The phenomenology of a double pulse impingement experiment is included in the descriptions below.

Images and Processing

Each nominal experiment run is recorded with at least two cameras: one side view and one top view, and some experiments are recorded with two top-view “stereo” cameras. The side view camera was exterior to the experiment tube and placed with a view slightly above the surface of the regolith. This means the viewing angle is slightly above edge-on. This allows us to view surface phenomena that would be impossible to see clearing with the camera lens centered on the regolith. As seen in Figure 22, video from the side is distorted because the polycarbonate tube was extruded, and the striations perturb the particle locations horizontally. Our top-down cameras are mounted inside the lid of the experiment chamber, equidistant from the centerline.

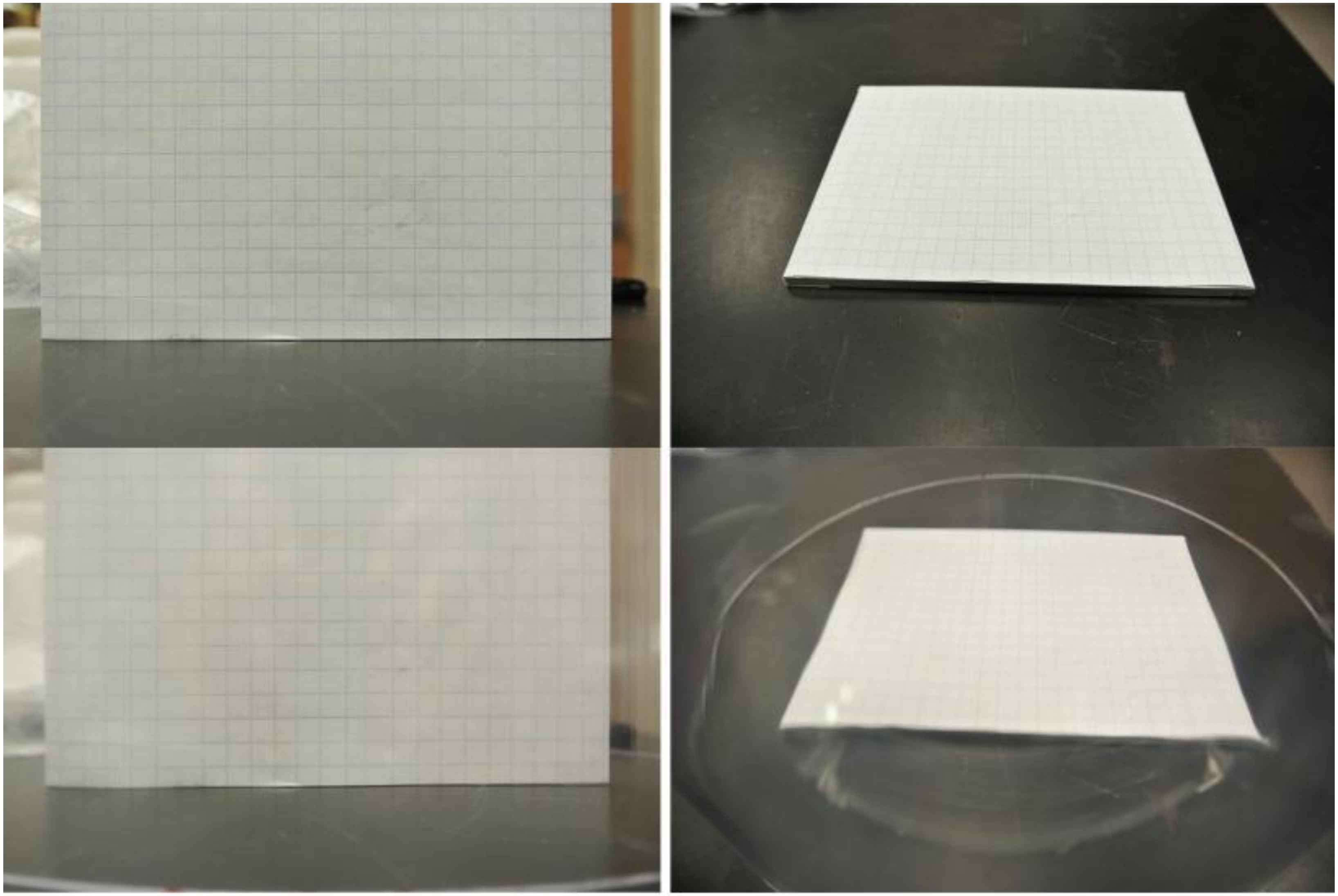

Figure 22: Optical distortion caused by the extruded polycarbonate tube. Graph paper is shown without (top) and with (bottom) the tube in place.

We record using wide-angle action cameras. To correct for the distortion caused by these lenses, we use a de-warping package called Argus (Jackson et al., 2016). By recording a known dot-grid pattern with each camera type used, Argus can determine a de-warping profile. This profile is then applied to the experiment videos before analysis. Running this de-warping algorithm on the calibration video allowed us to visually inspect that the program worked properly to correct optical distortion.

These de-warped frames are processed to make PSI phenomena easier to observe. We process frames using two methods. Difference frames are constructed by subtracting consecutive video frames. Background-subtracted frames are constructed by subtracting the average pre-experiment frame (with a buffer) from the current frame. This is summarized by Equations 13 and 14, where the variable *f* is an array containing image data.

$$\boldsymbol{f_{difference} = f_t - f_{t-1}} \tag{13}$$

$$\boldsymbol{f_{background\ subtracted} = f_t - f_{t<0,average}} \tag{14}$$

Difference frames show what changed between subsequent frames, and so give a sense of motion. If a particle moves, its new location will show as a light dot, and its previous location as a dark dot. If these locations overlap, the new area occupied will show as a lighter region, and the old area occupied as a darker. The overlapping region will take an intermediate value similar to the background. Background subtracted frames show what has changed since the experiment began. This type of image is better at highlighting the difference in structure between initial and current images. Each type, shown in Figure 23 and Figure 24 for both side and top-down views, has its advantages and limitations, so we use each as is effective to highlight the described phenomena.

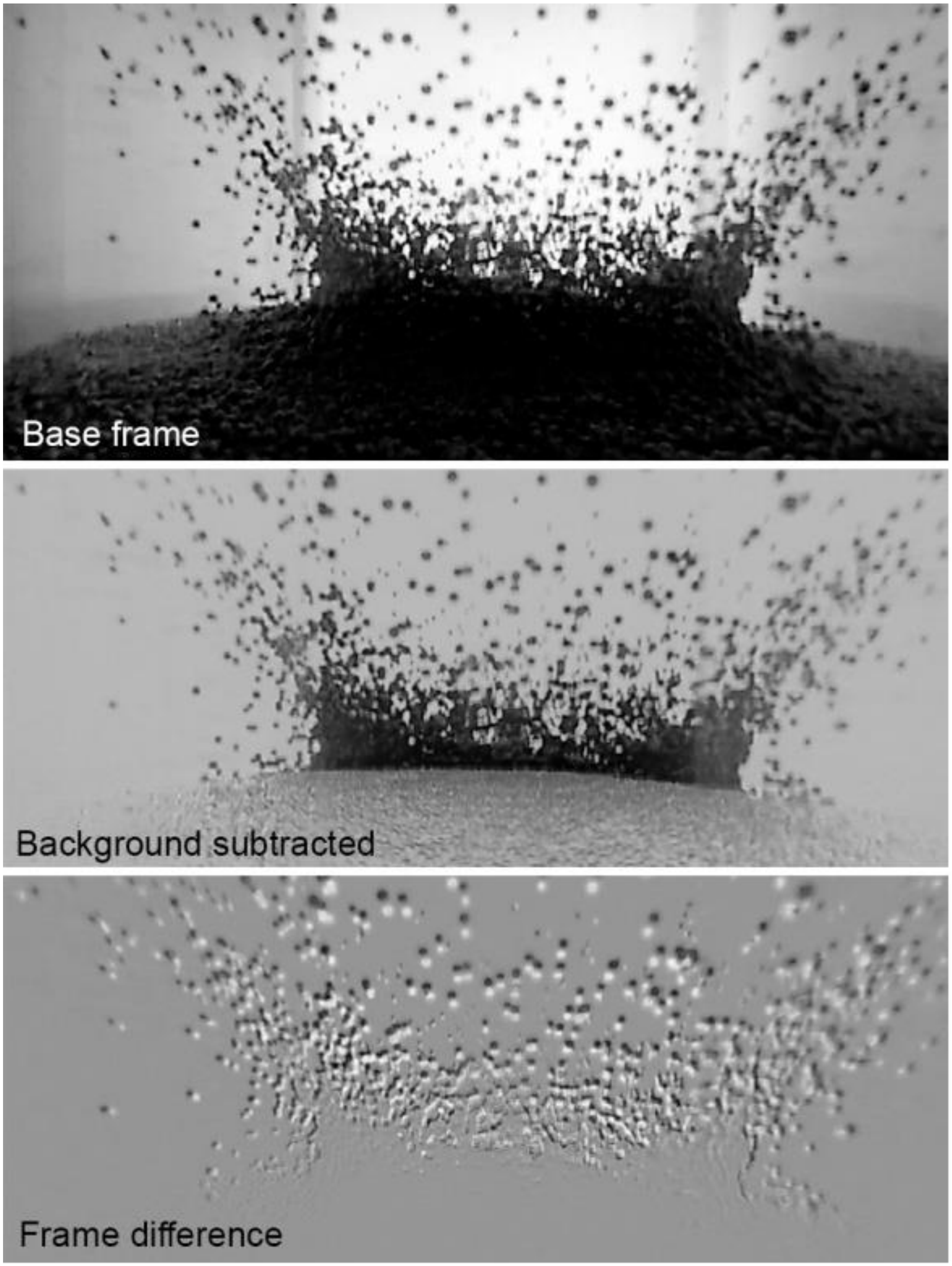

Figure 23: An example side-view frame showing the initial image (top), and the two processing methods, background subtraction (middle) and frame differencing (bottom).

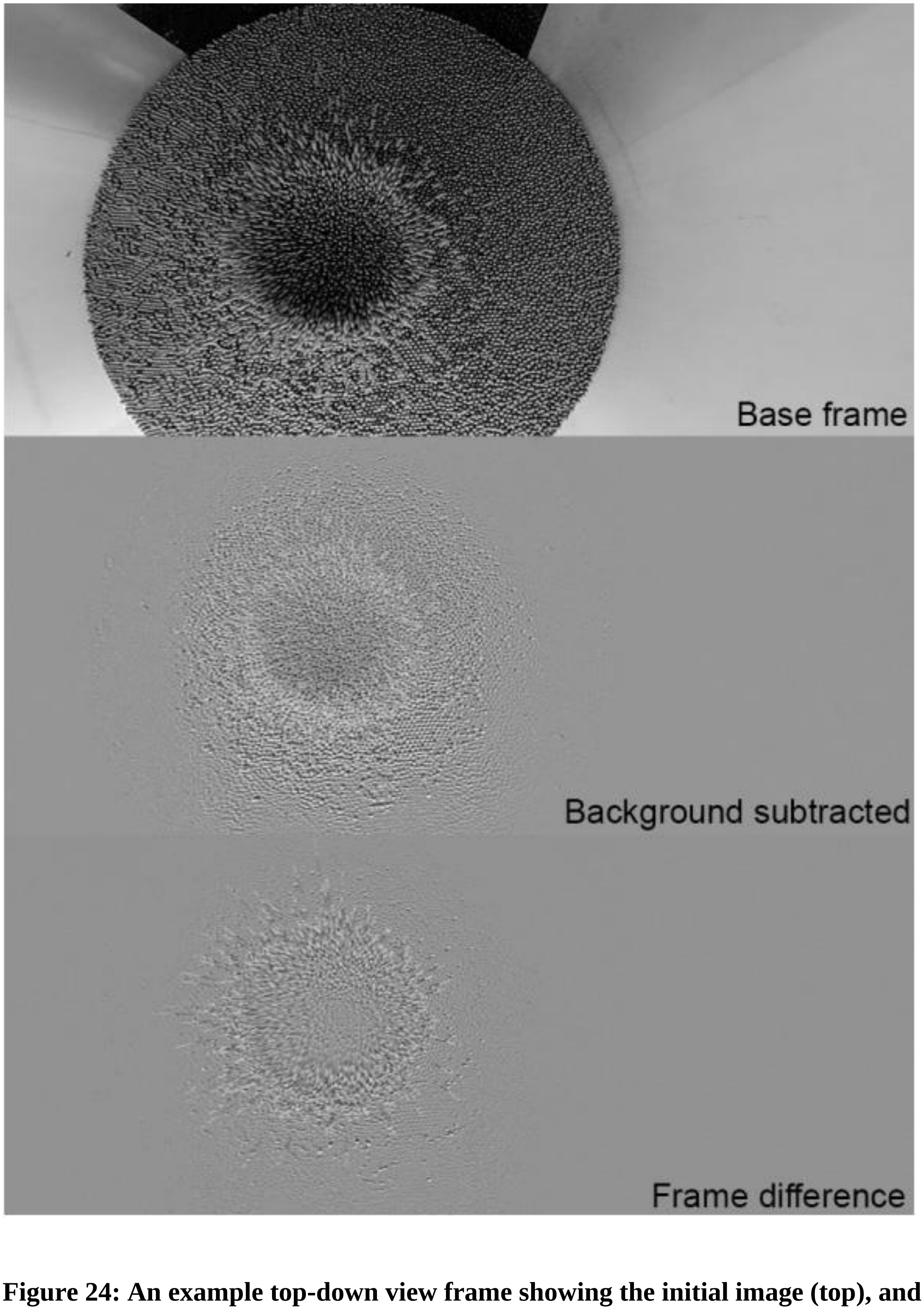

Figure 24: An example top-down view frame showing the initial image (top), and the two processing methods, background subtraction (middle) and frame differencing (bottom).

The first active frame (Frame 1) of each experiment was determined by visual inspection, based on when a disturbance first appears. One frame before this is then labeled as the initial frame, Frame 0, such that all frame indices begin at 0.

Plume Surface Interaction Phenomenology

Many features of PSI in vacuum microgravity resemble solid impactor experiments—minus the visible impactor—including both low and hypervelocity impact experiments. We often see what looks like an ejecta splash, where the particulate medium seems almost fluid-like in its reaction. In some cases, finer particles exhibit the streaming behavior typical of fluids. But there are also behaviors unique to particle-fluid interactions that appear in the GRIT experiment

The microgravity regime can be unintuitive. Most PSI experiments, even those conducted in a vacuum chamber, have been performed in an environment where gravity is a significant force. In microgravity, distinct behaviors appear. These “masked phenomena” can become important when gravitational force is absent. By observing experiments in microgravity we can begin to develop an intuition for what kind of forces are important in this regime.

As noted in the introduction, PSI has been categorized into four main categories (Mehta et al., 2011): bearing capacity failure (BCF), viscous shear erosion (VSE), diffusion driven flow (DDF), and diffuse gas eruption (DGE). The fifth observed category, diffuse gas explosive eruption (DGEE), may be considered an expansion on DGE or its own phenomenon. We will return to consider this taxonomy in later discussion.

Plume Behavior

There are several stages to plume flow in the GRIT experiment. Gas flows through an orifice in the center of the experiment chamber. Gas travels from the experiment lid's orifice to the regolith. Then it impinges on the regolith and interacts. Here we consider each of these stages from the standpoint of gas behavior before moving on to describe its effects on the granular medium.

The gas jet in the GRIT chamber comes from allowing ambient air in through a solenoid valve. The pressure differential between the ambient atmosphere and inside of the chamber is high enough that the flow will always be choked. Flow chokes at the narrowest point within the solenoid, at the speed of sound. Flow from the orifice moves downward and spreads radially outward before hitting the surface. In a perfect vacuum, flow would spread outward in all directions and the surface pressure distribution would take a shape resembling a Gaussian curve with the peak pressure directly under the nozzle. In the presence of an atmosphere or background pressure as in our experiment, flow tends to collimate, such that there is a narrower radial distribution of flow.

Next, the flow impinges on the granular surface. The flow may then (1) be redirected by the surface, but also (2) push material aside and (3) flow into, radially along, and then outward from the media. This behavior was seen in flow simulations and may be observed indirectly by several phenomena in our experiments, such as the dust-entrained flow and off-center lofting, which we will describe below.

Plume flow is the driver behind particle motion, and therefore the driver behind PSI. Particles are moved or ejected as the gas hits, flows through, and exits the medium. Theory and modeling suggest this flow is governed by soil permeability, and observations support this.

Developing a model for plume flow can be aided by considering limiting cases: That of a solid, impermeable barrier, and the case where there is no barrier at all. Imagine water from a garden hose directed straight down onto a concrete sidewalk. The water flow will splay outward, redirected by the hard surface. But before the water hits, its flow is practically unimpeded by air. The PSI cases we are interest in lie between these two bounds; between no impedance and total impedance to flow. Fine grained, tightly compacted granular media have low permeability, as their close-packing leaves little pore space, so we expect the behavior of these materials to be closer to that of a hard surface. Gas flow impinging on these surfaces deflects more than it penetrates. Media comprised of larger grains, however, tend to be less closely packed and thus allow the impinging gas to flow more freely. As we will see, and as suggested by our model, the range of PSI behaviors we observe are significantly influenced by these differences in soil permeability.

Surface Interactions

The two limiting cases of PSI behavior are impingement on a solid surface and uninhibited flow. Fluid impacting a solid surface is deflected but pushes against the surface, which suggests an impact-like regime to PSI. On the other end, if we imagine a porous medium which does not inhibit flow, PSI behavior will be entirely flow-driven. We expect most experiments to demonstrate a range of phenomena between these limiting cases . After outlining some general PSI behaviors, we will examine the range of PSI interactions exhibited by four different media which display these impact-like and flow-driven behaviors. We also catalog the behaviors that do not fit neatly into these categories.

General Behaviors

Because our experiment apparatus was intentionally constructed to be axially symmetric, we observe motion primarily in the radial and vertical directions. In the first few ms of PSI, fine particles are accelerated, if present, and serve as a tracer to plume flow. This is observed as flow-driven behavior in the CI simulant, where the breakup of larger particles due to previous experiments produced fine dust that is present throughout the simulant bed.

Impact-like behavior occurs next, with a time scale dependent on the simulant involved. Less massive particles are typically accelerated more quickly. Denser particles are slower and take more time to accelerate. A disturbance first appears as a small circular region centered on the surface of the granular bed. Material is displaced and lofted upward and outward from the center in a splash of ejecta. Fluid-like behavior in this splash may be observed as radial “fingers” emanating from the center; that is, small angular regions of higher-density ejecta.

This initial behavior takes on different characteristics at different pulse durations. Generally speaking, short-duration pulses are characterized by sparse ejecta directly around the pulse centerline. This ejecta is difficult to define clearly in terms of an ejection angle or shape, though the shortest pulses seem to loft ejecta at a higher angle—an exception to the relatively constant ejecta angle otherwise observed with moderate pulse durations. A general increase in angle is seen as pulse duration increases and gas bores deeper into the material.

In some cases, with lighter media, the initial gas “impacts” bears resemblance to hypervelocity impact experiments conducted by other researchers (Hermalyn & Schultz, 2010) in which an initial, high velocity component of ejecta precedes bulk ejecta. In our experiment, which consists of a gas wave front hitting granular media, we also observe—to a lesser extent—

this kind of “spurting” behavior immediately following gas “impact”. This produces the fastest particles, and like the hypervelocity impact experiments, we have difficulty characterizing these particles. Our overall time and velocity scales, however, are much smaller, with the fastest ejecta we observe is traveling on the order of tens of m/s.

Flow-driven behavior appears in two forms. First, in longer pulses, flow appears to drive the ejecta splash in a manner distinct from simple impacts. After impact-like behavior is observed, we see flow-driven crater boring and widening. This is especially apparent in more permeable media like glass beads and CI Orgueil at long pulse durations. It is not observed in impermeable media like sand. This crater widening also depends on whether or not gas bores to the base of the experiment chamber. When the pulse duration is sufficient, gas hitting a hard surface may spread outward and “bubble,” pushing up the entire mass of simulant with it.

Flow-driven behavior is also apparent off-center in more permeable media, where it manifests as a disturbance outside the impact-like splash. These disturbances may be perturbations or ejecta. This ejecta moves much more slowly than that originating from within the main splash area, though as pulses become longer in the CI Orgueil simulant, a clear definition between “main ejecta” and “off-center ejecta” breaks down.

Steel, 28.7 cm Nozzle Height

We began the GRIT experiments with 2mm diameter steel beads for a couple of reasons; 1) they were readily available when the GRIT apparatus was constructed, and 2) due to their higher density, we knew that the beads would accelerate more slowly than a simulant with more realistic density. However, because this was the first set of experiments, and because there was a limited amount of the steel beads available, we did not conduct these experiments with the same simulant depth as those which follow. This limits our ability to make one-to-one comparisons of the phenomena here relative to other materials, but these represent the first tests of PSI in vacuum microgravity and informed our approach moving forward. This first set was conducted with a 1.3 cm layer of steel beads in the base of the experiment chamber, meaning the effective height of our “nozzle” to the material surface was about 28.7 cm. For the first set with a 29 cm nozzle height, tests at Earth gravity (1*g*) only conducted for 10 ms, 100 ms, and 250 ms pulse times.

10 ms Pulse Behavior

A brief, 10 ms pulse to steel beads in microgravity results in one of the gentlest perturbations we observe in this experiment campaign. This is exciting because it tells us we are near the limits of PSI causing a measurable effect. As seen in Figure 25, a small splash of beads is created by the plume and, aside from a few stray particles outside this center region, most of the effect is confined to an area roughly 8 cm wide. Some particles are disturbed but remain in place. Others travel upward slowly, but a slight gravitational bias can be seen in their trajectories toward the end of the experiment.

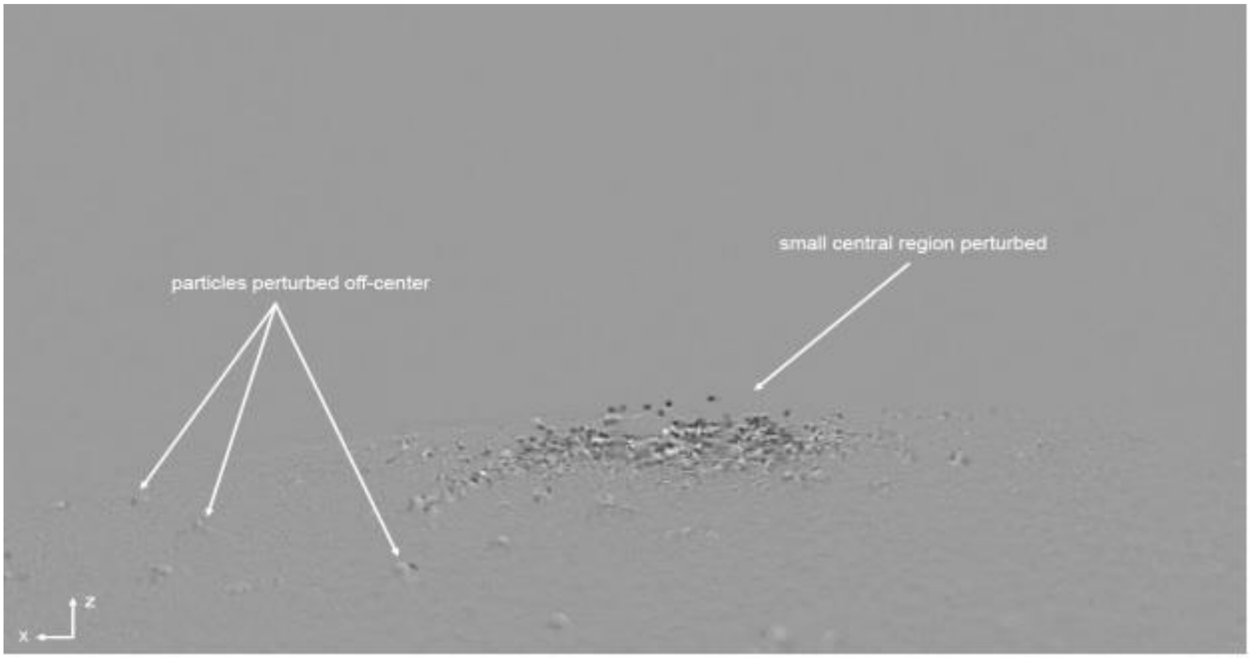

Figure 25: A background-subtracted frame, 375 ms into a 10 ms pulse experiment in steel beads in μg. Lofting is visible on-center, with some perturbed particles in the surrounding regions.

Off-center perturbation of particles appears to have a radial dependence with time. Beads toward the edge of the experiment are perturbed as late as ~160 ms into the experiment—a full 150 ms after the experiment pulse stops. This suggests the perturbation is due to gas moving more slowly within the material rather than gas motion across the surface. Experiments conducted at 1*g* with this pulse duration show no effect on the surface. Comparison to our Drop Tower control experiments—drops with no pulse at all—show that these effects are not due to a jolt or bump to the experiment as it is released. Though there are slight drop induced effects for lighter simulants, steel beads remain motionless during control drops.

We see these off-center circulatory effects of gas flow moving forward through the experiment set. Already this experiment highlights the ways in which PSI interactions are unlike impact experiments, with distinct phenomena clearly present.

25 ms Pulse Behavior

Ejecta are still sparse for a 25 ms experiment, shown in Figure 26, but a much larger region on the surface is affected by the impinging plume. We see a few individual beads disturbed toward the edge of the experiment area. Though sparse, we begin to see something like a discernable, shallow ejecta angle caused by the main splash. Some beads are driven directly outward, rolling across the surface.

Figure 26: A background-subtracted frame, 375 ms into a 25 ms pulse experiment in steel beads in μg. The surface perturbation extends well beyond the area modified by the 10 ms pulse.

50 ms Pulse Behavior

At this pulse duration the ejecta begin to take a more well-defined shape but are still relatively sparse. Some beads are lofted at a very low angle, and as before some beads outside the ejecta area are driven outward, rolling across the surface. At this point the shallow ejecta angle is visible, seen in Figure 27, though the spready is not tightly defined. Notably, we do not see beads traveling at a steep angle.

Figure 27: Still frame from 208 ms into a 50 ms pulse experiment in µg. Outside the splash area, particles on the surface are perturbed, some rolling outward across the surface.

100 ms Pulse Behavior

The ejecta spray from a 100 ms pulse is more pronounced, and at this pulse duration the crater bottoms out, revealing the baseplate underneath, though a few individual particles remain in the center. The crater expands to over half the diameter of the tube by the end of the experiment. Experiments conducted at 1*g* show a slight perturbation of the surface. A few particles roll across the surface out from the impingement centerline, but none are lofted.

One of our experiments in this set, No. 55, is curious for its anomalous asymmetric behavior illustrated in Figure 28, Figure 29, and Figure 30. The experiment chamber was reset after each experiment by shaking to produce a roughly uniform simulant surface. Occasionally, however, the surface during the experiment would have a small slope or other remaining features. For experiment 55, rather than surface irregularity, the center region of the surface beads in a regular, close-packed arrangement prior to plume impingement. This is atypical for our experiment set, and we do not know what conditions produced this particle arrangement. Nevertheless, the effect on the experiment outcome was pronounced.

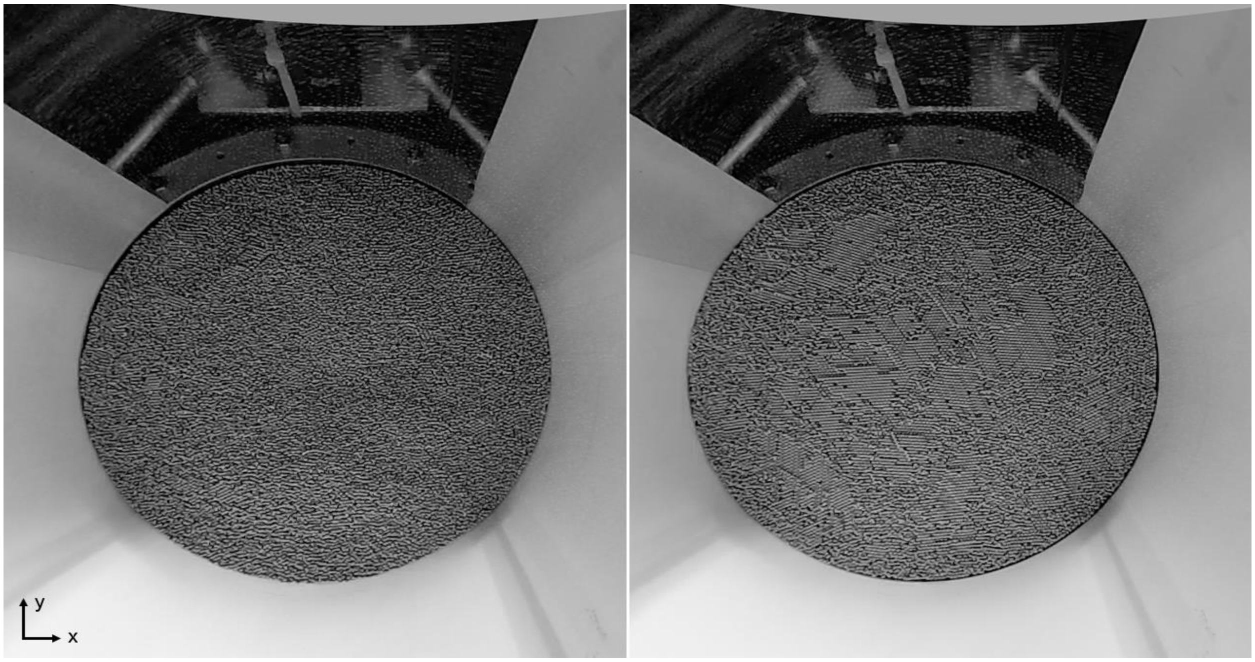

Figure 28: Surface prior to plume impingement. Left, experiment 56, shows a typical initial surface condition. On the right, experiment 55, with a regular packing arrangement visible in the center region.

In this experiment, the gas jet interacts with the surface to produce asymmetric ejecta, which appear as two thin sheets in the initial spray—sheets, it appears, that have been peeled off and lofted by the gas jet, as seen in Figure 29. A more typical ejecta spray follows. We see surface features affecting ejecta outcomes in other experiments, but this serves as a particularly illustrative example. Topography matters significantly for PSI outcomes, as surface features determine gas flow and may effect irregular ejecta patterns. Reference the differences shown in

Figure 29 and Figure 30, which can also be compared with the surfaces shown above in Figure 28.

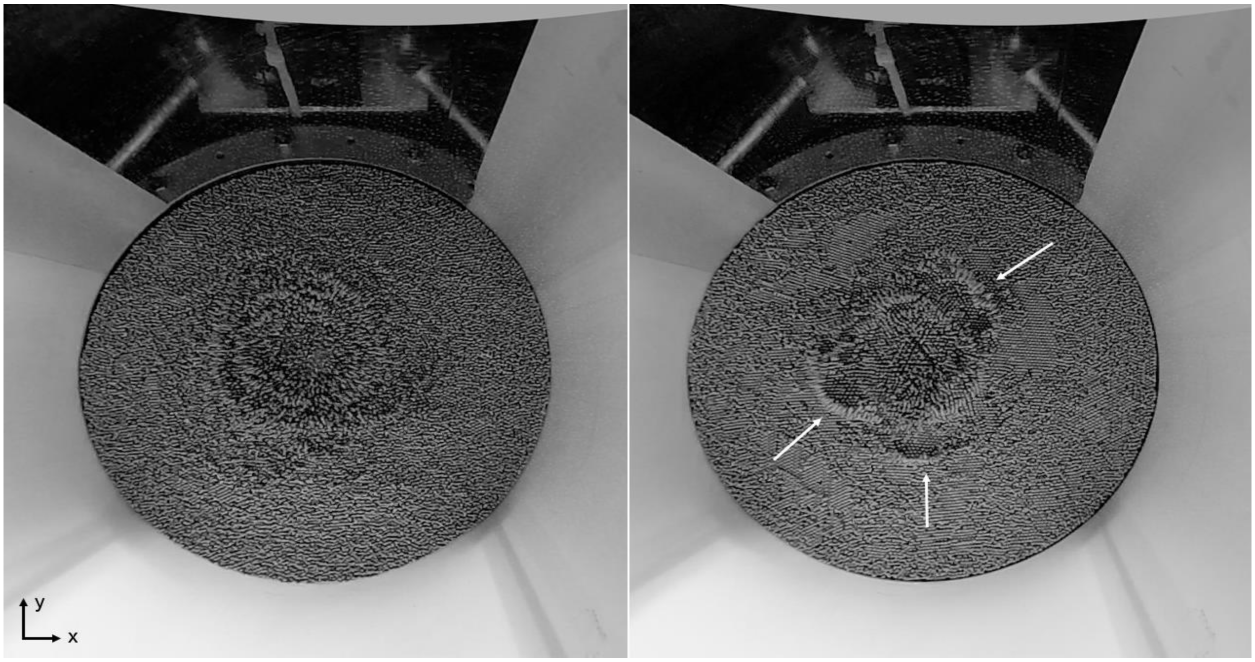

Figure 29: Top-down views from Experiments 56 (left) and 55 (right), 92 ms after experiment start (near the end of the 100 ms duration pulse). On the left, symmetric ejecta produced by the irregular surface. On the right, asymmetric features are indicated by arrows.

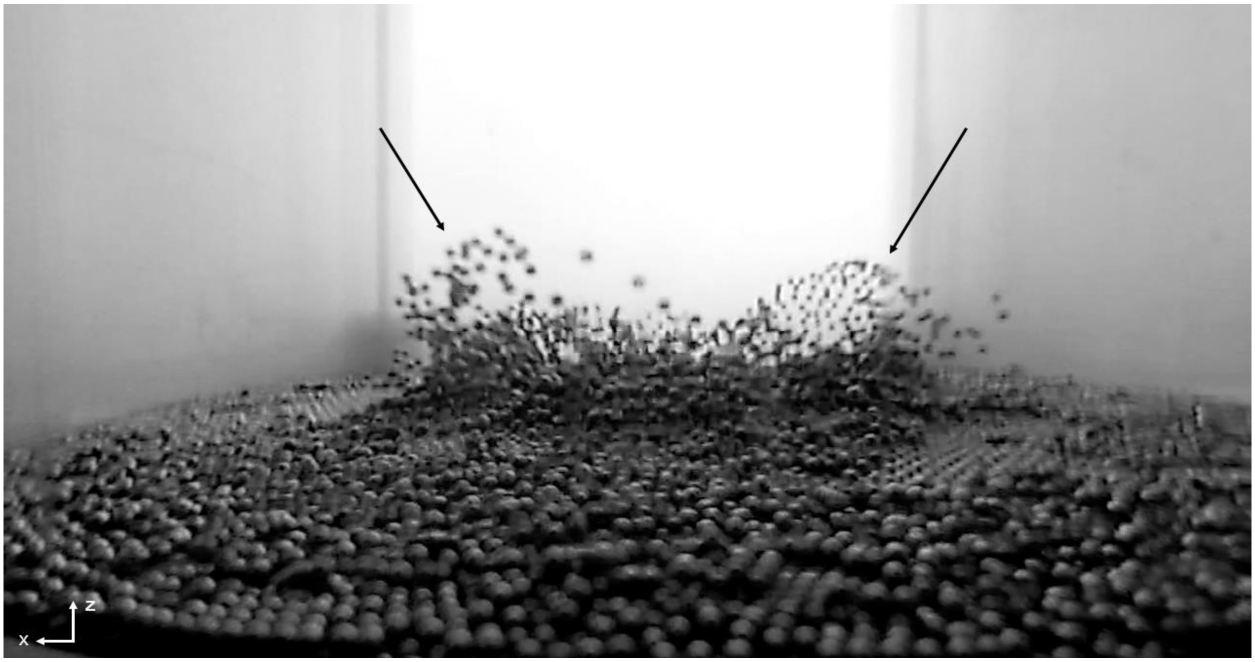

Figure 30: Side view from Experiment 55, 92 ms after experiment start, with sheet-like ejecta features indicated.

250 ms Pulse Behavior

The 100 ms pulse cleared a small region on-center but ceased shortly after. The 250 ms pulse drives this expansion significantly further and a region over half the diameter of the experiment baseplate is cleared of beads completely. From the side view we observe that the ejecta front is driven outward, and the surface appears to upwell, almost as it peeled back from underneath. Though off-center lofting has been present in shorter pulse durations, there was typically a sharper distinction between the surface and the ejecta spray. Here at a 250 ms pulse duration, off-center lofting, crater expansion, and this peeling effect combine to curve the surface—there is a smooth transition from surface to the PSI region. This leads to an overall observation that shorter pulses produce more “impact-like” behavior, while longer pulses produce “flow-driven” behavior.

Figure 31: Side view, 292 ms into a 250 ms pulse experiment in µg. At this nozzle height we see a shallow ejecta angle, possibly exacerbated by the shallow simulant depth.

Steel, 18.7 cm Nozzle Height

10 ms Pulse Behavior

These experiments appear similar to those just discussed, which were conducted at a greater nozzle height. As seen in Figure 32, there is a small, centered disturbance caused by plume impingement, resulting in gentle particle lofting. The area of effect is similar to that of the 29 cm height experiment. No particle motion occurs when this experiment is conducted at 1*g*.

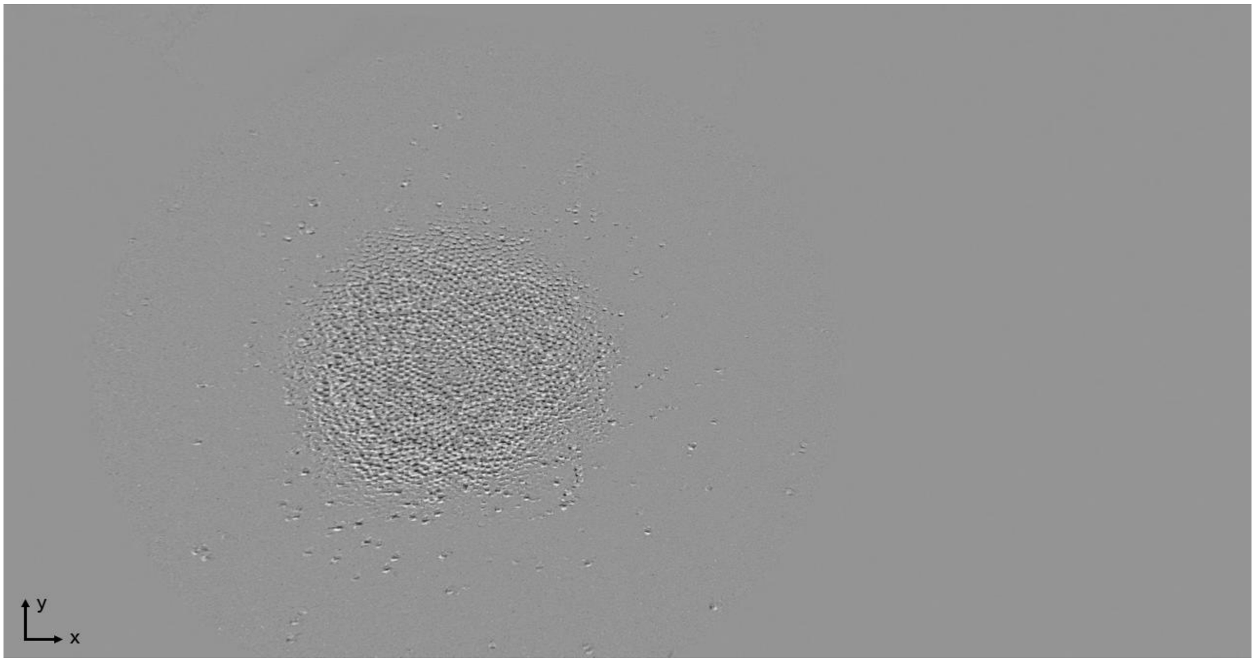

Figure 32: Top-down, background-subtracted view of the 10 ms pulse experiment in µg with steel bead simulant, showing the PSI area of effect.

25 ms and 50 ms Pulse Behavior

The effects of the 25 ms and 50 ms pulses are relatively similar to each other. The higher surface pressure in these experiments produce smoother, well defined craters like that in Figure 33 with higher velocity ejecta, as seen by the smearing of beads in the frame for a 50 ms pulse. Discrete features in the pre-PSI which were preserved by the gentler pulses are erased in these experiments. The 50 ms pulse jet bottoms out, clearing a small region of the baseplate. This was not seen until the 100 ms experiment at a 29 cm nozzle height. Off-center particle lofting is also visible in these experiments, produced by gas flowing through the material and resurfacing outside the main crater region.

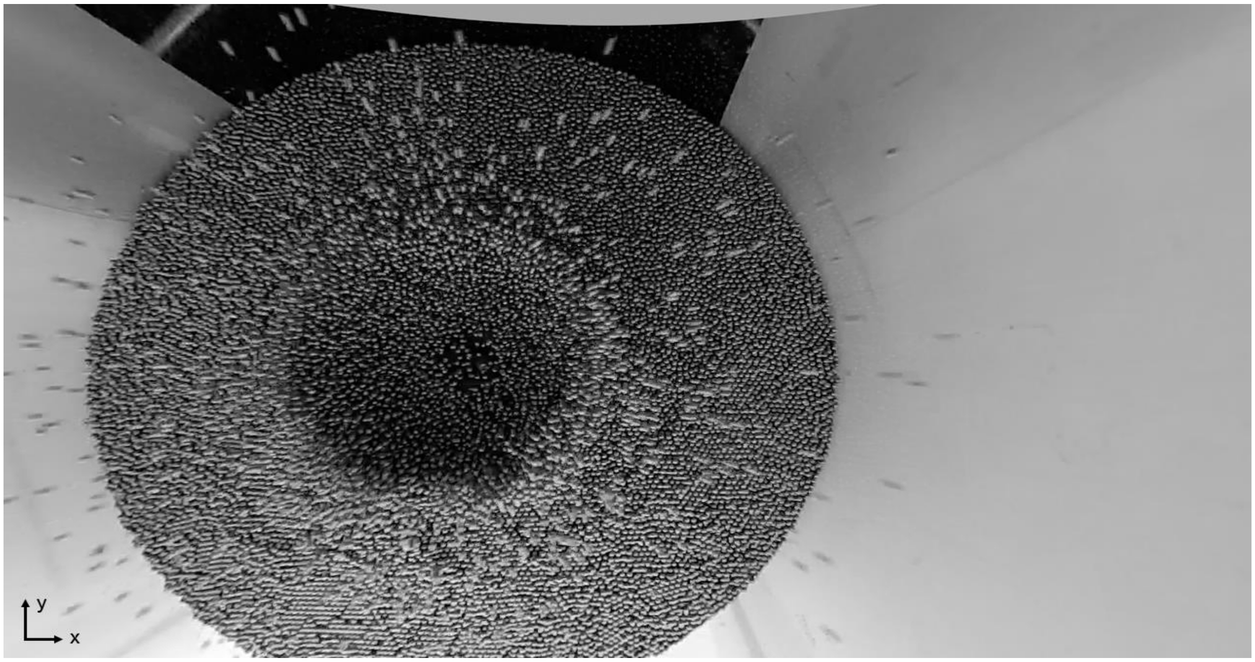

Figure 33: Top-down view, 200 ms into a 50 ms pulse steel bead experiment in µg. The pulse produces a well-defined crater and has just begun to clear to the baseplate on-center.

100 ms and 250 ms Pulse Behavior

These experiments bottom out quickly as the gas jet ejects beads and pushes them aside, up, and out. This crater grows outward quickly, as seen in Figure 34, reaching about half the width of the chamber in the 100 ms pulse case. There is a smooth, curved transition from the surface to the ejecta front. In the 250 ms pulse case, the camera is nearly obscured by the end of the experiment as most of the material in the chamber is peeled upward and outward by the gas flow.

Figure 34: Side view, 200 ms into a 100 ms pulse experiment into steel beads in μg. The ejecta splash smoothly transitions into the undisturbed surface.

The 100 ms pulse experiment conducted at 1*g* produces a small crater. A few beads are lofted on short, low trajectories but quickly fall back to the surface. This effect is more pronounced for the 250 ms experiment. Beads are scattered over most of the surface, and a small crater is formed on center.

Summary

While the steel bead experiments are not representative of a planetary surface, they give us a first look at the microgravity PSI phenomena. Differences between bench testing at 1*g* and drop testing in microgravity are twofold: Gravity damps behavior generally, reducing PSI significantly. But it also masks distinct phenomena. Much of the behavior we observe is unique to the microgravity environment.

On-center ejecta varies from small perturbations at short pulse durations to cratering and clearing the baseplate surface at longer pulse durations. Shorter pulses produce “impact-like behavior”. Longer pulses more closely tie the particle motion to the flow, driving material upward and outward, peeling back the entire surface layer, and showcase the difference between impactor experiments and PSI.

Off-center ejecta are visible even with shorter pulse durations. Gas injected into the surface of a permeable material flows outward and resurfaces off center, disturbing and possibly ejecting grains. This effect is much less pronounced than the on-center effect. At longer pulses, however, it becomes more difficult to distinguish between these two effects, as flow begins to drive bulk motion.

Sand

10 ms Pulse Behavior

In the first few ms of PSI, we observe an axisymmetric disturbance of the granular surface. In the first two frames, sand grains are visible near and then adhering to the side of the chamber tube. Given the limitations of our camera’s framerate, we may only approximate the velocities of these fastest particles. A particle originating at the plume centerline and reaching the edge one frame (8 ms) later would have a velocity of approximately 14 m/s; particles originating half a radius out from center and taking two frames would have a velocity of approximately 3.6 m/s. This is the upper bound we can estimate, although it is possible grains may be traveling faster. There are a small non-negligible number of grains accelerated quickly—

a crudely estimated 100 grains stick to the tube’s surface—traveling in this, fastest, velocity range.

This symmetric disturbance appears in background subtracted images as an annular region from the top-down camera view seen in Figure 35. It is blurred in the center, surrounded by the texture of moving grains. Each frame is 8 ms apart, so the pulse is completed after the first or second frame in which we see motion, but it takes about 58 to 67 ms (7 or 8 frames) for the surface disturbance to reach its radial maximum. From the side view we observe a wide distribution of velocities such that the mass fraction decreases with increasing velocity—that is, there are fewer particles at higher velocities.

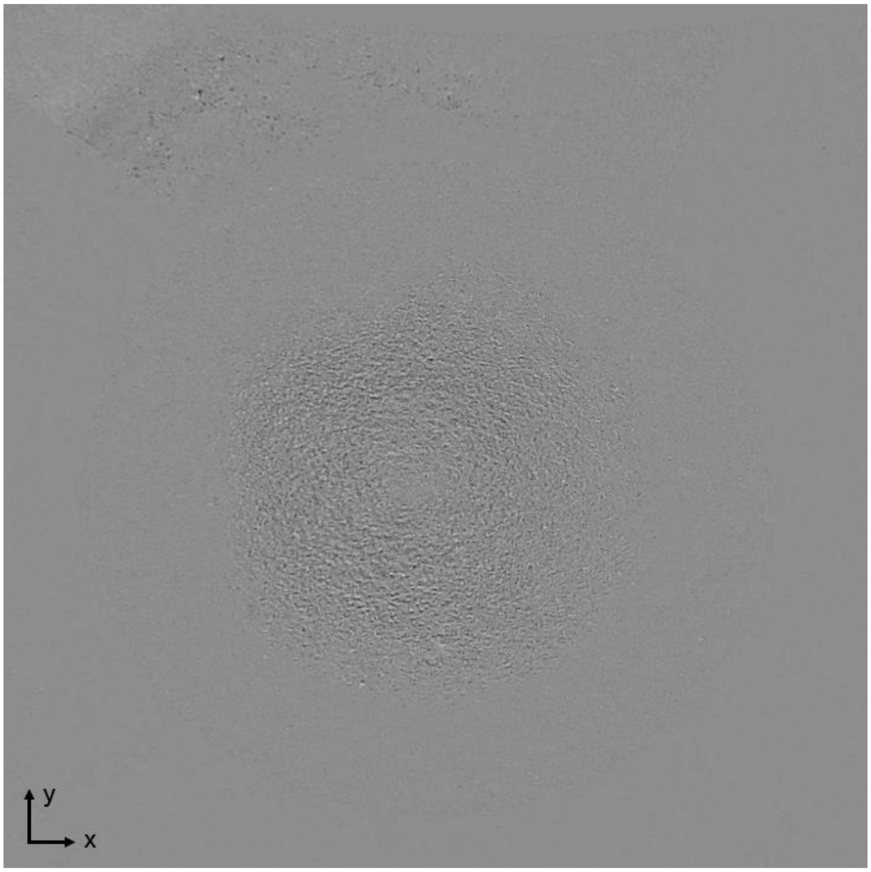

Figure 35: Top down view, background subtracted frame from a 10 ms pulse experiment into quartz sand in µg. The disturbed annular region forms almost immediately, here seen 25 ms after jetting starts.

Sand grains begin to move upward and outward the annular region which appears in the first few frames. At 117 ms into the experiment, pockets or gaps become visible in the top-down imagery, as shown in Figure 36 below. These gaps either fill in or are obscured as the experiment progresses, but they seem to be pockets of gas re-surfacing after injection into the sand. On-center, a larger, crack-like behavior persists. This can be observed with varying structure in each of the 10 ms experiments, and it persists through the end of the experiment (650 ms). Prior work with PSI in sand, at 1*g* and on larger scales, noted the appearance of a “small cavity or pocket on the surface” of their experiments, which “lifted into a bubble, or cake-like structure” (Alexander et al., 1966). These phenomena occurred between 50 and 300 ms; similar to the range we observe, though the behavior they describe is more dramatic. As we will note below, this type of behavior disappears at longer pulse durations. It appears that short pulses may inject gas into sand in a way that causes disruption but finds “cracks”, regions of lower strength, but maintains pre-existing structure.

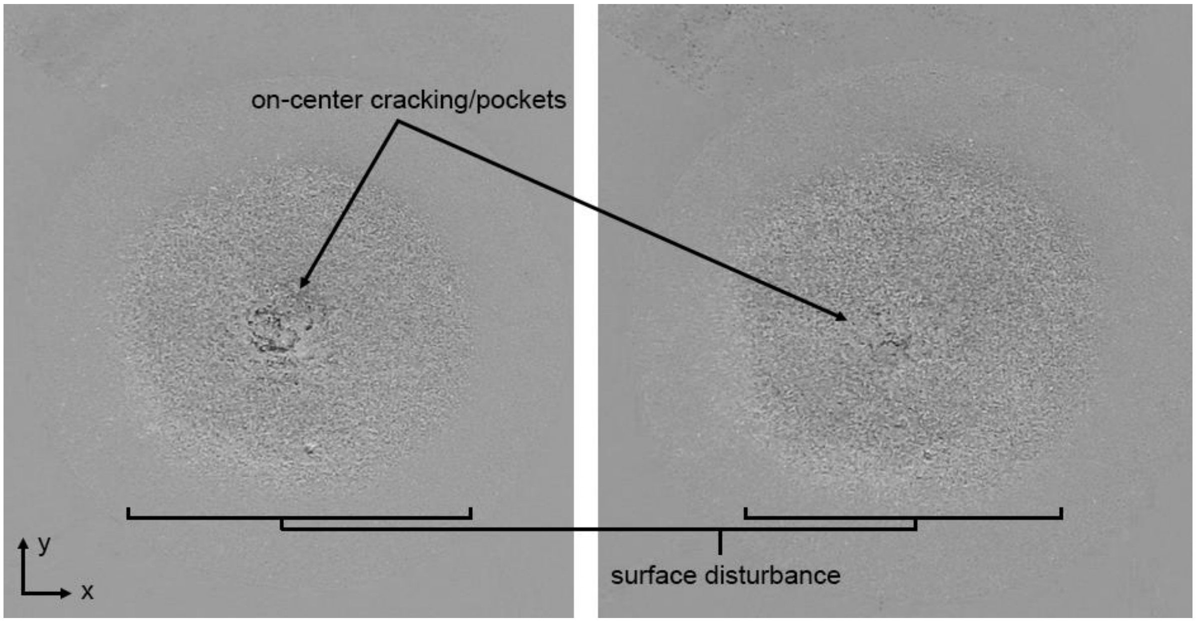

Figure 36: Top-down view, background subtracted, 36 ms into two separate 10 ms pulse experiments into sand in μg. Irregular on-center pockets or gaps are visible, caused by gas injection and emergence from beneath the surface.

While individual grains move at higher velocities than the bulk ejecta through the experiment, the region of highest density moves slowly upward and outward at an angle roughly 45 above the surface, and it becomes sparser over the course of the drop.

On the bench, at 1*g*, the pulse causes only a slight annular disturbance, though it should be noted that the experiment was not properly smoothed and a small crater was present at the beginning of these experiments. A few grains appear to stick to the wall 25 ms into the experiment, possibly due to a ramping effect by the crater slope. By 41.5 ms, surface motion has largely stopped. A few grains continue to rain down from the lid after this point, but it is unknown whether these were freshly lofted by this experiment run or grains which were stuck at the top and dislodged by the airflow.

25 ms Pulse Behavior

A noticeably louder thumping noise is present in the internal camera audio from the gas plume. An annular disturbance is present in Frame 1 which, to visual inspection, appears nearly identical to Frame 2 of the gentler 10 ms pulse experiment. In principle, the first portion of a given experiment should appear identical to the driven portion of a previous experiment, assuming similar flow. That is, the first 10 ms of this experiment ought to look like the first 10 ms of the previous experiment. Given the difficulty in determining a precise starting frame, and the fact that we have only 8 ms time resolution, it seems plausible that this is in fact the case for these two experiments.

After Frame 1 (8 ms), this experiment exhibits more violent behavior than the 10 ms pulse experiments. The plume is still actively driving PSI. Brightening of the entire simulant area occurs in Frames 2 and 3. The side view camera does not show this as a disturbance, so it may be due to lofted dust. The gas plume stops after Frame 3. The surface disturbance reaches its maximum radial extent between Frames 6 and 7. Gas pockets begin to appear in Frame 6. These appear to connect and evolve to form an open, irregularly shaped region. This region evolves as the experiment progresses. These pockets lose their distinct shape around Frame 45 and begin to be obscured or obliterated. This is a more complex version of the phenomenon described in the 10 ms experiment. In one experiment, No. 151, the region appears to be larger: a dark region in the background subtracted image indicates a couple-centimeter wide pocket formed by gas injection.

The side-view camera shows sand grains, likely reflected off the tube walls, beginning to deposit around the crater in Frame 7. This saturates the viewing area by Frame 13. Curiously, the ejecta angle for this pulse duration appears to be shallower than that of the 10 ms experiment. We hypothesize this is due to a kind of gas-suppression effect. A shorter pulse “punches” the sand, and the material rebounds. With a slightly longer pulse, sand is driven outward at a shallower angle as seen in Figure 37. From a side view, the ejecta flow reaches an apparent steady-state at Frame 16, remaining so until tapering begins around Frame 36. From a top down view this transition is not as apparent; it appears that ejecta’s radial motion slows and becomes sparser from around Frame 36 until the end of the experiment at Frame 79.

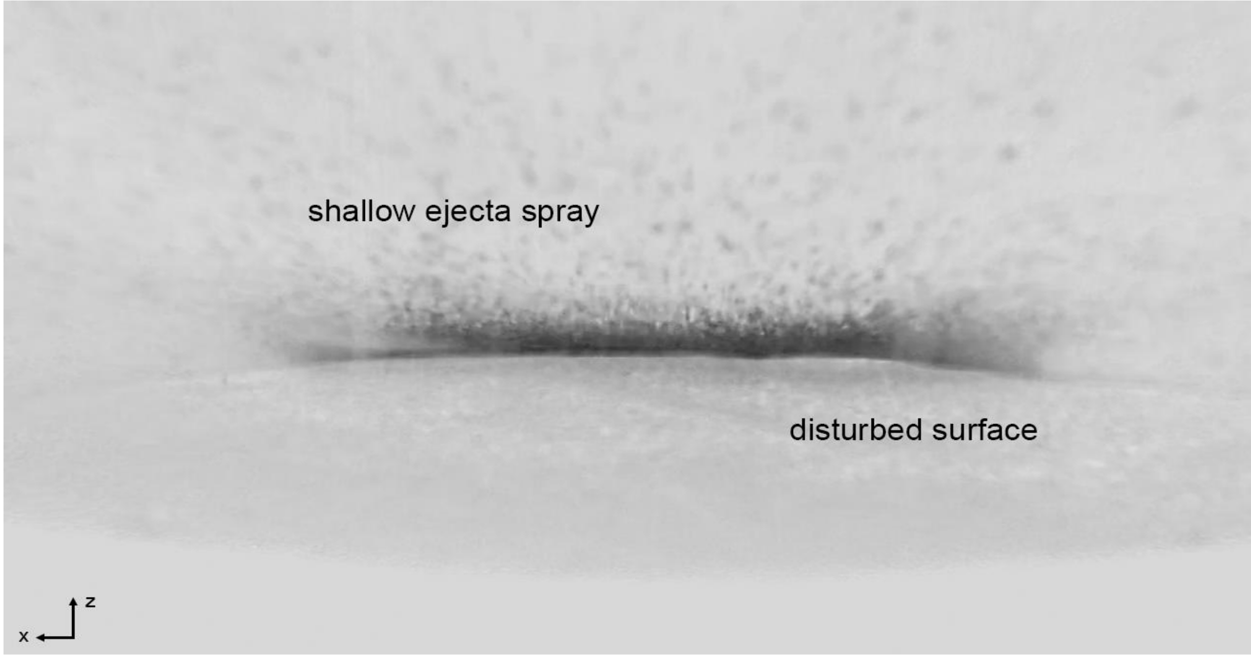

Figure 37: Side view, background subtracted, 83 ms into a 25 ms pulse duration experiment in µg using quartz sand. The curved outline of the surface is visible, and lighter regions indicate texture in the surface disturbance. The ejecta spray is sparse and relatively shallow.

At 1*g*, the apparent motion is subtler. The experiment was not fully reset so a small crater remains. Surface scouring is present to about one-half the interior tube radius. This disturbance appears to develop all at once in this annular region. Material is blasted outwards at a low angle. In Frame 4, a thin stream of material can be seen flowing out from the center. It migrates axially counterclockwise as it widens and dissipates over about six frames. Bulk motion ceases quickly by about Frame 14, and there is no noticeable change to the surface.

50 ms Pulse Behavior

In Frame 1, a blur of material begins to project outward. From a side view, this increases in Frame 2. Slower individual grains are visible ejecting at a similar low angle in Frame 4. The top camera indicates surface disturbance to about one half the testbed radius in Frame 1 with fines are visible at the edge. This indicates fine particles traveling at least 14 m/s.

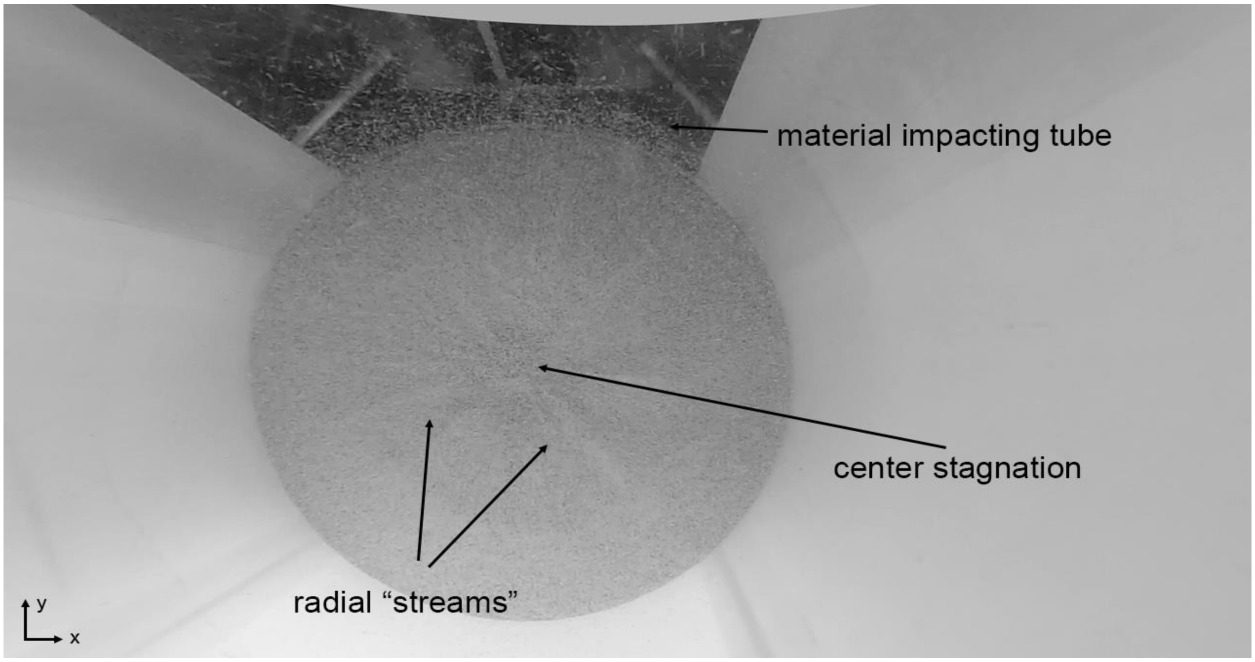

Figure 38: Top down, standard frame, 141 ms into a 50 ms pulse experiment into quartz sand in μg. Radial, streamer-like features are visible in the ejecta.

An annular region of ejecta spray with thin streamer-like features is prominent for the first half of Experiment No. 154, shown in Figure 38, spreading and losing its distinct features after the pulse ceases and the ejecta moves outward. In a circular region on the centerline of the pulse, the distinct pocket-like behavior has disappeared in all but one experiment. Sand on the centerline appears to be loosened and less dense from gas injection but the structure seen before is largely gone. There is also less apparent motion on the plume centerline.

At 1*g*, we observe similar behavior as the previous 25 ms test. The experiment was not reset, so a small crater was present before the jetting experiment began. This appears to direct some of the ejecta flow to a higher angle. The flow also dissipates quickly after the pulse ceases. The PSI area seems to be slightly narrow in experiment 144 vs. experiment 141, the 25 ms case. This may be due to the higher starting pressure, or it may be an artifact of the initial crater.

100 ms and 250 ms Pulse Behavior

At 100 ms and 250 ms pulse durations, there are no distinctly new features apparent. The disturbance area is wider, and from a side view ejecta quickly covers the viewing area. The longer pulse duration accelerates more material, and the central stagnation region is slightly larger. The ejecta angle is similar to the 50 ms pulse experiment. Any cratering produce by these experiments is shallow and indistinct. Some of these experiments show very clear streaming behavior, as in Figure 38. The center region in these experiments does not display the significant uplift and pocket-like behavior of previous experiments. Simulations indicant this behavior is due to gas which diffuses into the regolith and then diffuses back out after a pulse stops. Long duration pulses may instead accelerate this loosened material outward, lessening the effect. The experiments conducted at 1*g* do not show any distinct phenomena besides increased intensity due to pulse duration.

Double Pulse Behavior

Two of the 50 ms experiments conducted at 1*g* experienced an off-nominal double pulse. The beginning of each pulse was separated by about 250 ms. While this was not done intentionally, it allows an anecdotal comparison to the work of Manish Mehta, who conducted intentionally pulsed experiments and observed the PSI mechanism he terms Diffuse Gas Explosive Erosion (Mehta et al., 2011).

Given the delay between pulses, in our two experiments it does not appear that erosion during the second pulse was significantly more pronounced than during the first pulse. We do not observe DGEE in these two experiments.

Summary

Sand is a relatively impermeable medium, so its PSI behavior is primarily characterized by shallow surface erosion. Nevertheless we see diffusive behavior on-center which penetrates the medium and loosens material. This reveals underlying bulk structure after short pulses cease, and loosens material which may then be driven away by a longer pulse. This also gives us insight into the mechanism of DGEE. Short, repeated pulses injecting gas on-center and loosening material would cause a spray unlike the surface scouring behavior we observe for long duration pulses.

Glass Beads, 25 cm Nozzle Height

In moving from beach sand to a glass bead simulant, we keep the same grain density but increase permeability. The beads are round and lack and residual fines present in the sand. These size and morphology differences mean the beads are less cohesive. Recalling that permeability varies with the square of the grain diameter, we estimate our glass bead simulant is approximately one order of magnitude more permeable than the beach sand. Each of these will contribute to differences in material behavior. Experiments with glass beads were conducted at two nozzle heights. Phenomena are noted for both.

10 ms Pulse Behavior

Each 10 ms pulse produces a small crater. Compared to the sand experiments the ejecta is gentler, with lower particle velocities, but angled higher. Its crater is noticeably deeper. The familiar off-center disturbance is visible in these experiments, and beads outside the main ejecta spray are gently lofted upward as seen in Figure 39. This could be due to gas motion across the surface, but we will see from CI Orgueil experiments described below how off-center flow is traced in more permeable media, which means resurfacing gas is a likely contributor.

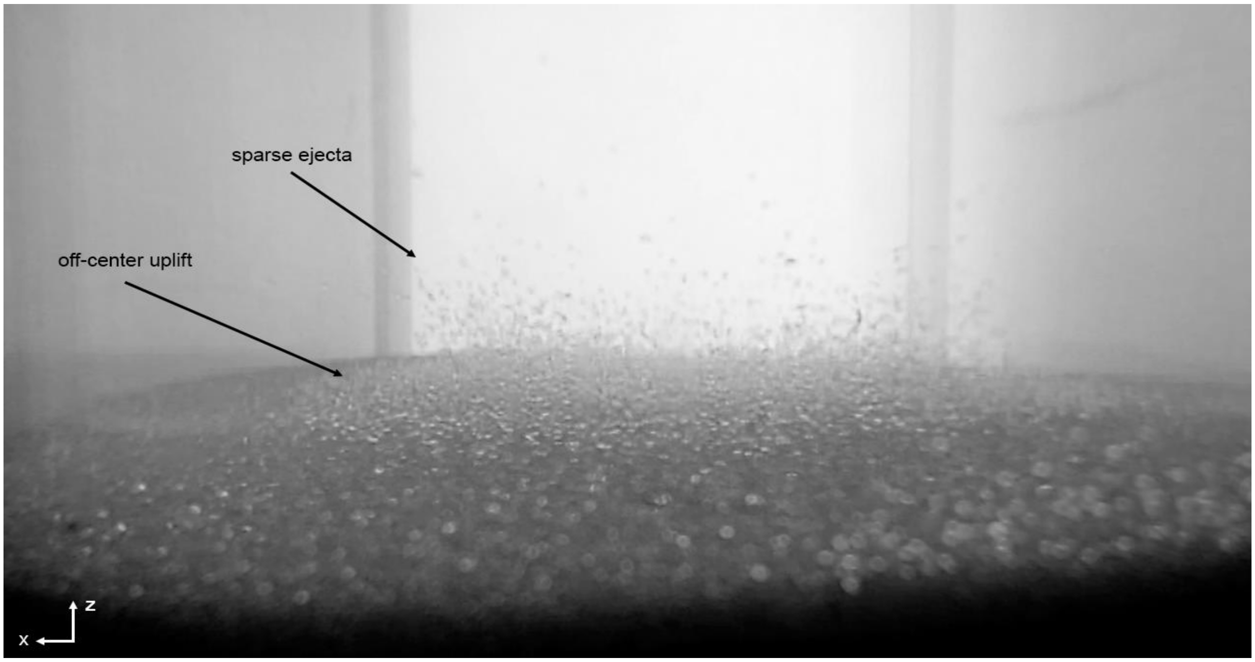

Figure 39: Side view of a 10 ms pulse into glass beads in μg, 208 ms into the experiment. Sparse ejecta are gently lofted, while off-center uplift is also visible.

Another clue to gas motion comes from two of the three 10 ms pulse drops. Additional narrower splashes appear superposed over the larger craters, seen in Figure 40. These become visible around Frame 3 in one experiment, and Frames 5 to 6 in another. They appear to be significantly deeper than the primary crater, and their shapes are slightly irregular.

There are a few possible explanations for this effect, which is noticeably absent from one of the three experiments. First, the gas flow could be contaminated with a small impactor—either solid or liquid. The former seems unlikely as there are multiple small craters in one experiment and we had not yet tested sand in the apparatus; the latter should be noticeable through a pressure anomaly. The difference in pressure was the same for all three experiments. Second, we observe an abundance of small impacts when the apparatus hits the ground from beads that were previously lofted. It is conceivable that, in the initial blast, a particle was lofted upward and then ricocheted back to the surface. Rebounding from the lid would require a particle velocity at least 20 m/s. Given our other observations, we judge this possible but less likely. Finally, it may be that injected gas finds a subsurface irregularity in the bead packing structure, creating a bubble which erupts into a small crater. Given the apparent depth of these small craters, we judge this plausible.

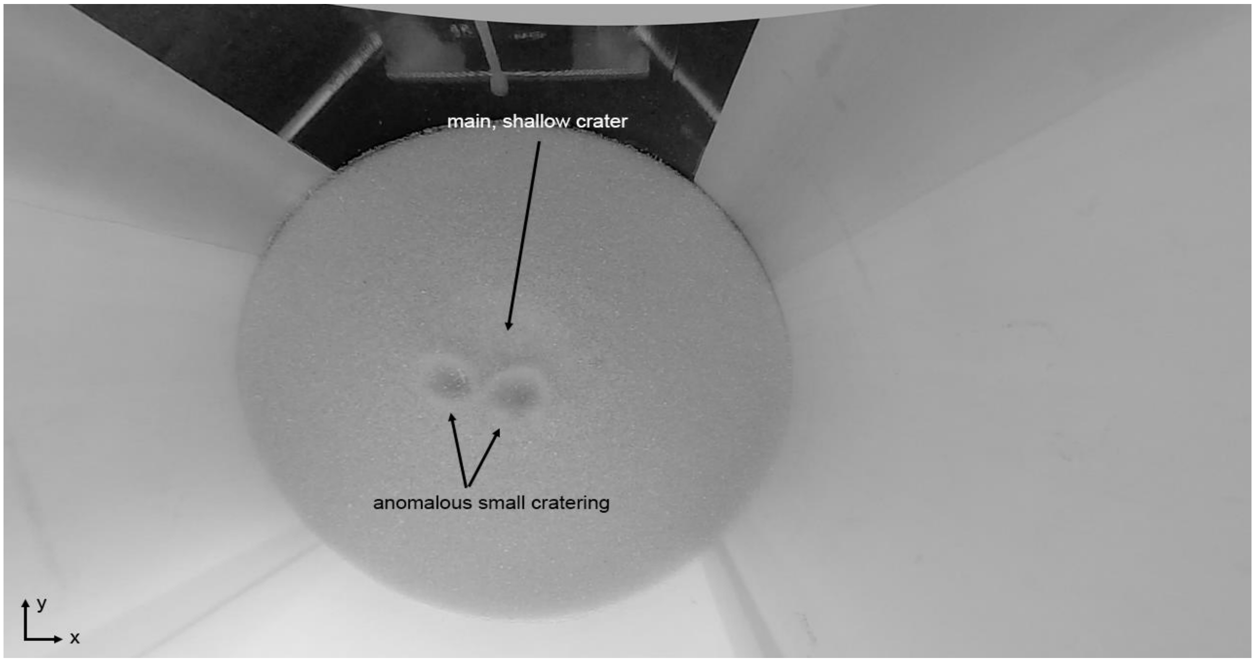

Figure 40: A top down view of a 10 ms pulse experiment into glass beads in μg. The primary crater is overlaid by two off-center craters. The origin of this effect is not completely clear.

One of these auxiliary craters appears well outside the main crater in Frame 60 of its experiment. It is smaller but appears to have the same morphology of the larger crater. It is more plausible that this is due to a bead ricochet since it appears late in the experiment drop.

A countable, small number of particles are disturbed and move in the test conducted at 1*g*. While only one bench test was performed, no anomalous cratering was observed.

25 ms Pulse Behavior

We observe a main crater produced by the gas jet as well as a more significant off-center disturbance of the simulant. This ejecta spray appears to be angled slightly lower relative to the surface than the 10 ms pulse. While there is large scale symmetry to the bead motion, we see small scale features within and outside the forming crater. Whatever asymmetric structure exists in the undisturbed simulant gives rise to smaller-scale features within the ejecta spray. While the pulse ends by Frame 4, the main crater radius does not appear to stabilize until around Frame 30. Outside the crater, beads at the surface are disrupted, loosened, and gently lofted.

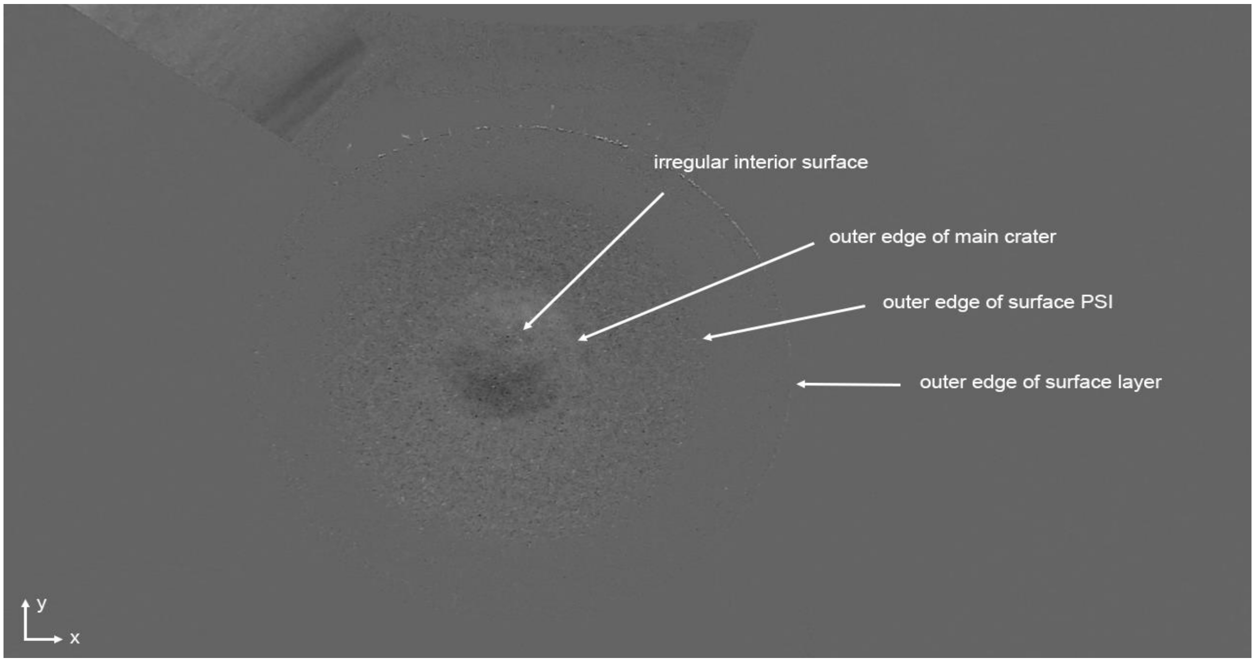

Figure 41: Top down, background subtracted frame, 83 ms into a 25 ms pulse experiment using glass beads in μg. Small-scale texture is visible within the forming crater; off-center PSI is also visible.

The experiment at 1*g* produces a small crater. Background subtracted images from the top-down camera such as Figure 41 show a slight off-center disturbance as well, but no off-center lofting is visible from the side.

50 ms to 250 ms Pulse Behavior

These experiment sets show largely similar behavior qualitatively, while the final crater size increases significantly with pulse duration. Gas injection causes a ejecta, lofting material in an impact-like splash but also lofting material outside the primary crater. The angle appears to increase slightly with pulse duration.

As pulse duration increases, this shallow ejection limits our ability to observe distinct features in the spray. Beads flying directly toward the camera quickly obscure the frame, seen in Figure 42, forming a thick band of particles impacting the interior of the tube. This obscuration is also visible from the top down cameras. As ejecta rebounds toward the center it obscures the expanding crater.

Figure 42: A side view frame of a 50 ms pulse into glass beads in μg, seen here at 83 ms into the experiment. Shallow ejecta splays outward and obscures much of the view.

Behavior in 1*g* is noticeably subdued. In the 50 ms case, and unlike behavior in microgravity, crater growth ceases rapidly after the pulse finishes. The same is observed for the 250 ms pulse, though it appears crater growth has largely stopped before the pulse finishes. We note these differences as further examples of gravitationally masked behavior.

Glass Beads, 15 cm Nozzle Height

10 ms Pulse Behavior

Compared to the 25 cm height test, ejecta behavior is largely similar. We observe the same splash-like behavior, and similar off-center disturbance of the glass beads. The ejecta angle is similar. The crater and ejecta spray caused by this experiment appear to be slightly more defined than its 25 cm height counterpart.

No test at 1*g* was conducted for this parameter set.

25 ms Pulse Behavior

If the differences between the 10 ms pulse tests were subtle, they become obvious at this pulse duration. From the side view, we observe clearly defined ejecta that looks similar to hard impactor tests. Outside this main splash, off-center ejecta is also visible as before, moving at a gentler velocity compared to the primary ejecta. The top-down camera shows a smooth surface on the interior of the crater. We no longer see the smaller scale features and irregularities present at first in the 25 cm test, but this smooth surface becomes textures toward the end of the experiment. Curiously, the crater width for this lower-height test does not appear to be significantly wider, though the increase in ejecta indicates it is deeper.

The experiment was not properly reset for the test at 1*g*; however images show a brief ejecta spray that ceases after the pulse stops. It does not significantly enlarge the crater present at the beginning of the test.

50 ms Pulse Behavior

The pulse for this experiment last six frames. In the first couple frames, we see a significant number of particles shot out away from the center. They cannot be seen distinctly but show up as long streaks in the video frames. The ejecta crater rapidly expands, its interior smooth, as beads continue to streak from its outer edge throughout the jetting pulse. From a side view, surface of the simulant seems to swell outward as the crater expands. There is bulk swelling and uplift of material around the neck of the ejecta spray—that is, the narrowest point where it connects to the surface, as shown in Figure 43.

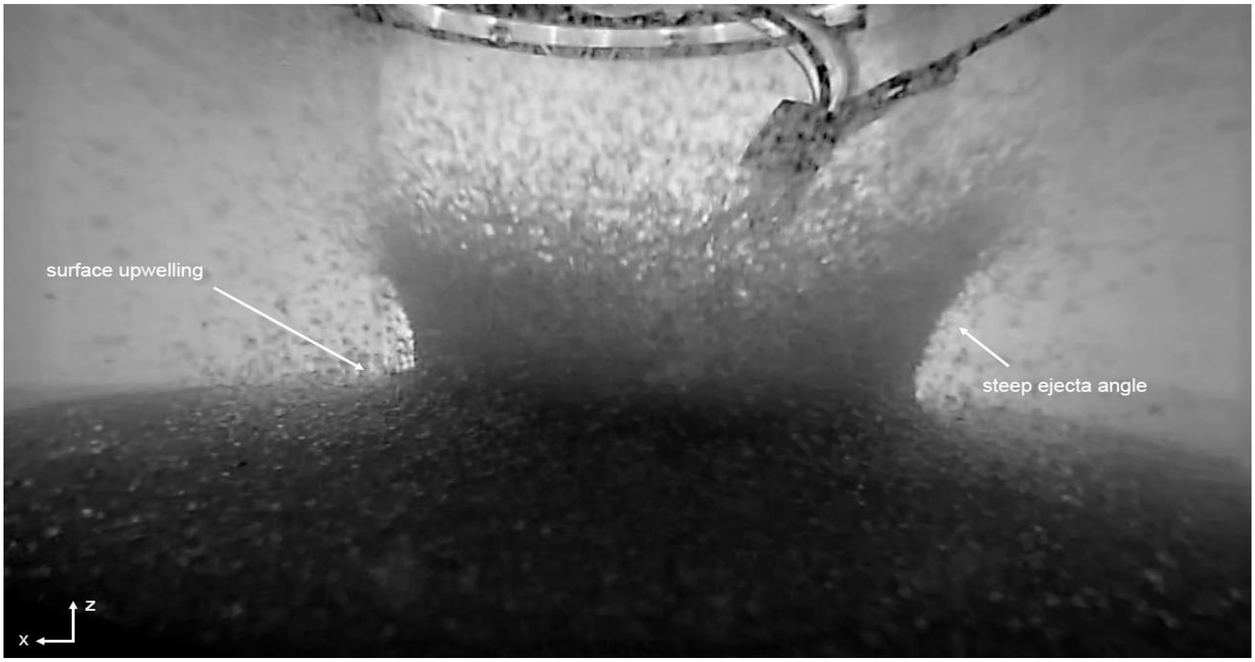

Figure 43: Well-defined ejecta from a 50 ms pulse into glass beads from 15 cm, here at 125 ms into the experiment in μg. Off-center lofting is also visible outside the primary ejecta wall.

Crater expansion continues well past cessation of the pulse but seems to stabilize by Frame 30. Small, bubble like features within the crater appear around Frame 25, giving texture to the smooth inside surface. The ejecta spray exhibits discontinuities as well.

The experiment at 1*g* is a subdued version of the microgravity experiment, exhibiting the off-center uplift so far only observed in microgravity. Uplift and ejecta production quickly cease when the pulse ends at Frame 6, followed by interior slope collapse in the crater as the beads seek their angle of repose.

100 ms Pulse Behavior

For the 100 ms pulse we see two stages to the ejecta motion. First, we note behavior similar to the 25 ms and 50 ms pulse cases. A well-defined ejecta spray occurs surrounded by gently lofted particles out to a terminal radius. The neck of the ejecta wall, however, soon upwells and widens as we began to observe in the 50 ms pulse. The behavior is much more pronounced, and the ejecta angle steep. This behavior is driven by the pulse until it ends at Frame 12, after which the material again continues expanding in a familiar ejecta spray. The upwelling near the surface remains, however, creating a smooth, curved transition from the material surface outside the PSI region to the ejecta wall itself.

Top-down video shows the gas flow driving this effect. It bores down into the simulant during the pulse, producing a steep ejecta angle, as shown in Figure 44. Crater expansion continues past the end of the pulse at Frame 12, and the platform beneath the regolith becomes visible at Frame 21 some 90 ms after the pulse ends. Though the crater is somewhat obscured by ejecta, it appears to stabilize in size around Frame 40.

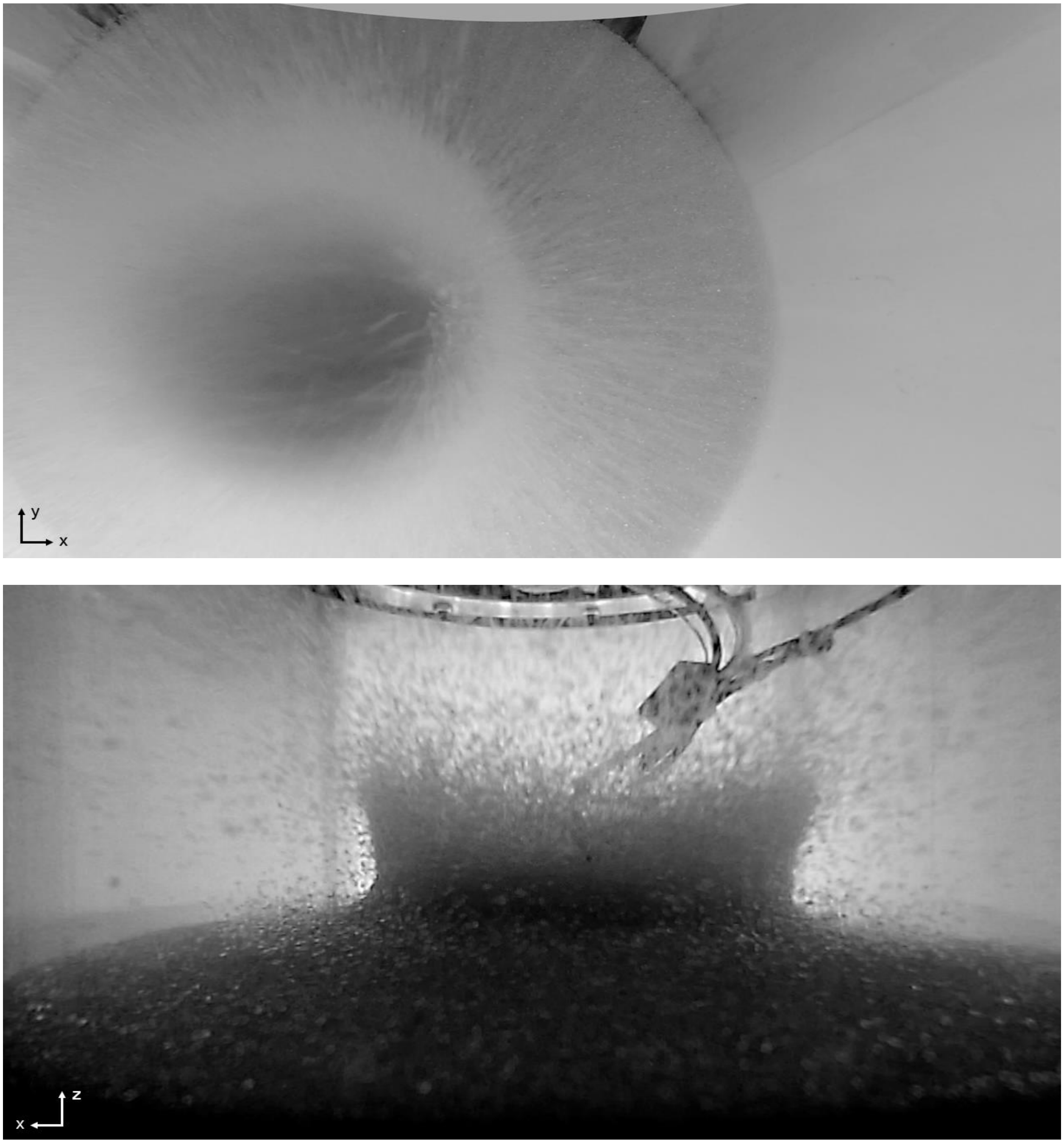

Figure 44: Top down (top) and side (bottom) views of a 100 ms pulse into glass beads, 100 ms into the μg experiment (at pulse cutoff). Gas bores down into the material, lofting it at a steep angle. Beads traveling at relatively high velocities streak in-frame.

At 1*g*, we see ejecta followed by what appears to be a damped version of this same bulging, uplifting phenomenon seen in the microgravity case. In this experiment, however, gravity reduces the height of this phenomenon and redirects it radially outward. Particles take pseudo-ballistic trajectories before the pulse ceases, and the ejecta is spread over a wider angular range. The ejecta spray collapses quickly after the pulse ceases at Frame 12. On the interior of the crater, this is followed by axisymmetric wall collapse which begins at the rim of the crater and moves inward.

250 ms Pulse Behavior

The first few frames of this experiment run look familiar. Beads are ejected in the initial spray, and beads outside this are gently lofted. By Frame 12, where the 100 ms pulse cuts off, we observe the same widening and upwelling of the simulant as gas pushes material upward and outward. This widening continues as a deep crater is formed. The top down camera shows crater expansion downward and outward, with the acrylic baseplate clearly visible by Frame 18 in a small central area. This area rapidly widens as the camera begins to be obscured by ejecta by the pulse end at Frame 30. From the side view, the ejecta plume continues to upwell into an almost hourglass shape. Though the top down view is obscured, it appears that gas may “blow out” material from the baseplate, creating a large hollow region underneath the simulant. Note that much of this expansion as seen from inside and outside the ejecta spray occurs after the pulse stops. No test at 1*g* was conducted for this parameter set.

Summary

Our experiment series with glass beads demonstrate a fascinating range of behaviors masked by 1*g*. These interactions may be characterized by an initial spray of material caused by the shock of gas first impacting the surface, followed by gas causing ejecta inside and outside the ejecta crater. After this, if the pulse duration is long enough, we see mass upwelling and expansion due to gas injection. Ejecta outside the main crater, which we term off-center lofting, is seen even in gentle PSI behaviors but only appears in 1*g* tests for long pulse durations.

As expected, moving the jet nozzle closer to the surface significantly enhances the amount of material disturbed and the cratering depth. It results in a higher ejecta angle and more well-defined ejecta cone. At longer pulse times, the closer nozzle injects gas which rapidly bores out material and causes mass upwelling.

CI Orgueil, 25 cm Nozzle Height

No experiments at 1*g* were conducted for this height.

10 ms Pulse Behavior

CI Orgueil simulant is highly permeable, and fine dust serves as a tracer to show gas flow. Off-center flow is visible in the Frame 1 as a stream of fine dust is carried out of the regolith. This flow out of the regolith remains visible for about seven frames. In two of the experiments, conducted earlier in the campaign, a small countable number of blocks are gently moved or perturbed by the jet but hardly lofted; some come to rest before the experiment period ends. The outlines of these particles can be seen in Figure 45. In a later experiment, a larger number of blocks are lofted with very small velocities, but near the end of the experiment these drift slowly back toward the surface. This is likely due to drag giving a slight effective gravity.

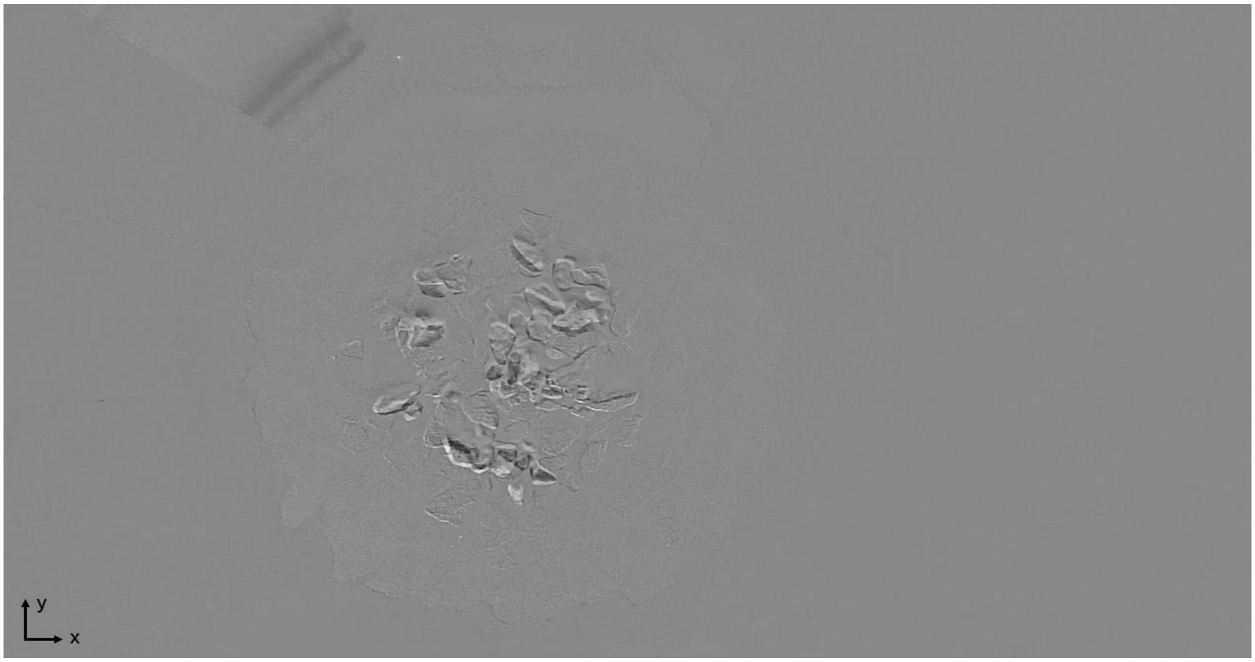

Figure 45: Background subtracted frame about halfway through a 10 ms pulse µg experiment into CI Orgueil simulant. The perturbed region is visible on center; most particle motion has ceased.

25 ms Pulse Behavior

The experiments with CI Orgueil are notable for their variety at these lower pulse durations. Gas injected is visible streaming up out of the regolith off-center, and this lofts particles with it in a much sparser version of the ejecta behavior seen in glass beads. Most are lofted gently, but there are a couple exceptions—in one experiment, a small block speeds away from the rest quickly. Most lofted blocks appear to come from this annular region about the centerline, though regolith on-center is also disturbed. This variability, seen in Figure 46, no doubt stems from small, local variations in gas flow caused by local variations in regolith block size and shape.

Figure 46: CI Orgueil particle lofting, here seen in a side camera view, 375 ms into a 25 ms pulse μg experiment. The results are irregular and asymmetric.

50 ms Pulse Behavior

With larger particles there is no well-defined, fluid-like ejecta splash similar to the glass bead experiments. Instead regolith blocks are lofted on a similar trajectory, but the visual effect is sparse (see Figure 47). Each experiment conducted here is once again unique; resetting the experiment mixes up the distribution of particles lending itself to significant variation relative to the glass bead experiments. While there is more variation in particle velocities experiment to experiment, the overall phenomena appears similar across the range of pulse durations.

In this case, injected gas again streams out lofting particles upward and outward—even particles on the centerline are pushed to the side. The fastest particles again appear to come from an annular region around the centerline. Particles on-center are perturbed, but do not make up the faster-moving ejecta. This interaction produces a crater, though its boundaries are much more difficult to define because of the large particle size and spacing in between blocks.

Figure 47: A side view of CI Orgueil simulant lofted in a 50 ms pulse µg experiment, seen here 375 ms after jetting was triggered. Compare the significant increase in ejecta to lower jetting durations.

100 ms Pulse Behavior

The behaviors previously described are enhanced in these experiment runs, and this lends more clarity to the mechanism of regolith displacement. As off-center blocks are lofted, particles closer to the center are displaced downward until the pulse ends. The gas flow destabilizes an entire center region; in this experiment, the baseplate becomes clearly visible by Frame 30 as blocks move up, out, and away from the center and a crater slowly clears. From the side, we see many of these particles are lofted at a steep upward angle, higher than the glass beads, and following the flow-line indicated by the dust tracers (shown in Figure 48) in the first few frames.

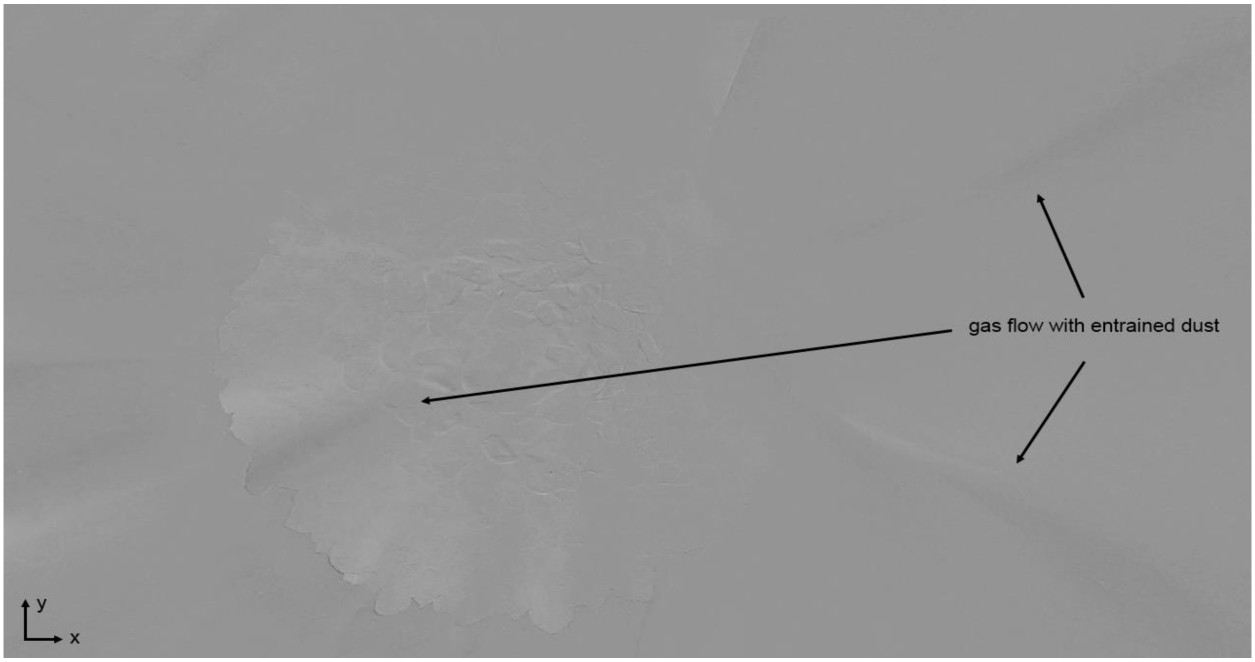

Figure 48: A top-down, frame-difference image taken 42 ms into a 100 ms pulse μg experiment into CI Orgueil simulant. Particle motion has just begun on-center, while streams of dust-entrained gas are visible moving outward.

250 ms Pulse Behavior

These experiments lose their distinct character. The gas jet bores a hole down through the regolith to the baseplate by Frame 20, then expands this cylindrical region as regolith is lofted steeply and vertically toward the top-view cameras. From the side, little detail is visible as the entire frame quickly fills with material traveling almost straight up. Note that this occurs for experiments conducted with regolith at the base of the apparatus, where nozzle distance is at its maximum.

CI Orgueil, 15 cm Nozzle Height

Experiments at 1*g* were conducted for each of the following; their results may be easily summarized. Though gas flow is clearly visible in each experiment due to dust, no particle motion occurred for a 10 ms pulse. At 25 ms and 50 ms pulses, a few particles were perturbed and rocked but did not move from their places. At 100 ms, a few particles are moved outward by the jet, and at 250 ms there is more significant albeit small radial motion. This last experiment also lofts a few of the smallest particles, but there is no significant lofting of any of the bulk regolith.

10 ms Pulse Behavior

These are similar to the experiments at a 25 cm nozzle distance. A small center region of particles are disturbed. One experiment appears more active than the rest; particles are gently lofted and a small crater region appears. For the other two, lofting does not occur. Particles are disturbed, and some settle back to the surface over the course of the experiment drop.

25 ms and 50 ms Pulse Behavior

These experiments are quantitatively similar. Gas injection produces more well-defined ejecta than when the nozzle is further away. Material is lofted at a roughly 45 degree angle from the surface. The differences between this and experiments at a 25 cm nozzle distance are likely due to increased surface pressure and a narrowed pressure distribution. The effects at this nozzle height appear similar but with a wider region of disturbance. Quantities lofted, however, appear roughly similar, as seen in Figure 49 and Figure 50.

Figure 49: Side view of a 25 ms pulse CI Orgueil µg experiment, seem 375 ms after jetting start. Compare this to Figure 46, which shows the same experiment at 25 cm nozzle height.

Figure 50: Side view of a 50 ms pulse CI Orgueil µg experiment, seem 375 ms after jetting start. Compare this to Figure 47, which shows the same experiment at 25 cm nozzle height.

100 ms and 250 ms Pulse Behavior

Each of these experiments is similar to the 250 ms experiment at a 25 cm nozzle height. The gas jet clears a cylindrical region into the regolith as it lofts material nearly vertically toward the top-view camera. In the 250 ms case, shown in Figure 51, this pulse appears to clear out the entire baseplate, lofting the entire mass of regolith simulant.

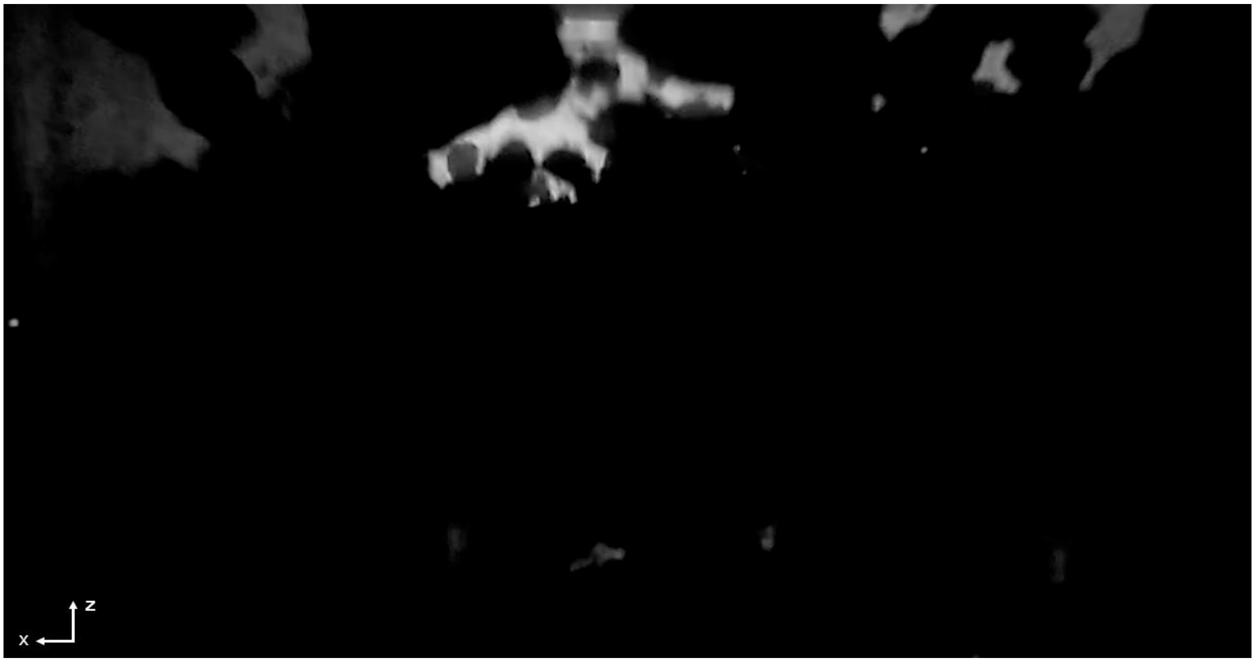

Figure 51: The side view camera frame is almost completely obscured during this 250 ms pulse duration μg experiment into CI Orgueil simulant, seen here 375 ms after pulse start.

Summary

Our CI Orgueil is a highly permeable simulant that, aside from the shortest pulse durations, is easily perturbed and lofted. Due to each particle’s mass, regolith blocks are lofted at lower velocities than seen in equivalent experiments conducted with sand or glass beads. This lofting is driven by the gas which injects into and immediately erupts out of the regolith in an annular region around the jet centerline. At longer pulse durations, most, if not all, of the regolith in the apparatus may be lofted by PSI.

Trends

We conducted experiments with four different media at two heights and five nominal pulse durations. Of these, the experiments conducted with quartz sand, glass beads, and CI regolith simulant were conducted with the same simulant depth. This allows a direct comparison of each simulant's behavior. Since grain density for each of these is similar, we may also draw conclusions about the effect of grain size on material behavior.

To be sure observed effects were due to the gas plume, control drops were performed with each simulant with no jetting. In each of these cases, no significant motion of the bulk simulant was observed. Individual particles, particularly at the edges, might be disturbed during experiment release, and continue slight motion through the drop.

It is intuitive to assume PSI behavior in 1*g* would differ from behavior in microgravity. We performed bench runs, however, to observe the magnitude of this difference. The difference is significant. For certain cases, there is a threshold pulse duration for observable PSI in 1*g*. Below this threshold, little or no particle motion was observed. Comparing each experiment drop to its benchtop counterpart, we observe that 1*g* serves to hinder or reduce PSI effects. Particle trajectories are shallower, tend to arc, and less material is ejected. This is particularly true of the steel simulant (highest particle density) but also apparent in lower density material like the glass beads.

Experiments were performed at two effective nozzle heights by placing a platform in the vacuum chamber. In a perfect vacuum, Robert's (1964) equation for surface pressure predicts a narrower pressure distribution with a higher peak pressure. Peak pressure decreases with the distance squared. By increasing the platform height 10 cm, from a 25 cm nozzle height to 15 cm, we expect peak surface pressure to increase approximately by a factor of 3. Controlling for other variables, reduced nozzle height significantly increases PSI effects. Ejecta volume, particle velocities, and crater depth all typically increase when the nozzle is closer to the surface. Ejecta are lofted at a higher angle relative to the surface, likely due to narrowing of the pressure distribution.

Comparing between quartz sand, glass bead, and CI simulants, ejecta angle, crater depth, and crater volume increase with particle size. The difference between quartz sand and the other simulants is quite pronounced, particularly at a larger nozzle height. Cratering in this fine-grained simulant tends to be shallow, and ejecta is directed outward and a low angle.

Regolith permeability increases with increasing particle size. Our quartz sand and glass bead simulants have similar grain densities, and the CI simulant density is within about a factor of two. While permeability models differ, most are proportional to the square of the particle radius. By crude estimate, our glass bead simulant is roughly 30 times more permeable than quartz sand, and the CI simulant 10,000 times more permeable than sand and 300 times more permeable than glass beads. Given the significance of this difference, it is reasonable to compare simulants whose grain densities vary by a factor of two.

Another intuitive result comes from variation in pulse duration. PSI effects tend to increase when pulse duration in increased: crater depth, ejecta volume, and particle velocity. Notably, however, ejecta angle is not significantly affected by pulse duration.

PSI Behavior Scale

We have described our experiment set in terms of its behavior and phenomena. These behaviors typically follow a progression, moving from disturbance, to lofting, to cratering, to bottoming out of the experiment, though this depends on the presence of gravity. These behaviors are determined by observing both the raw and background-subtracted frame sets since some behaviors are subtle.

Particle disturbance is defined to be motion or perturbation of the bulk simulant such that particles shift or move from their original location. This shift may not be substantial and includes particles whose relative arrangement does not change. Lofting is the liberation of particles from the base simulant layer such that they take an independent trajectory, as opposed to being simply perturbed or rolling across the surface. Cratering is here defined as a visible, well-defined impression or concave region caused by lofted simulant. In some experiments, too few particles are moved to result in a crater. In others, particularly the quartz sand experiments, a relatively significant amount of material moves but does not leave a visible crater. Bottoming of the experiment occurs when the platform underneath the simulant becomes visible due to cratering. Fracturing is only observed in the quartz sand experiments, and occurs when underlying structure is maintained as looser material ejects.

This progression of PSI behavior is constructed from a qualitative assessment of the data in a way that each step typically necessitates the step before it. Lofting is an enhancement to perturbation; cratering cannot occur without particle motion; bottoming cannot occur without cratering. These behaviors are summarized in Table 10 below where “Y” indicates the behavior is present in each experiment, “S” means the behavior is sometimes present, “N” indicates the behavior was not observed, and a dash indicates no observation.

We generally see more pronounced behavior with pulse duration, but a few deviations are noteworthy. First, we observe a fracturing behavior in quartz sand at low pulse durations that disappears as pulse duration increases. This was described above and is here captured under the "cratering" descriptor. Longer pulses produce smooth, even scouring that does not leave a well-defined crater. And in exception to the normal progression described above, we observe cratering without lofting in steel bead experiments at 1g due to the particles' weight.

Table 10: A summary of experiment behaviors for our experiment set, listed by material type, nozzle height, pulse duration, and gravity level. Behaviors which are observed in all cases are labeled "Y", in only some cases labeled "S", and if not observed labeled "N". A dash indicates no observation was made.

			Disturbed		Lofting		Cratering		Bottomed	
		Pulse (ms)	0 g	1 g	0 g	1 g	0 g	1 g	0 g	1 g
Quartz Sand	25 cm	10	Y	N	Y	N	S	N	N	N
		25	Y	Y	Y	Y	S	-	N	N
		50	Y	Y	Y	Y	N	Y	N	N
		100	Y	Y	Y	Y	S	Y	N	N
		250	Y	Y	Y	Y	Y	Y	N	N
Glass Beads	25 cm	10	Y	-	Y	-	Y	-	N	-
		25	Y	Y	Y	Y	Y	Y	N	N
		50	Y	Y	Y	Y	Y	Y	N	N
		100	Y	Y	Y	Y	Y	Y	N	N
		250	Y	-	Y	-	Y	-	N	N
	15 cm	10	Y	-	Y	-	Y	-	N	N
		25	Y	Y	Y	Y	Y	-	N	N
		50	Y	Y	Y	Y	Y	Y	N	N
		100	Y	-	Y	-	Y	Y	S	-
		250	Y	Y	Y	Y	Y	Y	Y	N
CI Orgueil	25 cm	10	Y	-	-	-	N	-	N	-
		25	Y	-	Y	-	Y	-	N	-
		50	Y	-	Y	-	Y	-	N	-
		100	Y	-	Y	-	Y	-	Y	-
		250	Y	-	Y	-	Y	-	Y	-
	15 cm	10	Y	N	S	N	N	N	N	N
		25	Y	N	Y	N	Y	N	N	N
		50	Y	Y	Y	N	Y	N	N	N
		100	Y	Y	Y	N	Y	N	Y	N
		250	Y	Y	Y	N	Y	N	Y	N
Steel Beads	28.7 cm	10	Y	N	Y	N	N	N	N	N
		25	Y	Y	Y	N	Y	Y	N	N
		50	Y	Y	Y	N	Y	Y	N	N
		100	Y	Y	Y	N	Y	Y	Y	N
		250	Y	Y	Y	N	Y	N	Y	N
	18.7 cm	10	Y	N	Y	N	N	N	N	N
		25	Y	Y	Y	N	Y	N	N	N
		50	Y	Y	Y	N	Y	N	Y	N
		100	Y	Y	Y	N	Y	N	Y	N
		250	Y	Y	Y	N	Y	N	Y	N

It is important to note that while the table categorizes behaviors, it does not indicate the behavior's severity. Surface scouring may produce particles with high velocity while other PSI may produce a crater by more gently lofting particles. Behavioral or phenomenological analysis tells us the range of states we might expect from a given PSI interaction; additional analysis is needed to tell us something about characteristic ejecta velocities and masses.

Summary

Qualitative analysis of experimental data reveals new behaviors and insight into PSI. We may also identify a few broad trends which will be further substantiated with quantitative analysis. A couple of these are trivial: Ejecta volume is correlated to pulse time. Ejecta volume increases significantly in microgravity. But these simple conclusions belie how remarkably different PSI in microgravity. A wide range of phenomena are masked by gravity. Gas jets which would have little or no effect on the bench produce striking results and significant PSI in microgravity.

PSI varies significantly based on the properties of the granular material with which it interactions. Grain size, shape, mass, and arrangement all affect experiment outcomes insofar as they direct flow. Angled surfaces or topography may guide surface flow. Larger particles or a regular packing arrangement of smaller particles may generate asymmetric ejecta spray.

Burst duration has a significant effect on PSI outcome. Short bursts tend to generate sparse ejecta, small perturbations, and leave underlying features in the surface intact. These may be termed more "impact-like" interactions. Intermediate pulse durations produce impact-like features with some visible off-center, flow-driven behavior depending on simulant permeability and properties. Longer bursts tend to erase and alter surface features, drive flow-like behavior, and produce significant mass ejecta.

Even brief PSI encounters with the surface of a small body may eject fine dust and small particles toward the interacting spacecraft. Prolonged jetting at the surface of a small body will produce significant mass ejecta. Spacecraft conducting surface operations must take this into account.

QUANTITATIVE ANALYSIS AND MODEL COMPARISON

Quantitative Analysis

The data we retrieve from the GRIT experiment show a range of fascinating and novel phenomena. As we have discussed, there are two motivating factors to PSI research. From a physics perspective, we would like to better understand gas-granular mechanics. From a practical, mission-oriented perspective, our understanding of these underlying physics allows us to assess hazards to space missions with near-surface operations. In this vein, we characterize ejecta where possible by velocity and ejecta angle. We also estimate experiment crater size and ejecta mass. We then discuss what trends and behaviors may be surmised from this data.

Our data are more easily described than quantified due to the limitations of our apparatus and the variability in video quality. Our drop tower experiments include a wide range of particle sizes and behaviors. Variation in color, opacity, and behavior presented challenges to quantify behavior with a single method. Glass beads are harder to distinguish than steel. The relatively high velocities of sand grains mean individual particles often blur. Nevertheless, we may characterize and bound simulant behaviors with a combination of analysis methods. These methods include pre-existing automated particle tracking code, manual particle tracking and crater size measurements, and custom methods developed for this experiment set. We will describe each of these in turn and present their results.

Assumptions, Error, and Calibration

Our side-view and top-down cameras are record two-dimensional projections of three-dimensional PSI behavior, the images must be corrected to account for lens distortions, and then converted from pixels to physical units. There are also several sources of error which are difficult to fully quantify, but we shall discuss them here as they apply to all methods described below.

In the measurements which follow, we assume that our side-view camera lens is orthogonal to and centered on the regolith surface; that is, the bottom half of the frame would be regolith and the top half vacuum above it. In reality, the lens centerline is above the simulant surface for most runs. This is necessary for a few reasons. First, an edge-on viewing angle did not allow us to observe surface phenomena clearly, particularly when the simulant surface is not smooth and level. From a top down camera view, it can be difficult to determine whether phenomena occur on or above the surface. Second, placing the camera lens level to the regolith surface means half the already tight viewing frame is left unused. For these reasons, though it introduces a perspective distortion, we found it the best compromise to place our camera lens slightly above the level of the simulant surface. Our calculations also assume that our top-down cameras are placed on the jetting centerline. For obvious reasons, this is impossible. Our cameras are positioned symmetrically about the center axis but offset as described above in the apparatus section. We note again that the use of wide-angle action cameras introduces a distortion error which is corrected for using a de-warping subroutine provided as part of the Argus package (Jackson et al., 2016).

The polycarbonate material used to form the cylinder wall of our vacuum chamber was extruded and has less than ideal optical clarity. Extrusion produces striations in the cylinder which introduces a primarily horizontal distortion of interior particle position; this distortion was noted in the previous chapter in Figure 22.

As mentioned above, our cameras record two-dimensional projections of three-dimensional behavior. To calibrate our images, we by placing a reference grid with a pattern of 1 cm squares in frame to retrieve a pixel-to-cm ratio. For the top down view, we took images with this grid placed at heights of 0, 5, 7.5, 10, and 15 cm above the baseplate. For a given experiment, we use a pixel-to-cm ratio which corresponds to the initial surface of the simulant. A pixel-to-cm ratio for the steel bead surface was retrieved from a quadratic fit to the other measurements. For the side view camera, we placed the reference grid in the center of the experiment, orthogonal to the camera lens centerline.

We assume, then, that particles move in the plane of the initial simulant surface (top-down), or on a plane which contains the jetting centerline (side-view). This effectively means we will underestimate particle velocities unless their motion is within those planes, which is typical only for the side-view camera. Particles forming the right and left edges, from the perspective of the side-view camera, will have the least error in their velocity measurements. From the top-down perspective, we retrieve the radial component of velocity and neglect the vertical component.

Ejecta Velocities

This section describes several methods used to characterize simulant ejecta velocities resulting from GRIT PSI. Due to varying video quality, particle size and speed, apparatus limitations, and lighting conditions, we were not able to apply a “one size fits all” method to the data analysis. Rather, a suite of methods was needed to allow us to variously characterize or bound ejecta behavior. This experience also gives us insight in to improved methods that may be used in future work to better characterize PSI in both laboratory and *in situ* cases.

Methods

Automated Particle Tracking

An extant particle tracking program written in Python is used to recover GRIT ejecta particle velocities and angles. This project, called Trackpy, consists of several steps to identify particles as features within images, refine their locations, then link together possible particle trajectories. This method requires some user tweaking and input based on particle size and characteristics. It is also most efficient and applicable when particles contrast well against the background, do not overlap, and have relatively small displacements frame-to-frame. These criteria apply to automated tracking in general, and not just the methods used by Trackpy. Due to a relatively low frame rate and variability in image quality, our data is not well optimized for automated tracking. Nevertheless, with image processing, tailoring of Trackpy's user settings, and a custom filtering algorithm developed for this data set, we retrieve results for the steel bead, glass bead, and CI Orgueil simulants.

We use the Trackpy Python module to locate particles and link their trajectories using methods originally developed for biological purposes but generally applicable to arbitrary particle motion (Allan et al., 2019; Crocker & Grier, 1996). Trackpy must be adjusted for each data set in order to achieve optimal results. A custom wrapper and data post-processor were written to filter spurious trajectories.

Trackpy allows the user to adjust the sensitivity and size of particle recognition. Each simulant type we used in GRIT has unique optical qualities, characteristics, and particle sizes. First, we check sample frames for the simulant type being tracked. We chose to use background subtracted or sequential difference images, depending on which yielded the clearest features for each simulant type. Trackpy looks for bright particle features, and then allows the user to preview its feature recognition results on sample frames. We used this to adjust and optimize its results to select unique features in each experiment type.

Once particle feature recognition has been configured, Trackpy may be run in its entirety for a simulant data set. Trackpy locates features in each experiment frame, then runs a program to link these features into particle trajectories. It will keep particles in memory and attempt to locate them in three subsequent frames should they be temporarily obscured or missing from a frame. Data output from Trackpy is a set of unique particles with their x-y coordinates over time. Because Trackpy was developed for arbitrary particle velocities, it is not idealized for the linear trajectories we expect our particles to take and generates a significant number of spurious trajectories. These are first filtered by track length; tracks less than 5 frames long are removed. Because our particles have relatively high density and high velocities, this still leaves a large number of invalid trajectories.

We next use linearity as a proxy for trajectory validity. First, each candidate particle trajectory is tested by fitting a line with the least squares regression method. If the resulting R^2 value from this linear fit is less than 0.9, the trajectory is rejected. But this does not guarantee the validity of a track. Particles may lie along a line, but this is no guarantee that they are a forward marching sequence. Therefore, we next take each remaining trajectory and step through the coordinates sequentially. If the angle between any pair of subsequent coordinates differs from the linear fit line by more than 30 degrees, the trajectory is rejected. These steps guarantee a forward-marching, near-linear trajectory.

It was observed during this procedure that some particle trajectories seem to err in only one data point, particularly at the beginning or end of a trajectory. To remedy this, if the particle trajectory passes the second, angle-fit test except for the first or last coordinate in the sequence, this coordinate pair is deleted rather than rejecting the entire trajectory. This allows us to recover valid trajectories that would otherwise have been rejected.

Recovered trajectories consist of particle coordinates given for each frame the particle was tracked. With coordinates, a pixel-to-cm conversion ratio, and a known per-frame time difference, we may calculate particle velocities between each frame. Ideally this velocity remains constant over the entire track, but due to the sources of error and distortion mentioned above, this is not always the case. The average velocity for each particle is calculated, and its maximum and minimum measured velocities are plotted as upper and lower bounds to each measurement.

Manual Particle Tracking

For the large, cm-scale particles of CI Orgueil it is feasible and effective to track individual particles (in some cases all lofted particles), especially for low pulse durations. For longer pulse durations with bulk lofting, we still recover what ought to be a representative sample of particle velocities. Manual tracking works best in this case because these particles are significantly larger than the automated tracking method described below was written to handle, and these results serve as a check to the automated tracking and set our expectation for normative results.

Undergraduate student assistants conducted manual particle tracking by visual inspection using the software package ImageJ. The software allows the user to step through frames and identify various features of interest. For this work, after identifying a particle, they clicked the particle’s geometric center as determined by visual estimate. The center was chosen rather than edge features because many particles rotate after ejection. Output from this method is a set of uncalibrated coordinates which was calibrated and processed in the same manner as the automated tracking results described below, except that trajectories were not filtered before plotting.

Projected Start Time

In the graphs below, for both automatic and manual particle tracking, we calculate a particle "start time" from when it would have crossed the experiment surface line. We fit the particle trajectories with a least squares linear regression, calculate where this line would intersect the unperturbed material surface, and use the average particle velocity to calculate travel time from this baseline. Since particles are often hard to distinguish until they reach a sufficient height above the simulant surface, this corrects to an approximate particle lofting time.

Frame-Averaged Experiment Profiles

Particle tracking presents us with difficulties due to variability in particle sizes and properties. Quartz sand in particular presents us with a challenge. We employ a potentially novel method to visualize and quantify particle motion as seen from our side-view cameras. It retrieves the vertical and horizontal velocity trends for each experiment, albeit as bulk features rather than individual components.

For this analysis, we consider a PSI experiment and imagine particle ejecta viewed from the side. In general, the density of this spray will decrease with height. There will also be irregularities, features visible within the spray – clumps or gaps in the ejecta, for example. These features—whatever their precise size or nature—will migrate with the spray as it evolves upward with a velocity approximate to that of the particles which cause it.

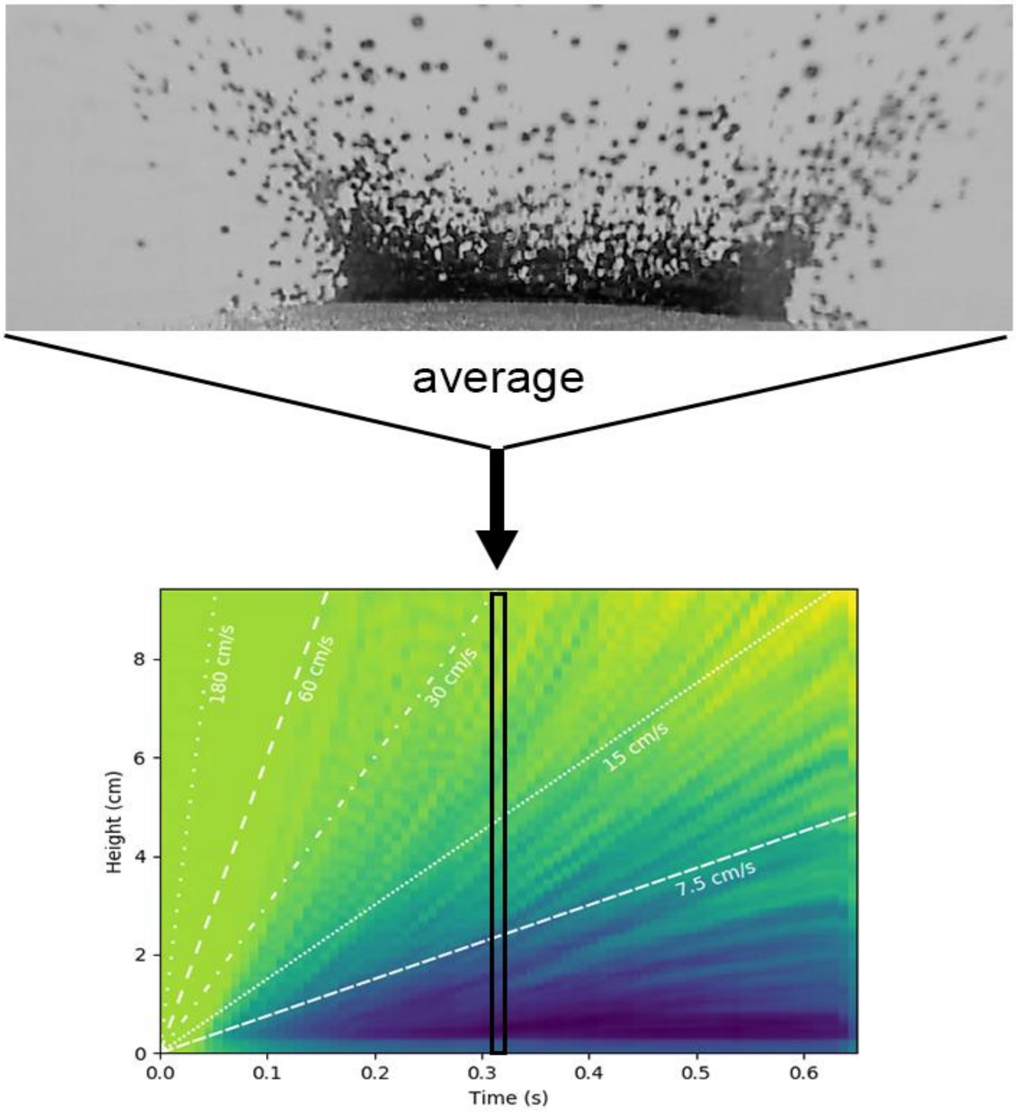

Figure 52: Illustration of our frame-average profile method. Each frame is row-averaged into a single column in the resulting image, giving us a profile of vertical velocity with time.

For each frame of this experiment, we may take a row-wise average, such that each row in the frame is condensed to one value in a single column. This process is illustrated in Figure

52. Doing this for each frame of the experiment produces a two-dimensional image where height lies along the vertical axis, and the frame count along the horizontal axis. The features we discussed earlier can be preserved in this average. Deviations from asymmetry show up and move vertically—or, now that we have placed these frame-averages alongside each other, move upward in position and right-ward in time. Because a line on a position vs. time graph is a velocity, we thus recover the vertical component of velocity for the boundaries and features we observe in this frame-averaged experiment profile.

Results and Analysis

Manual Particle Tracking

A student assistant tracked all distinct particles through each CI Orgueil experiment. This is possible because there are far fewer particles ejected per experiment than with finer-grained media. For these experiments, then, we have a complete or at least representative sample of particle behavior—the latter when the entire mass is ejected and tracking every particle may not be feasible. We see that average particle velocity is indeed dependent on pulse duration—a fact that will become much clearer in our velocity profiles below. This experiment set also allows us to suggest a relationship between pulse time and average particle velocity. Each tracked particle is represented by a dot in Figure 53 below, which plots the average measured velocity. The error bars represent upper and lower bounds to velocities calculated at each step.

For both experiment sets we see similar lower bounds on the pulse duration. Gentle perturbations produce particle velocities around 10 cm/s. Spread increases with pulse duration. Particles ejected from a 50 ms pulse range from 20 cm/s up to around 90 cm/s for the 15 cm nozzle height. This range is similar for the 25 cm nozzle height, except for the lower bound dropping slightly. The distribution, however, is markedly different. These more pronounced differences show in the mid-range of pulse durations. Lower end and higher end behaviors are subtly different. This makes sense, since we see lofting of the entire regolith mass at high pulse durations. If we compare number of tracked particles per experiment between nozzle heights, the numbers are roughly equivalent. The 250 ms pulse seems to be an outlier. Fewer particles are tracked at the 15 cm nozzle height for that experiment time. These numbers are shown in Table 11 below.

Table 11: Manual Tracking Statistics, CI Orgueil Only

	15 cm Nozzle Height			25 cm Nozzle Height		
Pulse	**Number Exp.**	**Total Particles**	**Tracked/Exp**	**Number Exp.**	**Total Particles**	**Tracked/Exp**
10	4	9	2.3	3	6	2.0
25	4	56	14.0	3	29	9.7
50	3	46	15.3	5	66	13.2
100	3	36	12.0	3	37	12.3
250	3	11	3.7	3	36	12.0

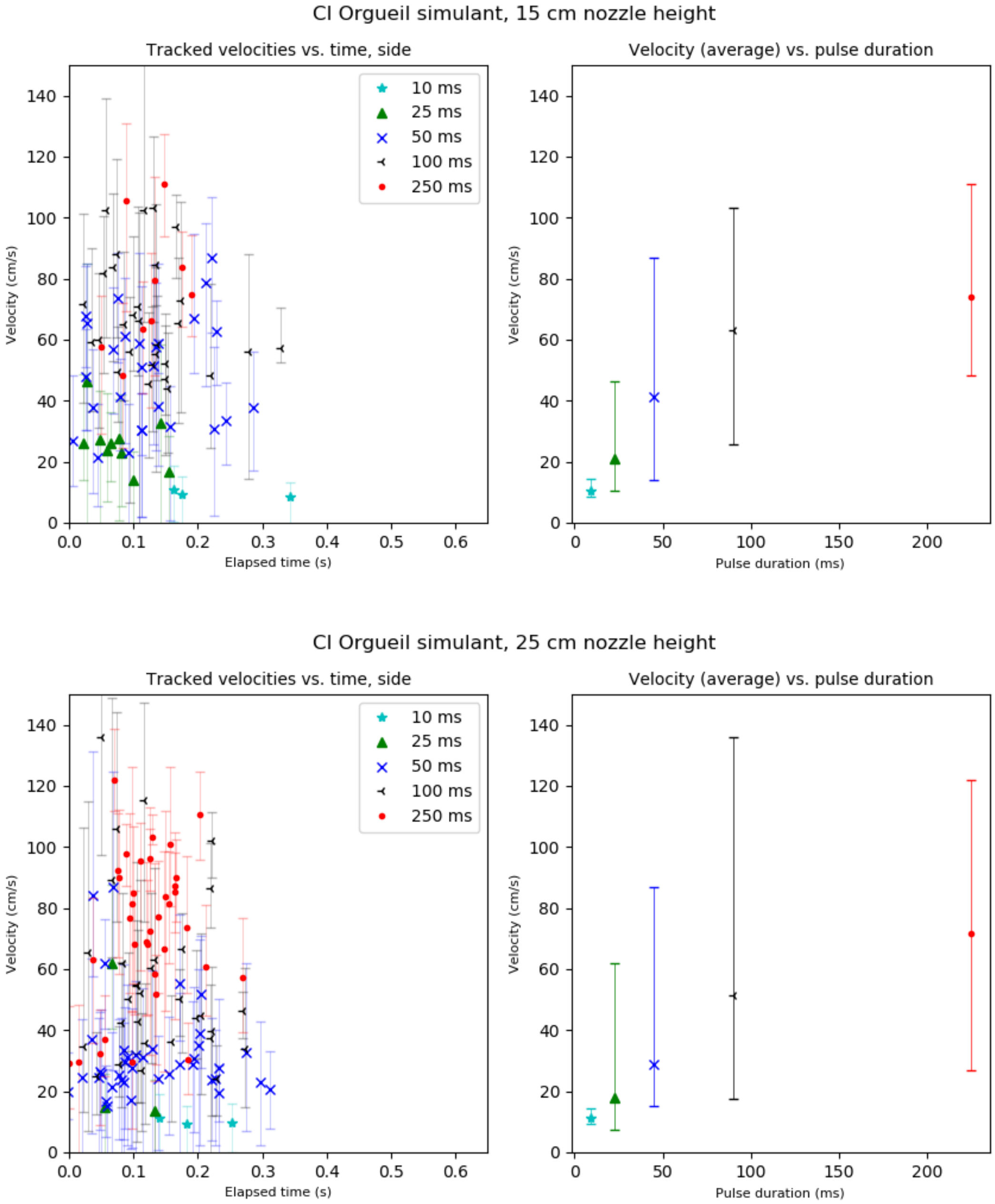

Figure 53: Manual tracking results for CI Orgueil experiments. (Left) Initial particle velocities, from when tracking begins. Each particle is plotted as a single dot. (Right) Corresponding average velocities per pulse time.

If we assume the distributions are representative, on a linear plot we see average particle velocities approaching some maximum. This trend was also visible in at least some of the automated tracking conducted earlier, though obscured in some sets by algorithmic bias. What are we to make of the trend? The relationship becomes clearer when we plot pulse duration on a log scale, as seen in Figure 54. At this scale it appears that there are two asymptotes towards maximum and minimum pulse durations. This gives us a clue to the physical phenomena behind the event and a suggestion as to how we might model it. What is happening in the experiment? Gas flows through regolith and lofts it. More simply, gas flows around a particle and imparts a drag force, accelerating the particle with the flow.

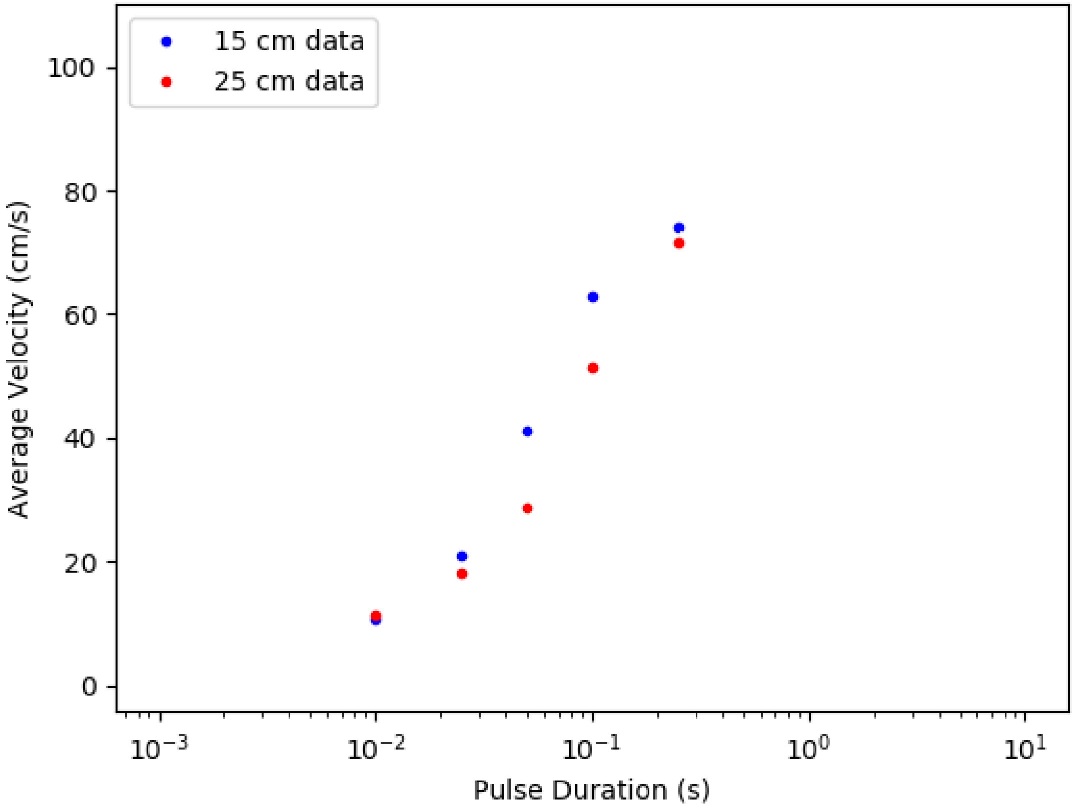

Figure 54: Average particle velocities, determined with manual tracking, for the CI Orgueil experiments in microgravity. Nozzle distance is indicated by the legend. The data displayed here are the averages shown in Figure 53 above.

Let us reduce the problem to a single particle in a uniform, steady flow with some initial velocity u_0 which lasts for some duration t_p. The drag force on the particle is given by Equation 15 and, neglecting gravity, this is the only force on the particle. It will accelerate relative to a stationary observer but its velocity relative to the stream will approach zero as it is caught in the flow, so that the particle's velocity u relative to the stream is given by Equation 16.

$$F_{drag} = \frac{1}{2}\rho u^2 C_d A \tag{15}$$

$$u = u_0 - v \tag{16}$$

Applying Newton's Second Law we arrive at a differential equation in the form of Equation 17, whose solution is given by Equation 18. In this last iteration the physical constants are all stated explicitly, a cubic particle is assumed since our regolith blocks are irregularly shaped, and the particle area and mass are expressed as functions of particle density and side length a.

$$ku^2 = -\frac{du}{dt} \tag{17}$$

$$v(t) = u_0\left(1 - \frac{1}{1+\frac{1}{2}\frac{\rho_{gas} C_d}{\rho_{particle} a} u_0 t}\right) \tag{18}$$

Does this result match our intuition? It does, as it indicates that at the start of the experiment, the particle velocity will equal zero and as time tends to infinity, the particle velocity will approach u_0. More importantly, how does this function compare to our observed data? Rounding our simulant particle density to $1\,\frac{g}{cm^3}$, assuming a particle side of 1 cm (in the middle of our simulant's size range), and drag coefficient of 1.15 (that of a square cross-section), we fit this equation to our data varying flow velocity and gas density, as shown in Figure 55.

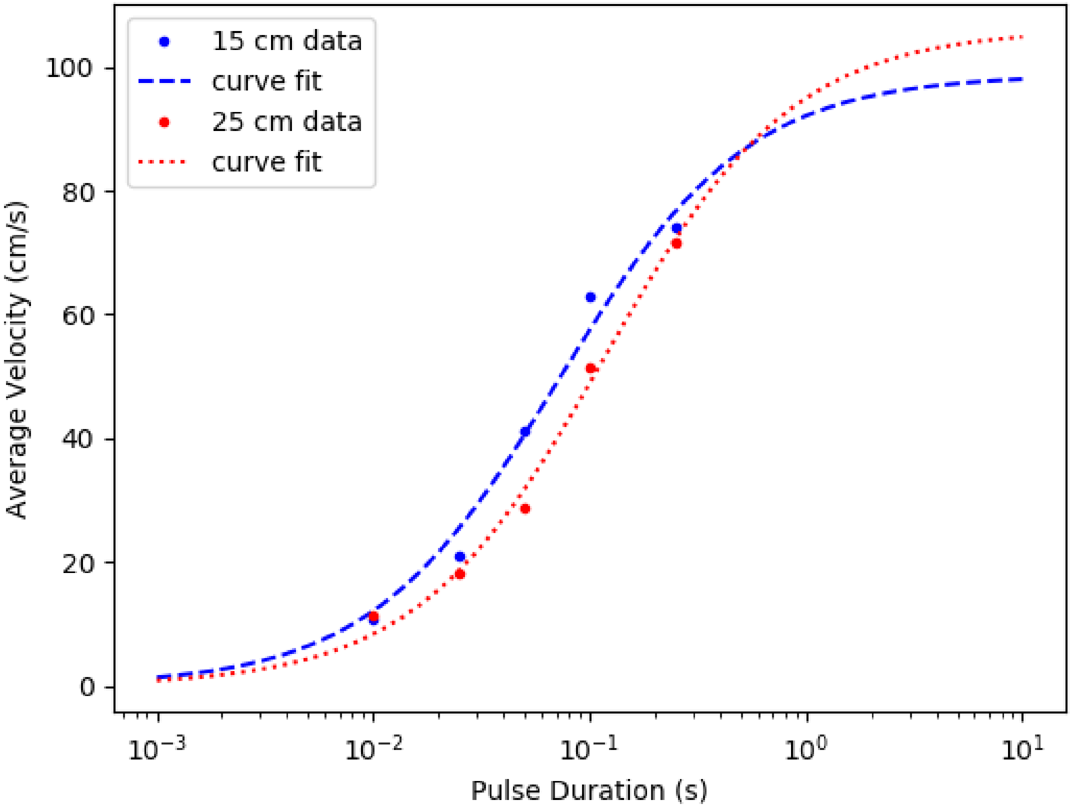

Figure 55: Average particle velocities, determined with manual tracking, for the CI Orgueil experiments in microgravity fitted with the drag force equation (Equation 18) and assumed particle parameters.

We see a remarkable consistency between our model conjecture and the experimental data. We fit Equation 18 to our data leaving flow velocity (maximum particle velocity) and gas density as free parameters. Fitting these parameters for the 15 cm and 25 cm nozzle distance gives us a $98.7\,\frac{m}{s}$ and $106\,\frac{m}{s}$ maximum particle velocity, and $2.5\,\frac{kg}{m^3}$ and $1.4\,\frac{kg}{m^3}$ gas density, respectively. We know that the flow in the experiment chamber's feedthrough chokes at the speed of sound for the gas, which is $340\,\frac{m}{s}$. This sets a logical upper bound since, as the gas diffuses through the medium, it can be expected to slow, so our value seems reasonable. As the density of air is $1.2\frac{kg}{m^3}$, this indicates local gas density may exceed ambient density.

More plausibly, the coefficient of drag is not well represented as a constant. Gas flowing through a converging-diverging nozzle goes supersonic past the choke point; that is, when the nozzle diverges. While we do not have a proper nozzle attached to the interior of our experiment, the flow chokes and then expands into the chamber, and it seems plausible that the flow becomes a supersonic front which impinges on the regolith. Whether or not this is the case, the drag coefficient is a function of flow velocity, increasing as that velocity approaches Mach 1. This may account for what seems to be a high gas density in our model fit. And this equation, as a simplification, certainly only approximates the real experiment. It shows, however, that at some level a treatment of basic gas-drag mechanics are applicable to PSI, and can serve as a check to simulation work.

Automated Particle Tracking

We derive velocities from steel bead, glass bead, and CI Orgueil simulant experiment runs using the automated tracking algorithms described above. The size and velocities of particles in the quartz sand experiments, however, did not lend themselves to discrete particle tracking. It is important to note that, while we plot every *tracked* particle, this is not a representative sample of particle motion. Tracked particles are those which were easier to see, more well defined, and typically with lower velocities than the maximum, though exceptions exist. Sometimes particles reflected off the experiment chamber wall are tracked. In plotting particles from our top-down cameras in which two videos were taken, we do not attempt to identify or remove duplicate measurements. Due to the pseudo-random nature with which particles are tracked, and the relatively small number of tracks measured compared to the number of particles, this overlap ought to be small for most experiments. Finally, a number of runs were discarded if the resulting tracks were erroneous. With these limitations in mind, these particle tracks give us insight into the bulk behavior for each experiment type. The results are shown in Figure 56 through Figure 61.

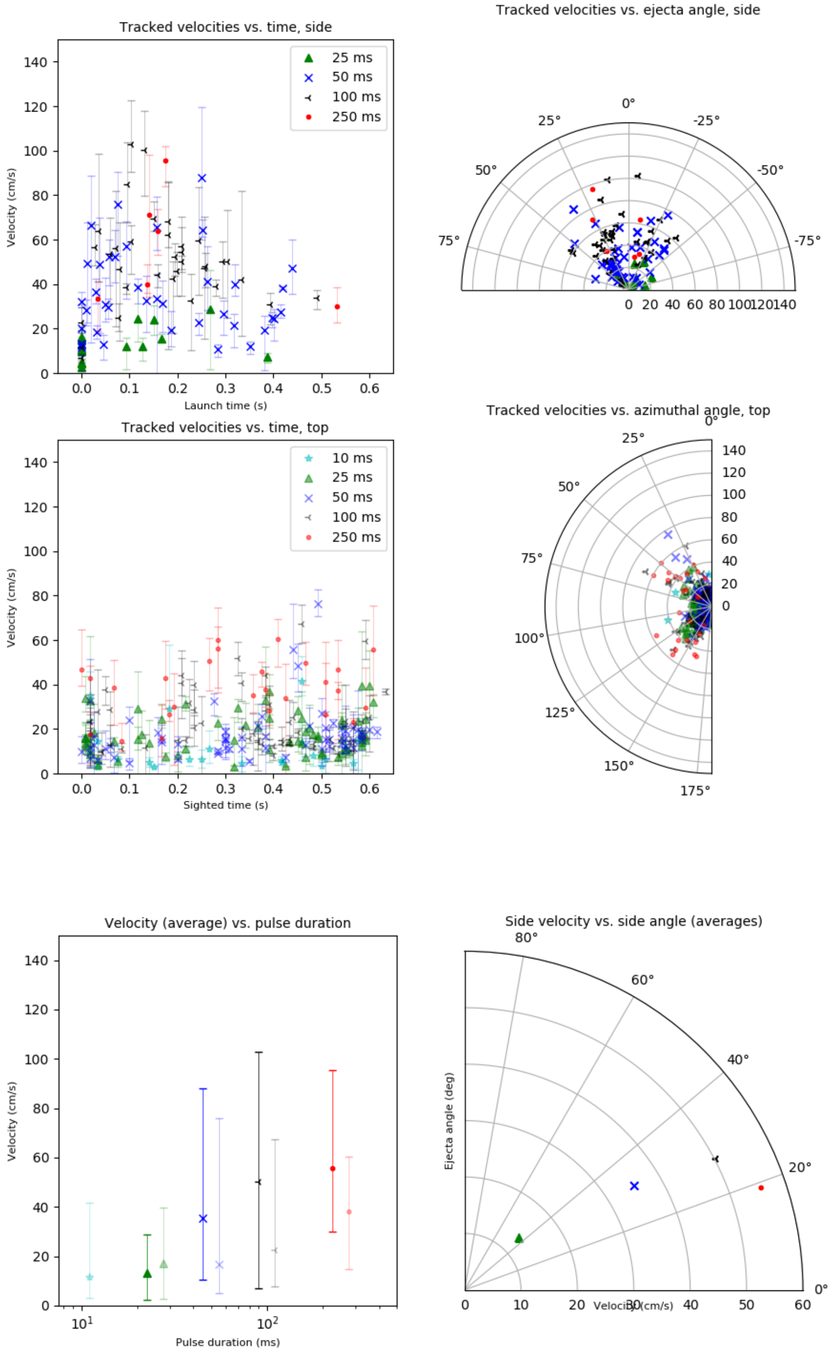

Figure 56: Automatic tracking results with CI Orgueil simulant, 15 cm nozzle height. The top and middle plots show individual particles. The bottom plots show average velocities, with minimum and maximum velocities bracketed.

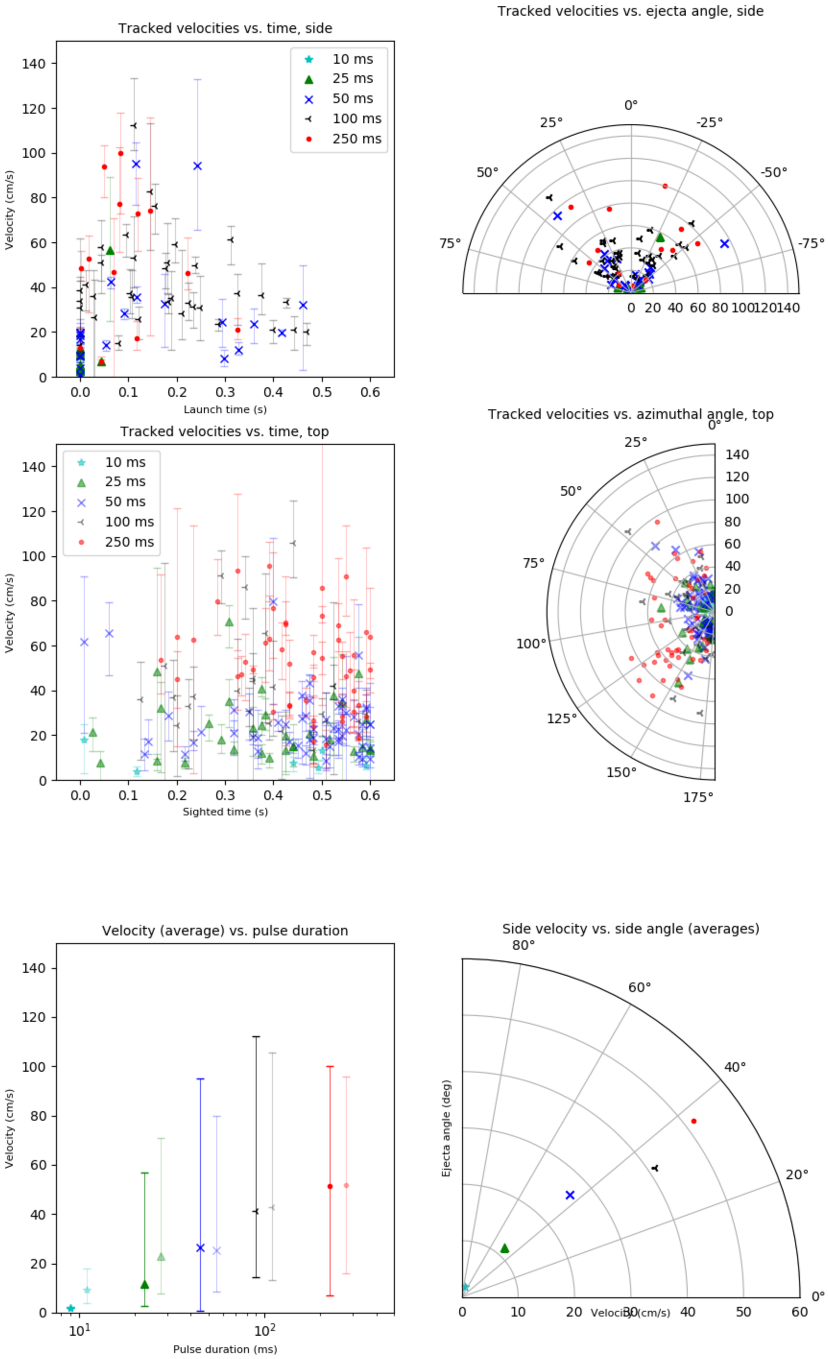

Figure 57: Automatic tracking results with CI Orgueil simulant, 25 cm nozzle height. The top and middle plots show individual particles. The bottom plots show average velocities, with minimum and maximum velocities bracketed.

We examine the results of CI Orgueil particles first since we can make a direct comparison to manually tracked particles. The average velocity tracked by TrackPy is lower than that found by manual tracking due to selection bias. An examination of the tracked particles shows tracking obscured by lofted fines. It also shows us a number of particle fragments significantly smaller than the grains sieved for this set of experiment runs were tracked for some experiments.

As we attempt to back-project to a particle launch time, many particles end up with a negative launch time and are assigned a launch time of $t = 0$. This projection back to a negative time may occur if the tracked particle ricocheted, or it may represent that the particle started below the initial surface.

The glass bead experiments were the most difficult to track—excluding the quartz sand simulant, which was not tracked at all. This can be seen by the lack of data for several parameter combinations. As pulse times increase, ejecta moves much more quickly, looking less like individual particles and more like an entire mass, rendering the algorithm unsuited for this use. Our lowest pulse experiments, however, produce excellent results and we achieve something like a representative sample in the output. The particle velocities we measure in the 10 ms pulse experiments likely represent an actual lower bound on velocity across all experiments of that type.

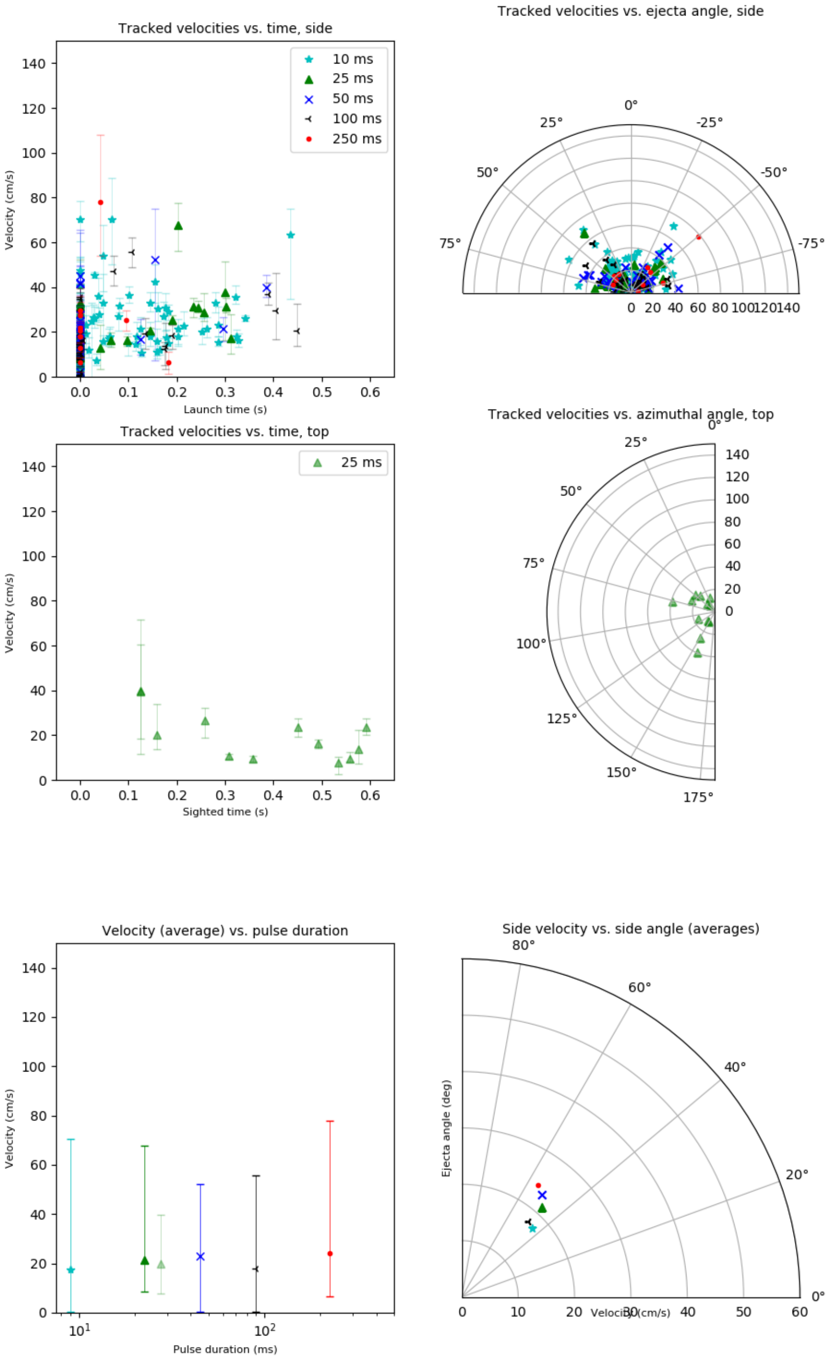

Figure 58: Automatic tracking results with glass bead simulant, 15 cm nozzle height. Individual tracked particle velocities and angles are plotted for (top) side and (middle) top-down views. The bottom plots show average velocities, with error bars set by minimum and maximum velocities.

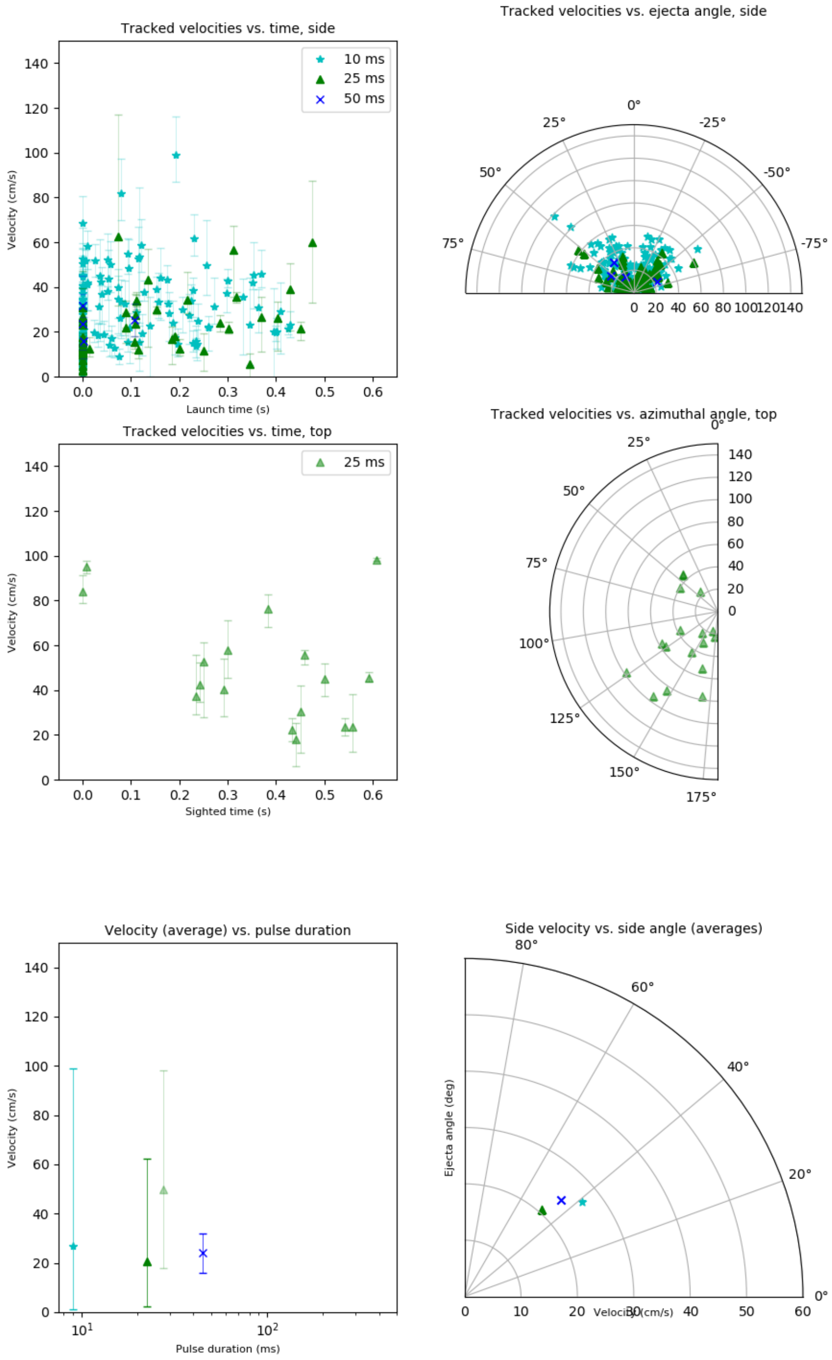

Figure 59: Automatic tracking results with glass bead simulant, 25 cm nozzle height. Individual tracked particle velocities and angles are plotted for (top) side and (middle) top-down views. The bottom plots show average velocities, with error bars set by minimum and maximum velocities.

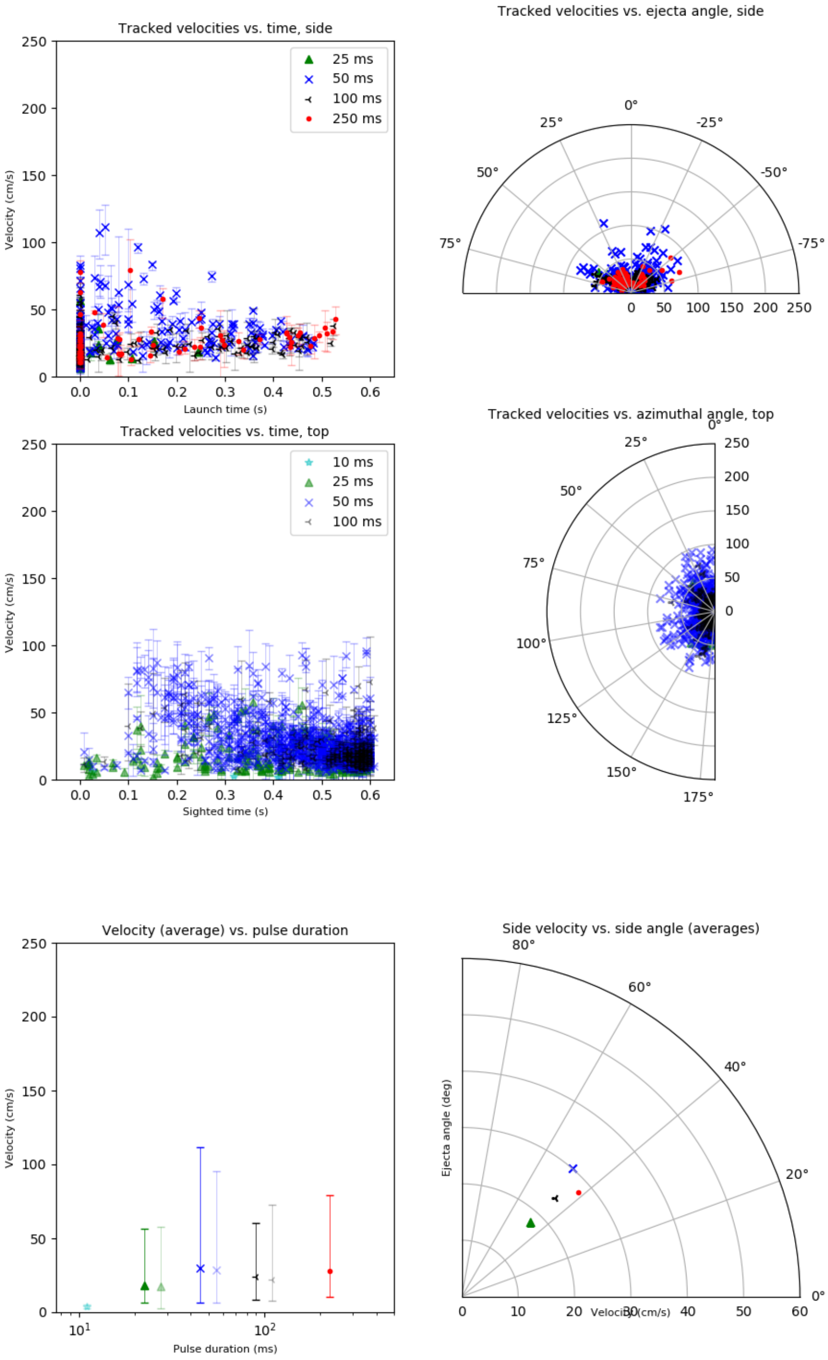

Figure 60: Automatic tracking results with steel bead simulant, 15 cm nozzle height. Individual tracked particle velocities and angles are plotted for (top) side and (middle) top-down views. The bottom plots show average velocities, with error bars set by minimum and maximum velocities.

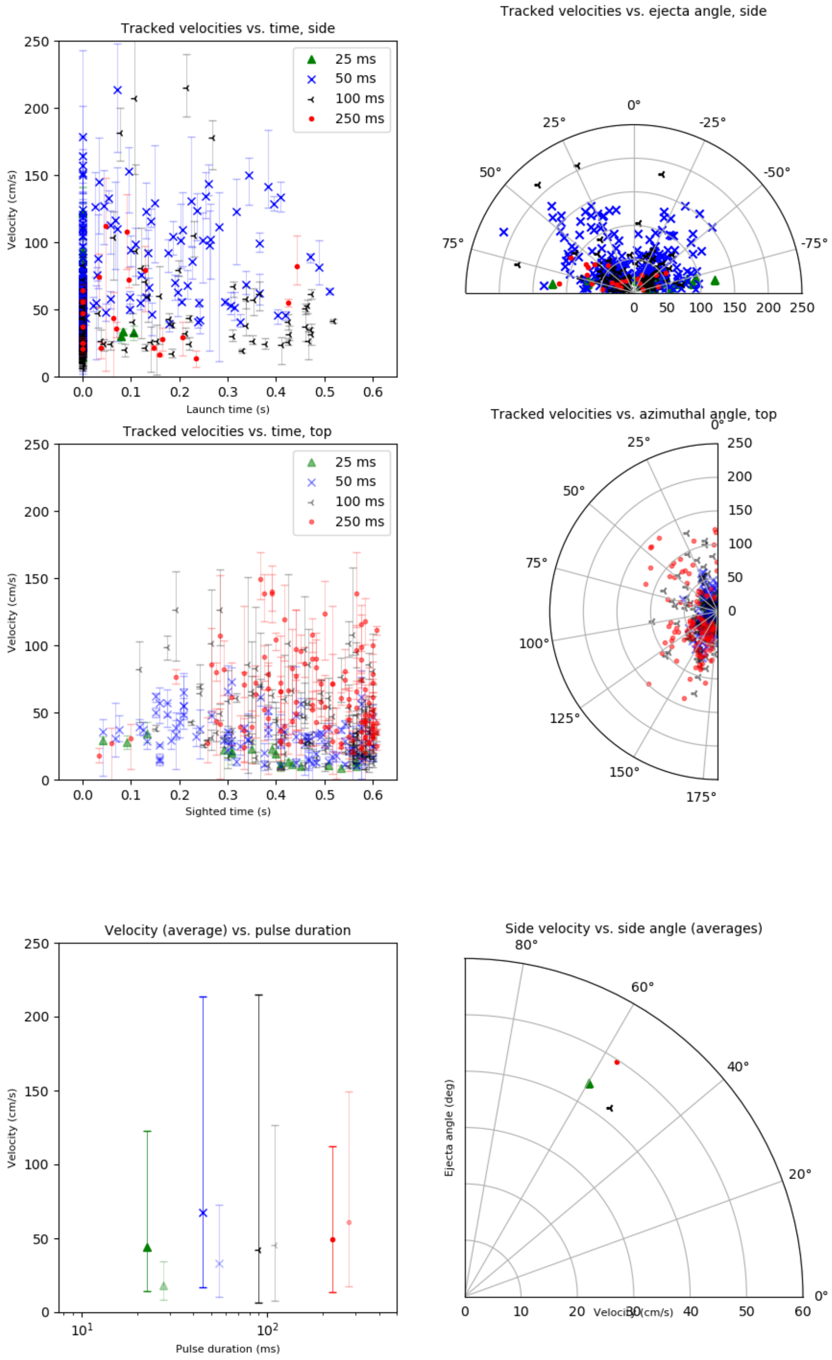

Figure 61: Automatic tracking results with steel bead simulant, 25 cm nozzle height. Individual tracked particle velocities and angles are plotted for (top) side and (middle) top-down views. The bottom plots show average velocities, with error bars set by minimum and maximum velocities.

Selection bias again affect the steel bead experiments. In general, since particle velocities tend to increase with pulse duration, a lower pulse distribution should serve as a bound for the actual distribution of a longer pulse; that is, the actual 250 ms pulse velocity maximum is not significantly lower than the 100 ms pulse experiment, though this is what we track and plot in Figure 61.

These graphs indicate a weak dependence of launch angle on pulse duration. We have already observed, however, that the ejecta angle may vary with both pulse duration, height, and simulant. It seems likely, then, that our automated tracking results here reflect an algorithmic bias. This could be caused by lighting conditions with the experiment, or it may be due to it being easier to track particles ejected around 45 degrees. At this angle particles are less likely to overlap than when launched closer to the surface and are likely to move slower in frame than particles shooting straight up.

Frame-Averaged Velocity Profiles

Taking frame-averaged velocity profiles allows us to characterize bulk velocity behavior and, for some material, individual outliers. Individual particle tracks and local density maxima in the ejecta can be seen as striations in these profiles. This allows us to visually distinguish bulk behavior and individual sparse behavior. The boundary between sparse ejecta and bulk behavior is sometimes gradual, which mirrors our difficulty in clearly defining ejecta boundaries for certain runs. Bulk behavior is, however, characterized by relatively uniform opacity and a lack of gaps in between particle tracks. Velocity lines are overlaid on these graphs to easily read off characteristic velocities. Example graphs for each simulant type are shown below in Figure 62 through Figure 65; a graph for each experiment type is located in Appendix D.

Once again, in these figures dark blue represents a region obstructed by ejecta, while yellow indicates the background. Ideally, for a perfect background subtraction, we would see this region solid yellow and featureless. Due to imperfections in the video quality and lighting, however, the background sometimes appears with a green tinge—this can be thought of as a raised background level, which makes ejecta features slightly harder to distinguish by comparison.

Steel beads, as with other tracking methods, perform well in this assessment as shown in Figure 62. They are opaque and contrast well. Individual particles and features are visible as striations in the figure. An example of this type of behavior can be seen in Figure 62 below. The ejecta spray is well defined but remains moderately sparse through most of the experiment. The bottom part of the ejecta wall, however, is opaque and can be seen in the deep blue region. We retrieve velocities by comparing striations angles in the figure to plotted velocity lines. In this figure, sparse velocities are bounded at roughly 60 cm/s, while bulk velocity is roughly 30 m/s based on this graph and its counterparts.

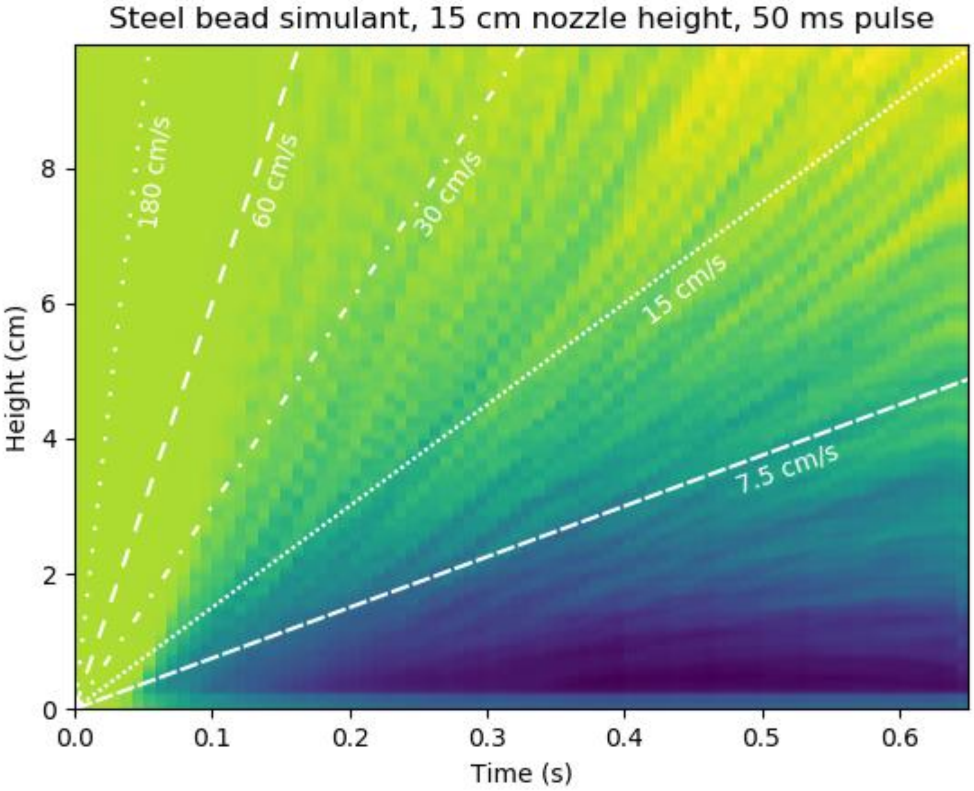

Figure 62: A frame averaged profile for steel bead simulant. Bulk ejecta is represented in the lower part of the image as solid blue. Discrete features are visible as stripes which migrate in time.

Velocity data are difficult to recover for the quartz sand experiments. Given the time it takes for a grain to strike the side, we can calculate an upper particle velocity bound in the low tens of m/s. Our profile graphs corroborate that number. They also show that while bulk flow increases with particle time, light grains accelerate rapidly with all but the gentlest pulse. Comparing the angle of the shaded region in these experiments to the reference lines as in Figure 63 indicates velocities over 180 cm/s are seen every experiment run, but sparser particles moving more quickly do not leave tracks in these relatively low-spatial-resolution frames. The profiles give us insight into how ejecta mass increases and show that the bulk of the simulant is lofted around a meter per second in velocity for longer pulse times.

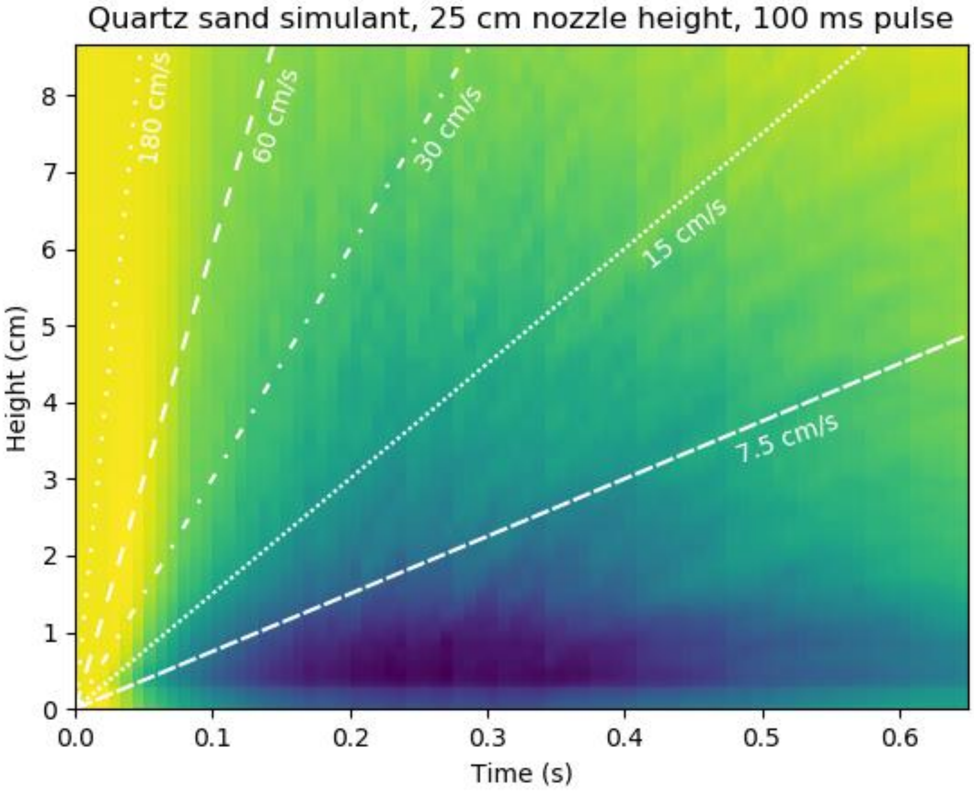

Figure 63: Profile for a quartz sand experiment with a 100 ms jetting duration. The flow is nearly vertical. Our categorization of bulk velocity at 180 cm/s is a rough upper bound; some particles likely travel up to an order of magnitude faster.

An example profile for glass beads is shown below in Figure 64. The glass beads we used were transparent and did not contrast well against the background, making particle tracking difficult. Due to their higher speeds, the fastest particles do not appear clearly in consecutive frames, and often appear smeared. Our frame profile is therefore a useful tool for recovering bulk behavior, though the fastest particles are once again lost to the background in this method.

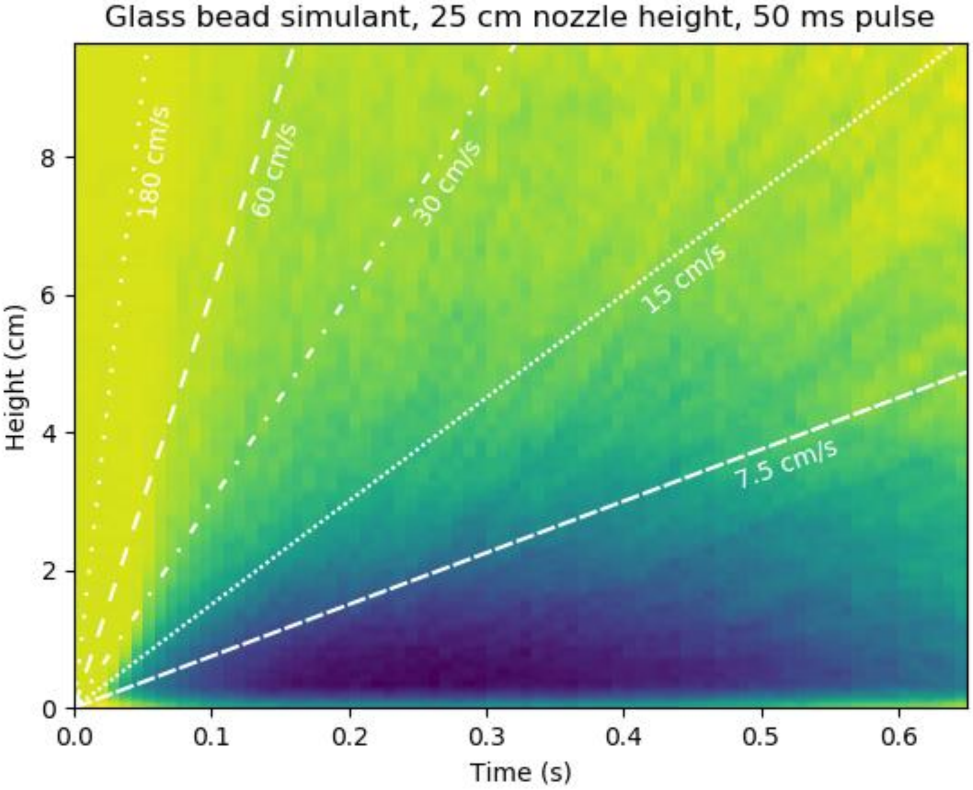

Figure 64: Profile for a glass bead experiment, which are typically lower-contrast due to the beads' translucency. Faint striations are visible parallel to the 180 cm/s line. The ejecta plume is opaque to approximately 3 cm height, with ejecta becoming sparser with height.

Charts for CI Orgueil simulant are perhaps the most curious. Large, individual particles are often visible painting a stripe across the figure, as below in Figure 65. The fine dust we previously observed—entrained by the gas flow instantly during PSI—shows up as a vertical line on the left side of each graph. As its slope is nearly vertical, we can only say its velocity well exceeds the 180 cm/s line plotted on each chart. CI Orgueil PSI shows the most variation in particle velocities, ranging up to 60 cm/s in the example profiles, while bulk motion is under 10 cm/s.

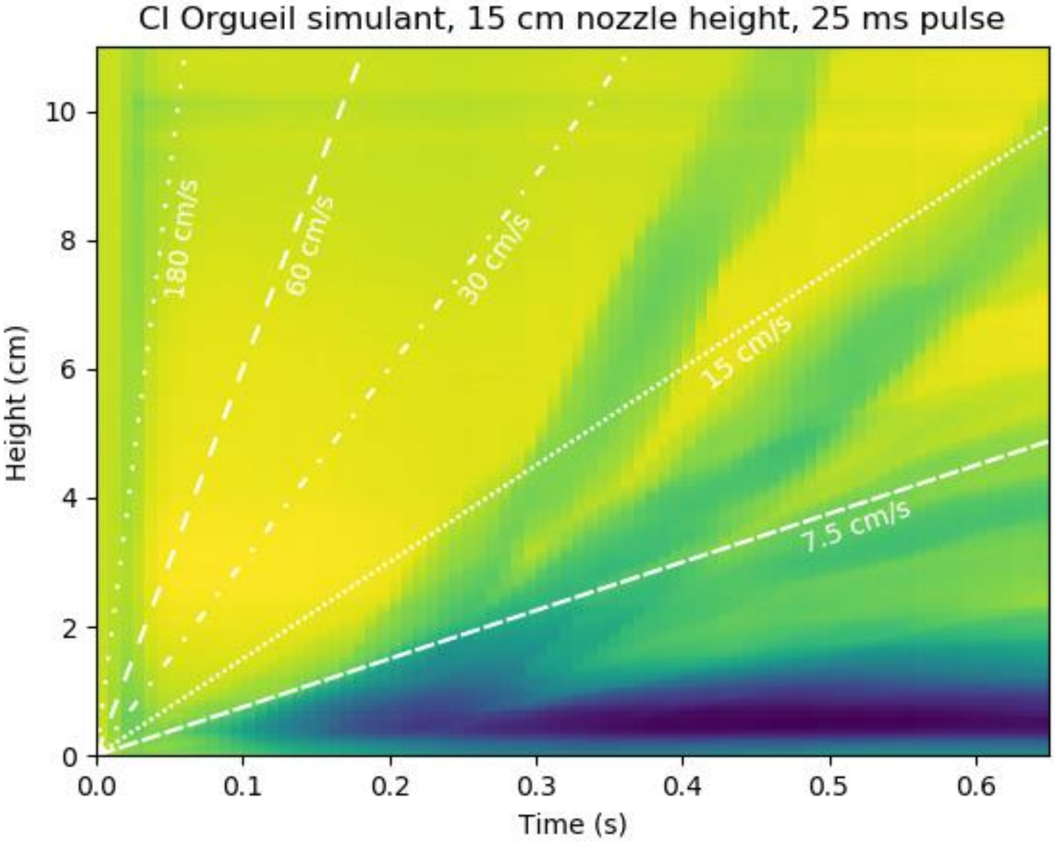

Figure 65: Example profile from a CI Orgueil experiment. On the left, a thin streak shows dust entrained flow quickly rising with the gas jet. Particles are slower to follow, painting broad bands across the frame. We see slight bulk uplift rising slowing, at velocities under 10 cm/s.

Compiled Velocity Profiles

Each of these methods described previously give us a window into PSI ejecta velocity behavior, and by combining results we can examine velocity trends . We summarize these results in Figure 66 and Figure 67. It is important to distinguish between both types and levels of confidence in these measurements. Manual particle tracking is the most reliable and representative method. Automated tracking is accurate but narrow, exhibiting a noticeable selection bias toward particles the algorithm is suited to find. Our frame-averaged experiment profiles allow us to quantify, however imprecisely, velocity behavior that would otherwise be difficult to assess, particularly with quartz sand experiments. This last measurement type should be considered more like an experiment categorization, setting bounds to bulk and sparse behavior.

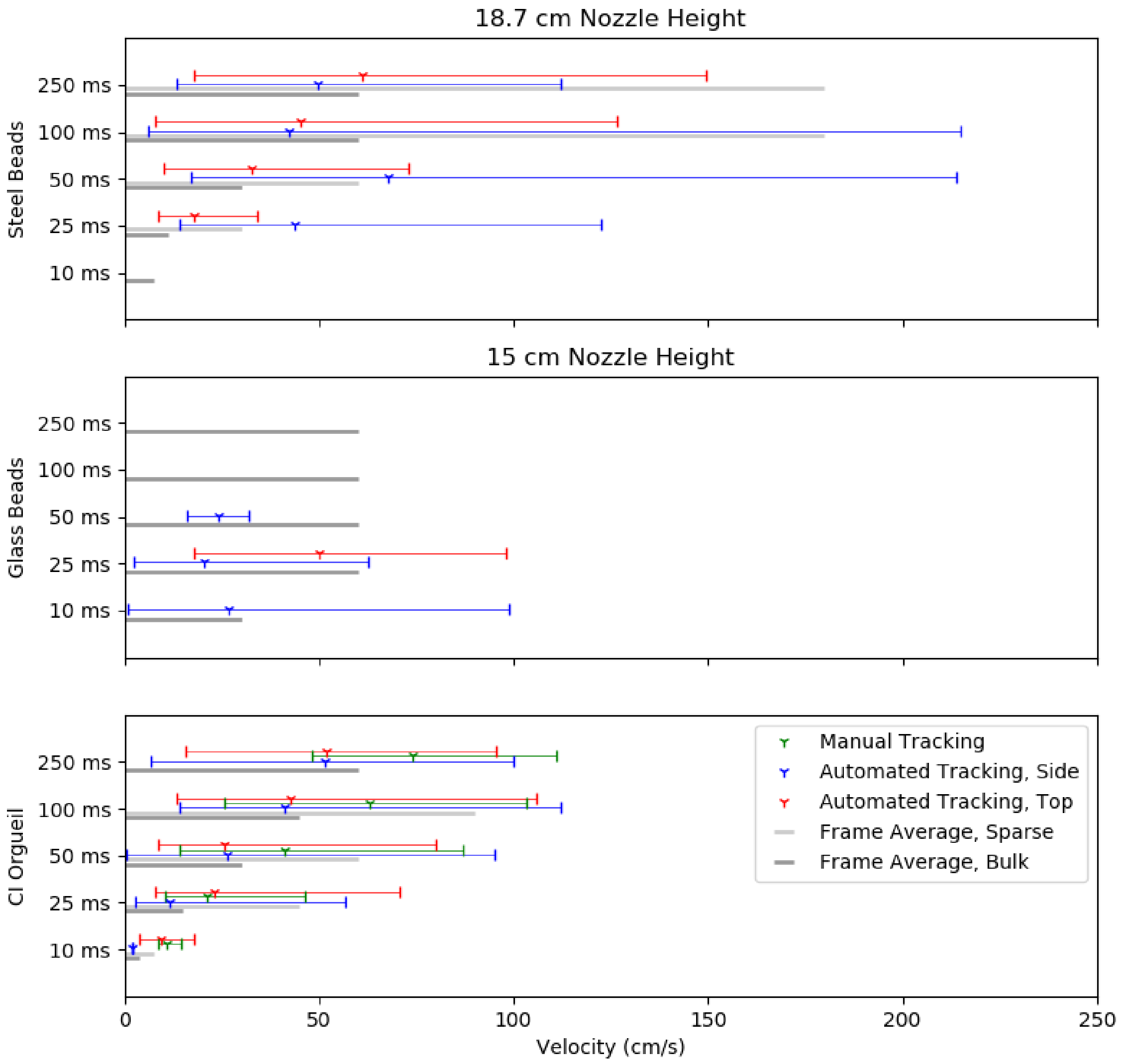

Figure 66: Compiled particle velocities as determined by all velocity analysis techniques for experiments conducted on a 10 cm diameter platform (lower nozzle height) for steel, glass, and CI Orgueil experiments. Error bars indicate the minimum and maximum velocities seen for that experiment type.

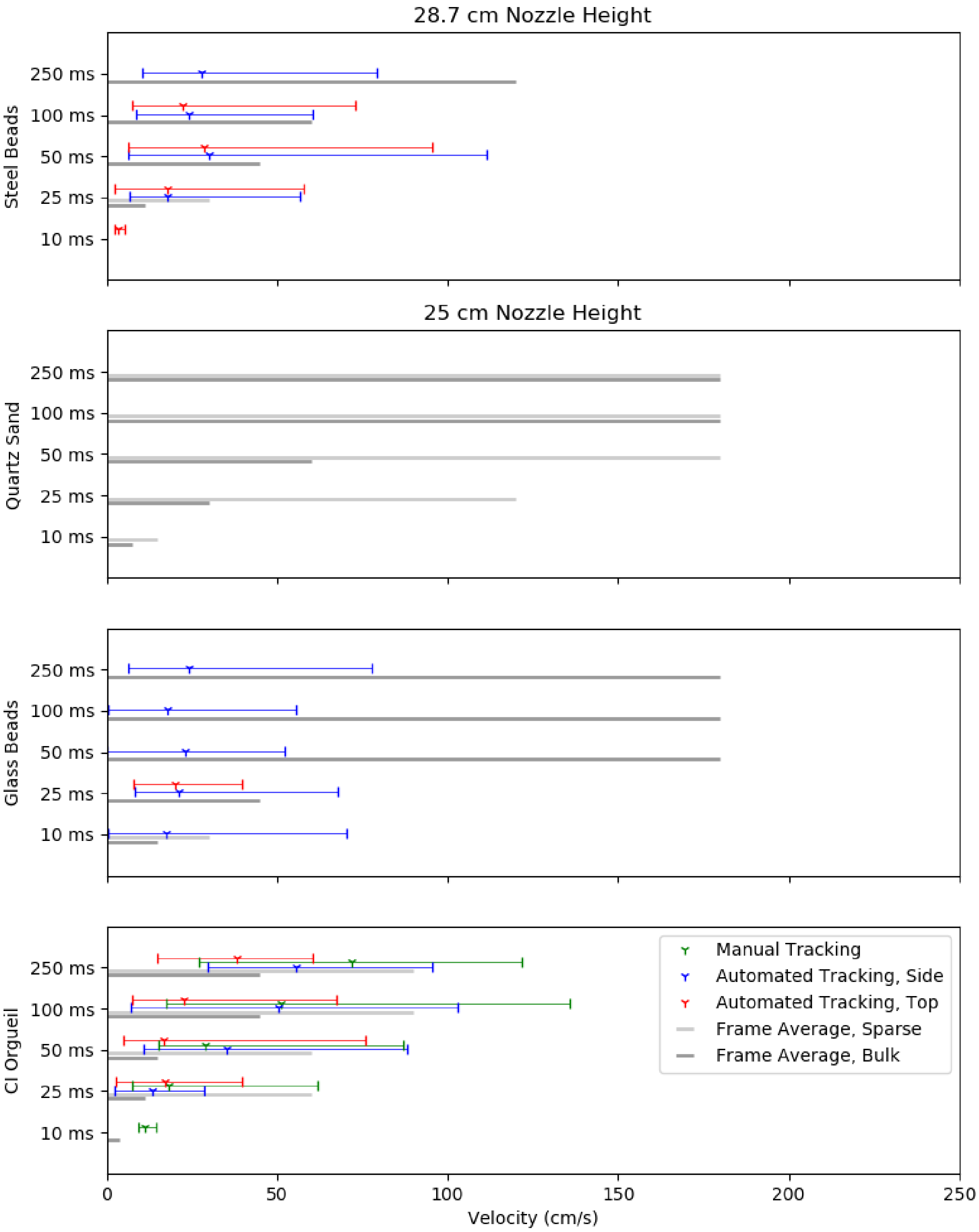

Figure 67: Compiled particle velocities as determined by all velocity analysis techniques for experiments conducted on the apparatus baseplate (higher nozzle height) for steel, sand, glass, and CI Orgueil experiments. Error bars indicate the minimum and maximum velocities seen for that experiment type.

This aggregate data still paints an incomplete picture based on our phenomenological study. The highest velocity particles are missing, due to our camera’s limited frame rate, which means lower-pulse-time experiments are more thoroughly characterized. The data should also be interpreted in light of the fact that bulk ejecta increases with pulse duration. There is validity however, to the observation that the bulk velocity maximum does not necessarily change significantly with pulse duration, and this fits with the model developed earlier. Longer pulses will loft more material, but that material is accelerated toward a maximum entrained velocity.

What of the material we characterized best, the CI Orgueil simulant? Average particle velocities increase when the nozzle is lowered; recall that this increases the magnitude of surface pressure. Curiously, some peak velocities are higher for the more distant nozzle. This can be attributed to a few particles ejected at randomly higher velocities that were able to be tracked. CI Orgueil simulant has irregular particle sizes, shapes, and packing arrangements. We see off-center flow directed through narrow channels up and out of the bulk regolith. This may entrain some particles with higher than expected velocities based on particle averages. This behavior is distinct, however, from the initial burst seen during most experiments with finer grained particles. Those particles are accelerated quickly as the shock front of the plume hits the surface. Data from the summary plot shown above (Figure 66 and Figure 67) in graphical form is also recorded in Table 12 below and categorized by measurement type.

Table 12: Velocity measurements based on each method described: Automated tracking (AT), manual tracking (MT), and frame-averaged profiles (FA). Where possible, we distinguish between sparse (background partially obscured) and bulk (background completely obscure) profiles in our FA analysis.

Material	Nozzle Height (cm)	Pulse Time (ms)	AT Side (cm/s)	MT Side (cm/s)	AT Top (cm/s)	FA Side, Sparse (cm/s)	FA Side, Bulk (cm/s)
Steel Beads	19	10	-	-	9.0	-	7.5
		25	18.0	-	17.9	30	11.25
		50	30.1	-	28.8	60	30
		100	24.0	-	23.7	180	60
		250	27.7	-	28.3	180	60
	29	10	157.0	-	73.8	-	-
		25	43.8	-	36.8	30	11.25
		50	67.6	-	57.0	-	45
		100	42.3	-	43.7	-	60
		250	49.6	-	59.4	-	120
Beach Sand	25	10	-	-	-	15	7.5
		25	-	-	-	120	30
		50	-	-	-	180	60
		100	-	-	-	180	180
		250	-	-	-	180	180
Glass Beads	15	10	17.5	-	17.5	-	30
		25	21.3	-	21.0	-	60
		50	20.7	-	20.7	-	60
		100	18.3	-	18.3	-	60
		250	24.0	-	24.0	-	60
	25	10	26.7	-	26.7	30	15
		25	20.6	-	27.3	-	45
		50	16.6	-	16.6	-	180
		100	14.3	-	14.3	-	180
		250	19.2	-	19.2	-	180
CI Orgueil	15	10	-	10.7	11.3	7.5	3.8
		25	13.3	19.1	18.1	45	15.0
		50	35.3	44.0	28.8	60	30.0
		100	50.2	44.9	51.3	90	45.0
		250	55.6	64.3	71.7	-	60.0
	25	10	1.9	9.6	10.7	-	3.8
		25	11.7	18.1	21.0	60	11.3
		50	26.3	27.5	41.2	60	15.0
		100	41.2	42.6	63.0	90	45.0
		250	51.6	59.2	74.0	90	45.0

Crater Measurements

Methods

As with the velocity determination, each of these four regolith simulant types produces challenges that necessitate different methodologies to estimate the crater size, depth, and mass. PSI interaction with CI Orgueil simulant lofts fine dust in the first few ms of each experiment, which is challenging to our analysis methods. Frame differencing and thresholding methods no longer reveal just particle motion but show the swirl of dust-entrained gas, obscuring features of interest. Then too, the large particle sizes of CI Orgueil simulant relative to the crater size hamper our ability to neatly define crater boundaries compared to simulants with smaller particle size like the glass beads. Nevertheless for each of these experiment sets we have attempted to measure or estimate features of interest: namely the crater volume and mass resulting from PSI. For some experiments where measurements are more easily determined, we also examine the time dependence of crater growth.

We have no direct method for measuring crater mass. Instead it must be estimated from other parameters. Two methods include measuring the transient crater diameter, which is not always clearly defined for some materials, and taking side and top-down measurements to determine crater diameter. Both measurements are taken in ImageJ and calibrated using the methods described in the image analysis above. From the side view, when an ejecta splash is clearly defined, we may measure the narrowest point in the splash as an estimate of crater diameter. In the top down view, crater shading is used to measure the diameter of the splash level with the original surface. This gives us an effective inner and outer crater diameter that can be used as an accuracy check to our measurements and calibration, since the inner diameter will necessarily be smaller than the outer.

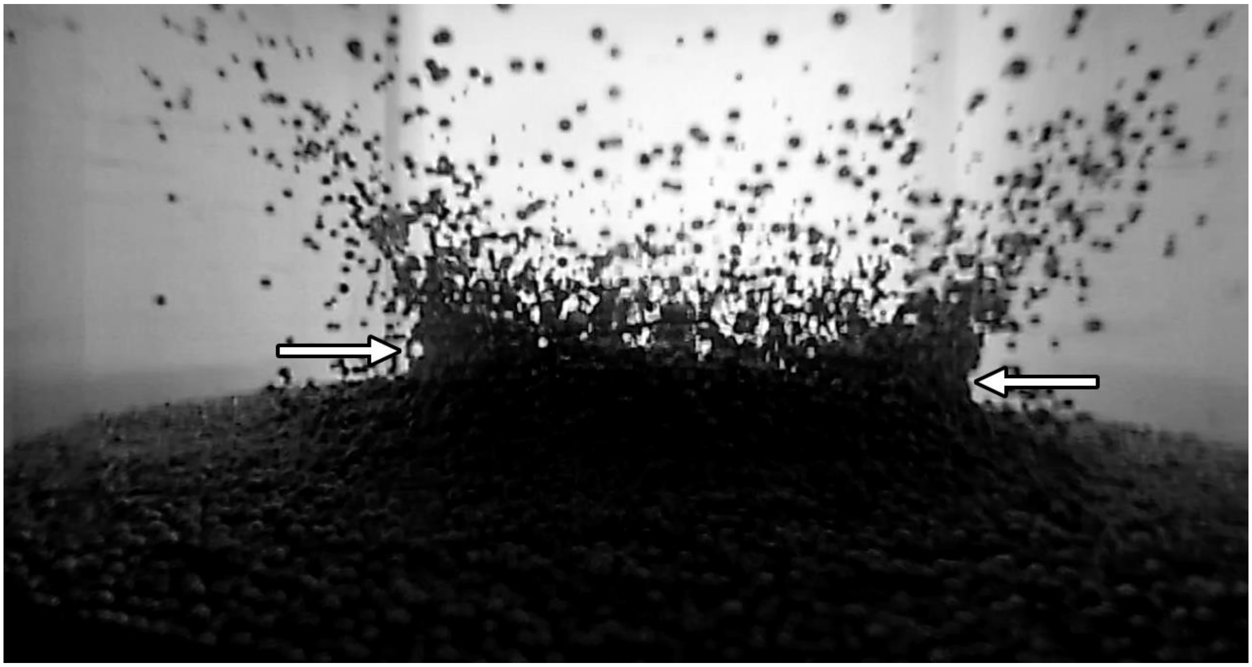

Figure 68: Example crater splash with the crater neck indicated. This narrowest point is measured as a proxy for crater diameter.

While we took stereo images for some experiments, lack of consistency and accurate calibration precludes us from using these images to determine crater depth. Instead we determined the depth-to-diameter ratio for each simulant type. Since the PSI effects bottom out for each simulant type except the quartz sand and the initial material depth is known, we may calculate a depth-to-diameter ratio at the instant before material clears away from the bottom surface. This ratio is then applied to the other experiments of that type to estimate depth based on measured crater diameter.

Estimated depth for some of the CI Orgueil experiments is determined by observing how many layers of particles are blown away in the PSI process, or by directly measuring particle dimensions and approximating with the volume of an ellipsoid for each particle. In some cases, ejecta is produced in a monolayer. In others, intermediate depths can be calculated by observing particle ejection and counting the number of particles stacked. In either case, a sample of measured particle diameters is used to approximate material depth. When the experiment bottoms out, we have a definite lower bound to the crater.

Crater mass may also be estimated by considering the cross-sectional area of particles as seen from the side camera view. This is subject to several limitations and approximations. The first is line of sight. In one limit, particles are sparsely ejected, such that every particle ejected is visible to the camera. In another limit, particles are densely ejected to form a cone-like structure. In the first limit, the observed particle cross section would be the true cross section, accounting for particle distance. In the second limit, the observed cross section tells us nothing about interior structure and most particles will be partially or completely obscured. Applying this method naively will tend to under-count particles ejected. This is mainly applied to the quartz sand simulant.

The other problem we face results from perspective. Particles nearer the camera appear larger, particles farther away smaller, and this apparent cross section decreases with the square of the distance from the camera. Assuming an ideal setup, the pixel to centimeter ratio determined by camera calibration is strictly valid only in the plane which bisects the experiment tube vertically and lies orthogonal to the camera lens’s centerline. In the latter case mentioned above, this is not so much of a problem, as we can calculate the surface area of a cone when viewing a two-dimensional projection with axisymmetry. In the sparse case, if we assume an axisymmetric ejecta spray, there will be as many particles behind the plane as in front. Total area, however, will be slightly overestimated. Our experiments span this entire range from sparse to opaque.

Because the cross-sectional area of ejected particles will be, in general, underestimated, any computation from this metric serves as a lower bound to ejected mass. Taking the observed area obscured by ejecta and dividing by an assumed average particle cross section, we estimate the number of particles visible to the camera, then multiple by particle mass to estimate total ejecta mass.

To measure crater expansion with time, we take measurements for the two experiment sets with the most well-defined PSI ejecta. Both steel beads and glass beads at low nozzle height produce ejecta with easily discernable boundaries. The ejection angle is high enough that a "neck" is formed near the surface of the material. This neck—the narrowest point in the ejecta spray—is measured over the course of the experiment as it corresponds to internal crater diameter. While it is a slight overestimate of crater diameter itself, it shows the same growth trend.

Results

We measured the neck width for thirteen glass bead and twelve steel bead experiments and plot the dependence of transient crater diameter with time in Figure 69. As in work by Donahue et al. (2005) and Metzger et al. (2009), we plot these with the logarithm of time and find that these PSI interactions appear to increase linearly with the logarithm of time. This seems to hold well for certain glass bead experiments, but a couple diverge from this trend. The 100 ms and 250 ms pulse durations do not remain linear with time, but these experiments quickly bottom out to the shallow baseplate. The 50 ms and 25 ms pulse steel bead experiments, as well as the glass bead experiments, follow the log-linear trend. What is curious here is that both sets of experiments that seems to trend with the pulse duration, with the shorter pulses following a similar growth rate, as do the three longer duration pulses. We are using the neck of the ejecta crater as a proxy for crater growth, and these longer duration experiments see a more significant upwelling. Because the gas is redirected from the baseplate outward toward the interior crater wall, we suggest this accelerates crater expansion such that it does not follow a standard increase with the logarithm of time.

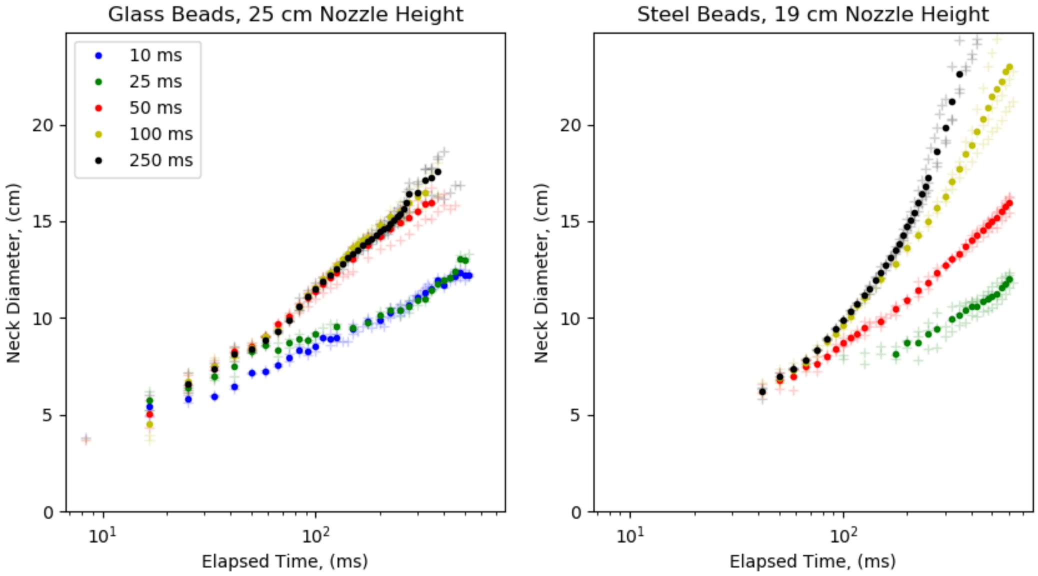

Figure 69: Neck width (as a proxy for transient crater diameter) versus elapsed experiment time for steel and glass bead experiments, plotted with the logarithm of time. Individual experiment measurements are shown as crosses; dots represent an overall average at that time for experiments with identical parameters.

We therefore partially confirm the result of Metzger et al. (2009) which noted crater expansion—both radius and depth—to increase linearly with the logarithm of elapsed experiment time. Their behavior can therefore be described by a power law. Rajaratnam and Beltaos (1977) saw this behavior up to a characteristic depth after which the expansion was nonlinear to a maximum. We do not see this behavior in our experiments; rather the steel bead experiments seem to show something closer to a linear relationship once the experiment bottoms out. Our crater volume and mass estimates are summarized in Table 13 below. These measurements are listed by experiment parameter set and the measurement method is noted. Volume results are also presented in Figure 70; graphs for mass estimates would differ only by a constant factor.

Table 13: Maximum average ejected mass and volume by experiment parameters.

Material	Nozzle Height	Pulse Duration	Volume Ejected (cm^3)	Mass Ejected (g)	Method
Glass Beads	15	10	80.3	127.1	Crater/Cylinder
	15	25	164.9	261.2	Crater/Cylinder
	15	50	523.1	828.5	Crater/Cylinder
	15	100	770.0	1219.4	Crater/Cylinder
	15	250			
	25	10	43.8	69.3	Crater/Cylinder
	25	25	124.5	197.2	Crater/Cylinder
	25	50	160.0	253.4	Crater/Cylinder
	25	100	595.5	943.2	Crater/Cylinder
	25	250			
Quartz Sand	25	10	0.9	1.3	Cross-Section
	25	25	2.5	3.9	Cross-Section
	25	50	4.1	6.4	Cross-Section
	25	100	4.7	7.4	Cross-Section
	25	250	7.2	11.3	Cross-Section
CI Orgueil	15	10	19.9	16.4	Particle/Cylinder
	15	25	129.3	107.1	Cylinder
	15	50	268.8	222.6	Paraboloid
	15	100	680.6	563.6	Paraboloid/Cylinder
	15	250	1932.4	1600.0	Estimate
	25	10	20.1	16.7	Particle/Cylinder
	25	25	99.9	82.7	Paraboloid
	25	50	161.5	133.7	Paraboloid
	25	100	305.8	253.2	Paraboloid
	25	250	995.9	824.6	Cylinder
Steel Beads	18.7	10		0.0	Crater/Cylinder
	18.7	25	70.4	328.1	Crater/Cylinder
	18.7	50	134.2	625.0	Crater/Cylinder
	18.7	100	155.9	726.1	Crater/Cylinder

Material	Nozzle Height	Pulse Duration	Volume Ejected (cm^3)	Mass Ejected (g)	Method
	18.7	250	270.2	1258.8	Crater/Cylinder
	28.7	10	0.0	0.0	Crater/Cylinder
	28.7	25	0.0	0.0	Crater/Cylinder
	28.7	50	67.6	314.9	Crater/Cylinder
	28.7	100	155.5	724.5	Crater/Cylinder
	28.7	250	252.5	1176.6	Crater/Cylinder

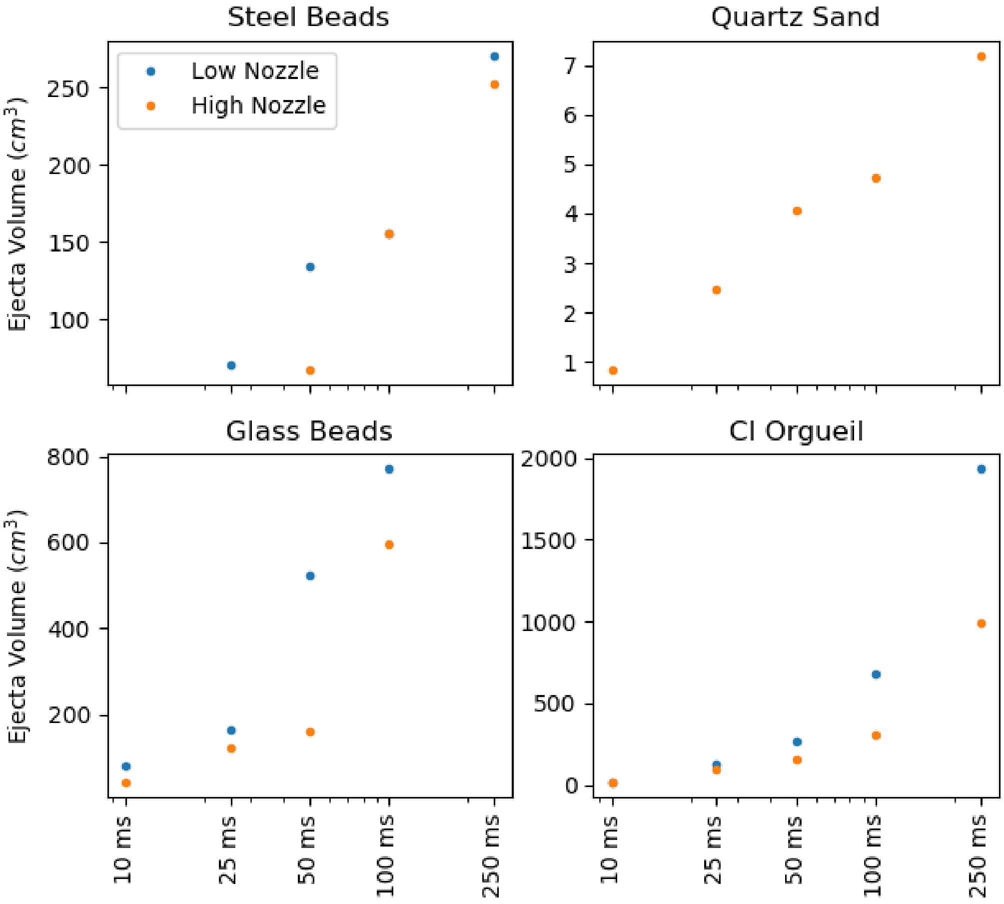

Figure 70: Averaged ejecta volume measurements for each experiment type conducted. Volume for the steel bead and quartz sand experiments appears to increase with the logarithm of jetting duration Volume for the glass bead and CI Orgueil experiments increases linearly with jetting duration. Ejecta was too sparse to measure for the 10 ms steel bead experiments; glass beads obscured the lens for the 250 ms pulse.

Since ejecta mass and volume differ only by a constant factor we may discuss their behavioral trends together. Note that these given times are different than in the time-growth measurements above. Both glass beads and CI Orgueil simulant ejecta appear to increase linearly with time. The quartz sand and steel beads increase logarithmically with time. Given the uncertainty in these measurements and the relatively small number of data points, we do not feel confident in confirming the power law derived by Metzger et al. (2009).

PyRIC Model Comparison

We apply our PyRIC model to each set of experiment parameters and examine predicted ejecta mass. Robert's (1964) equation is used to determine a surface pressure distribution; ambient pressure is treated as the "chamber pressure" and the flow is assumed to choke at the speed of sound. Ambient pressure increases linearly over the course of the experiment based on the change in pressure seen in our experimental apparatus for each parameter set. Model runs are terminated at the end of each pulse and regolith instability calculated by grid-cell pressure offset from ambient. Most of the results for these model runs do not compare well, in particular for the steel bead and glass bead experiments, as their behavior is not primarily explained by diffusion driven flow. We will neglect these cases for the moment, examine the CI Orgueil and quartz sand flow and volume estimates, then return to discuss the others.

Flow Comparison

Two examples will be illustrative of the end cases where our model shows promise. Figure 71 and Figure 72 below show model runs for CI Orgueil and quartz sand simulants, respectively. CI Orgueil is significantly more permeable than quartz sand. That permeability difference is about three orders of magnitude. Air flows freely, relatively speaking, through CI Orgueil but does not permeate the sand significantly. This is indicated by our model; note in Figure 71 how the gas has permeated the entire space within the first one-thousandth of a second. But the end of the sand run, it is apparent from Figure 72 that gas has not intruded very far into the sand. And our model predicts no ejecta in the latter case; in the former, the white line designates the region of instability.

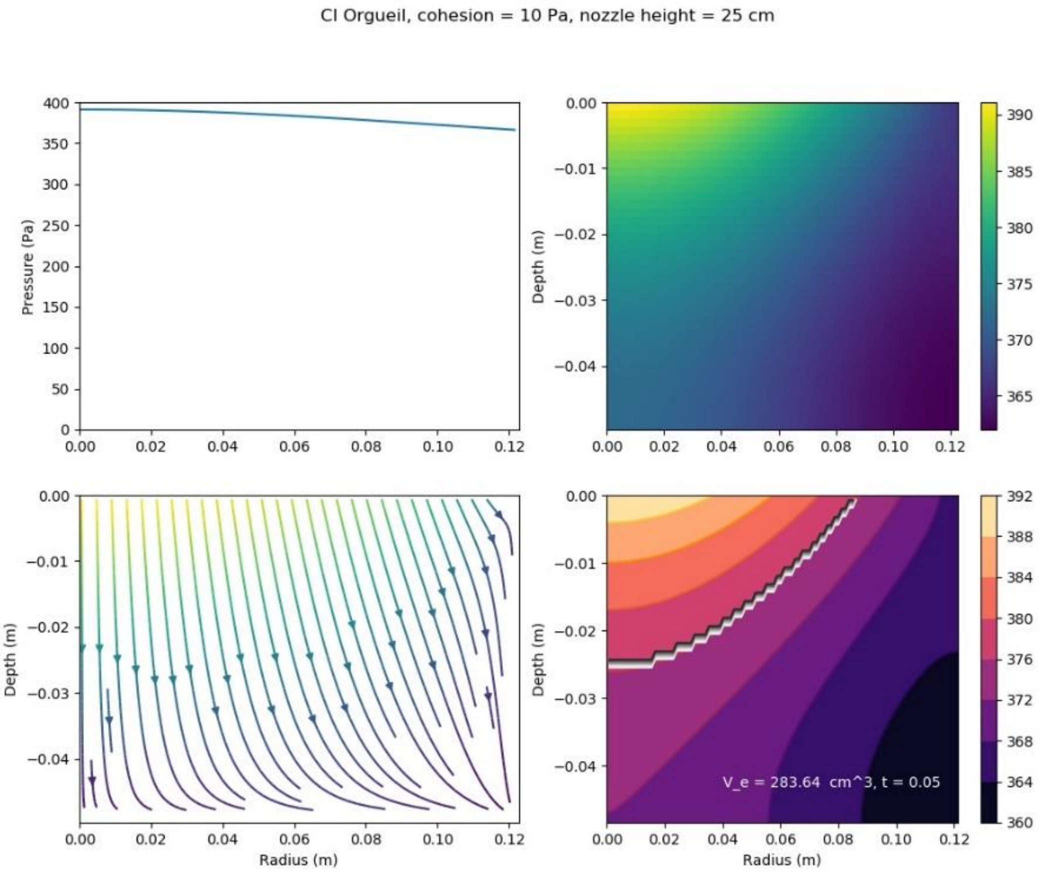

Figure 71: Flow visualizations at jetting cutoff for a 50 ms CI Orgueil experiment run. Top left: The surface pressure distribution used as a boundary condition. Top right: Pore pressure within the simulated region (in Pa). Bottom right: Pore pressure shown as a contour plot with predicted region of instability overlaid in white. Bottom left: Streamlines show the direction of gas flow and are shaded according to the intensity of the pressure gradient.

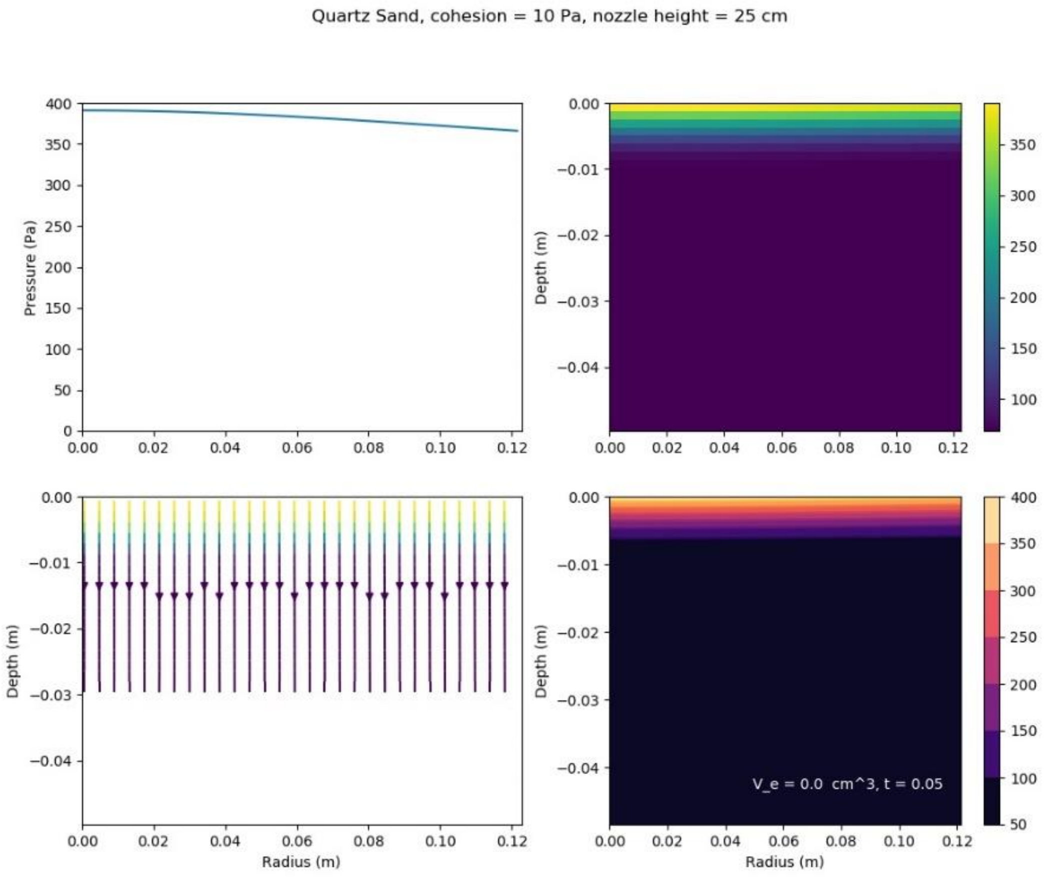

Figure 72: Flow visualizations at the end of a 50 ms quartz sand experiment run. Top left: The surface pressure distribution used as a boundary condition. Top right: Pore pressure within the simulated region (in Pa). Bottom right: Pore pressure shown as a contour plot with predicted region of instability overlaid in white. Bottom left: Streamlines show the direction of gas flow and are shaded according to the intensity of the pressure gradient.

From our experiments we saw that viscous shear erosion (VSE) is the primary PSI mechanism for quartz sand. However, because our model is based on gas diffusion it is not intended to predict VSE. But it does correctly indicate that no diffusion driven flow will occur here. Likewise, for CI Orgueil, the gas permeates quickly to destabilize the regolith. We see matching behavior in the end-member cases. In-between, however, glass and steel beads are complex mixture of phenomena that is not well-captured in the model.

Mass Comparison

Most of our quantitative predictions from this model neither accurately represent the measured ejecta nor do they show the proper trend, except again in the end member cases. The result for sand is trivial but relevant: no instability predicted. The best result we obtain comes from the CI Orgueil series at 25 cm nozzle height, an instance of which is shown above. Results from the 15 cm nozzle height are shown as an example of poor model performance. Varying cohesion as a parameter, model calculated ejecta volume is plotted in Figure 73 and Figure 74 below along with our experimental result for each pulse duration.

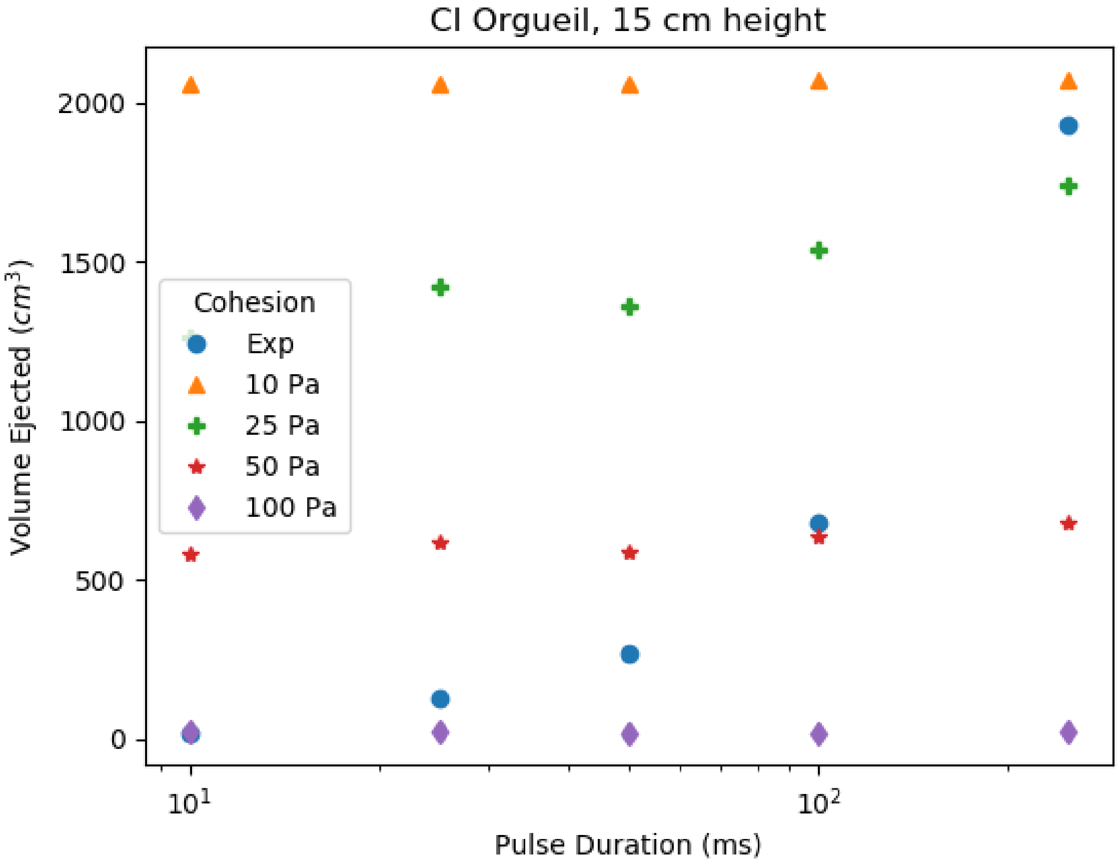

Figure 73: Modeled ejecta volume for the 15 cm nozzle distance CI Orgueil experiment set as a function of regolith cohesion, with points plotted for each experiment pulse duration. Experiment data is also plotted for comparison.

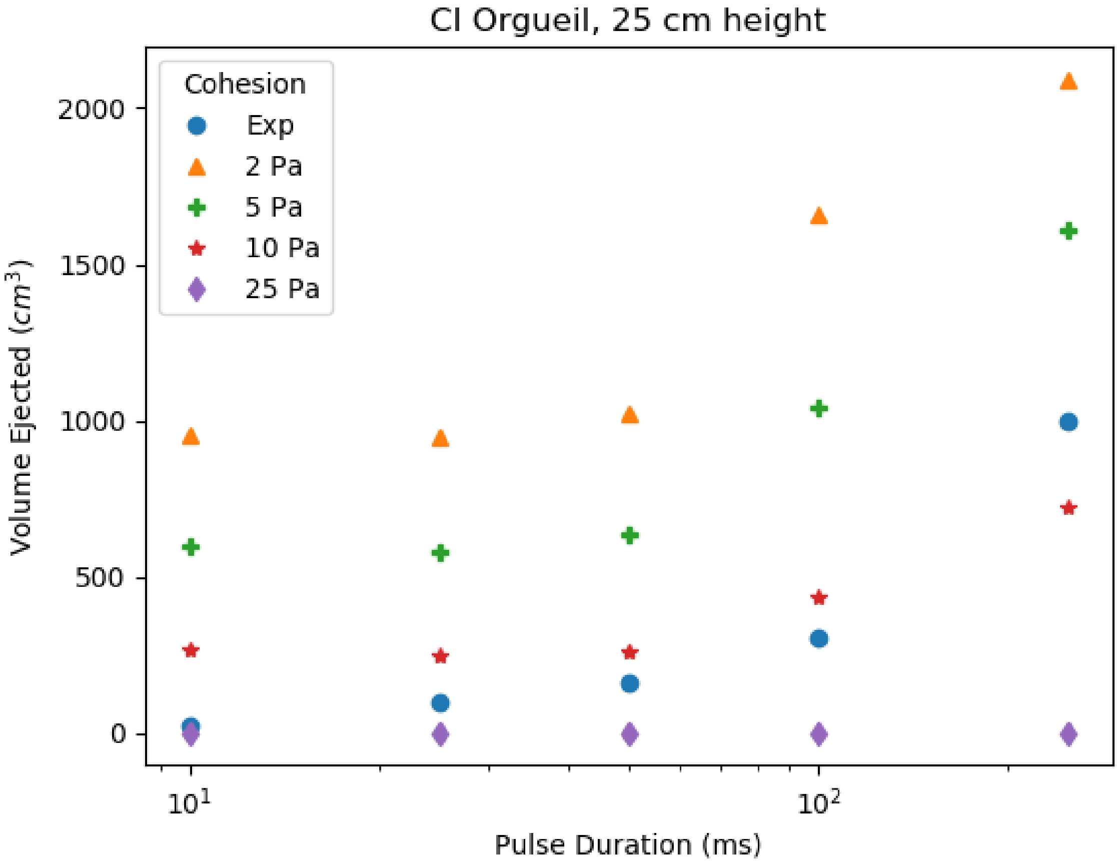

Figure 74: Modeled ejecta volume for the 25 cm nozzle distance CI Orgueil experiment set as a function of regolith cohesion, with points plotted for each experiment pulse duration. Experiment data is also plotted for comparison.

The set of CI Orgueil runs with a 25 cm nozzle height captures both an estimate for volume ejected and also the trend shown by experiment data. This is not the case for the lower nozzle height, which prediction is roughly flat over the set. Because the forces in question here are relatively low, modeling ejecta is a delicate balance between surface pressure distribution, regolith permeability, and cohesion. Misunderstanding one of these results could lead to a faulty outcome. We see, however, that the correct trend can be predicted by the model for high-permeability regolith.

Summary

This chapter presents measurements of PSI ejecta velocities and masses for our experiment set. We find peak velocities for particles to be as high as tens of m/s, while a typical bulk range is from cm/s to hundreds of cm/s. Ejecta volumes range from a handful of individual particles up to lofting most of the simulant mass. Regolith permeability enhances this effect; erosion for quartz sand does not end up at significant depth in our experiments. We measure the expansion rate of PSI cratering in microgravity to take a power law form, expanding with the logarithm of time.

We run our model for these experiment cases and find that it is best suited for high permeability cases, when the quasi-static assumption of the model is most applicable. Our model can predict volume trends, but additional work is needed to expand its capability into other regimes.

CONCLUSIONS AND FUTURE WORK

This dissertation has detailed a course of computational and experimental work which seeks to understand the phenomena of plume surface interactions in vacuum microgravity. A summary of our results and recommendations for future work follows. As a summary of the experiment comparison from Chapter 5 flows naturally out of discussing Chapter 2, we arrange those conclusions in the section below.

Modeling Plume Surface Interactions and Experiment Comparison

We developed a physics-based flow solver which can be used to estimate regolith ejecta from plume-surface interactions. A custom solver written in Python expands the PSI model of Scott and Ko (1969) to handle arbitrary environmental parameters. The program produces a surface pressure distribution using Robert's (1964) equation based off of engine parameters or takes an arbitrary boundary condition specified by the user. This boundary condition, which may be time dependent, is then used to solve Darcy's Law. We implement features like automatic timestep adjustment to optimize run time and prevent algorithmic instability.

With the flow profile solved, we may calculate regions of instability in the regolith to estimate ejecta mass and volume. Our model gives valuable qualitative insight into the flow patterns which produce PSI and are confirmed by our experiment campaign. These insights include (1) off-center lofting, predicted by our model for permeable regolith and seen with all simulants except the very impermeable quartz sand. This occurs when gas injected on-center diffuses out and up through regolith off-center in an annulus, carrying material away from the surface. (2) Ejecta caused by on-center re-eruption. Our model predicted on-center lofting could occur in relatively impermeable regolith if gas was injected on-center and the engine cutoff. This could be considered a single-pulse case of DGEE. We see gas pockets form in quartz sand at short pulse times and see high angle lofting from glass beads at the shortest pulse time. This phenomenon disappears at longer pulse times as other modes of erosion dominate. Since our model considers regolith to be static, it makes sense that this effect only appears for short pulse times.

Our model sees moderate success at quantitative predictions of regolith ejecta in our comparison to the experiment campaign conducted by Land and Scholl (1969). In the best fit to experiment, our model predicts most crater volumes to within a factor of five. This experiment set does not give us much insight into why the model might be more or less applicable. Comparison to the GRIT experiment sheds additional light on the process, but our model has limited success replicating the results of the GRIT experiment because of the range of PSI regimes.

We see from experiment that VSE is the primary mechanism for PSI in quartz sand. Our model predicts the effect of diffusion drive flow on quartz sand and finds no ejecta—which matches the experiments! By contrast, CI Orgueil gives us conditions closest to our model: namely, highly permeable regolith that is quasi-static during short pulses. While it would take further optimization to predict ejecta volume, our model does indicate the dominance of diffusion driven flow for highly permeable regolith.

What of the in-between cases? While DDF plays a role, both steel and glass beads are too permeable for VSE to dominate and too impermeable for gas to flow unimpeded. More complex modeling is needed to predict these effects. This gives us some confidence in the results of our ARM study, though it is primarily applicable to bulk material. Lofting fines and gentle surface perturbations are likely to be factors even when mitigating steps are taken.

PyRIC is a useful tool for understanding gas flow through regolith. Improving its fidelity and reliability means reducing the number of assumptions at play. It could be improved by (1) a better tool to calculate surface pressure distribution, as Robert's (1964) equation applies to hard vacuum; (2) a more robust treatment of permeability that includes changes with gas density; (3) determining the effects of changing temperature and pressure on gas viscosity; (4) modeling regolith motion during a model run. This last step is likely to be hardest, but our experimental work gives insight into a basis for calculating regolith velocities with flow properties.

Experiments and Observations

We have conducted a series of over 200 bench and drop tower experiments with various regolith simulants to understand plume surface interactions in vacuum microgravity. This is the first treatment of the phenomena in systemic fashion, and the video data collected show us novel behaviors within gas-granular systems. We can summarize our qualitative findings in terms of phenomena and trends, some of which are directly related. Observing PSI in vacuum microgravity reveals new phenomena that would be otherwise masked by gravity.

We observe trends that might be expected: PSI behaviors are significantly more pronounced at reduced gravity. PSI behaviors are more intense with increased jetting time; it increases ejecta volume—both crater depth and crater width—though the size appears to approach a maximum under these experiment conditions. Reducing the nozzle height increases ejecta mass and increases ejecta angle. The latter effect appears to be the case due to a narrower pressure distribution.

Ideally, we could compare quartz sand, glass bead, and CI Orgueil simulants to each other directly to draw conclusions about the effect of particle size—and therefore permeability—

on PSI. But their other properties are somewhat different. We have a distribution of particle sizes in the CI Orgueil simulant, and its density is half that of the glass and sand. That said, a few conclusions are warranted, as reduced gravity makes density somewhat less important, and the difference in particle sizes between simulants is significant. We see roughly equivalent volumes ejected comparing glass beads to CI Orgueil, meaning the mass ejected in the former case is significantly higher. Compare this to quartz sand, where relatively little mass is ejected. In the latter case, this may also be due to particle morphology. We would expect to see more pronounced PSI from glass beads of equivalent diameter.

Aside from these trends we observe a number of interesting, novel behaviors that show up prominently in microgravity but are masked in 1*g*. Once again, off-center lofting occurs when injected gas circulates outward and upward, back through the surface in an annulus outside the centerline, and raises material up with it. This can occur concurrently with a main ejecta crater and may be close enough to blend into that ejecta spray.

Gentle pulses into quartz sand create a gas pocket on center that maintains some of the underlying structure present in the material. This behavior disappears at moderate jetting times. When particle sizes are larger or more massive, underlying structure can shape the ejecta spray and redirect gas flow. We see the former in one experiment with steel beads, and the later numerous times in CI Orgueil.

Viscous shear erosion appears to be the driving mechanism for PSI in fine grained, low permeability materials, while diffusion driven flow dominates our larger grained, high permeability experiments. Intermediate to these, bearing capacity failure can be seen in intermediately size particles, with the presence of minor diffusion driven flow.

Our experiment campaign could be improved upon in future work. This set of experiments has given us insight into the use of lighting, material contrast, and camera specifications when conducting PSI experiments. Ensuring proper contrast of the simulant with a backdrop is critical for later analysis. Uniform lighting is also of benefit, and framerates higher than a consumer action camera can provide would aid in particle tracking.

But to continue understanding PSI, expanding on the parameter space in a systematic fashion will be crucial. Building up a set of experiments at various nozzle heights, jetting durations, and material properties will allow us to characterize the full range of phenomena which may occur. And rather than using unlike simulants, controlling for particle size could be a valuable next step in a new campaign; that is, conducting experiments with glass beads, for example, and only changing particle size.

Quantitative Analysis

We analyze video of the GRIT experiment campaign to characterize bulk behaviors of regolith during PSI. Because behavior and material properties vary significantly between simulants, we used several methods to measure ejecta properties. For velocity measurements, this includes manual particle tracking, automatic particle tracking, frame averaged profiles, and visual inspection. Interior and exterior crater diameter measurements are taken manually and compared with depth/diameter ratios and simulant density to determine mass ejected.

Aggregating our velocity measurements gives us a picture of bulk regolith behavior. Particle velocities have an upper bound in the meters to tens of m/s range, depending on particle type. These fastest particles are the most difficult to characterize and bear superficial similarity to the descriptions of “spurts” from hypersonic impact experiments, albeit at a significantly slower scale. Even the shortest duration pulses can produce “fast” particles traveling up to about 1 m/s.

If initial particles are accelerated with a “kick”, the bulk flow comes from a mechanism related to the bulk properties of the material. Bulk velocities increase with pulse time and approach the flow velocity asymptoticly. These velocities range, on average, from cm/s to tens of cm/s. This behavior is consistent with equations of motion derived from a consideration of particle drag in a steady flow. While the phenomena are more complex overall, this insight may assist further computational efforts to model the effects of PSI.

Crater diameters are measured manually from top-down and side view cameras, allowing us to recover ejecta volume and mass estimates. While we cannot confirm the trend noted by Donahue et al. (2005) that shows crater depth grows with the logarithm of time, we observe diameter growth also follows this trend, excepting when the experiment bottoms out. Donahue et al. (2005) notes this was seen in the case of hydraulic jets by Rajaratnam and Beltos (1977), and the result was also shown in 1*g* experiments by Metzger et al. (2009). This result of radial growth as a power law appears independent of gravity level.

Our experience analyzing this data suggests improvements to the GRIT setup that would enable improved methods and more rapid analysis. More extensive use of automated particle tracking would significantly speed velocity measurements. Automated methods benefit from uniform background lighting, opaque simulants, and a higher framerate than our action cameras were able to record. A camera capable of ~1000 fps would likely yield inter-frame displacements small enough to track the fastest particles, though this should be tested and tailored for individual experiments. Strobe lighting could also compensate to effectively freeze-frame high-velocity particles, but it would not solve the displacement issue between frames.

As our experiments are axisymmetric, using a sheet laser to illuminate a plane orthogonal to the camera could also be useful. This has been applied with success to prior low velocity impact experiments conducted at the Center for Microgravity Research. Dusty simulants were a challenge for our setup; illuminating a plane might aid in resolving particles.

Our dual camera setup was useful for redundancy in case of problems with a unit inside the vacuum chamber, but our initial plan to perform stereo image analysis was not realized. Optical distortion and inconsistency in camera placement proved a challenge, one that further analysis may solve. The camera setup may be improved, however, if stereo imaging is desired to analyze crater topography.

Multiple image analysis techniques were attempted over the course of our analysis, not all of which yielded acceptable results. Improvements would be useful to the rapid analysis of future datasets. As an example, the particle tracking algorithm we used was written for particles undergoing random motion. Because we expect linear trajectories from our experiments, modifications to this module’s track linking capability could likely improve speed, prevent the introduction of spurious trajectories which must be filtered, and recover particle trajectories that were missed by the stock software.

APPENDIX A: GRIT ARDUINO CODE

The following code controls GRIT’s onboard Arduino. It detects when the experiment breaks free of the drop tower harness, then triggers an air pulse. This code was modified and adapted from a prior CMR experiment. The “pulse_time” variable may be changed for each experiment run.

```
//GRIT code
//Wesley Chambers
//20 July 2018

//Pin assignments

int pulse_time = 250;     // This controls air pulse time (in
milliseconds).

int relay_pin_out = 7;

int armed_pin_sig = 2;

int contact_pin_vlt = 11;
int contact_pin_sig = 10;
int contact_pin_gnd = 9;

int armed_pin_LED = 4;
int contact_pin_LED = 3;

bool COUNT = 0;
bool ARMED_LOGIC   = 0;
bool CONTACT_LOGIC = 0;

void setup() {
  // put your setup code here, to run once:

  pinMode(armed_pin_sig, INPUT);

  pinMode(relay_pin_out, OUTPUT);

  pinMode(contact_pin_sig, INPUT);
  pinMode(contact_pin_vlt, OUTPUT);
  pinMode(contact_pin_gnd, OUTPUT);

  pinMode(armed_pin_LED, OUTPUT);
  pinMode(contact_pin_LED, OUTPUT);
```

```
  //Initialize pin states

  digitalWrite(relay_pin_out, LOW);

  digitalWrite(contact_pin_vlt, HIGH);
  digitalWrite(contact_pin_gnd, LOW);

  digitalWrite(armed_pin_LED, LOW);
  digitalWrite(contact_pin_LED, HIGH);

  Serial.begin(9600);
}

void loop() {

  Serial.print("Start loop.\n");


    // Read armed and contact logic
  ARMED_LOGIC   = digitalRead(armed_pin_sig);
  CONTACT_LOGIC = digitalRead(contact_pin_sig);

    // Show Logic by print and LED
  Serial.print("Armed Logic:");
  Serial.print(ARMED_LOGIC);
  Serial.print("\t Contact Logic:");
  Serial.println(CONTACT_LOGIC);

    //Contact Light indication
  if(CONTACT_LOGIC==true){
       digitalWrite(contact_pin_LED, HIGH);    }
  if(CONTACT_LOGIC==false){
       digitalWrite(contact_pin_LED,  LOW);
       delay(25);
       digitalWrite(contact_pin_LED,  HIGH);
       delay(25);}
  if(ARMED_LOGIC==false){
       digitalWrite(armed_pin_LED,  LOW);    }

  while(ARMED_LOGIC==true){

      // Read armed and contact logic
       ARMED_LOGIC   = digitalRead(armed_pin_sig);
       CONTACT_LOGIC = digitalRead(contact_pin_sig);
```

```
       digitalWrite(armed_pin_LED,  HIGH);

         // Falling event (false means its not in contact)
       if(CONTACT_LOGIC==false and COUNT==false){
              //Activating Launcher
            delay(75);

            Serial.print("### Firing Solenoid ### \n");
            digitalWrite(relay_pin_out,   HIGH);
            delay(pulse_time);
            digitalWrite(relay_pin_out, LOW);
            Serial.print("### Long Delay ### \n");

            COUNT = 1;

            delay(3000);   // 1 min cooldown (enough time to
turn off the arm or power switch)

       ARMED_LOGIC   = digitalRead(armed_pin_sig);
       CONTACT_LOGIC = digitalRead(contact_pin_sig);
    }


  }
  Serial.print("End loop.\n");
}
```

APPENDIX B: GRIT ELECTRICAL SCHEMATICS

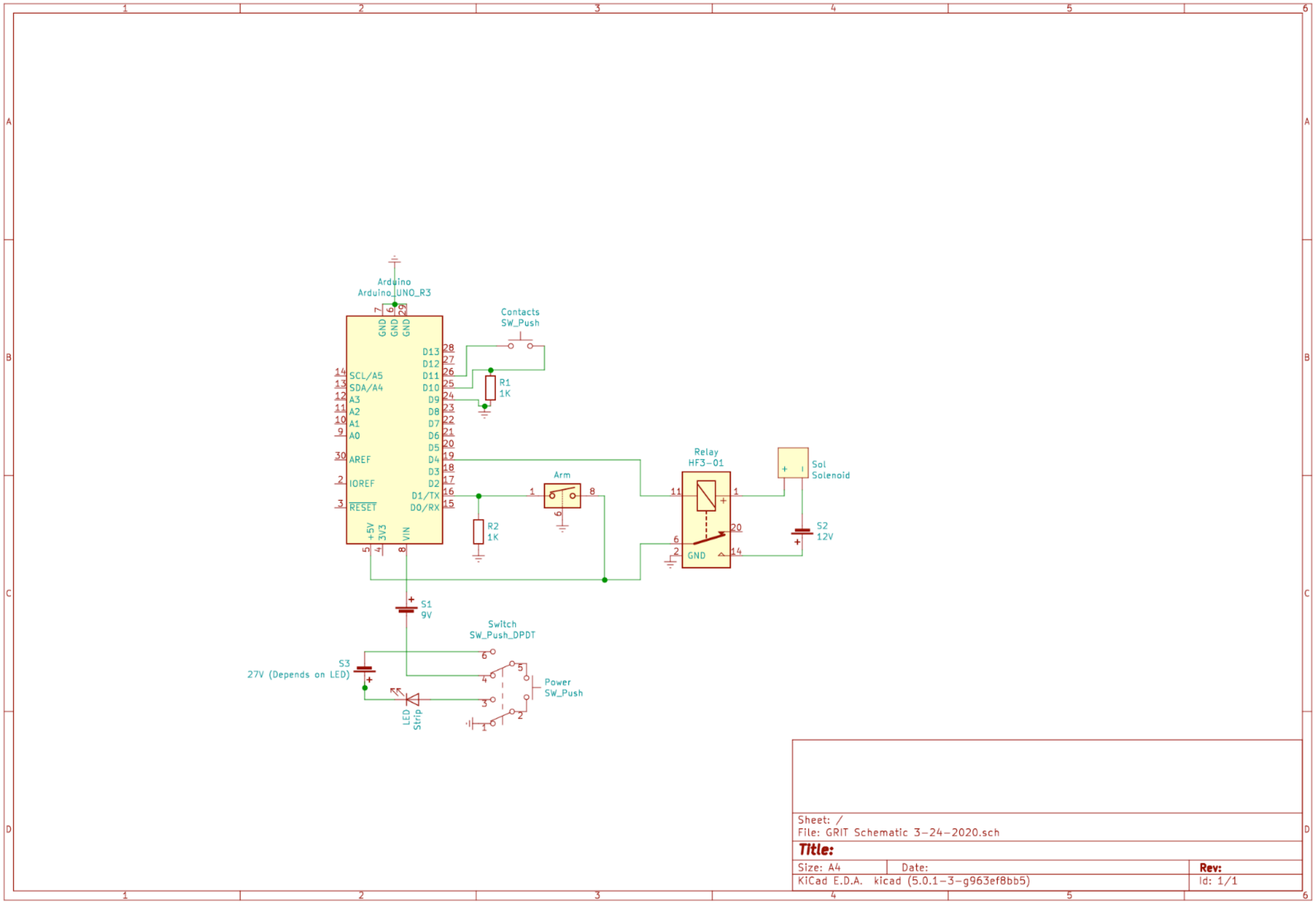

Figure 75: GRIT electrical schematic. The switch between main and auxiliary power sources was later replaced by in-line diodes.

APPENDIX C: MODEL CRATER PROFILES

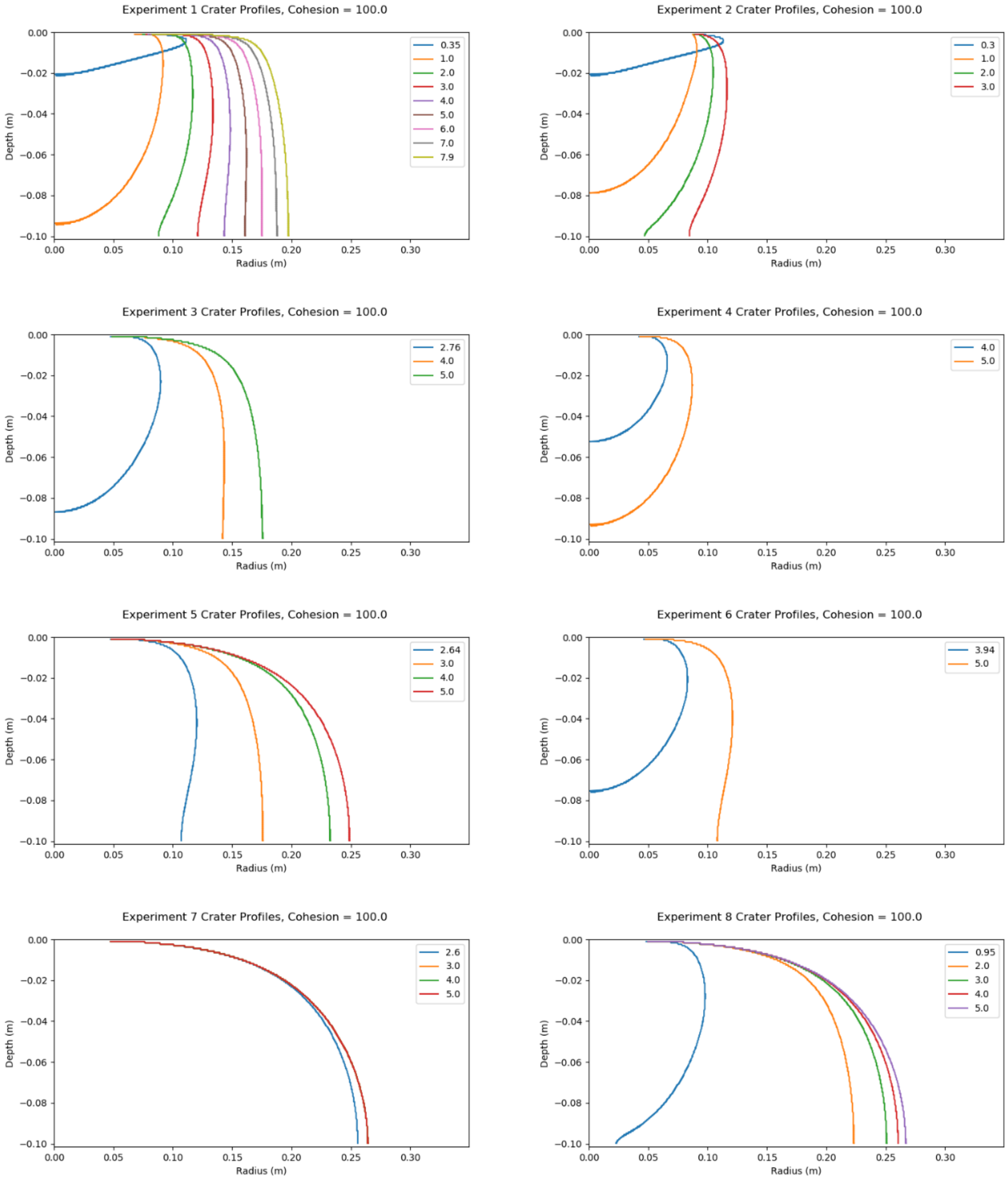

Figure 76: Instability profiles generated by our model for comparison to Land and Scholl (1969) experiments 1 through 8. Each line plots the instability region for an elapsed time (s) given in the legend assuming a cohesion value of 100 Pa.

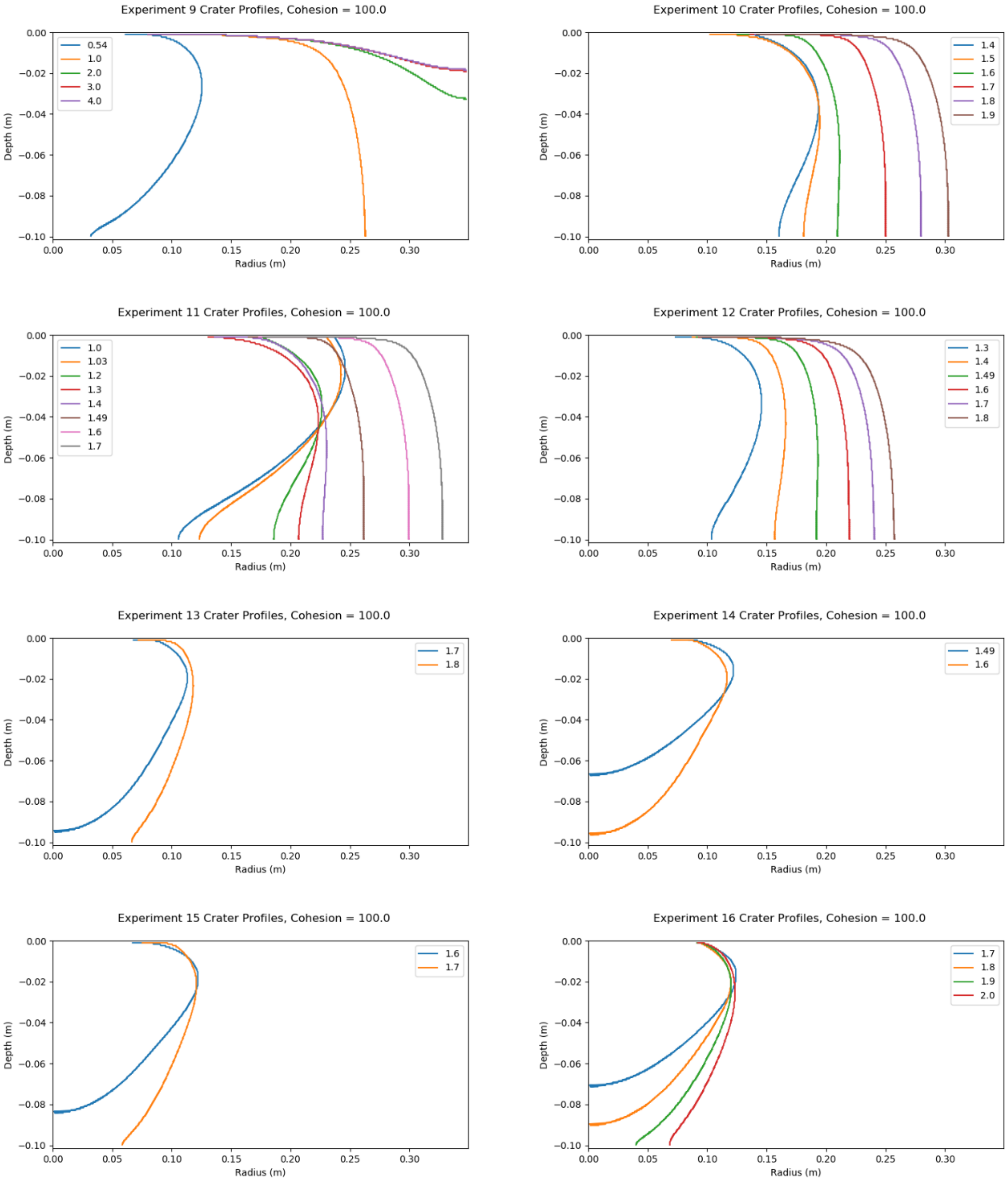

Figure 77: Instability profiles generated by our model for comparison to Land and Scholl (1969) experiments 9 through 16. Each line plots the instability region for an elapsed time (s) given in the legend assuming a cohesion value of 100 Pa.

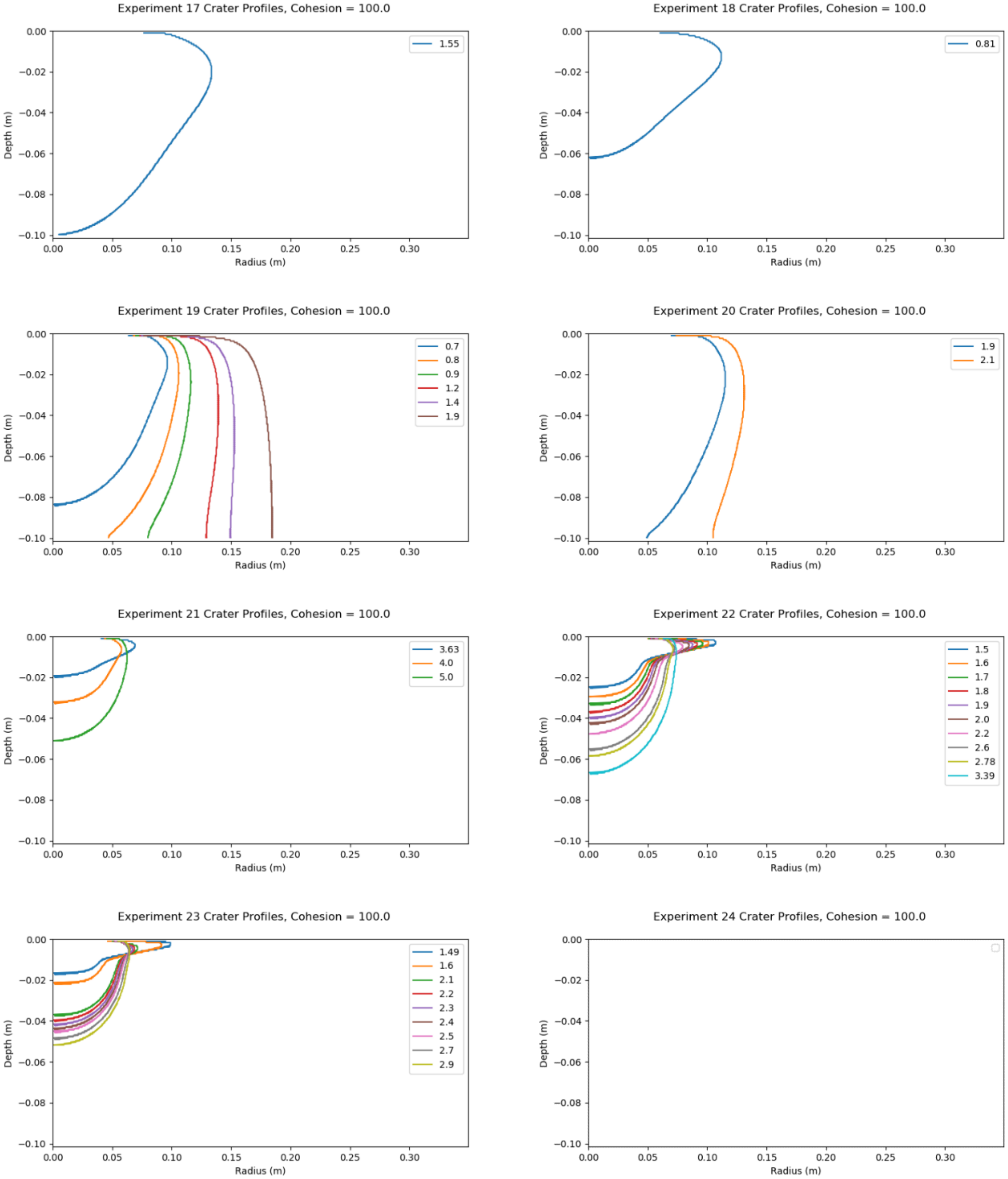

Figure 78: Instability profiles generated by our model for comparison to Land and Scholl (1969) experiments 17 through 24. Each line plots the instability region for an elapsed time (s) given in the legend assuming a cohesion value of 100 Pa.

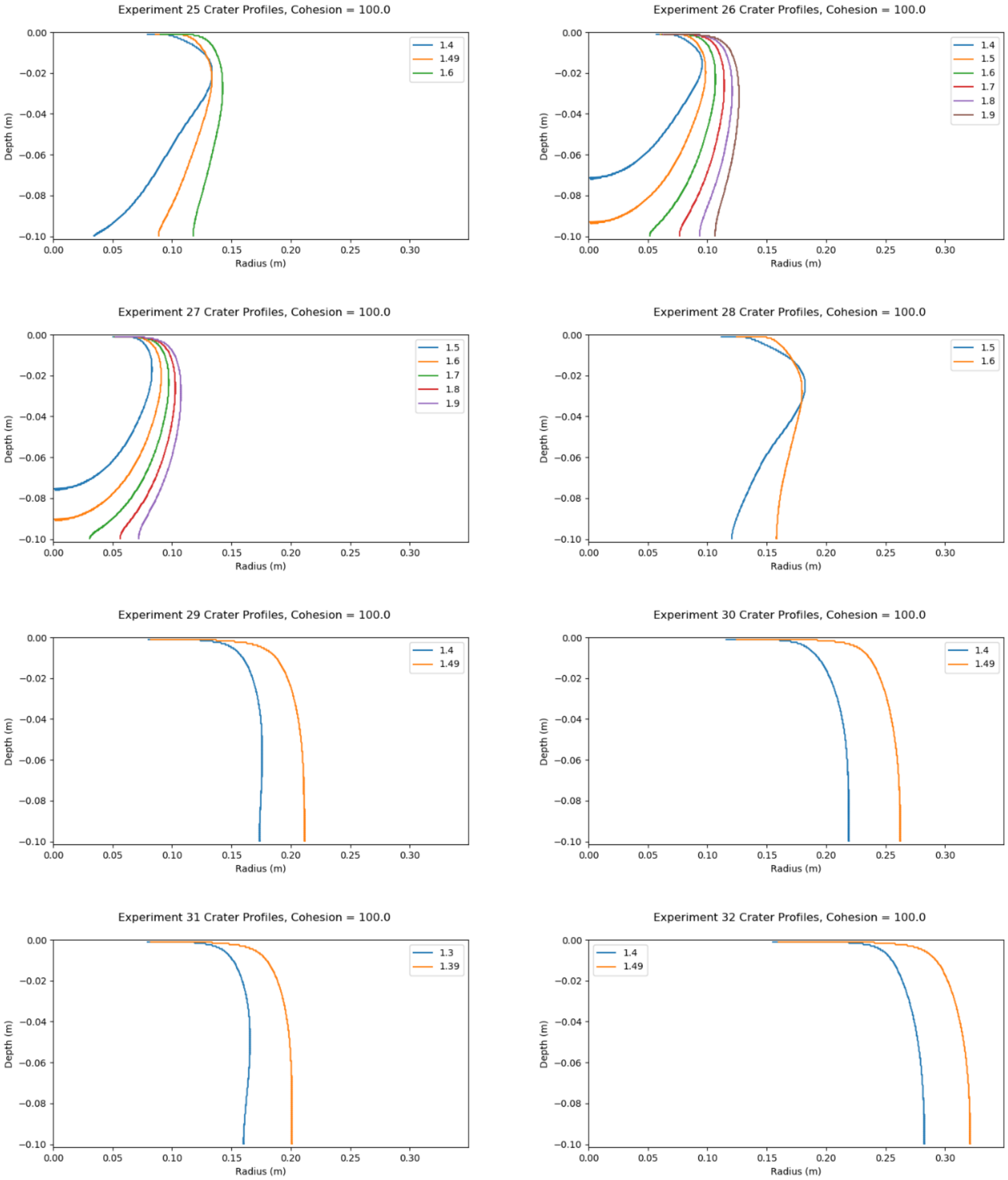

Experiment 25 Crater Profiles, Cohesion = 100.0

Experiment 26 Crater Profiles, Cohesion = 100.0

Experiment 27 Crater Profiles, Cohesion = 100.0

Experiment 28 Crater Profiles, Cohesion = 100.0

Experiment 29 Crater Profiles, Cohesion = 100.0

Experiment 30 Crater Profiles, Cohesion = 100.0

Experiment 31 Crater Profiles, Cohesion = 100.0

Experiment 32 Crater Profiles, Cohesion = 100.0

Figure 79: Instability profiles generated by our model for comparison to Land and Scholl (1969) experiments 25 through 32. Each line plots the instability region for an elapsed time (s) given in the legend assuming a cohesion value of 100 Pa.

APPENDIX D: FRAME-AVERAGED VELOCITY PROFILES

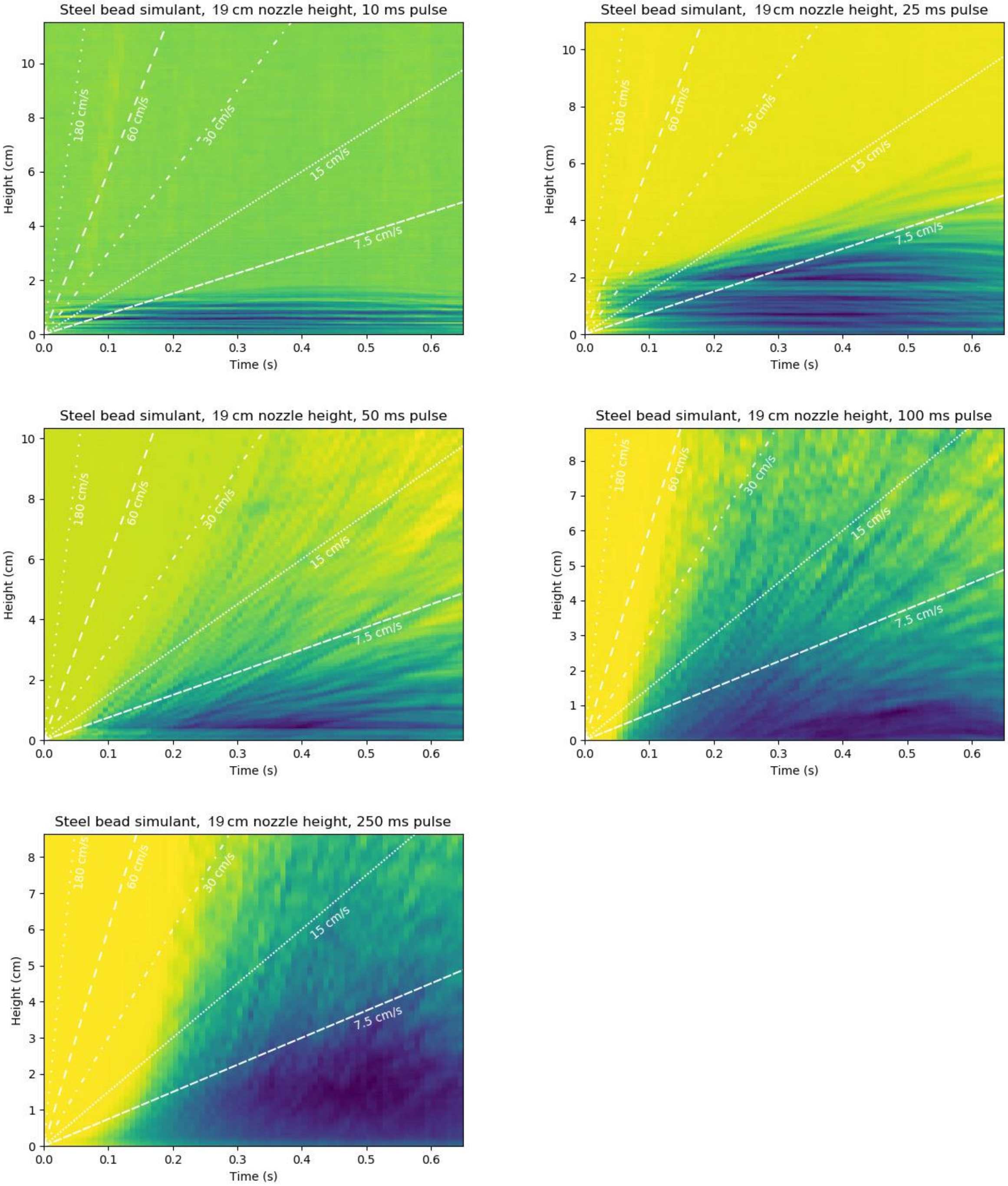

Figure 80: Frame averaged velocity profiles for steel bead simulant experiments conducted at a 19 cm nozzle height, generated as described in Chapter 4. Profiles are shown for example experiments at 10, 25, 50, 100, and 250 ms pulse durations. Shading indicates the presence of ejecta on a scale from yellow (no ejecta) to blue (ejecta blocks backlight). Velocities are indicated by the labelled white lines. Striation angles may be compared with these lines to determine particle velocity trends.

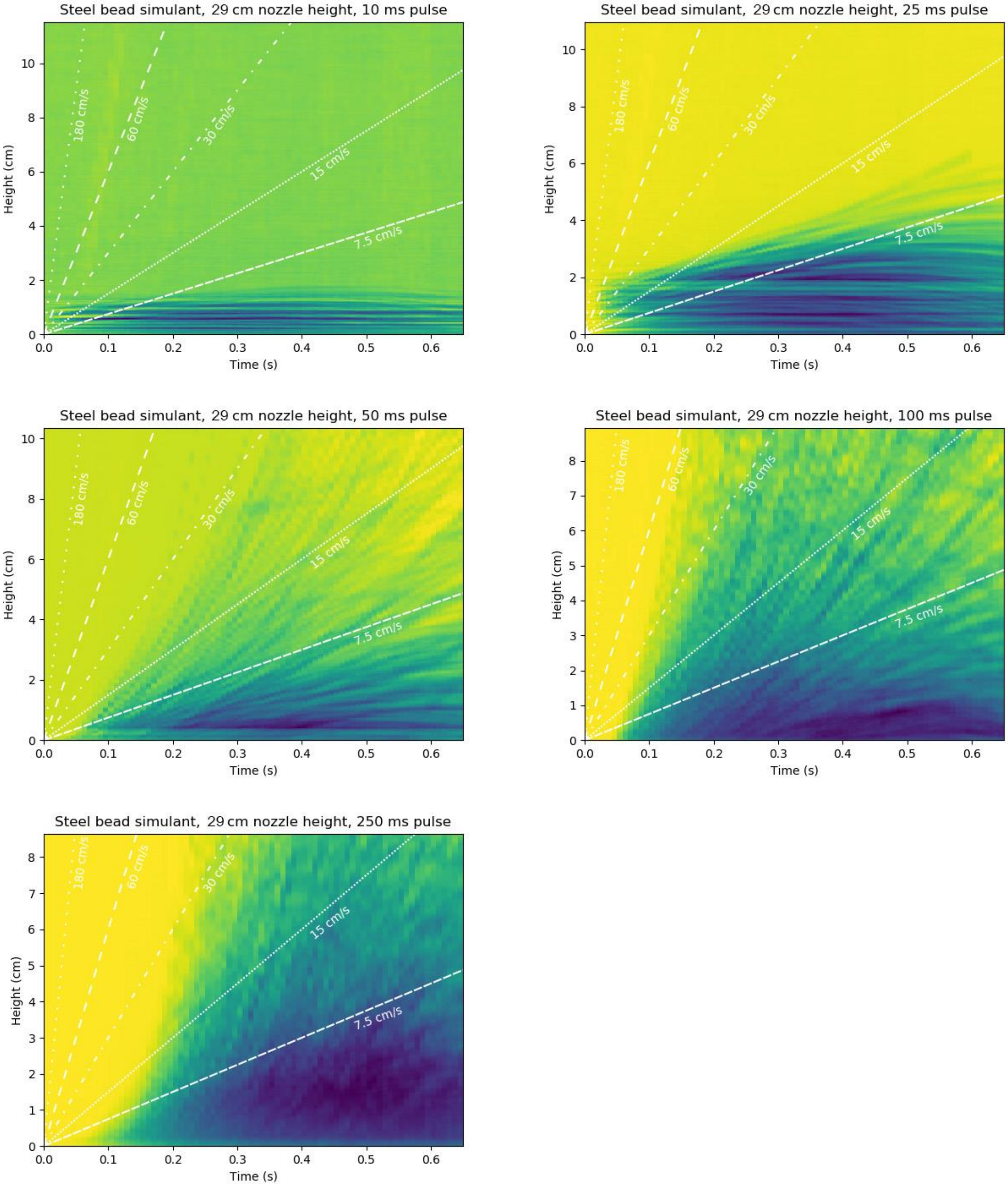

Figure 81: Frame averaged velocity profiles for steel bead simulant experiments conducted at a 29 cm nozzle height, generated as described in Chapter 4. Profiles are shown for example experiments at 10, 25, 50, 100, and 250 ms pulse durations. Shading indicates the presence of ejecta on a scale from yellow (no ejecta) to blue (ejecta blocks backlight). Velocities are indicated by the labelled white lines. Striation angles may be compared with these lines to determine particle velocity trends.

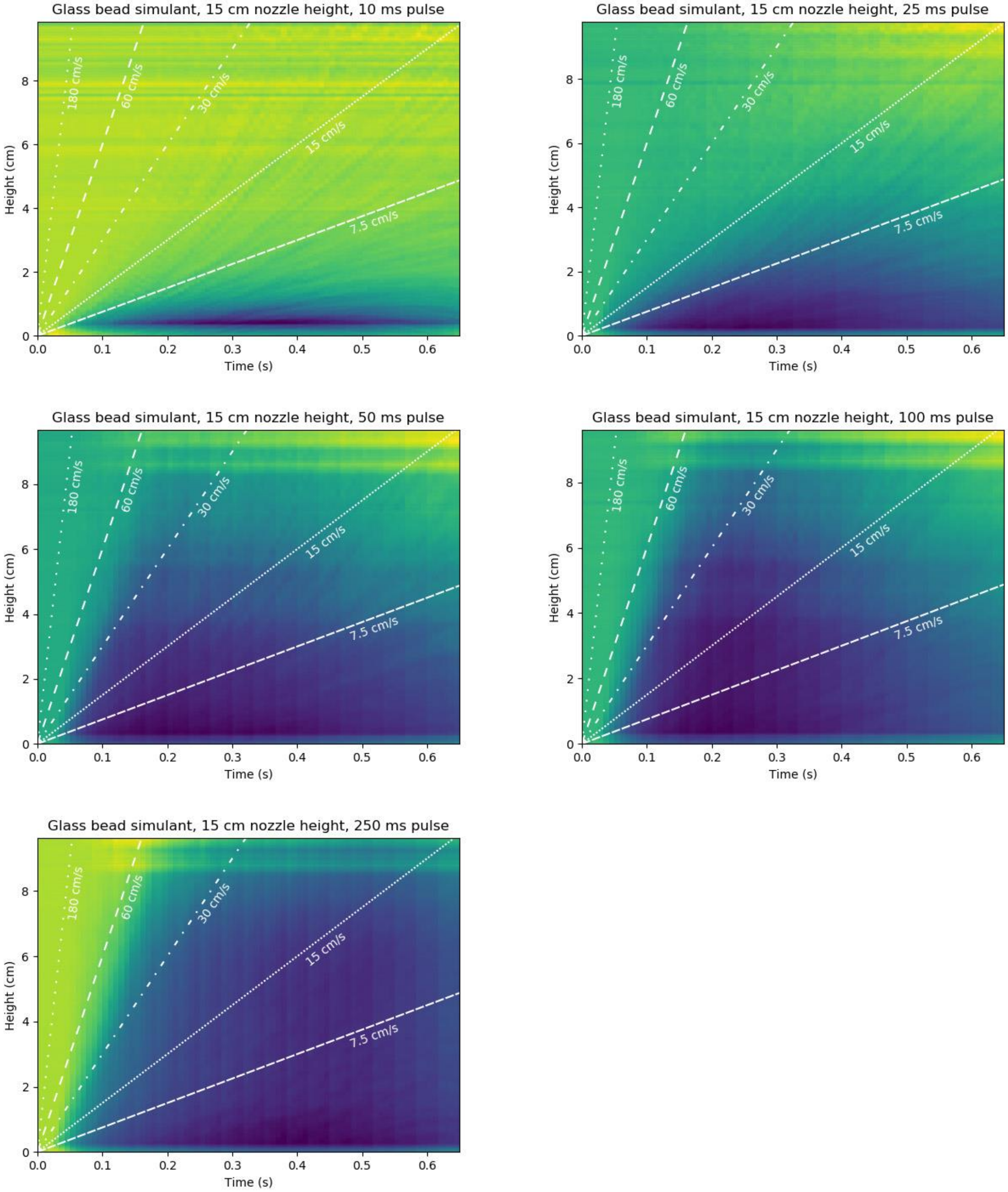

Figure 82: Frame averaged velocity profiles for glass bead simulant experiments conducted at a 15 cm nozzle height, generated as described in Chapter 4. Profiles are shown for example experiments at 10, 25, 50, 100, and 250 ms pulse durations. Shading indicates the presence of ejecta on a scale from yellow (no ejecta) to blue (ejecta blocks backlight). Velocities are indicated by the labelled white lines. Striation angles may be compared with these lines to determine particle velocity trends.

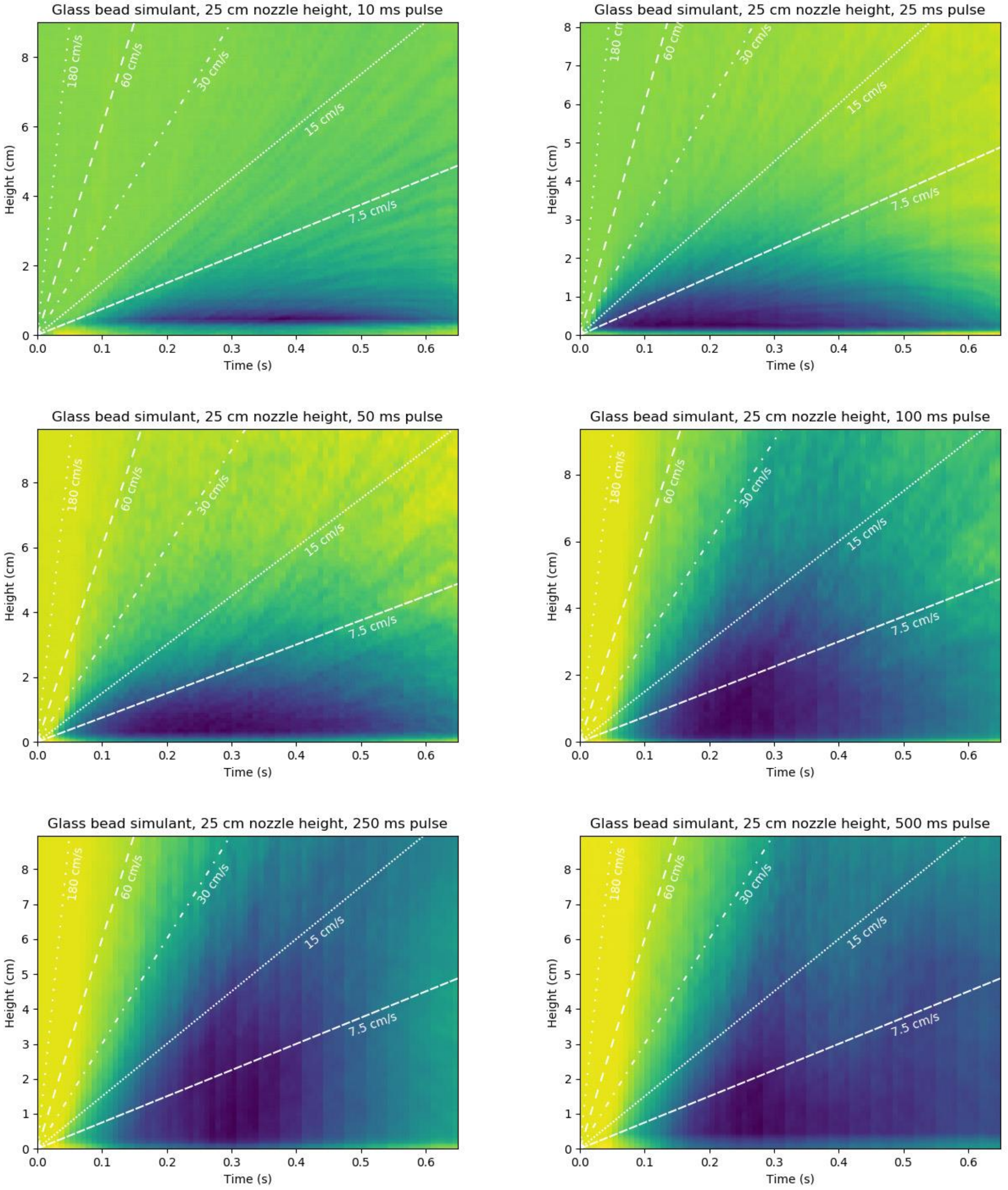

Figure 83: Frame averaged velocity profiles for glass bead simulant experiments conducted at a 25 cm nozzle height, generated as described in Chapter 4. Profiles are shown for example experiments at 10, 25, 50, 100, and 250 ms pulse durations. Shading indicates the presence of ejecta on a scale from yellow (no ejecta) to blue (ejecta blocks backlight). Velocities are indicated by the labelled white lines. Striation angles may be compared with these lines to determine particle velocity trends.

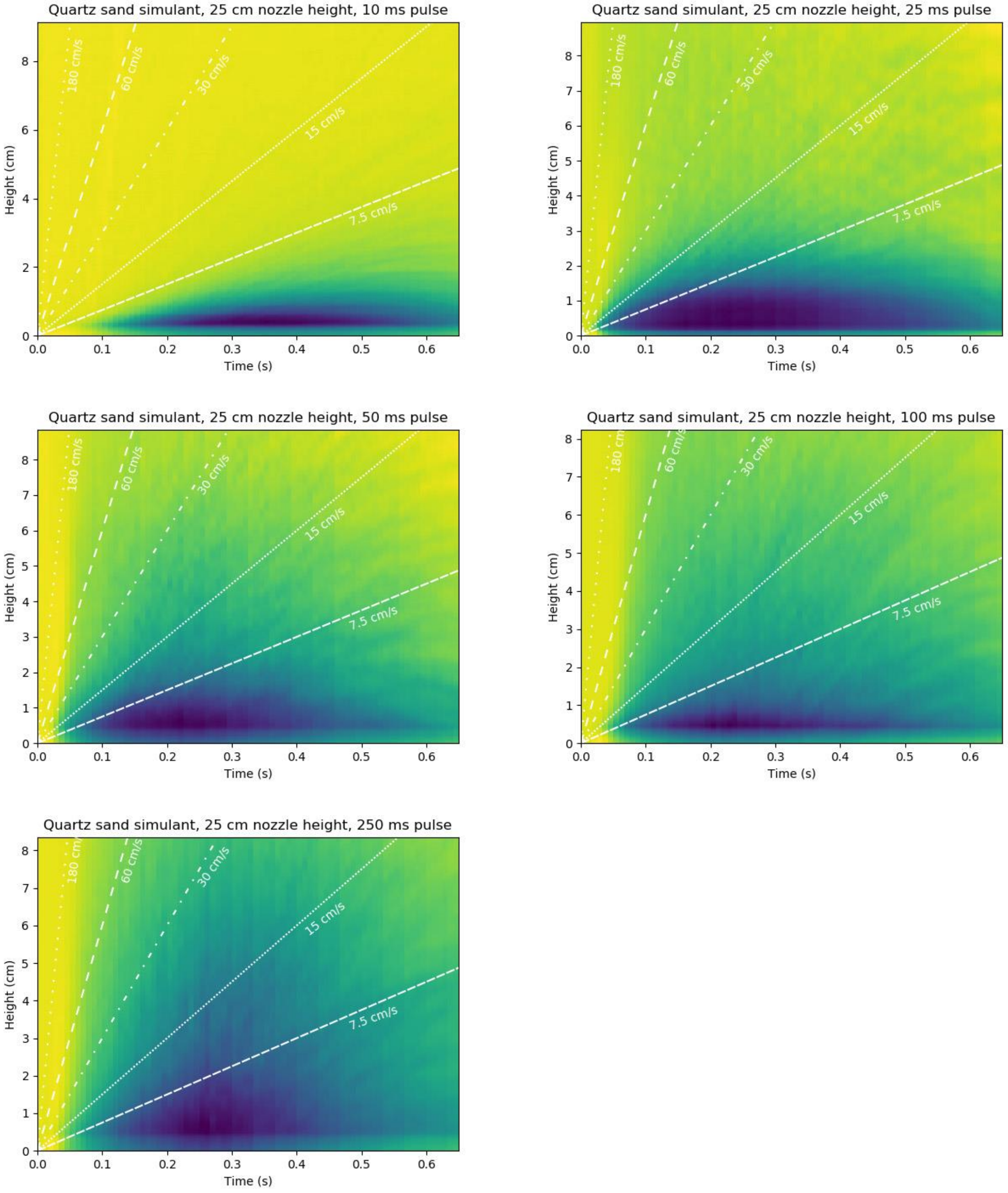

Quartz sand simulant, 25 cm nozzle height, 10 ms pulse

Quartz sand simulant, 25 cm nozzle height, 25 ms pulse

Quartz sand simulant, 25 cm nozzle height, 50 ms pulse

Quartz sand simulant, 25 cm nozzle height, 100 ms pulse

Quartz sand simulant, 25 cm nozzle height, 250 ms pulse

Figure 84: Frame averaged velocity profiles for quartz sand simulant experiments conducted at a 25 cm nozzle height, generated as described in Chapter 4. Profiles are shown for example experiments at 10, 25, 50, 100, and 250 ms pulse durations. Shading indicates the presence of ejecta on a scale from yellow (no ejecta) to blue (ejecta blocks backlight). Velocities are indicated by the labelled white lines. Striation angles may be compared with these lines to determine particle velocity trends.

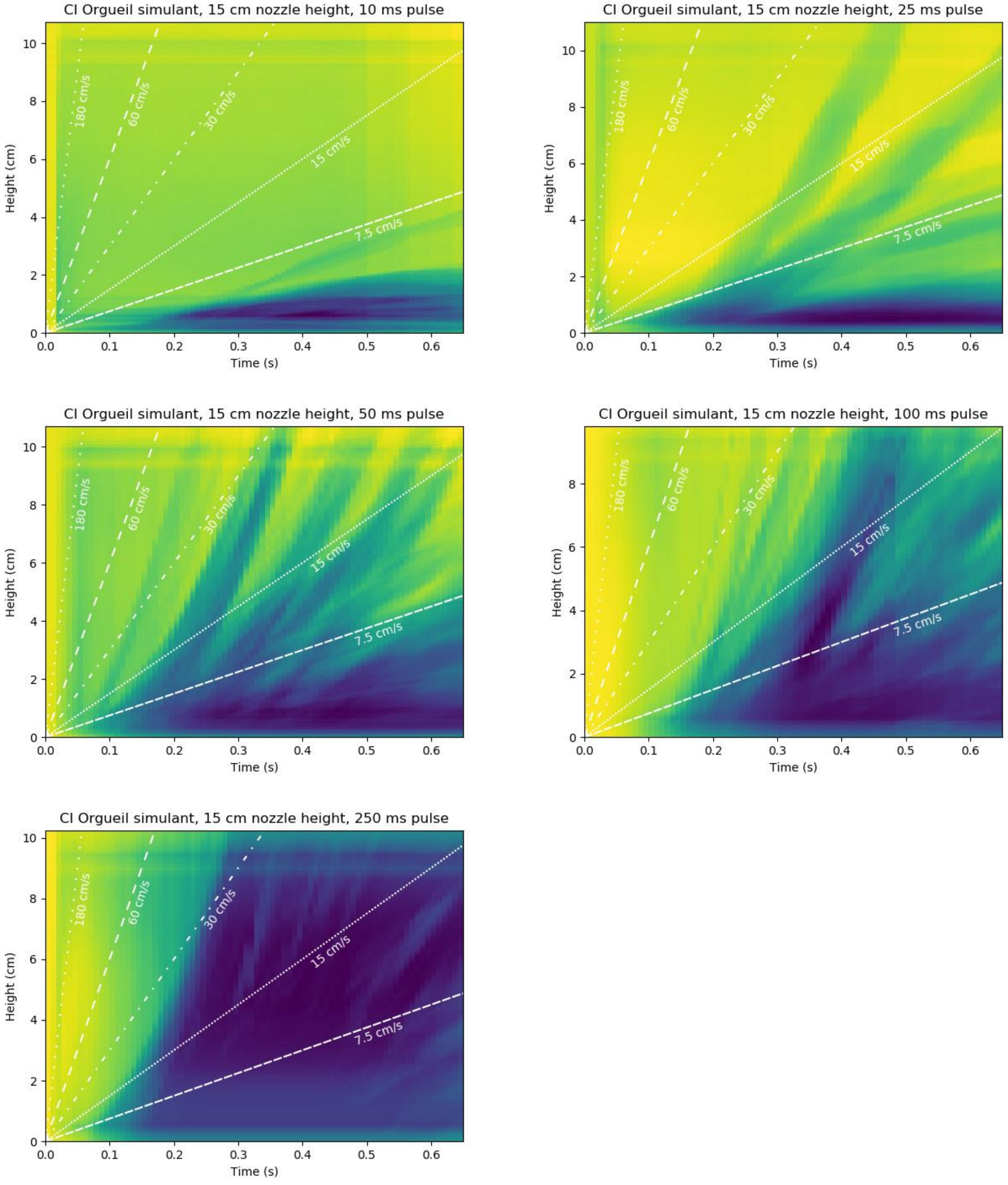

Figure 85: Frame averaged velocity profiles for CI Orgueil simulant experiments conducted at a 15 cm nozzle height, generated as described in Chapter 4. Profiles are shown for example experiments at 10, 25, 50, 100, and 250 ms pulse durations. Shading indicates the presence of ejecta on a scale from yellow (no ejecta) to blue (ejecta blocks backlight). Velocities are indicated by the labelled white lines. Striation angles may be compared with these lines to determine particle velocity trend

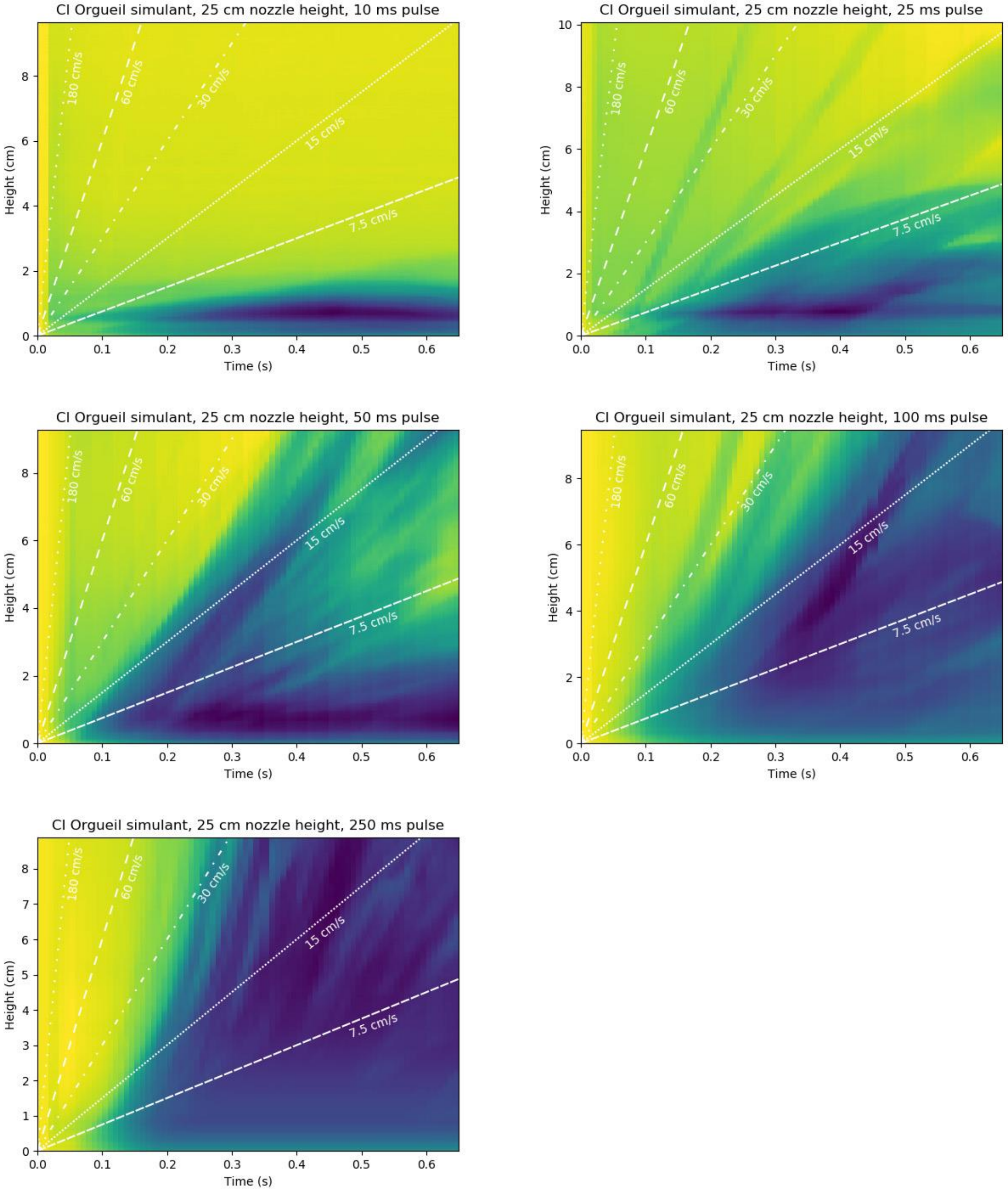

Figure 86: Frame averaged velocity profiles for CI Orgueil simulant experiments conducted at a 25 cm nozzle height, generated as described in Chapter 4. Profiles are shown for example experiments at 10, 25, 50, 100, and 250 ms pulse durations. Shading indicates the presence of ejecta on a scale from yellow (no ejecta) to blue (ejecta blocks backlight). Velocities are indicated by the labelled white lines. Striation angles may be compared with these lines to determine particle velocity trends.

APPENDIX E: COPYRIGHT PERMISSION LETTER

Dear Wesley,

Thank you for your inquiry. As an original author of an ASCE journal article or proceedings paper, you are permitted to reuse your own content (including figures and tables) for another ASCE or non-ASCE publication (including thesis), provided it does not account for more than 25% of the new work.

A full credit line must be added to the material being reprinted. For reuse in non-ASCE publications, add the words "With permission from ASCE" to your source citation. For Intranet posting, add the following additional notice: "This material may be downloaded for personal use only. Any other use requires prior permission of the American Society of Civil Engineers. This material may be found at [URL/link of abstract in the ASCE Library or Civil Engineering Database]."

Each license is unique, covering only the terms and conditions specified in it. Even if you have obtained a license for certain ASCE copyrighted content, you will need to obtain another license if you plan to reuse that content outside the terms of the existing license. For example: If you already have a license to reuse a figure in a journal, you still need a new license to use the same figure in a magazine. You need a separate license for each edition.

For more information on how an author may reuse their own material, please view: http://ascelibrary.org/page/informationforasceauthorsreusingyourownmaterial

Sincerely,

Leslie Connelly

Manager, Publications Marketing

American Society of Civil Engineers

1801 Alexander Bell Drive

Reston, VA 20191

LIST OF REFERENCES

Alexander, J. D., Roberds, W. M., & Scott, R. F. (1966). Soil Erosion by Landing Rockets. *NASA*.

Allan, D., Wel, C. van der, Keim, N., Caswell, T. A., Wieker, D., Verweij, R., Reid, C., Thierry, Grueter, L., Ramos, K., apiszcz, zoeith, Perry, R. W., Boulogne, F., Sinha, P., pfigliozzi, Bruot, N., Uieda, L., Katins, J., … Ahmadia, A. (2019). *soft-matter/trackpy: Trackpy v0.4.2*. https://doi.org/10.5281/ZENODO.3492186

Banfield, D., Spiga, A., Newman, C., Forget, F., Lemmon, M., Lorenz, R., Murdoch, N., Viudez-Moreiras, D., Pla-Garcia, J., Garcia, R. F., Lognonné, P., Karatekin, Ö., Perrin, C., Martire, L., Teanby, N., Hove, B. Van, Maki, J. N., Kenda, B., Mueller, N. T., … Banerdt, W. B. (2020). The atmosphere of Mars as observed by InSight. *Nature Geoscience*. https://doi.org/10.1038/s41561-020-0534-0

Belbin, S. P., & Merrill, R. G. (2014). Boulder capture system design options for the asteroid robotic redirect mission alternate approach trade study. *AIAA SPACE 2014 Conference and Exposition*.

Britt, D. T., Cannon, K. M., Donaldson Hanna, K., Hogancamp, J., Poch, O., Beck, P., Martin, D., Escrig, J., Bonal, L., & Metzger, P. T. (2019). Simulated asteroid materials based on carbonaceous chondrite mineralogies. *Meteoritics and Planetary Science*. https://doi.org/10.1111/maps.13345

Chambers, W. A., & Metzger, P. T. (2016). Regolith Instability Caused by Gas Diffusion: A Case Study of the Asteroid Redirect Mission. *Earth and Space 2016: Engineering for Extreme Environments - Proceedings of the 15th Biennial International Conference on*

Engineering, Science, Construction, and Operations in Challenging Environments. https://doi.org/10.1061/9780784479971.008

Clark, L. V. (1970). Effect of Retrorocket Cant Angle on Ground Erosion - A Scaled Viking Study. *NASA*.

Crocker, J. C., & Grier, D. G. (1996). Methods of digital video microscopy for colloidal studies. *Journal of Colloid and Interface Science*. https://doi.org/10.1006/jcis.1996.0217

Donahue, C. M., Metzger, P. T., & Immer, C. D. (2005). Empirical Scaling Laws of Rocket Exhaust Cratering. *56th International Astronautical Congress*.

Hermalyn, B., & Schultz, P. H. (2010). Early-stage ejecta velocity distribution for vertical hypervelocity impacts into sand. *Icarus*. https://doi.org/10.1016/j.icarus.2010.05.025

Hutton, R. E. (1968). Comparison of Soil Erosion Theory with Scaled LM Jet Erosion Tests. *NASA*.

Immer, C., Lane, J., Metzger, P., & Clements, S. (2011). Apollo video photogrammetry estimation of plume impingement effects. *Icarus*, *214*(1), 46–52. https://doi.org/10.1016/j.icarus.2011.04.018

Jackson, B. E., Evangelista, D. J., Ray, D. D., & Hedrick, T. L. (2016). 3D for the people: Multi-camera motion capture in the field with consumer-grade cameras and open source software. *Biology Open*. https://doi.org/10.1242/bio.018713

Klinkmüller, M., Schreurs, G., Rosenau, M., & Kemnitz, H. (2016). Properties of granular analogue model materials: A community wide survey. *Tectonophysics*, *684*, 23–38. https://doi.org/10.1016/j.tecto.2016.01.017

Krumbein, W. C., & Monk, G. D. (1943). Permeability as a Function of the Size Parameters of Unconsolidated Sand. *Transactions of the AIME*. https://doi.org/10.2118/943153-g

Land, N. S., & Clark, L. V. (1965). Experimental Investigation of Jet Impingement on Surfaces of Fine Particles in a Vacuum Environment. *NASA*, *February*.

Land, N. S., & Scholl, H. F. (1969). Scaled Lunar Module Jet Erosion Experiments. *NASA*.

Lemmon, E. W., McLinden, M. O., & Friend, D. G. (n.d.). Thermophysical Properties of Fluid Systems. In P. J. Linstrom & W. G. Mallard (Eds.), *NIST Chemistry WebBook, NIST Standard Reference Database Number 69*.

Mazanek, D. D., Merrill, R. G., Belbin, S. P., Reeves, D. M., Earle, K. D., Naasz, B. J., & Abell, P. A. (2014). Asteroid redirect robotic mission: Robotic boulder capture option overview. *AIAA SPACE 2014 Conference and Exposition*. https://doi.org/10.2514/6.2014-4432

McKay, D. S., Heiken, G., Basu, A., Blanford, G., Simon, S., Reedy, R., French, B. M., & Papike, J. (1991). The Lunar Regolith (Chapter 7). In *Lunar Sourcebook*.

Mehta, M. (2010). *Plume-Surface Interactions due to Spacecraft Landings and The Discovery of Water on Mars*.

Mehta, M., Renno, N. O., Marshall, J., Rob Grover, M., Sengupta, A., Rusche, N. A., Kok, J. F., Arvidson, R. E., Markiewicz, W. J., Lemmon, M. T., & Smith, P. H. (2011). Explosive erosion during the Phoenix landing exposes subsurface water on Mars. *Icarus*, *211*(1), 172–194. https://doi.org/10.1016/j.icarus.2010.10.003

Metzger, P. T., Immer, C. D., Donahue, C. M., Vu, B. M., Latta, R. C., & Deyo-Svendsen, M. (2009). Jet-induced cratering of a granular surface with application to lunar spaceports. *Journal of Aerospace Engineering*, *22*(1), 24–32. https://doi.org/10.1177/1350508414549885

Metzger, P. T., Immer, C. D., Lane, J. E., & Clements, S. (2008). *Cratering and Blowing Soil By Rocket*. *10*.

Metzger, P. T., Lane, J. E., Immer, C. D., & Clements, S. (2010). Cratering and blowing soil by rocket engines during lunar landings. *Lunar Settlements*, 551–576. https://doi.org/10.1201/9781420083330

Rajaratnam, N., & Beltaos, S. (1977). Erosion by Impinging Circular Turbulent Jets. *ASCE J Hydraul Div*.

Reeves, D. M., Naasz, B. J., Wright, C. A., & Pini, A. J. (2014). Proximity operations for the robotic boulder capture option for the asteroid redirect mission. *AIAA SPACE 2014 Conference and Exposition*. https://doi.org/10.2514/6.2014-4433

Roberts, L. (1964). Exhaust Jet — Dust Layer Interaction During a Lunar Landing. In N. Boneff & I. Hersey (Eds.), *Proceedings of the 13th International Astronautical Congress* (pp. 21–37). Springer-Verlag.

Romine, G. L., Reisert, T. D., & Gliozzi, J. (1973). Site Alteration Effects from Rocket Exhaust Impingement during a Simulated Viking Mars Landing: Part I. *NASA*.

Scott, R. F., & Ko, H. Y. (1968). Transient rocket-engine gas flow in soil. *AIAA Journal*, *6*(2), 258–264. https://doi.org/10.2514/3.4487

Shen, H., Roithmayr, C. M., & Cornelius, D. M. (2014). Controlled ascent from the surface of an asteroid. *AIAA/AAS Astrodynamics Specialist Conference 2014*. https://doi.org/10.2514/6.2014-4303

Small Bodies Assessment Group. (2014). *Report of the Small Bodies Assessment Group Asteroid Redirect Mission Special Action Team*. http://www.lpi.usra.edu/sbag/documents/SBAG_ARM_SAT_Full_Report.pdf

Susorney, H. C. M., Johnson, C. L., Barnouin, O. S., Daly, M. G., Seabrook, J. A., Bierhaus, E. B., & Lauretta, D. S. (2019). The global surface roughness of 25143 Itokawa. *Icarus*.

https://doi.org/10.1016/j.icarus.2019.01.021

Walsh, K. J., Jawin, E. R., Ballouz, R. L., Barnouin, O. S., Bierhaus, E. B., Connolly, H. C., Molaro, J. L., McCoy, T. J., Delbo', M., Hartzell, C. M., Pajola, M., Schwartz, S. R., Trang, D., Asphaug, E., Becker, K. J., Beddingfield, C. B., Bennett, C. A., Bottke, W. F., Burke, K. N., … Lauretta, D. S. (2019). Craters, boulders and regolith of (101955) bennu indicative of an old and dynamic surface. *Nature Geoscience*. https://doi.org/10.1038/s41561-019-0326-6